

N74-29116

**Hamilton  
Standard**

**U**  
DIVISION OF UNITED AIRCRAFT CORPORATION  
**A®**

**FINAL REPORT**

**RI 1170 ADVANCED  
STRAPDOWN GYRO**

**Contract NAS 12-687**

**HSER 6197**

Reproduced by  
**NATIONAL TECHNICAL  
INFORMATION SERVICE**  
US Department of Commerce  
Springfield, VA. 22151

**PRICES SUBJECT TO CHANGE**

203

TABLE OF CONTENTS

<u>Section</u>		<u>Page</u>
1.0	INTRODUCTION	1
2.0	RI 1170 FINAL REPORT	2
	2.1 Summary	2
	2.2 Report Abstract	2
3.0	EXPERIMENTAL DESIGN AND DEVELOPMENT	4
	3.1 Description of RI 1170 Advanced Strapdown Gyro	4
	3.2 Electronics Design	5
	3.2.1 Electronics Description	5
	3.2.1.1 Pulse Torque Servo Amplifier (PTSA)	6
	3.2.1.2 MSE/TCE Description	17
	3.2.2 Summary of 1170 Electronic Development Activity	17
	3.2.2.1 Hybrid Implementation	17
	3.2.2.2 Fabrication	17
	3.2.2.3 Design Problems	20
	3.2.3 MSE Electronics Redesign	21
	3.2.4 Synchronization	25
	3.3 Electronics Packaging	25
	3.3.1 System Configuration	26
	3.3.1.1 System Disc Locations	29
	3.3.1.2 System Interaction	31
	3.3.2 Hybrids	33
	3.4 Deliverable Hardware	37
	3.4.1 General Variations From Original Design	37
	3.4.1.1 Capacitive Pickoff	37



TABLE OF CONTENTS (Continued)

<u>Section</u>	<u>Page</u>
3.4.2.5 RI 1170 Start-Stop Failure Report	58
3.4.2.5.1 Introduction	58
3.4.2.5.2 History of Wheel S/N 010	59
3.4.2.5.3 Analysis Methods and Equipment	59
3.4.2.5.4 Results of Analysis	59
3.4.2.5.4.1 Postive Thrust Plate, P/N 31158-1	60
3.4.2.5.4.2 Negative Thrust Plate, P/N 31159-1	60
3.4.2.5.4.3 Probe Analysis Results for Thrust Plates	60
3.4.2.5.4.4 Shaft, P/N 31157-1	60
3.4.2.5.4.5 Rotor Halves, P/N 31153-1	68
3.4.2.5.5 Conclusions	68
3.4.2.6 RI 1170 Gyro No. 2 Failure (Wheel S/N 021)	68
3.4.2.7 Speedring Rework of Wheel 021 Shaft and Wheel S/N 011 Rotor	70
3.4.3 Integrated RI 1170 Gyro S/N 3	70
3.4.4 Breadboard System	70
3.4.5 Excitation and Synchronization Unit	72
3.4.6 Electronics Design Critique	73
4.0 GYRO EVALUATION - SINGLE AXIS TEST	75
4.1 Gyro S/N 1	75
4.2 Gyro S/N 2	115
4.3 Gyro S/N 3	117

TABLE OF CONTENTS (Continued)

Section

APPENDIX A - OPERATING INSTRUCTIONS FOR THE EXCITATION  
AND SYNCHRONIZATION UNIT

APPENDIX B - AN ANALYSIS OF THE FAILURE OF RI 1170 GAS  
BEARING S/N 12

APPENDIX C - MATHEMATICAL ANALYSIS GAS BEARING WHEEL  
COMPUTER PROGRAM

APPENDIX D - COMPARISON OF TYPICAL GAS BEARINGS

FINAL REPORT

RI 1170 ADVANCED STRAPDOWN GYRO

CONTRACT NAS 12-687

1.0 INTRODUCTION

The RI 1170 Advanced Strapdown Gyro Program is a study and design program whose purpose was to analytically determine the design concept requirements for strapdown navigational gyro applications. A design for a single-channel gyro loop with integral pulse torquing electronics, heater controllers, and suspension system electronics was generated and the hardware purchased, fabricated, assembled, and tested.

As part of this program, an interim report was written by Hamilton Standard titled, "The Design of An Advanced Strapdown Gyroscope", Report No. HSER 5579. The interim report detailed the complete analyses, tradeoffs, and designs for both the gyroscope and the integral electronics. This final report details the results of the fabrication and testing of the hardware and, further, discusses any design or fabrication changes from the original design report.

2.0 RI 1170 FINAL REPORT

2.1 Summary

Since the original design report was completed, the emphasis has been placed on fabrication and test of hardware. The intent of the hardware phase of the program was directed toward completing several full-up single channel sensor systems as well as testing and evaluating certain assemblies of the system design. As a result, three complete gyros were fabricated. During the course of testing, one of the gyros, S/N 2, failed due to a gas bearing wheel seizure. A second unit, S/N 1, completed a long series of tests and was integrated with a set of breadboard electronics mounted external to the gyro. The third unit, S/N 3, has been used to study the problems associated with integration and installation of the hybrid electronics consisting of a PTSA, temperature controller and Digital Control Electronics.

2.2 Report Abstract

The major components of the RI 1170 gyroscope are described. A detailed functional description of the electronics including block diagrams and photographs of output waveshapes within the loop electronics are presented. An electronic data flow diagram is included.

Those gyro subassemblies that were originally planned for this development effort and subsequently changed or modified for one reason or another are discussed in detail. Variations to the original design included the capacitive pickoffs, torquer flexleads, magnetic suspension, gas bearings, electronic design, and packaging. The selection of components and changes from the original design and components selected are discussed.

Device failures experienced throughout the program are reported and design corrections to eliminate the failure modes are noted. Major design deficiencies such as those of the MSE electronics are described in detail. Modifications made to the gas bearing parts and design improvements to the wheel are noted. Changes to the gas bearing prints are included as well as a mathematical analysis of the 1170 gas bearing wheel by computer analysis. The mean free-path effects on gas bearing performance is summarized.

The report discusses the packaging concept of the electronics including the selected locations for the hybrid discs within the system. With regard to the system packaging, the report discusses the importance to the placement of the electronic assemblies and the existing interaction of the various electronic modules. The advantages of using the hybrid circuits, and a brief description of the fabrication of the wafer along with manufacturing techniques and processes are presented.

2.2 (Continued)

Photographs of a wafer are shown. The problems of testing the wafers and the advantages and disadvantages of the as-packaged design noted. Problems with the wafer fabrication are noted as well as variations to the original design.

The 1170 wheels were tested independently and numerous parameters recorded at various wheel speeds. The wheels were slew tested, start/stop tested, static stiffness tested and the results reported. An analysis of critical gas bearing surfaces on a wheel which failed to start is presented along with SEM photos. A test summary on each of the wheels tested is included.

A chronological summary of each of the gyros tested is presented. A test summary including test procedures, test data and results of testing mostly with Gyro S/N 1 are included. Performance tables and graphs are incorporated.

Single channel breadboard hardware which has been delivered is discussed.

An appendix to the report includes the operating procedure for the interface unit, wheel failure report, and computer program for the mathematical analysis of the gas bearing wheel.

### 3.0 EXPERIMENTAL DESIGN AND DEVELOPMENT

#### 3.1 Description of RI 1170 Advanced Strapdown Gyro

The HSES 1170 gyroscope is a single-degree-of-freedom, floated, rate integrating gyro designed for use with an internal pulse rebalance loop and heater controller. The following is a brief description of its major components.

- Spin Motor - The hysteresis synchronous motor used in this gyro is operated at a synchronous speed of 48,000 rpm. The motor is three-phase, four-pole, wound in 24 slots for optimum performance, and is excited at 1.6 KHz.
- Gas Bearing - A self-acting gas bearing wheel, which operates with hydrogen as a lubricant, is employed in this design. A split rotor is used to give a high angular momentum to mass ratio. The grooves in the journal are helical to suppress half-speed whirl and to lower the attitude angle. Spiral grooved thrust bearings are incorporated. Clearance in the bearings is 40 micro-inches. The bearing surfaces are beryllium oxide and aluminum oxide ceramics.
- Float - The "H" type float is made from beryllium oxide. This construction offers high stability, low expansion and high thermal conductivity.
- Pickoff - The capacitive pickoff is gold-plated Kapton cemented onto the outside of the float sleeve and the inside of the inner return path of the torquer. Buffer preamplifiers are built into the gyro to reduce noise problems.
- Torquer - The torquer is a moving coil, permanent magnet design utilizing platinum cobalt magnets. There are two windings - a main winding of output equivalent to 60 deg/sec input rate and a command winding of 1 deg/sec output. Temperature compensation is provided in the rebalance loop by means of a sensing thermistor.
- Flexleads - Seven axial helix flexleads are utilized. They are made from gold-plated aluminum ribbon. The leads are specially soldered to their mounting clips. The lead is made from 0.030 x 0.001 inch ribbon.

3.1 (Continued)

- Active Magnetic Suspension - The utilization of an active magnetic suspension was originally planned for the output axis. It was designed to withstand a radial load of one pound without physical contact. For suspension purposes, common windings on a stator both sensed and drove the float. To separate the signals, two discrete frequencies were used. An active servo loop provided a current to balance the radial and axial forces on the float. The suspension system used five loops, four radially (X and Y at each end), and one axially (Z channel). The loops are in microcircuit form, integrated with the gyro. This design concept proved to be unwieldy; and, although the breadboard electronics included the MSE, a ball bearing suspension was subsequently incorporated in its place in the final S/N 3 gyro.
- Case and Mounting Interface - The gyro is mounted on a plane normal to the input axis, and is designed to be field replaceable without realignment. The case carries the gyro heater system.
- Rebalance Electronics - A dual scale factor pulse torque servo amplifier is employed. It is scaled for 0 to 30 deg/sec and 30 to 60 deg/sec. The rebalance loop, including the digital control electronics, was designed to be integral with the gyro, so that each gyro is normalized, and field recalibration is not necessary after interchanging gyros.
- Temperature Controller - A 20 watt heater is used for gyro fine temperature control. Platinum resistance sensors are utilized. The control electronics are in microcircuit form, integral with the gyro; they operate from a 28 V DC line.

3.2 Electronics Design

3.2.1 Electronics Description

The RI 1170 gyro electronics were designed to provide the following functions:

- Torque Rebalance
- Float Suspension
- Temperature Control

These circuits were designed for operation within the gyro in order to form an integrated single channel sensor/electronics assembly.

3.2.1 (Continued)

Torque rebalance is provided by a pulse torque servo amplifier (PTSA). This circuitry maintains float position by bucking out rate induced float torques through a permanent magnetic torque generator. The PTSA operates in a quantized forced limit cycle mode. The quantized forced limit cycle approach has been used by HSES in strapdown guidance systems aboard the Lunar Module, the Delta Vehicle and the Viking Lander.

Suspension of the float is attained through electro-magnetic attraction. Four coils at each end of the gyro are arranged in opposing pairs, each exerting a pulling effect on the float. The drive to the coils is varied by either a closed loop active system or a passive system in which inductance changes of the coil tune a resonant LC circuit and change the coil current.

Thermal control of the gyro is maintained by width modulating the heater voltage in proportion to the platinum sensor resistance. This technique is used to minimize power dissipation in the control element.

Since all electronics required for a single channel, exclusive of power sources, are contained within the gyro, size constraints mandated the use of hybrid circuits. The extremely high packing density required that the hybrid circuits be stacked in an interconnected array. The penalty paid for the stacked array was the loss of independent functional modules.

3.2.1.1 Pulse Torque Servo Amplifier (PTSA)

The gyro is operated in a rebalance mode maintained by the PTSA. The PTSA receives an error signal from the inertial sensor which is amplified and converted to a width modulated digital torquing signal. This signal is used to rebalance the inertial sensor, and must with the other torques acting on the gyro's float sum to zero. With the exception of error torques, the PTSA derived torque must equal the rate induced torque.

The PTSA output is a precisely controlled 1 KHz rectangular current waveform. The mean value of the torquing current is varied by precisely controlling, in discrete steps, the duty cycle of the current waveform. During closed loop operation, the integral of the 1 KHz rectangular torquing waveform corresponds to the sensor output.

The PTSA may be visualized in four sections; amplifier and demodulator, quantizer, bridge and driver, and current regulator. The gyro error signal is amplified and converted to a DC signal by the amplifier and demodulator section. Frequency compensation is added to the DC signal to achieve a desirable closed loop gyro/PTSA frequency response. A 1 KHz sawtooth

## 3.2.1.1 (Continued)

signal is summed with the error signal in the quantizer, which is then level detected to produce a 1 KHz width modulated error signal. The width modulated signal is gated with a digital signal to provide a precisely controlled retorqueing signal. This signal is used to drive the 'H' bridge current switches in the bridge and driver section. The current regulator is used to provide a constant current to the 'H' bridge. The level of the current through the bridge directly affects the current integral and hence the scale factor. In this design, the current regulator can operate at two discrete levels to provide a high scale factor, high-rate capability and a low scale factor, low rate capability.

Figure 3.2-1 is a block diagram of the PTSA.

#### Amplifier and Demodulator

The gyro utilizes a capacitive bridge pickoff operating at 50 KHz to determine float angular position. Since the capacitive bridge is a high impedance device, the design of the bridge preamplifier required a combination of both high input impedance and high common mode rejection. The available integrated circuit amplifiers do not satisfy these requirements because the common mode rejection becomes negligible at high frequency.

The RI 1170 preamplifier uses source follower FET inputs driving bipolar emitter followers and then a stage that provides a differential output and a sum output. To enhance the common mode rejection above that normally provided by a differential amplifier, bootstrapping of both FET's gate bias and the drain voltage for common mode signals, has been incorporated through use of the sum signal. The high common mode rejection reduces the sensitivity to interference that couples into the pickoff bridge.

Noise on the pickoff signal is further reduced by the use of filtering at the carrier frequency. Since the electronics are of hybrid construction, the use of LC filtering is precluded, requiring the use of active filtering. Unity gain transistor circuits were used for the active elements in the filters because at the time of design, multiple amplifier IC's were not available. Figures 3.2-2 and 3.2-3 are photographs of the pickoff signals before and after filtering.

The AC pickoff signal is converted to a DC signal by a synchronous demodulator circuit that uses an IC amplifier switched between the inverting and non-inverting mode by MOS FET choppers at the pickoff excitation frequency. The DC pickoff signal undergoes further processing to provide stable gyro/PTSA loop characteristics. To minimize capacitor values, consistent

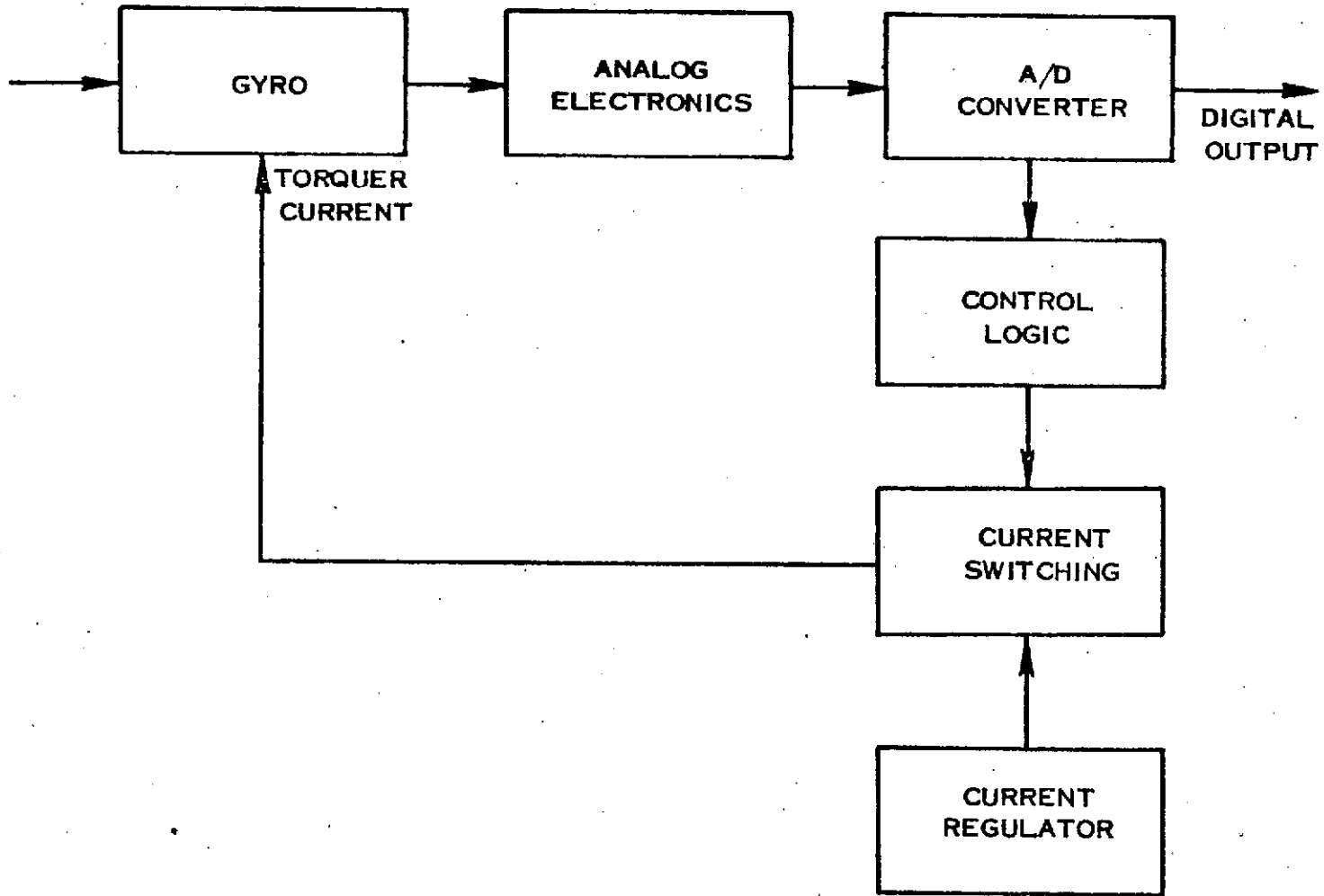


Figure 3.2-1 Gyroscope - PTSA Block Diagram

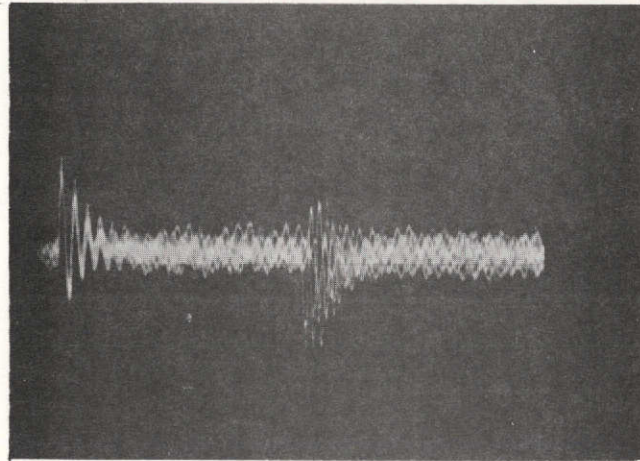


Figure 3.2-2. RI 1170 Pickoff Signal Before Filtering

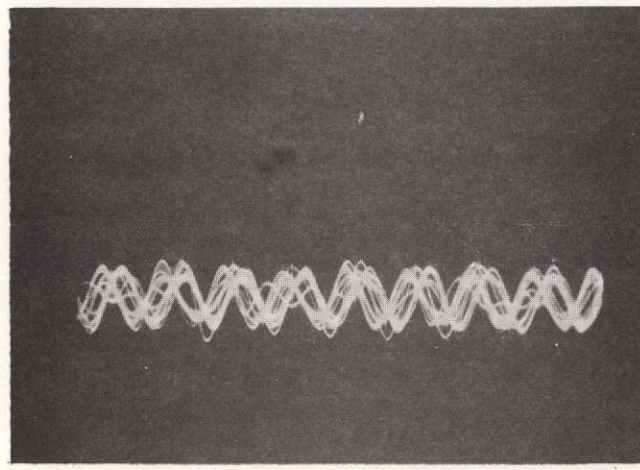


Figure 3.2-3. RI 1170 Pickoff Signal After Filtering

## 3.2.1.1 (Continued)

with hybrid design, compensation components were placed in the feedback of the IC amplifier.

Quantizer

The processed DC pickoff information is converted to a quantized width modulated 1 KHz binary signal in the quantizer. The DC signal is converted to a width modulated binary by summing the DC signal with a 1 KHz sawtooth, Figure 3.2-4, and level detecting the resultant signal in a logic chip. The logic chip is used as a latch that is reset by the 0-16 blanking. The 0-16 blanking and 240-256 blanking signals were incorporated to restrain the duty cycle of the width modulated torquing signal from reaching 0% or 100% at which time, due to the loss of switching, scale factor linearity would be degraded. The width modulated binary with the blanking restraint is quantized by passing it through a flip flop which constrains switching of the binary to occur in synchronism with the clock. A second flip flop provides buffering to improve trimming stability. Figure 3.2-5 is a photograph showing the 240-256 blanking, 0-16 blanking, a 1 KHz synchronization pulse and the data out; in this case, 16 pulses/limit cycle since the loop is hardover negative.

A feature of the quantizer is that the amplitude of the ramp is adjusted to maintain gyro/PTSA loop gain constant when the scale factor is switched between hi and low mode. Without this feature, the closed loop bandwidth would be higher in the hi scale factor mode.

Current Regulator

Figure 3.2-6 is a simplified schematic of the current regulator showing how the regulator sense resistors are selected. S1-B is a composite MOS FET/BIPOLAR transistor arrangement with an effective infinite impedance for the input signal. The offset of S1-B does not affect the voltage at the sense resistor. S1-A is a MOS FET switch that may be used in this application because amplifier input current is negligible causing no voltage drop across the FET to occur .

$V_{CC}$ , the current regulator supply voltage, is switched between 29 V and 37.2 volts to maintain the current regulators compliance range when the high scale factor current increases the torquer load voltage. The current regulator's gain is maintained constant when the sensing resistor is changed by changing the output transistor's emitter resistor,  $R_e$ .

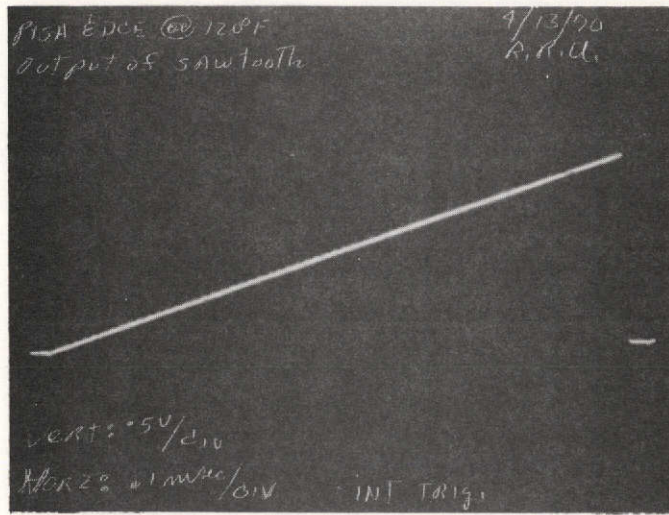


Figure 3.2-4. 1 KHz Sawtooth Waveform

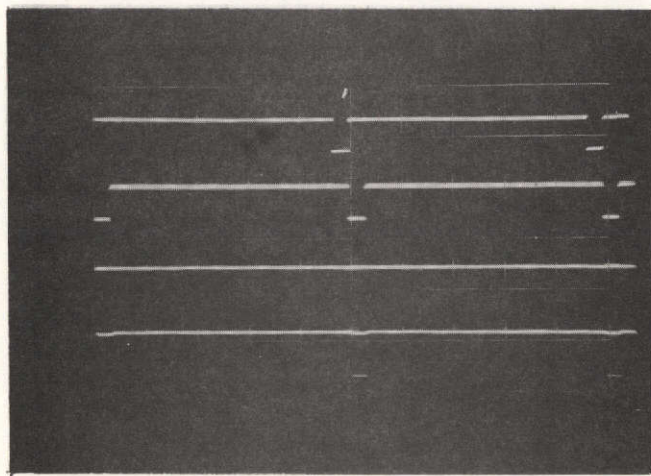


Figure 3.2-5. 240-256 Blanking Signals

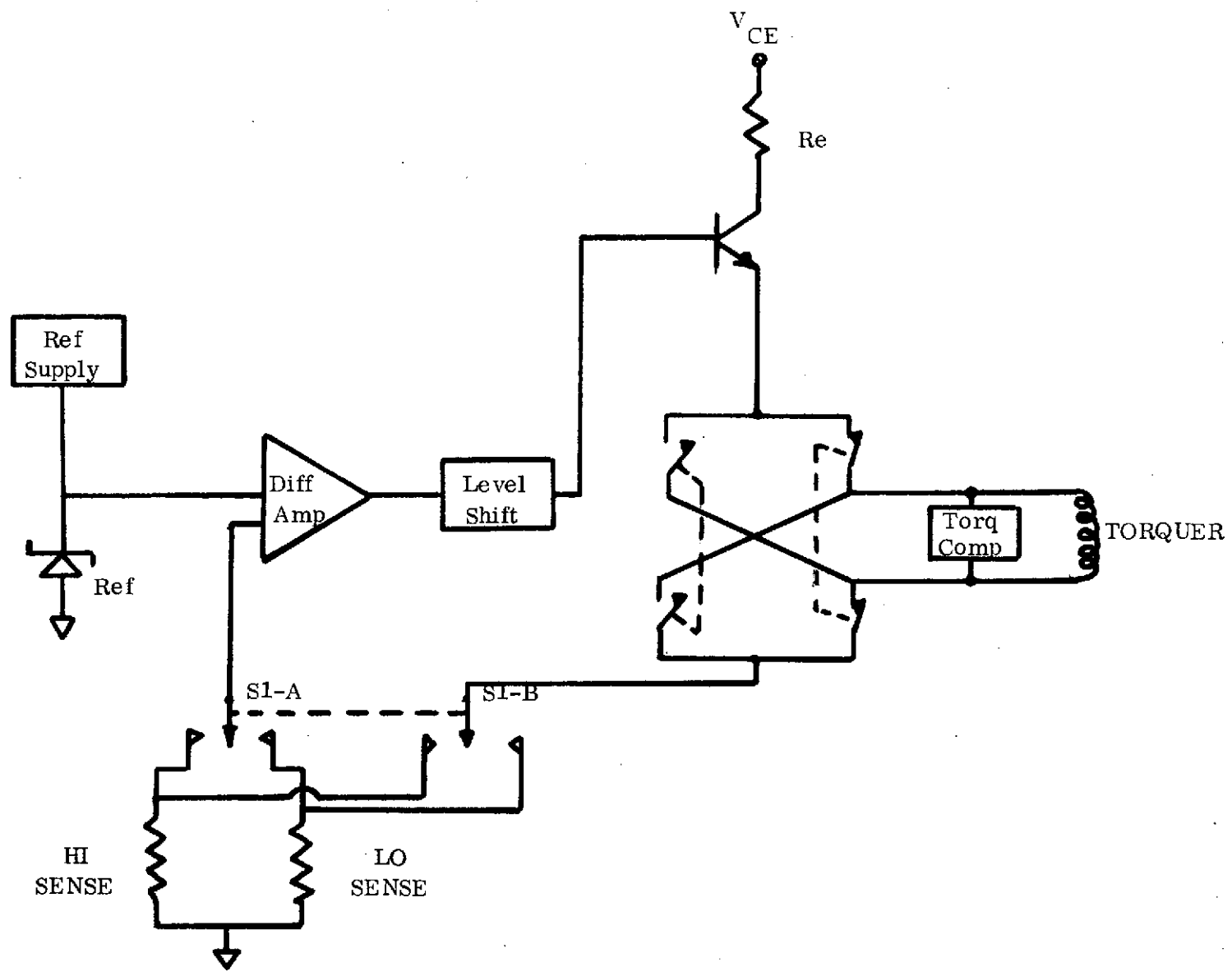


Figure 3.2-6 Current Reg Simplified Schematic

## 3.2.1.1 (Continued)

Figure 3.2-7 is a photograph of the switching transients generated by the reversals of current through the 'H' bridge. The extremely fast switching transient is beyond the ability of the regulator to follow. The slower switching transient is within the response time of the regulator and is compensated for after approximately 3  $\mu$ sec.

Bridge and Driver

The bridge and driver operate, in conjunction with the quantizer's output, to alternate a constant current signal through the torquer to form the width modulated torquing signal. The design of the PTSA prevents modules other than bridge and driver from introducing negligible performance errors. Errors that are significant are those which cause changes to the current-time integral at the torquer. The dominant causes of these errors in 'H' bridges are: switching signals (base drive to the switching transistors), leakage currents and switching times. In the design of this PTSA, these error sources have been minimized by the design configuration and the selection of components. Switching signals have been almost eliminated as an error source by the use of composite bipolar - MOS FET arrangement. This arrangement has the advantage of the current capability of a bipolar transistor and the almost infinite input impedance.

Switching time has been minimized by operating the bridge transistors in a non-saturated mode. The driver circuit for the bridge was designed to be non-saturating and also includes an FET to form an active load maintaining a low output impedance for both states of the driver. Figure 3.2-8 shows the switching of the torquer indicating a switching time of 300 nsec.

Circuit configuration limits performance affecting leakage to those of the base emitter junctions of the bridge transistors. This leakage current is normally small and is maintained stable by the temperature control of the gyro. The configuration of the bridge ensures low voltage sensitivities which is desirable for dual scale factor operation where both currents and voltages within the bridge have two stable levels.

Figure 3.2-9 is a photograph of the voltage across the gyro torquer in the low mode where torquer current is 72.5 mA. Figure 3.2-10 is a photograph of the voltage at each terminal of the torquer referenced to ground. The torquer is basically an inductive load that is compensated by a resistor capacitive network to appear resistive. The voltage waveform shows that torquer compensation is sufficient to maintain torquer voltages within the compliance range of the current regulator.

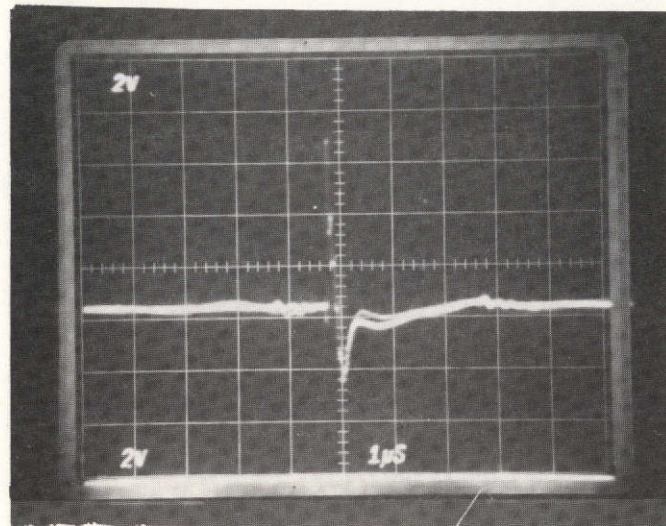


Figure 3.2-7. Switching Transients Generated By Reversals of Current Through The 'H' Bridge

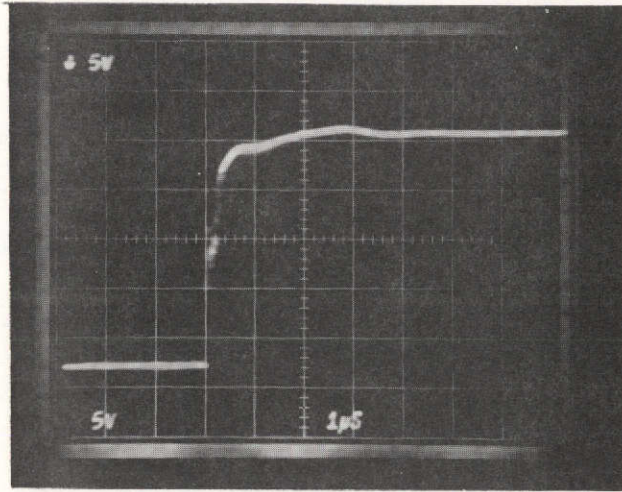


Figure 3.2-8. Torquer Switching

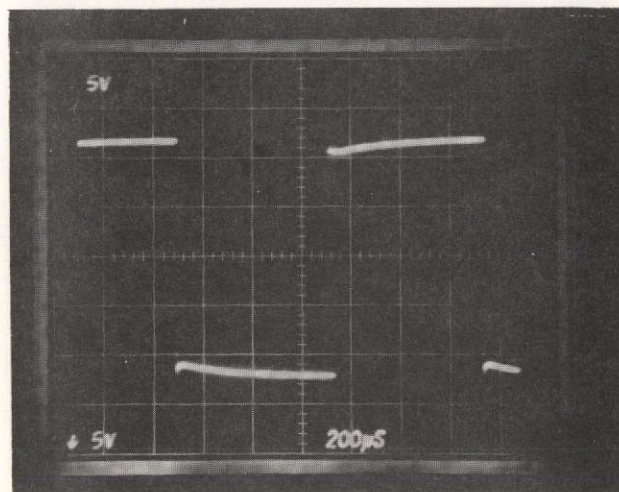


Figure 3.2-9. Torquer Voltage - Low Mode

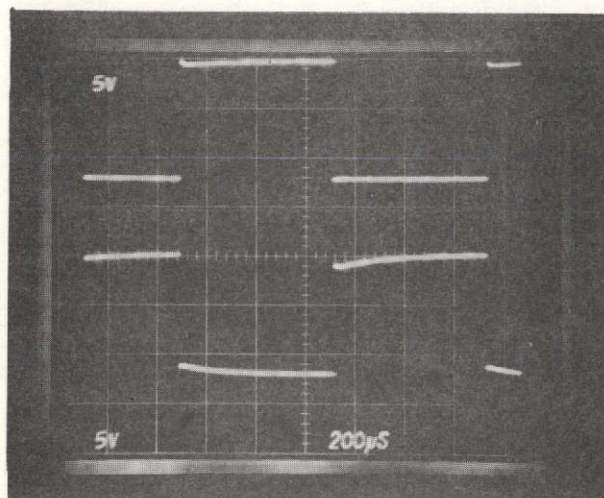


Figure 3.2-10. Torquer Voltage Referenced to Ground

## 3.2.1.1 (Continued)

Figures 3.2-11 and 3.2-12 are photographs of positive and negative rate inputs to the system.

Figure 3.2-13 is a photograph of the torquer voltage with the PTSA in the high mode where torquer current is 145 mA. Figure 3.2-14 shows the torquer currents referenced to ground.

3.2.1.2 MSE/TCE Description

The original Magnetic Suspension Electronics (MSE) and the present Temperature Control Electronics (TCE) are described in detail in the Design Report, HSER 5579. The MSE design is described in Section 3.2.3 of this report.

3.2.2 Summary of 1170 Electronic Development Activity

At the close of Phase I, the 1170 electronic design and analysis had been completed on all 1170 circuits. Phase II covered the fabrication of the hybrid circuits and integration of the electronics into the gyros. The highlights of the activities and problems of this phase are discussed below.

3.2.2.1 Hybrid Implementation

The hybrid implementation selected utilized a mother substrate with small functional substrates mounted on it. A detailed description of this system is covered in Section 3.3.2.

3.2.2.2 Fabrication

MOS FETS - The initial design incorporated MOS FET's as switching elements. The devices selected, and actually tested in the Phase I breadboard were Fairchild devices selected for both their high breakdown voltage and superior life characteristics of the silicon nitride passivation. These units did not have internal zener protection and could not be handled safely in the chip form required in the hybrid fabrication. Several devices were suggested by FMI as alternates. None were completely satisfactory but those providing the minimum compromise were tested. The devices finally selected were the IT 1701 and the M116, a P-Channel and N-Channel, respectively. These devices are zener protected, have suitable leakage and switching characteristics but have lower voltage rating than the original devices. The PTSA was modified to accept these lower breakdown voltages resulting in a maximum rate capability of 60 deg/sec.

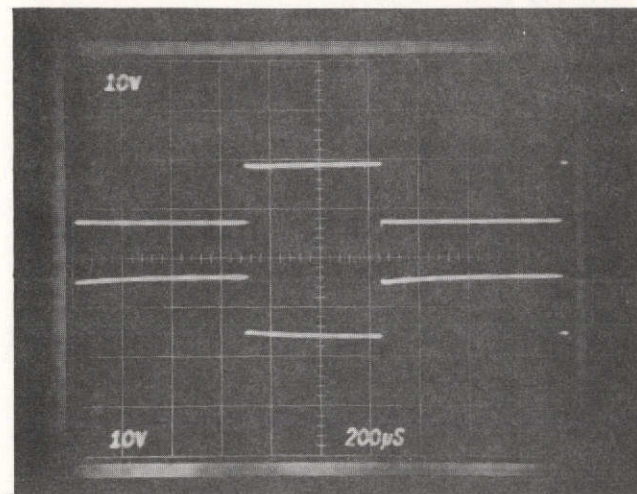


Figure 3.2-11. Positive Rate Input

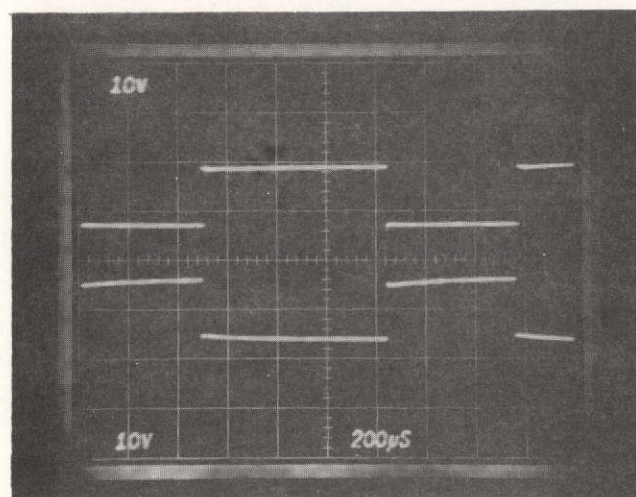


Figure 3.2-12. Negative Rate Input

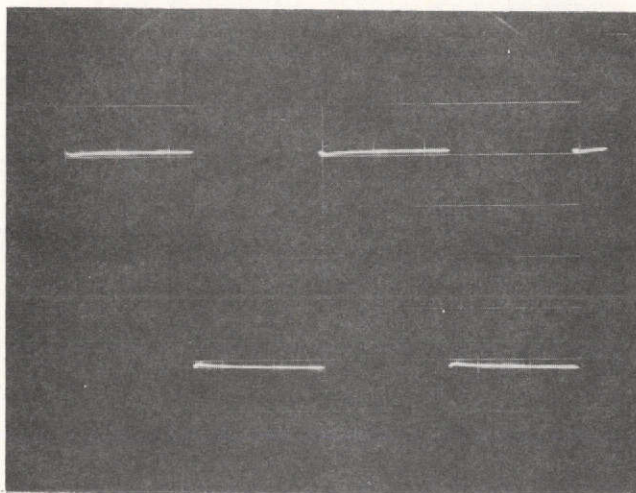


Figure 3.2-13. Torquer Voltage - High Mode

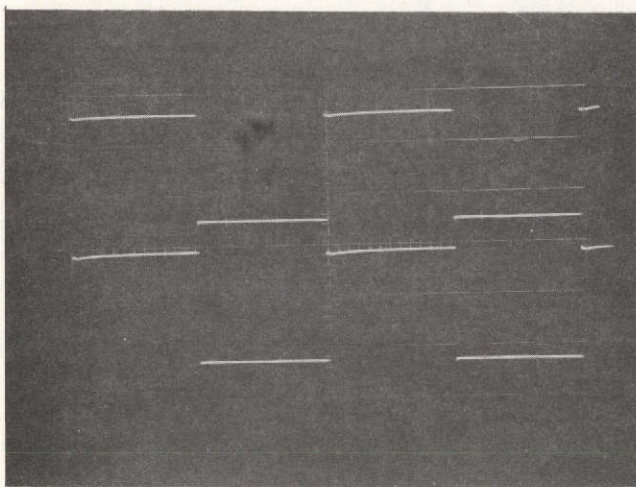


Figure 3.2-14. Torquer Currents Referenced to Ground

## 3.2.2.2 (Continued)

Device Failures - Approximately twelve (12) discs (out of a total 28) failed after fabrication had been completed. Typically, the failure resulted from a defective part rather than from handling or design problems. Replacement of the defective part generally corrected the problem. Other unique or recurring problems are noted below.

Pre-Amps - The PTSA pre-amps were packaged separately from the hybrid discs, in 3/8" x 3/8" flat packs. These were then placed within the gyro in contact with the gyro fluid. Several units failed, and the problem was traced to leaks in the package seal. While a better seal was possible, it was decided to remove the pre-amps and relocate them within the end caps. This modification was successful and represents the final configuration.

3.2.2.3 Design Problems

MSE Amplifier Oscillation - The first units tested showed high frequency oscillations on the output amplifier/driver. Local feedback was added around the LM101 through the addition of R86 and R87 (10 megohms).

MSE Oscillation - General noise pickup coupled with type B operation appeared as hysteresis or chatter in the MSE loop. This problem and its solution are detailed in Paragraph 3.2.3.

Amplifier - The original layouts had the 7 V demodulator reference routed below the PTSA amp and demod board. Pickup at this point resulted in noisy operation. The demod reference was rerouted around the board, and the problem was corrected.

PTSA IC 2 - SN 54H103 - This TI device has a separate ground pad which must be used as the chip ground. Use of the substrate, as is common practice, is not satisfactory for this chip. The original artwork did not connect to this ground and resulted in the loss of PTSA B&D Q1 and Q2.

PTSA CR Q13 and Q14 - The loss of current regulator signals, E34 and E35, while the hi-mode bridge drive, 37.5 V, is present will cause Q13 and Q14 to fail. Such a condition occurs when +5 V is lost or when the 115 V 60 Hz is interrupted. To protect against these failures, protect and monitor circuits have been incorporated into the interface unit. In addition, for normal operation, a manual power sequencing is required. The BB rack uses customer provided power supplies and has no automatic protect provision. A manual supplied with the BB rack describes the required rack operating considerations.

## 3.2.2.3 (Continued)

DC/DF IC 6, 7, & 8 - As designed, these IC's were improperly decoded. Corrections were made with minor rework of the substrate.

3.2.3 MSE Electronics Redesign

The initial loop design of the MSE is shown in Figure 3.2-15. This circuit was breadboarded, tested, and committed to hybrid implementation. The first marriage of the loop and the gyro MSE simulator occurred after the completion of the MSE hybrid fabrication. At this time, it was discovered that the MSE exhibited a "dual null" due to noise, and a redesign was effected which resolved the problem with minimum impact on the completed hybrid electronics.

Referring again to Figure 3.2-15, the initial design was such that the loop operated in a Class B mode. Either amplifier/driver for coil 1 or coil 2 was on. The comparator circuit selected an amplifier/driver based on the sign of the demodulated error signal output. This implementation represents a high efficiency in the power delivered to the MSE coils. Minimum power dissipation was designed to maximize the rate capability of the suspension within the component limitation of the electronics.

In operation, the hybrids exhibited "dual nulls" which in some cases were separate and stable in the absence of external inputs, and in others were close and resulted in a chattering or oscillation between these modes. The problem was traced to the noise pickup within the densely packaged hybrids. The electrical null defined by the coil and the 1.5 KHz excitation varied due to different levels of pickup in the drive amplifiers. If the noise joined with the excitation to generate separate nulls, bi-stable operation was observed. When the noise provided overlapping nulls, oscillations occurred.

To resolve the problem, the loop was redesigned as shown in Figure 3.2-16. While this reduced the maximum rate capability and increased the steady state dissipation, it minimized the impact on the hybrids.

Figure 3.2-16 shows schematically the redesigned loop. The amplifier/driver are fed a constant amplitude 200 Hz sine wave drive signal. The individual amplifier/drivers are enabled on a variable duty cycle established by the DC error signal and a 26.3 KHz ramp at the comparator. The timing is shown in Figure 3.2-17. The uppermost signal is the 200 Hz constant amplitude drive to the amplifier/drivers. Below it in exaggerated time scale, is the 26.3 KHz ramp. Superimposed on the ramp is a slewed error signal, swinging from positive to negative extremes. The resulting output

ORIGINAL SUSPENSION

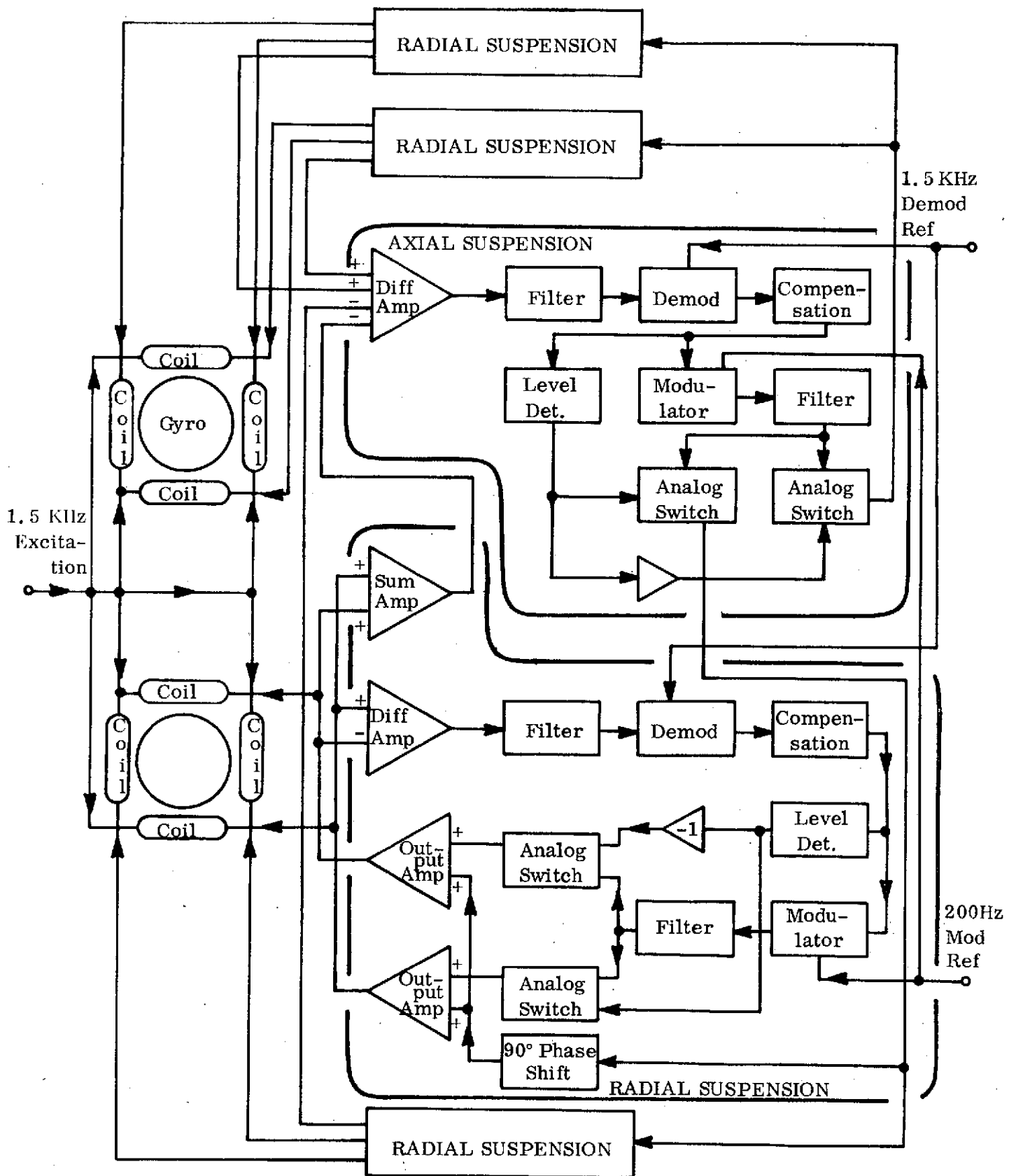


Figure 3.2-15

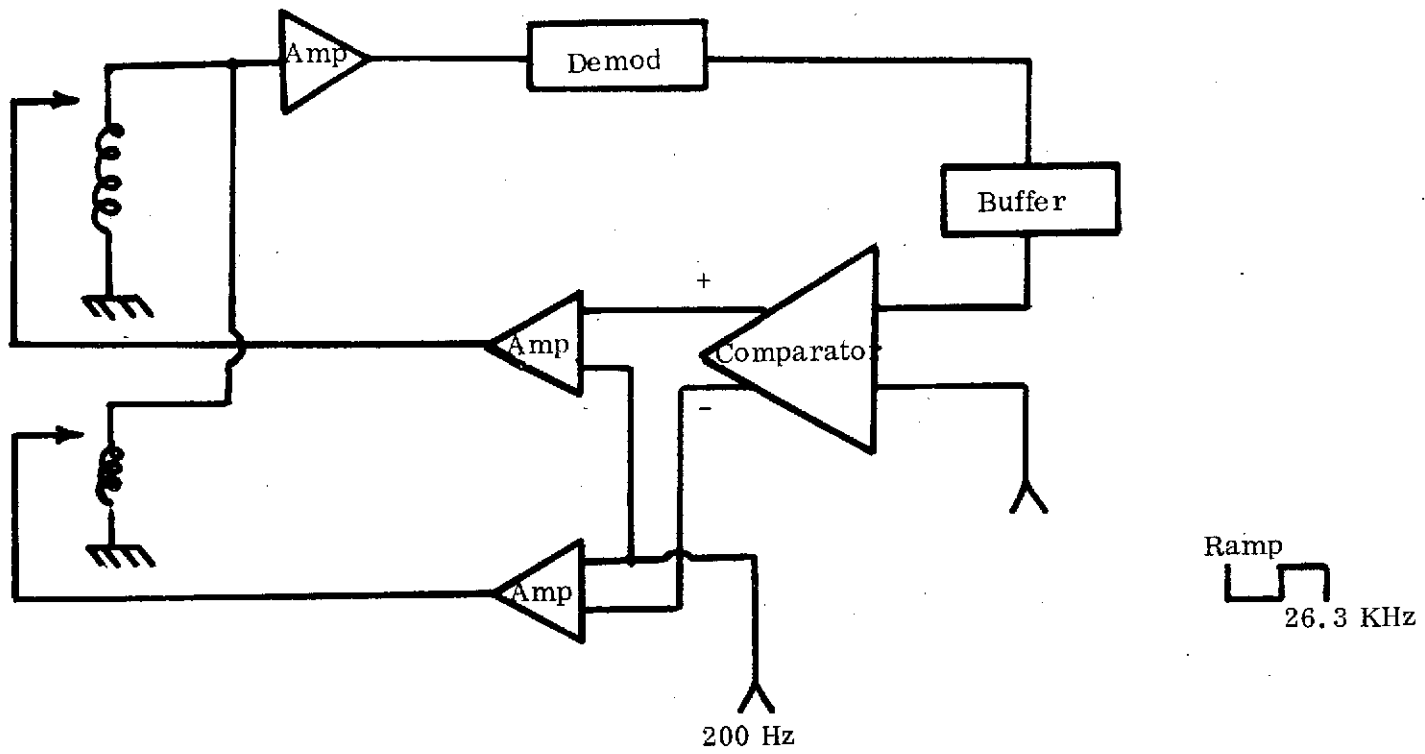


Figure 3.2-16 MSE Design

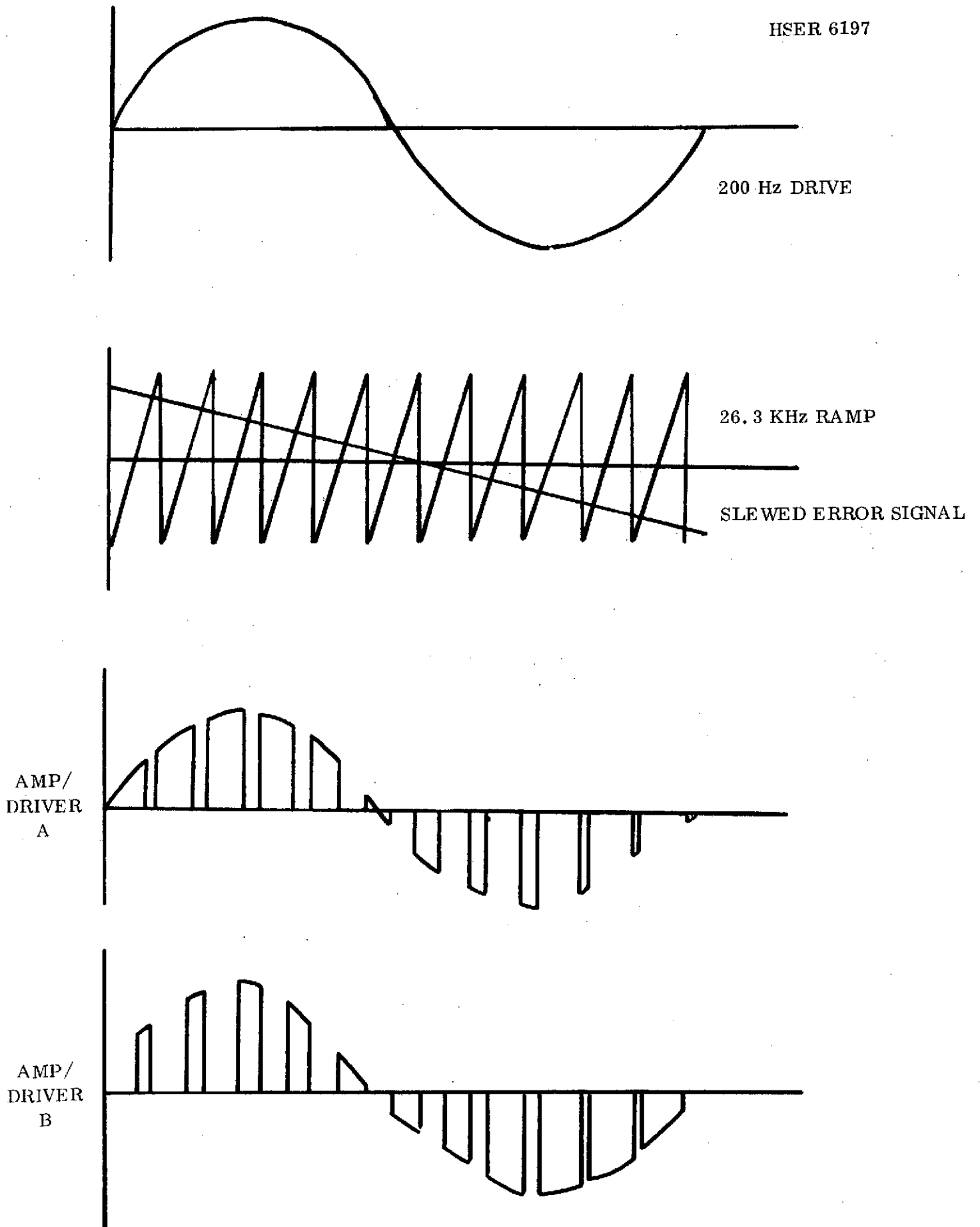


Figure 3.2-17 Redesigned MSE Timing

3.2.3 (Continued)

of the comparison of these two signals is shown as a chopped error signal out of amplifier/drivers, A and B. During the positive excursion of the error signal, line A is on longer than B. A negative error signal reverses the weighing. Note that the rebalance torque is proportional to the square of the current and direction of the rebalance forced is achieved by selecting A or B.

The magnitude of the rebalance current is proportional to the magnitude of applied 200 Hz drive.

3.2.4 Synchronization

The 1170 synchronizer circuitry was designed and fabricated to improve the gyro stability and eliminate the use of several generators. This also facilitates interfacing the necessary signals needed to operate the gyro and MSE.

The synchronizer circuitry consists of two plug-in cards (C3 sync amplifier and C4 synchronizer). C4 contains the countdown electronics used to produce the 200 Hz, 1.6 KHz and 26.36 KHz signals used in the MSE electronics, and the 51 KHz signals used for the gyro excitation and PTSA demodulator reference.

The input frequency to the countdown in the synchronizer is 4.096 MHz and is the same frequency used in the DCE. Also located on C4 are the phase shift networks for the demodulator reference (51 KHz) and the amplifier for the 26.36 KHz signal and 1.6 KHz square wave signal.

Card C3 contains the filters and output amplifier for the 200 Hz sine wave, the 1.6 KHz sine wave and the 51 KHz sine wave. Each input section is an active filter for a particular frequency. The output section of the 51 KHz amplifier has a center-tapped transformer to obtain 0° and 180° phasing. This is necessary for gyro pickoff excitation.

3.3 Electronics Packaging

The RI 1170 is designed to be a completely replaceable unit. With the removal of one unit and the replacement of another within the system application, there should be no need for recalibration or trimming. With electronics having to be trimmed and/or calibrated for each gyro, one way to ensure this rapid replaceability is to change both the gyro and its associated electronics simultaneously. For convenience, it is desirable to have both contained within the same fixture.

## 3.3 (Continued)

Under normal packaging techniques, the electronics ordinarily require as much, if not more, room than the gyro itself. By going to hybrid circuitry, we have eliminated the packaging of each individual component and the bulk associated with wiring. The construction of the circuits using chips and gold traces on ceramic discs reduced the electronics package size to such an extent that including the circuitry within the gyro became a viable approach. See Figure 3.3-1 for the final packaging configuration.

Perhaps a more important reason for proceeding in this manner were the number of connections to the gyro that would be required. Every sensor now currently used would have to be brought to the outside world for use by the electronics. See Figure 3.3-2. Among these are:

- a. Gyro Pickoff for PTSA
- b. Torquer Output from PTSA
- c. Thermal Sensor for TCE
- d. Heater to TCE
- e. Coil Connections for MSE

In addition, to ensure proper operation, it would have been necessary to maintain the electronics at a predetermined temperature because of thermal stability of some critical components such as the reference zener diode and the current sensing resistor. This would have required the fabrication of an additional temperature controller.

By including all the electronics as well as the gyro in one package, the RI 1170 becomes an attractive unit in an application oriented environment.

3.3.1 System Configuration

For the development phase of this program, each system was interfaced with its own power supplies and excitation signals. This approach allowed testing to determine the feasibility of the RI 1170 concept. As discussed in the Design Report (HSER 5579, dated 15 February 1970), an active suspension system was selected. Without the independence of each system, the effect of the MSE on the Rebalance Loop Electronics (and vice versa) could not be ascertained.

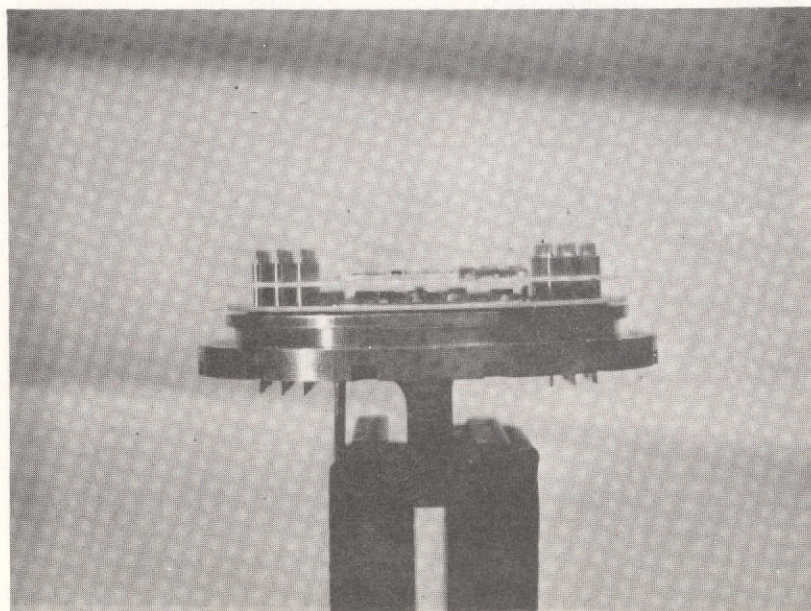
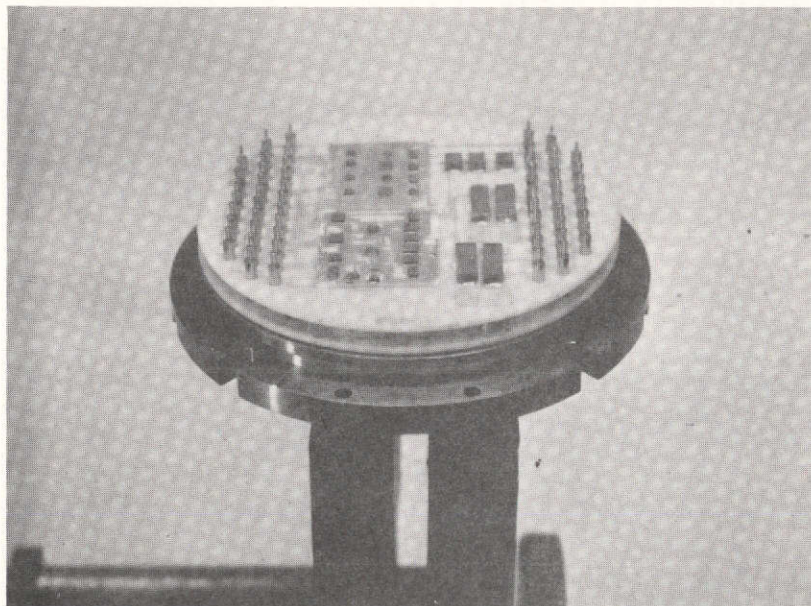


Figure 3.3-1. RI 1170 Hybrid Disk Configuration

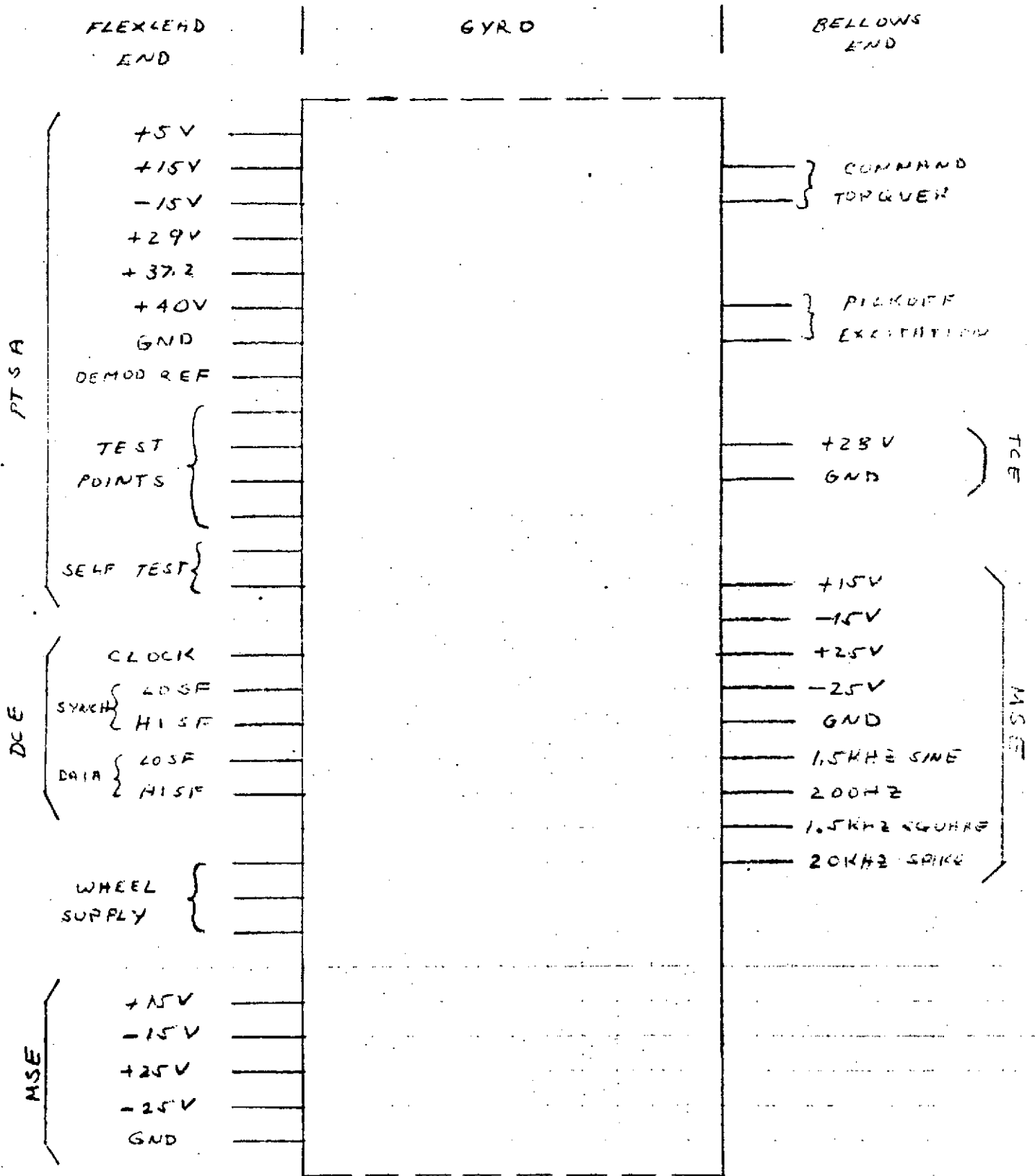


FIGURE 3.3-2 RT-1170 ELECTRONICS INPUT/OUTPUT SIGNALS

3.3.1 (Continued)

The TCE required its own supply so that the gyro could be brought to temperature and maintained there without having any of the control electronics functioning. This allowed the gyro to initiate operation at proper temperature without having to worry about damage to the unit due to improper viscosity of gyro fluids.

3.3.1.1 System Disc Locations

The RI 1170 electronics consist of three independent systems. They are:

Rebalance Loop Electronics

Magnetic Suspension Electronics

Temperature Controller Electronics

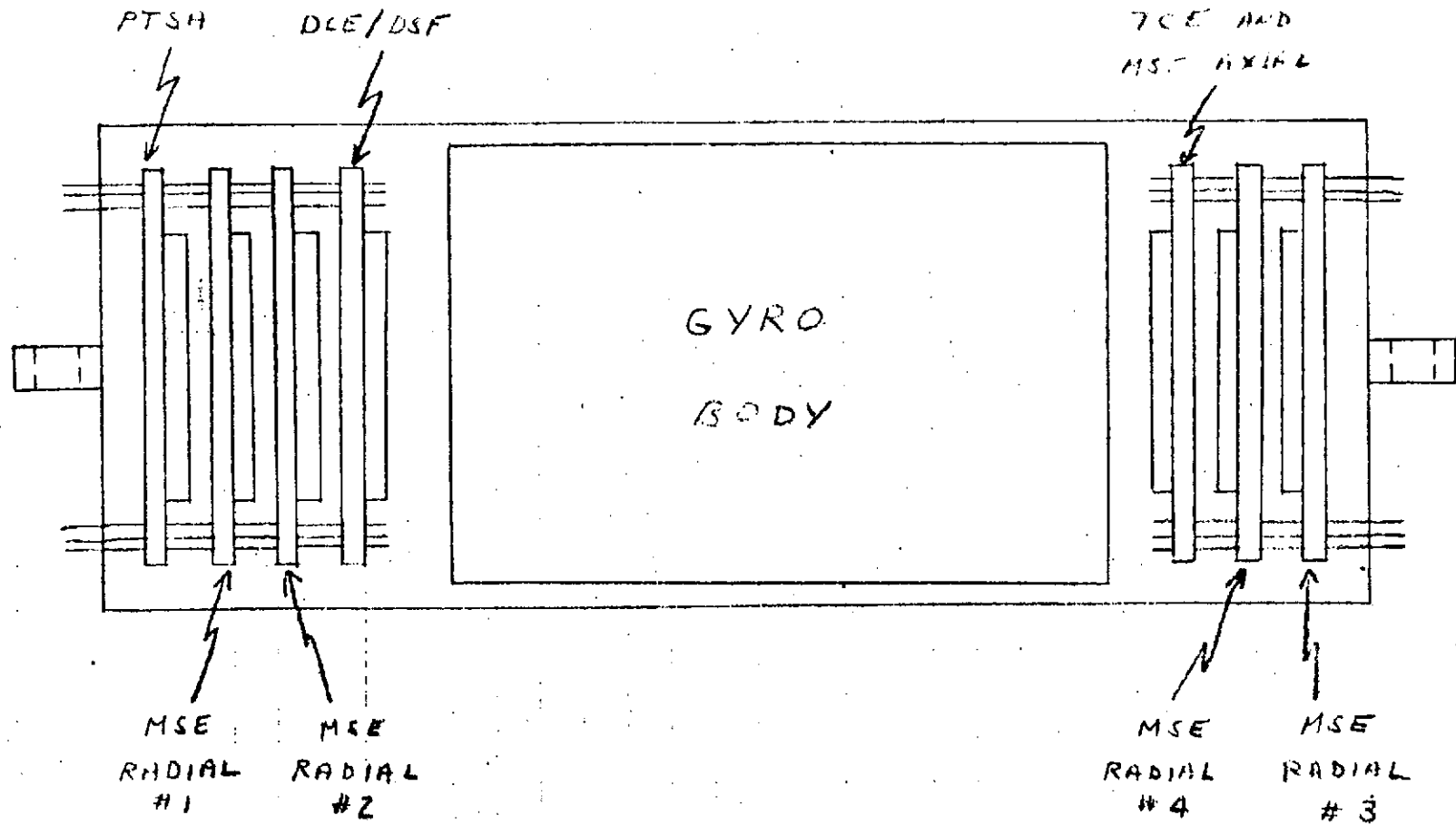
Four hybrid discs are mounted at the flexlead end of the gyro. Two of these discs constitute the Rebalance Loop Electronics. The PTSA is mounted in the end cap assembly (Figure 3.3-3) so that it is closest to the current sensing resistors and the precision reference zener diode. The second board is the other part of the Rebalance Loop Electronics and contains the DCE with Dual Scale Factor (DSF) select logic.

The second independent system is the Magnetic Suspension Electronics (MSE). Because of the float suspension mechanism, there are two degrees of freedom in the radial direction (normal to the gyro body axis) at each end of the gyro assembly and an additional degree of freedom along the gyro axis. Controls for motion in these directions are referred to as radial and axial displacements, respectively. As an aid to proper suspension, a MSE radial channel is supplied for each radial degree of freedom at each end of the gyro assembly. There is one hybrid disc for each MSE radial channel. Two hybrid discs for radial control were to be at the flexlead end, and the other two radial channels of the MSE were to be located in the end cap at the bellows end of the RI 1170 gyro.

The last disc at the bellows end of the gyro, contains the remainder of the MSE, the axial channel, and the Temperature Control Electronics (TCE). Both these systems are mounted on the same disc to improve packaging density and packaging efficiency. Because of the power required in the output drive transistors of the TCE, they are mounted directly into the end cap on the bellows end of the gyro.

FILIFLAD END

BELLOWS END



30

FIGURE 3.3-3 RI-1170 ELECTRONIC HYBRID D. C. FORCE MGMT

HSER 6197

3.3.1.1 (Continued)

The gyro is designed to accept all MSE discs; however, only the MSE/TCE disc is included in gyro S/N 3.

3.3.1.2 System Interaction

One of the influencing factors determining the placement of the hybrid disc within the gyro end caps is the need for interaction with the gyro itself as well as with other electronics modules.

The PTSA is placed at the flexlead end of the gyro assembly because it is at this end that the connection to the gyro torquer is made. Placement of the other electronics assemblies then results from placement of the PTSA. Since the PTSA is the only assembly that uses the DCE, the DCE is placed in close proximity, on the same side of the gyro as the PTSA.

Suspension force coils exist on both ends, flexlead and bellows end, of the RI 1170. The radial channels of the MSE must then be near their respective force coils, thereby necessitating two radial channels at each end of the gyro. This then results in four hybrid discs at the flexlead end of the gyro.

Due to their small size, the MSE axial channel and the TCE are mounted on the same hybrid disc. Since the TCE is an independent system and the MSE axial channel feeds all four MSE radial channels, the placement of this disc was not crucial. The bellows end was selected to minimize the number of output pins on each end cap assembly and to balance the number of hybrid discs on each end of the gyro.

Figure 3.3-5 gives a pictorial representation of the interdependence of the electronic system constituting the RI 1170 gyro electronics which guided packaging design. The PTSA interacts directly with the gyro proper and the DCE. The PTSA pickoffs are located on either side of the gyro and are fed differentially into the PTSA. All necessary timing information is obtained from the DCE. The DCE also controls the determination of operation in the high scale factor (145 ma) or low scale factor (72.5 ma) modes. Except for test points and supply connections, all data are transmitted to the outside world via the DCE, the only connection of the rebalance loop electronics to the outside.

As stated previously, the TCE is a completely self-contained system. By turning on power to the TCE, the RI 1170 is supplied with the proper power to heat and maintain the temperature of the gyro assembly. The heater coils are mounted around the gyro body for optimum heating efficiency.

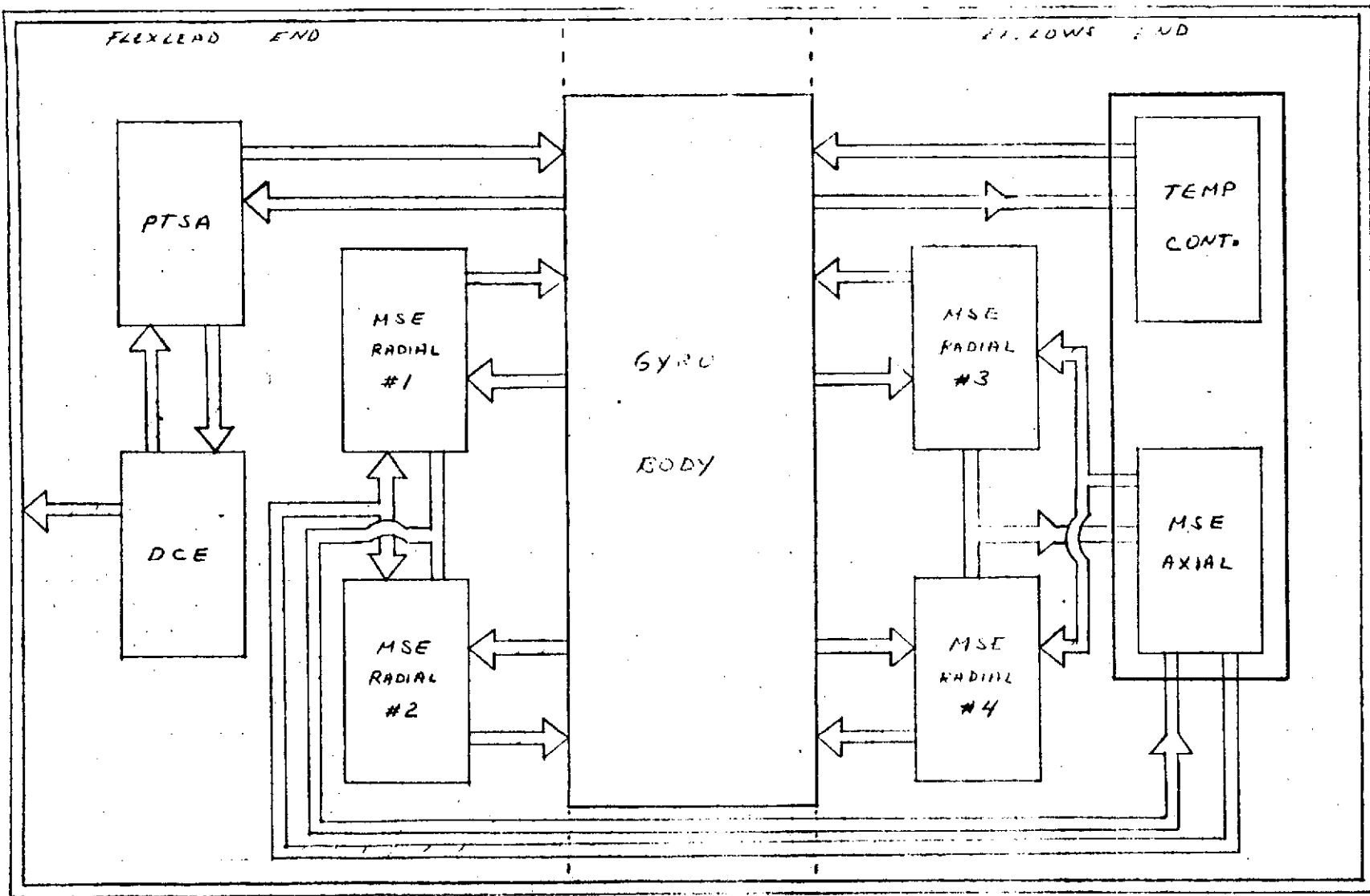


FIGURE 3.3-5 RI-1170 ELECTRONICS CONTROL DATA FLOW

## 3.3.1.2 (Continued)

Temperature is sensed by a platinum sensor connected in a Wheatstone bridge configuration at the TCE. The heater is connected to the output transistors in such a manner so that if a failure should occur, the gyro would not overheat, thus protecting the entire unit.

3.3.2 Hybrids

There are many advantages to using a hybrid circuit. The hybrid can be more reliable due to the reduced number of necessary connections. It also offers a great reduction in size and weight over the standard packaging techniques in use throughout industry today. The 1170 channel concept could only be implemented through the use of a hybrid electronics concept.

The electronics are divided into seven hybrid wafers. Each wafer is approximately 2 1/4 inches in diameter. Figure 3.3-6 gives an overall view of the basic construction technique utilized in fabricating the wafers. This particular wafer is the Pulse Torque Servo Amplifier circuit. Figures 3.3-7 through 3.3-9 are magnified sections of Figure 3.3-6. All the wafers consist of one large substrate which contains the gold conductors necessary for interconnection of wafers and for interconnection of the circuit substrates. Also found on the large, or mother, substrate are the decoupling capacitors which are located at the point of entry for the individual conductors involved. The size of the conductor is determined by the amount of current it must carry. The screen painting technique is used to apply the conductor patterns to the substrate. Conductor patterns are generated on the screen by the use of a development process which leaves clear areas on the screen through which the film (ink) can be deposited on the substrate. The conductor elements are produced on the substrate when ink is forced through the clear areas of the screen by use of a blade or squeegee. The substrate is then fired at a very high temperature. The actual circuitry is located on smaller rectangular shaped substrates which are attached to the mother substrate by means of a non-conductive adhesive. The conductor lines and pads are placed on the circuit substrates using the same technique employed on the mother substrate. Once the conductors have been fired, the components are placed on the substrates, using either conductive or non-conductive adhesives as the individual part requires.

All semiconductor devices and integrated circuits cover the temperature range of  $-55^{\circ}\text{C}$  to  $+125^{\circ}\text{C}$  and are passivated, with exceptions where the manufacturer's design specifically calls for no passivation. Discrete resistors and capacitors are used throughout to facilitate rework necessitated by design changes, failures, etc. The components are connected to the conductors by means of 0.001" diameter aluminum wire and ultrasonic

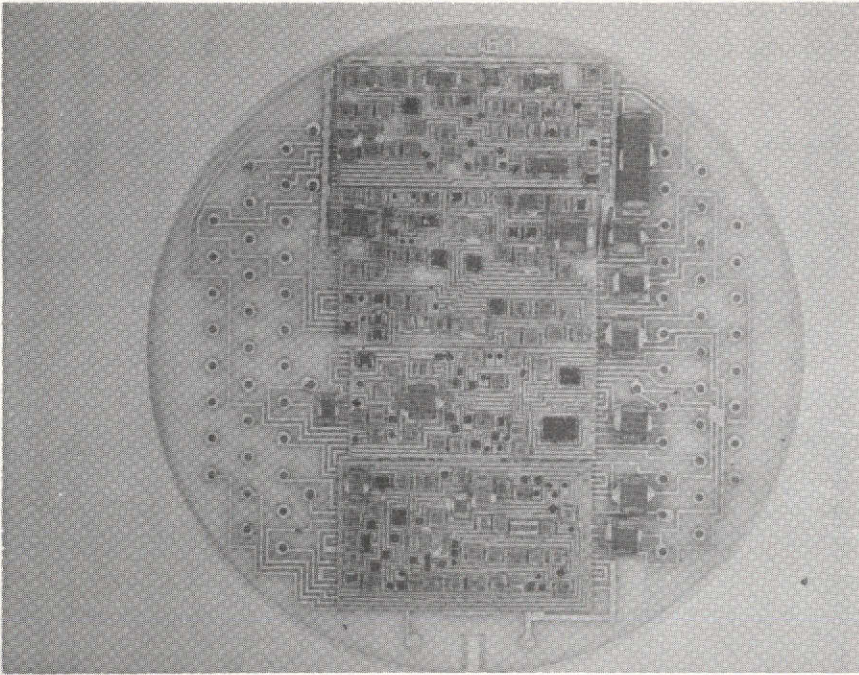


Figure 3.3-6  
C-167 Wafer  
Pulse Torque  
Servo Amplifier

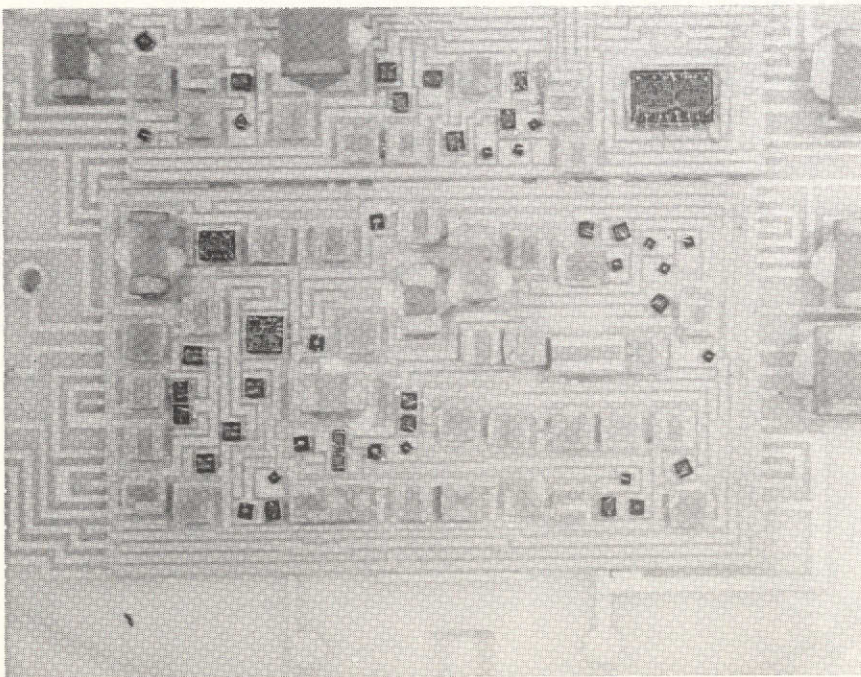


Figure 3.3-7  
C-167 Wafer

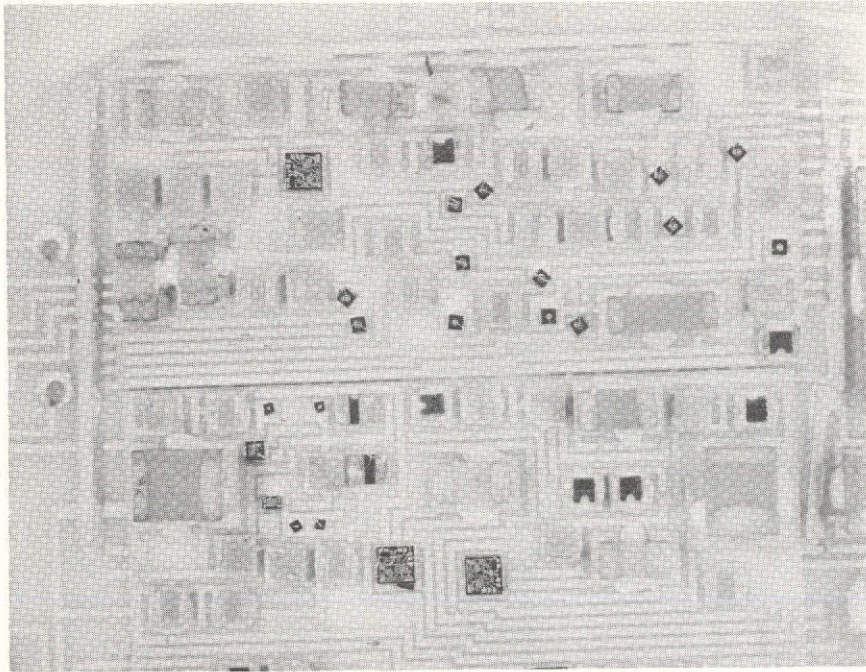


Figure 3.3-8  
C-167 Wafer

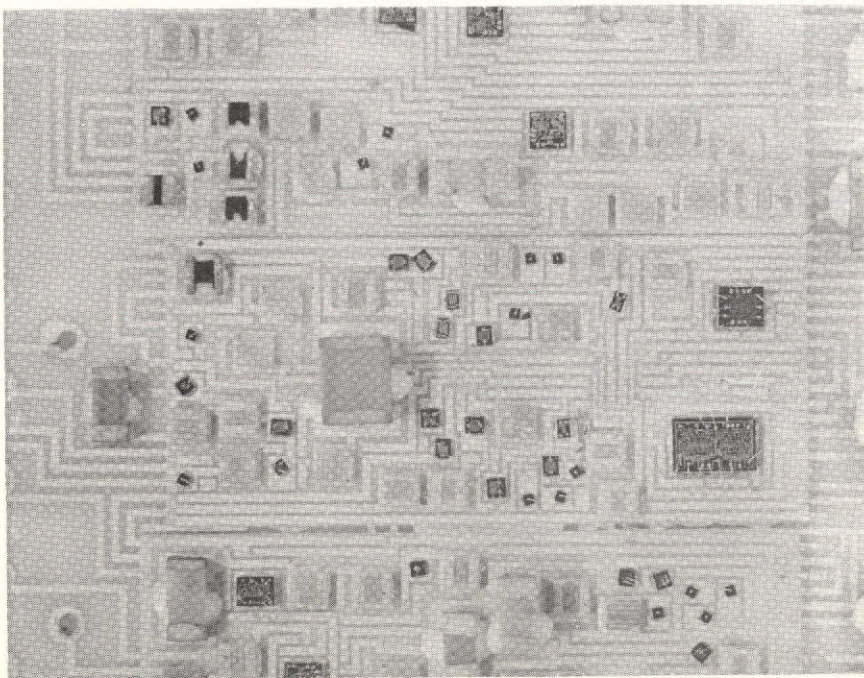


Figure 3.3-9  
C-167 Wafer

3.3.2 (Continued)

bonding. The connection of wire leads is made using ultrasonic vibrations.

To perform electrical testing, special test fixtures are required. The main considerations are:

1. Maintenance of the integrity of the interconnect pads of the mother substrate. This is accomplished by using mechanical contact fingers as opposed to soldering.
2. Protection against mechanical damage any time the wafer is used outside of its protected environment.
3. Access to the circuit substrates while the circuit is in an operating condition, to permit probe testing of the circuits. The unit would be placed under a microscope and the probes positioned at those points of interest within the circuit. In so doing, one is able to evaluate and confirm that the circuit is meeting the design criteria as intended. This also provides a useful tool for fault isolation of units which are not operating correctly.

The testing of the wafers is necessarily a tedious task due to the precautions one has to take in handling the wafer and positioning the probes for testing. Extreme care must be exercised whenever the wafer is being tested outside of the main gyro housing, since the slightest touch would prove devastating to the wafer.

The main advantage of this package design is the fact that the wafers are reworkable. In the event there is a design change, the use of all discrete components permits one to change values, delete, or add components. By reworking the wafer, the time and expense of building a new wafer is saved. As might be expected in a development program such as this, failures are occasionally encountered, such as, by accidentally applying the wrong voltage, improper loading, etc. In some cases, the failed component will overstress other components to a point where it necessitates their being replaced. The design is such that it will permit replacement of failed or stressed components.

### 3.4 Deliverable Hardware

#### 3.4.1 General Variations From Original Design

During the course of the RI 1170 Development Program, several deviations from the original conceptual design were considered. Those variations in configuration that were eventually employed are discussed below.

##### 3.4.1.1 Capacitive Pickoff

The fabrication of the capacitive pickoff has presented problems because of the difficulty of plating and etching a suitable pattern of capacitor plates on the inner surface of a cylinder. In the early stages, few vendors with a photo-etching capability showed any interest in the project since they were too preoccupied with large volume printed circuits to be motivated by a few prototype pickoffs. A cooperative vendor was located and every effort was made to produce a pickoff assembly. Many problems arose, however, including attack of the plastic sleeve by the photo-etchants, crazing and peeling of the copper plating on the plastic sleeve and the inability to deposit copper on the beryllia float sleeve. In light of these difficulties, it was decided that the pickoffs for the first three gyros would be fabricated in the same manner as the original prototypes. That is, by etching the pickoff patterns onto very thin copper clad flexible plastic film and epoxy bonding them to the appropriate surfaces of the pickoff assembly. There is every indication that by further effort the original problems can be overcome by the use of plasma or vapor deposition on a more suitable plastic substrate.

##### 3.4.1.2 Torquer

The torquer configuration discussed in the Design Report specified that the torquer would be wound with aluminum ribbon. The advantage of aluminum over copper was the weight consideration (to allow for flotation). Considerable difficulty was experienced during the attempt to wind the torquer with this aluminum ribbon. Parallel calculations determined that copper wire would float, thereby making the weight consideration less critical. It was therefore decided to utilize copper wire for its ease of handling.

##### 3.4.1.3 Flexleads

The aluminum flexleads were designed to be electron beam welded to the clips. After considerable development work in conjunction with outside vendors, it was found that although satisfactory welds could be produced, they could not be produced on a regular basis. In most cases, the unreliability stemmed from metallurgical weaknesses due to severe thermal gradients within the clip-lead interface. Satisfactory assemblies were

3.4.1.3 (Continued)

finally produced by a soldering technique based on that used at MIT Draper Labs for aluminum leads.

3.4.1.4 Magnetic Suspension

Initial testing of the prototype magnetic suspension system resulted in unstable operation of all five external control loops. Subsequent investigation and analysis found that this was mainly attributable to cross-over distortion and noise in the loop output stages. The circuit elements were redesigned and further testing of the prototype system demonstrated proper functioning; however, its performance relative to gyro closed loop operation has not been proven to be totally satisfactory.

3.4.1.5 Electronics Packaging

The electronics packaging was originally predicated on the use of hermetically sealed microcircuits to be located in the gyro end caps. This concept had to be abandoned when it became evident that the volume required was unacceptably large. Changes in packaging technique to use unsealed boards and then sealing within the gyro required redesign of the case and end caps.

3.4.2 Spin Motor Data

3.4.2.1 Design

3.4.2.1.1 Original Design Report

See HSER 5579.

3.4.2.1.2 Modifications to Design

3.4.2.1.2.1 Print Changes

As the RI 1170 wheels were being constructed by Speedring Corp., and later as the RI 1170 wheels were being tested, it became necessary to incorporate design changes which Inertial Instruments believed to be necessary for more successful operation and easier manufacturing of the RI 1170 gas bearing wheels. The following changes have been made on the prints as noted. The changes below are those pertaining to the gas bearing assembly only.

3.4.2.1.2.1 (Continued)

Source: "RI 1170 Mod Book"

<u>Drawings</u>	<u>Addition or Change and Date Conceived</u>
31157, 31158, 31159	Gas bearing groove depths to be measured with a stylus, .0005 in. maximum radius. 5 Sept 1969
31150	Change torque specification on Ti 6A14V bolts from 20-25 oz-in. to 40-50 oz-in. 3 Nov 1970
31155	After assembly of wheel half and hysteresis ring, temperature cycle per HSSC 2304 before completing final wheel assembly. 26 Oct 1970
31153	Change flatness specification from <span style="border: 1px solid black; padding: 2px;">-.0001</span> to <span style="border: 1px solid black; padding: 2px;">-.00001</span> 16 Oct 1970
31261	Show position of shaft holes relative to stator connection points. 21 Oct 1970

3.4.2.1.2.2 Ambient Pressure Modification

The environment of the wheels in Gyros No. 2 and No. 3 was 1.5 atm abs of helium gas; however, for the purpose of attempting to increase slew capacity, the ambient pressure of helium was changed to 2.0 atm abs in Gyro No. 1. Below is a comparison between the results of computer analysis using actual wheel dimensions and an atmosphere of 2.0 atm abs helium and the results of computer analysis using actual wheel dimensions and an atmosphere of 1.5 atm abs helium:

<u>Parameter</u>	<u>Actual Dimensions 2.0 Atm Abs</u>	<u>Actual Dimensions 1.5 Atm Abs</u>	<u>Units</u>
Slew Capacity	4.5	4.1	rad/sec
Cross Aniso	+.0020	+.0014	deg/hr/g <sup>2</sup>
Norm Aniso	-.0002	-.0017	deg/hr/g <sup>2</sup>
Total Mechanical Power	4.6	4.3	watts

## 3. 4. 2. 1. 2. 2 (Continued)

<u>Parameter</u>	<u>Actual Dimensions 2. 0 Atm Abs</u>	<u>Actual Dimensions 1. 5 Atm Abs</u>	<u>Units</u>
<u>Journal</u>			
Load Capacity	83	76	g's
Mechanical Power	1. 3	1. 3	watts
<u>Thrust Plate</u>			
Load Capacity	72	72	g's
Mechanical Power	1. 1	1. 1	watts

It can be seen from the preceding table that increasing the wheel environmental pressure does theoretically enhance the slew capacity and the radial load capacity of the wheel. Theoretically, all parameters are still within specification limits with the exception of the slew capacity which was improved by the additional 0. 5 atm abs helium, but still was less than the minimum specification of 5. 0 rad/sec.

3. 4. 2. 1. 2. 3 RI 1170 Wheel Computer Analysis

The mathematical analysis of the RI 1170 gas bearing wheel under any running conditions was done by a computer program - AWL5. Due to observed slew capacities less than nominal in most cases, a review of the calculation method employed in AWL5 was conducted, and a more accurate method for calculating wheel movement during slew was employed. This resulted in a lower theoretical slew capacity than before. This lower slew capacity more accurately predicts the observed slew capacity; therefore, the new calculation method was permanently incorporated into AWL5. Also, the effects of wheel misalignment and thrust plate misalignment on predicted slew capacity were also incorporated. The latest version of AWL5 is listed in Appendix C. It has been found that this program now adequately predicts actual running conditions of gas bearing wheels.

3. 4. 2. 1. 2. 4 Mean Free Path Effects

After the preliminary design of the RI 1170 gas bearing wheel had been completed, an experimental program was established to test the effect

3.4.2.1.2.4 (Continued)

of molecular mean free path on gas bearing performance, in general, and on RI 1170 gas bearing performance in particular.

The mean free path of a gas is the average distance traversed by a gas molecule before it strikes another gas molecule. When this distance is on the order of magnitude of the clearances in the gas bearing, the gas viscosity is apparently reduced. This apparent reduction in viscosity will adversely affect the performance of the wheel. The effect will only be significant if any of the following conditions is present to a significant extent:

1. Ambient pressure is low.
2. The mean free path of the gas is large.
3. The clearance is small.

Using the design parameters of the RI 1170 wheel, an analysis was performed to determine if this effect would significantly affect the performance of the gas bearing. The analysis revealed that the mean free path effect will not significantly affect the performance of the RI 1170 gas bearing operating at or near the operating point outlined by preliminary design.

Reference: G02BA0000A, URA-18, 20 Nov 1970,

3.4.2.2 Actual Parts

3.4.2.2.1 Compliance of Parts to Drawings

All the wheels shipped to HSES by Speedring Corp. were accompanied by the actual dimensions as measured by Speedring. However, all the dimensions directly bearing on the performance of the gas bearing were checked in the Metrology Lab at HSES by Quality Control. A comparison of the dimensions as measured by HSES and Speedring is presented below along with the specifications to which the gas bearing parts were manufactured. The data on all the gas bearing wheels are presented; although, only Wheels S/N 020, S/N 021, S/N 022 were eventually built into RI 1170 gyros.

COMPARISON OF DIMENSIONS  
(HSES AND SPEEDRING)

WHEEL S/N 020

Dimension	Spec Value (in.)	Speedring Value (in.)	HSES Value (in.)
<b>PART: METALLIZED ROTOR HALF</b>			
		<b>P/N 31150-1</b>	<b>Dwg 31150-C</b>
Bore Size (Dia)	.375 Ref A	.374996	.374994 Note 10
Bore Roundness	5 $\mu$	2 $\mu$	2 $\mu$ Note 10
Bore Straightness	5 $\mu$	3 $\mu$	4 $\mu$ Note 10
Flatness (Thrust End)	$\perp$ 5 $\mu$ Note 1	$\perp$ 4 $\mu$ Note 1	2 $\mu$ Note 11
Flatness (Interface)	100 $\mu$	OK	0 $\mu$ Note 11
<b>PART: PLAIN ROTOR HALF</b>			
		<b>P/N 31150-1</b>	<b>Dwg 31150-C</b>
Bore Size (Dia)	.375 Ref A	.374996	.374993 Note 10
Bore Roundness	5 $\mu$	2 $\mu$	.5 $\mu$ Note 10
Bore Straightness	5 $\mu$	3 $\mu$	4 $\mu$ Note 10
Flatness (Thrust End)	$\perp$ 5 $\mu$ Note 1	$\perp$ 2 $\mu$ Note 1	0 $\mu$ Note 11
Flatness (Interface)	100 $\mu$	OK	2 $\mu$ Note 11
<b>PART: SHAFT</b>			
		<b>P/N 31157-1</b>	<b>Dwg 31157-A</b>
Shaft Diameter	$\frac{.375}{.374}$	.374914	.37491 Note 7
Shaft Length	$\frac{.831}{.830}$	.830779	.83092 Note 7
Groove Depth Range (Hole End)	$\frac{43 \mu}{63 \mu}$	$\frac{40 \mu}{60 \mu}$	$\frac{53 \mu}{66 \mu}$ Note 9
Groove Depth Range (Opp Hole End)	$\frac{43 \mu}{63 \mu}$	$\frac{35 \mu}{65 \mu}$	$\frac{49 \mu}{81 \mu}$ Note 9

## WHEEL S/N 020 (Continued)

Dimension	Spec Value (in.)	Speedring Value (in.)	HSES Value (in.)
<b>PART: SHAFT (Cont'd)</b>			
		<b>P/N 31157-1</b>	<b>Dwg 31157-A</b>
Av Groove Depth (Hole End)	$(53 \pm 10) \mu$	$52 \mu$ Note 2	$60 \mu$ Note 9
Av Groove Depth (Opp Hole End)	$(53 \pm 10) \mu$	$45 \mu$ Note 2	$61 \mu$ Note 9
<b>PART: NEGATIVE THRUST PLATE</b>			
		<b>P/N 31159-1</b>	<b>Dwg 31159</b>
Groove Side Flatness	$5 \mu$	OK	$2 \mu$ Note 11
Groove Depth Range	$\frac{80 \mu}{120 \mu}$	$\frac{70 \mu}{80 \mu}$	$\frac{80 \mu}{110 \mu}$ Note 3 Note 4
Av Groove Depth	$(100 \pm 20) \mu$	$76 \mu$ Note 2	$97 \mu$ Note 4 Note 3
<b>PART: POSITIVE THRUST PLATE</b>			
		<b>P/N 31158-1</b>	<b>Dwg 31158</b>
Groove Side Flatness	$5 \mu$	OK	$2 \mu$ Note 11
Groove Depth Range	$\frac{80 \mu}{120 \mu}$	$\frac{70 \mu}{120 \mu}$	$\frac{90 \mu}{130 \mu}$ Note 3 Note 5
Av Groove Depth	$(100 \pm 20) \mu$	Approx $105 \mu$ Note 2	$113 \mu$ Note 5 Note 3
<b>BORE - SHAFT CLEARANCE</b>			
			<b>Dwg 31150</b>
	$(40 \pm 5) \mu$	$41 \mu$	$\frac{42 \mu}{41.5 \mu}$ Note 10 Note 11
<b>THRUST PLATE - ROTOR CLEARANCE</b>			
			<b>Dwg 31150</b>
	$(40 \pm 5) \mu$	$35 \mu$	$35 \mu$ Note 7

NOTES: (1) Flatness Not Explicitly Specified (7) Measurements Made On Supermike  
(2) Averaged From Speedring Data (9) Averaged From HSD Tallyrond Data  
(3) Measured With Indiac On Surface Plate (10) Measured on Federal  
(4) 5 Grooves Checked (11) Measured Optically  
(5) 8 Grooves Checked

COMPARISON OF DIMENSIONS  
(HSES AND SPEEDRING)

WHEEL S/N 021

Dimension	Spec Value (in.)	Speedring Value (in.)	HSES Value (in.)
<b>PART: METALLIZED ROTOR HALF</b>			
		P/N 31150-1	Dwg 31150-C
Bore Size (Dia)	.375 Ref A	.374990	.374984 Note 6
Bore Roundness	5 $\mu$	2 $\mu$	2 $\mu$ Note 10
Bore Straightness	5 $\mu$	3 $\mu$	2 $\mu$ Note 10
Flatness (Thrust End)	$\perp$ 5 $\mu$	$\perp$ 3 $\mu$ Note 1	< 5 $\mu$ Note 11
Flatness (Interface)	100 $\mu$	OK	< 5 $\mu$ Note 11
<b>PART: PLAIN ROTOR HALF</b>			
		P/N 31150-1	Dwg 31150-C
Bore Size (Dia)	.375 Ref A	.374990	.374988 Note 10
Bore Roundness	5 $\mu$	2 $\mu$	3 $\mu$ Note 10
Bore Straightness	5 $\mu$	3 $\mu$	3 $\mu$ Note 10
Flatness (Thrust End)	$\perp$ 5 $\mu$ Note 1	$\perp$ 2 $\mu$ Note 1	< 5 $\mu$ Note 11
Flatness (Interface)	100 $\mu$	OK	< 5 $\mu$ Note 11
<b>PART: SHAFT</b>			
		P/N 31157-1	Dwg 31157-A
Shaft Diameter	$\frac{.375}{.374}$	.374908	.374895 Note 7
Shaft Length	$\frac{.831}{.830}$	.830966	.831030 Note 7
Groove Depth Range - (Hole End)	$\frac{43 \mu}{63 \mu}$	$\frac{40 \mu}{90 \mu}$	$\frac{42 \mu}{96 \mu}$ Note 9
Groove Depth Range + (Opp Hole End)	$\frac{43 \mu}{63 \mu}$	$\frac{35 \mu}{70 \mu}$	$\frac{42 \mu}{72 \mu}$ Note 9

## WHEEL S/N 021 (Continued)

Dimension	Spec Value (in.)	Speedring Value (in.)	HSES Value (in.)
PART: SHAFT (Cont'd)		P/N 31157-1	Dwg 31157-A
Av Groove Depth - (Hole End)	$(53 \pm 10) \mu$	$55 \mu$ Note 2	$62 \mu$ Note 9
Av Groove Depth + (Opp Hole End)	$(53 \pm 10) \mu$	$52 \mu$ Note 2	$57 \mu$ Note 9
PART: NEGATIVE THRUST PLATE		P/N 31159-1 S/N 002	Dwg 31159
Groove Side Flatness	$5 \mu$	OK	$< 5 \mu$ Note 11
Groove Depth Range	$\frac{80 \mu}{120 \mu}$	$\frac{80 \mu}{170 \mu}$	$\frac{100 \mu}{160 \mu}$ Note 3
Av Groove Depth	$(100 \pm 20) \mu$	$110 \mu$ Note 2	$136 \mu$ Note 3
PART: POSITIVE THRUST PLATE		P/N 31158-1 S/N 006	Dwg 31158
Groove Side Flatness	$5 \mu$	OK	$< 5 \mu$ Note 11
Groove Depth Range	$\frac{80 \mu}{120 \mu}$	$\frac{40 \mu}{90 \mu}$	$\frac{80 \mu}{100 \mu}$ Note 3
Av Groove Depth	$(100 \pm 20) \mu$	$70 \mu$ Note 2	$88 \mu$ Note 3
BORE-SHAFT CLEARANCE			Dwg 31150
	$(40 \pm 5) \mu$	$41 \mu$	$45 \mu$ Note 10 Note 7
THRUST PLATE - ROTOR CLEARANCE			Dwg 31150
	$(40 \pm 5) \mu$	$45 \mu$	$45 \mu$ Note 7

- NOTES:**
- (1) Flatness Not Explicitly Specified
  - (2) Averaged From Speedring Data
  - (3) Measured With Indiac On Surface Plate
  - (7) Measurements Made On Supermike
  - (9) Averaged From HSD Tallyrond Data
  - (10) Measured On Federal
  - (11) Measured Optically

COMPARISON OF DIMENSIONS  
(HSES AND SPEEDRING)

WHEEL S/N 022

Dimension	Spec Value (in.)	Speedring Value (in.)	HSES Value (in.)
PART: METALLIZED ROTOR HALF		P/N 31150-1	Dwg 31150-C
Bore Size (Dia)	.375 Ref A	.374991	.374988 Note 10
Bore Roundness	5 $\mu$	2 $\mu$	0 $\mu$ Note 10
Bore Straightness	5 $\mu$	3 $\mu$	3 $\mu$ Note 10
Flatness (Thrust End)	$\perp$ 5 $\mu$ Note 1	$\perp$ 4 $\mu$ Note 1	< 5 $\mu$ Note 11
Flatness (Interface)	100 $\mu$	OK	< 5 $\mu$ Note 11
PART: PLAIN ROTOR HALF		P/N 31150-1	Dwg 31150-C
Bore Size (Dia)	.375 Ref A	.374991	.374991 Note 10
Bore Roundness	5 $\mu$	2 $\mu$	1 $\mu$ Note 10
Bore Straightness	5 $\mu$	3 $\mu$	4 $\mu$ Note 10
Flatness (Thrust End)	$\perp$ 5 $\mu$ Note 1	$\perp$ 4 $\mu$ Note 1	< 5 $\mu$ Note 11
Flatness (Interface)	100 $\mu$	OK	< 5 $\mu$ Note 11
PART: SHAFT		P/N 31157-1	Dwg 31157-A
Shaft Diameter	$\frac{.375}{.374}$	.374909	.374900 Note 7
Shaft Length	$\frac{.831}{.830}$	.830932	.831050 Note 7
Groove Depth Range - (Hole End)	$\frac{43 \mu}{60 \mu}$	$\frac{40 \mu}{60 \mu}$	$\frac{42 \mu}{72 \mu}$ Note 9
Groove Depth Range + (Opp Hole End)	$\frac{43 \mu}{60 \mu}$	$\frac{40 \mu}{60 \mu}$	$\frac{36 \mu}{84 \mu}$ Note 9

## WHEEL S/N 022 (Continued)

Dimension	Spec Value (in.)	Speedring Value (in.)	HSES Value (in.)
PART: SHAFT (Cont'd)		P/N 31157-1	Dwg 31157-A
Av Groove Depth - (Hole End)	(53 ±10) μ	50 μ Note 2	56 μ Note 9
Av Groove Depth + (Opp Hole End)	(53 ±10) μ	50 μ Note 2	55 μ Note 9
PART: NEGATIVE THRUST PLATE		P/N 31159-1 S/N 001	Dwg 31159
Groove Side Flatness	5 μ	OK	< 5 μ Note 11
Groove Depth Range	$\frac{80 \mu}{120 \mu}$	$\frac{80 \mu}{190 \mu}$	$\frac{120 \mu}{190 \mu}$ Note 3 Note 4
Av Groove Depth	(100 ±20) μ	98 μ	151 μ Note 3 Note 4
PART: POSITIVE THRUST PLATE		P/N 31158-1 S/N 007	Dwg 31158
Groove Side Flatness	5 μ	OK	5 μ Note 11
Groove Depth Range	$\frac{80 \mu}{120 \mu}$	$\frac{80 \mu}{150 \mu}$	$\frac{90 \mu}{160 \mu}$ Note 3 Note 5
Av Groove Depth	(100 ±20) μ	100 μ Note 2	120 μ Note 3 Note 5
BORE - SHAFT CLEARANCE			Dwg 31150
	(40 ±5) μ	41 μ	44 μ Note 10 Note 7
THRUST PLATE - ROTOR CLEARANCE			Dwg 31150
	(40 ±5) μ	45 μ	75 μ Note 7

- NOTES: (1) Flatness Not Explicitly (7) Measurements Made On Supermike  
(2) Averaged From Speedring Data (9) Averaged From HSD Tallyrond Data  
(3) Measured With Indiac On Surface Plate (10) Measured On Federal  
(4) 5 Grooves Checked (11) Measured Optically  
(5) 8 Grooves Checked

3.4.2.2.2 RI 1170 Bearing Materials

Aluminum oxide and beryllium oxide were chosen as the materials to be used for the RI 1170 gas bearing. As stated in the design report, these two ceramics should provide good start-stop reliability and have the desirable thermal characteristics. Refer to the design section for additional details.

The following table summarizes which specific ceramics were used for the RI 1170 wheel parts.

<u>Wheel S/N</u>	<u>High Purity Alumina</u>		<u>High Purity Beryllia</u>
	<u>Thrust Plate</u>	<u>Rotor Halves</u>	<u>Shaft</u>
010	Coors AD 995	Coors AD 995	Brush Cold Pressed
011	Coors AD 995	Coors AD 995	Brush Hot Pressed
012	Coors AD 995	Coors AD 995	Brush Cold Pressed
020	Coors AD 995	Coors AD 995	Brush Thermolox 998
021	Coors AD 995	Coors AD 995	Brush Thermolox 998
022	Coors AD 995	Coors AD 995	Brush Thermolox 998

According to manufacturer's information:

<u>Parameter</u>	<u>Coors AD 995</u>	<u>Brush Thermolox 998</u>
Thermal Conductivity (100°C)	.064 cal/cm <sup>2</sup> /cm/sec/°C	.5 cal/cm <sup>2</sup> /cm/sec/°C
Specific Gravity (Typ.)	3.84	2.86
Coefficient of Thermal Expansion (25°C - 200°C)	6.8 x 10 <sup>-6</sup> $\frac{\text{in.}}{\text{in. } ^\circ\text{C}}$	6.3 x 10 <sup>-6</sup> $\frac{\text{in.}}{\text{in. } ^\circ\text{C}}$

## 3.4.2.2.2 (Continued)

The above values are typical values obtained from testing many samples. The value of the above parameters will, however, be different (slightly) for each sample. The following important facts can be readily deduced from the above data:

1. Beryllia (RI 1170 shaft) will conduct bearing heat away almost 10 times as fast as the alumina (RI 1170 rotor and thrust plate material).
2. Both materials are relatively light.
3. Thermal expansion coefficients match very closely.

3.4.2.3 Wheel Tests

Before the RI 1170 gas bearing wheels could be placed in a float frame for use in a gyro, sufficient testing had to be performed to ensure that the wheel would run reliably in the gyro.

The following were considered the most important tests to be performed, and gave sufficient data to determine the wheel reliability. Table 3.4-1 shows which tests were performed on which wheels.

3.4.2.3.1 Running Parameters

This is an important test to see if the wheel will run efficiently as designed. If the wheel is not running efficiently after it is built in the clean room, there is little purpose in further testing the wheel until the problem has been diagnosed and corrected; therefore, this test was the first test conducted on the RI 1170 gas bearing wheels.

During the test, wheel speed was varied and the following parameters were recorded at each speed:

1. Time to reach synchronous speed\*
2. Time to coast to a stop\*
3. Minimum synchronization voltage (and running voltage)
4. Current drawn during operation
5. Mechanical power developed by the wheel\*
6. Electrical power drawn by the wheel
7. Mechanical torque developed by the wheel\*
8. Wheel efficiency

\*These parameters were not measured for all wheels.

TABLE 3.4-1  
RI 1170 WHEEL TEST

WHEEL S/N	RUNNING PARAMETERS	SLEW CAPACITY	START STOP	STATIC STIFFNESS
010	X	X	X	X
011	X	X	Y <sup>1</sup>	X <sup>2</sup>
012	Y*	Z	Z	Z
020	X	X	Y <sup>1</sup>	Z
021	X	X	Y <sup>1</sup>	Z
022	X	X	Z	Z

X = Test Performed

Y = Test Performed On a Limited Basis

Z = Test Not Performed

1 → Start Stops Accumulated During Testing (See Graph of Running Time and Start-Stops).

2 → Erratic Data (Too Much Experimental Error).

\* → Wheel Failure Forced Cancellation of Further Testing (See Failure Report).

## 3.4.2.3.1 (Continued)

A comparison of the above parameters with parameters determined previously for similar gas bearings and with design predictions told if the wheel being tested was operating at or near its designed operating point.

3.4.2.3.2 Slew Test

Due to the fact that the RI 1170 gyro is to be used in a strapdown configuration, the slew capacity of the gyro wheel must be higher than that of a gas bearing wheel in a gimballed configuration. Slew capacity, therefore, must be determined for each wheel and compared with specifications.

Slew capacity was defined as the slew rate at which electrical power which the wheel draws has increased 40% above the zero slew rate electrical power. This method of determining slew capacity was chosen instead of the capacitance probe method because of the relative ease with which the test could be performed. The wheel was mounted (SA horizontal) on the rate table, and slew capacities were obtained for different wheel speeds as the table rate was increased in each direction of rate table rotation.

3.4.2.3.3 Start-Stop Test

A necessary piece of information concerning the performance of a gyro wheel is how long the wheel will last in service. In the case of a gas bearing, this will depend upon how well the bearing can sustain starts and stops.

The start-stop test involved running the wheel up to its operating speed from a complete stop and then letting the wheel coast down until it comes to rest. Starting and stopping is performed on the journal and thrust plates until the rotor fails to lift off and reach synchronous speed. The number of starts and stops before failure to start is monitored automatically by a rig which continuously starts and stops the wheel. Having obtained the number of starts and stops before "failure", wheel service life can be estimated. See Figure 3.4-1 for the number of start/stops and the running hours logged by each RI 1170 gas bearing.

3.4.2.3.4 Static Stiffness

In order to find how much the wheel will yield when subjected to a given load, static stiffness tests were performed on a limited basis. This test essentially determines the "spring constant" of the pressure field

RI 1170 GAS BEARING WHEEL RUNNING DATA

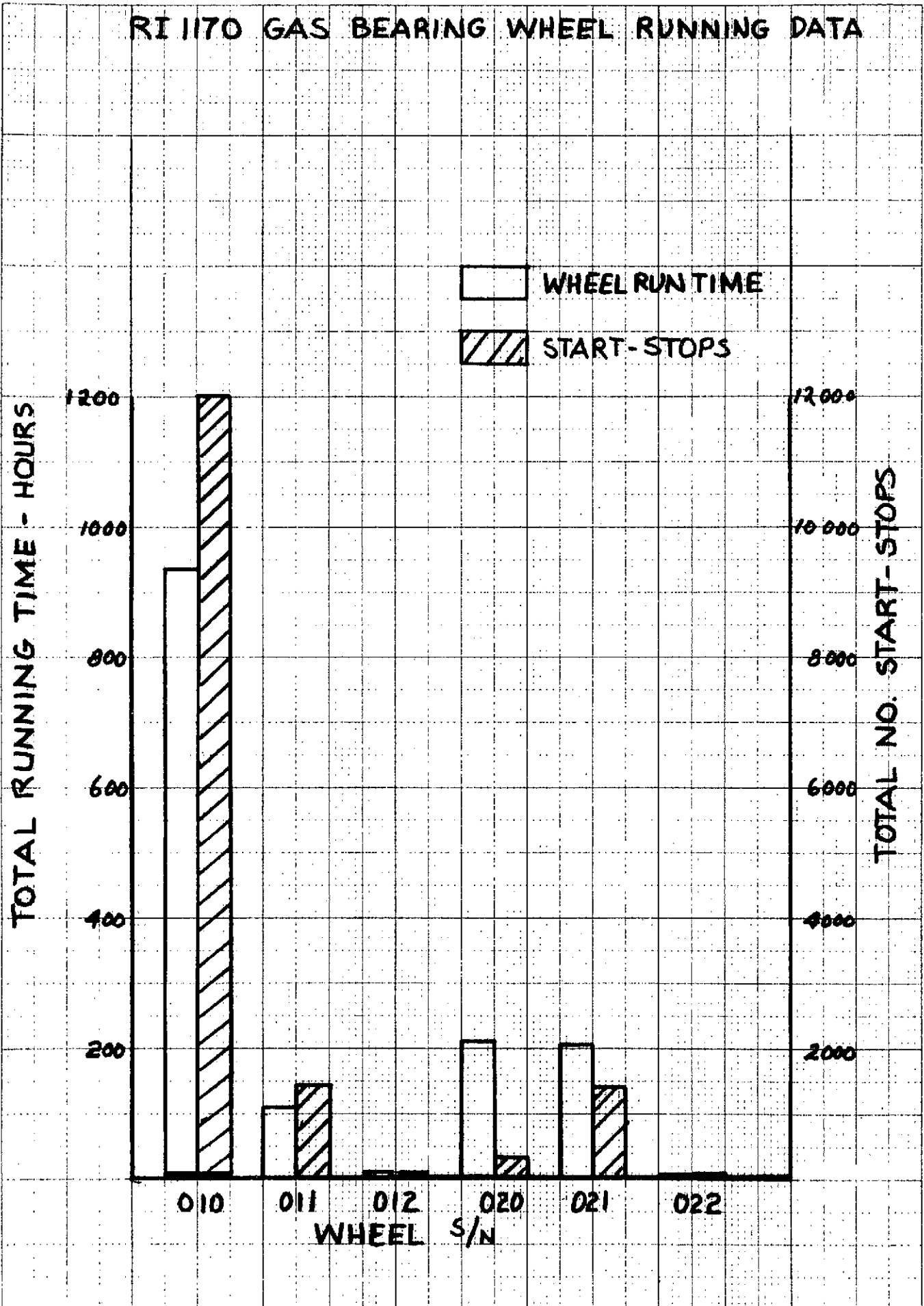


Figure 3, 4-1

## 3.4.2.3.4 (Continued)

developed as the wheel is running.

Radial and axial static stiffness tests were performed. An essential, and difficult, part of this test is accurately measuring displacements. The measurement of the microinch displacements is accomplished by employing .001" capacitance probes coupled with a Wayne-Kerr meter. Wheel speed and gas pressure was varied to vary the compressibility number ( $\lambda$ ).

From a knowledge of the static stiffness, the radial and axial load carrying of the wheel can be estimated.

3.4.2.4 Results3.4.2.4.1 Wheel Test Results

Table 3.4-2 summarizes the results of the testing completed before the decision to build the wheel into the gyro was made. Not all parameters for all wheels are available because the measuring of several parameters was not believed necessary at the time the wheel was being tested. The values listed under the heading, "DESIGN GOALS" are nominal values obtained from the "RI 1170 Design Report". All actual values were obtained directly or indirectly from experimental data.

Running voltage,  $V\phi$ , is a somewhat arbitrary voltage because there is more than one voltage at which the wheel will run successfully. In most cases, the running voltage is set to a value which will allow the wheel to reach synchronous speed in a reasonable time and which does not cause the wheel's electrical power to exceed a reasonable value.

Varying applied wheel voltage, will also vary the current drawn by the wheel. The current drawn by the wheel,  $I\phi$ , is also affected by the magnetic state of the stator and hysteresis rings and therefore is somewhat unpredictable. A value of current over the design goal is not particularly significant as long as it does not result in the wheel's electrical power value being excessive.

It can be seen that all RI 1170 wheels other than Wheel 010, have a slew capacity below the design or specification goals. This occurred in spite of theory telling us that the slew capacity will be above the specification value of 5.0 rad/sec. This is difficult to explain because of the definition which must be used to define slew capacity (see description of slew test). For example, Wheel 011 has an average slew capacity of 3.5 rad/sec

TABLE 3.4-2  
RI 1170 TEST SUMMARY

Parameter**	Design Goal	S/N 010 Actual	S/N 011 Actual	S/N 012* Actual	S/N 020 Actual	S/N 021 Actual	S/N 022 Actual	Comments
$V\phi$ (Running) (volts)	100	80	80	NA	83	89	89	See Note 1
$I\phi$ (Running) (amps)	.090	.100	.083	NA	.090	.137	.115	See Note 1
RUT (sec)	NA	NA	NA	NA	NA	32	30	
RDT (sec)	NA	NA	NA	NA	NA	192	141	
$P_{ELECT}$ (watts)	11.3	7.6	5.46	NA	7.46	6.08	5.40	
$P_{MECH}$ (watts)	5.5	NA	NA	NA	NA	4.08	4.26	
$T_{MECH}$ (gm-cm)	9	NA	NA	NA	NA	8.3	8.7	
$\eta$	48.5% min	NA	NA	NA	NA	67%	79%	
CW Slew Capacity (rad/sec)	5.0 min	6.2	3.6	NA	<3.2	2.6 @2 atm abs	2.5 @2 atm abs	See Notes 2 and 3
CCW Slew Capacity (rad/sec)	5.0 min	6.0	3.4	NA	NA, Due to Wheel Seizure	2.6 @2 atm abs	2.3 @2 atm abs	See Notes 2 and 3
Static Stiffness	See Graphs 1 and 2	See Graphs 1 and 2	NA	NA	NA	NA	NA	

\* Wheel suffered catastrophic failure after little running - no data available.

\*\* See Table 3.4-3 notation list for definitions of symbols.

Hamilton Standard  
DIVISION OF UNITED AIRCRAFT CORPORATION

HSER 6197

54

TABLE 3.4-3

NOTATION LIST

<u>SYMBOL</u>	<u>DEFINITION</u>
$V_{\phi}$	Wheel Phase Voltage
$I_{\phi}$	Wheel Phase Current
RUT	Run Up Time (Time To Reach Synchronous Speed)
RDT	Run Down Time (Time To Coast To A Stop From Synchronous Speed)
$P_{ELECT}$	Electrical Power Drawn By Wheel
$P_{MECH}$	Mechanical Power Developed By Wheel
$T_{MECH}$	Mechanical Torque Developed By Wheel
$\eta$	Wheel Efficiency $P_{MECH}/P_{ELECT}$

TABLE 3. 4-2 (Continued)

NOTE 1

The wheel running voltage,  $V\phi$ , was set at or below the design goal value as long as run up time and wheel electrical power were satisfactory. The RI 1170 wheels operated well when the running voltage was set between 80 and 90 V; therefore, the testing was performed at wheel voltages set in this range.

NOTE 2

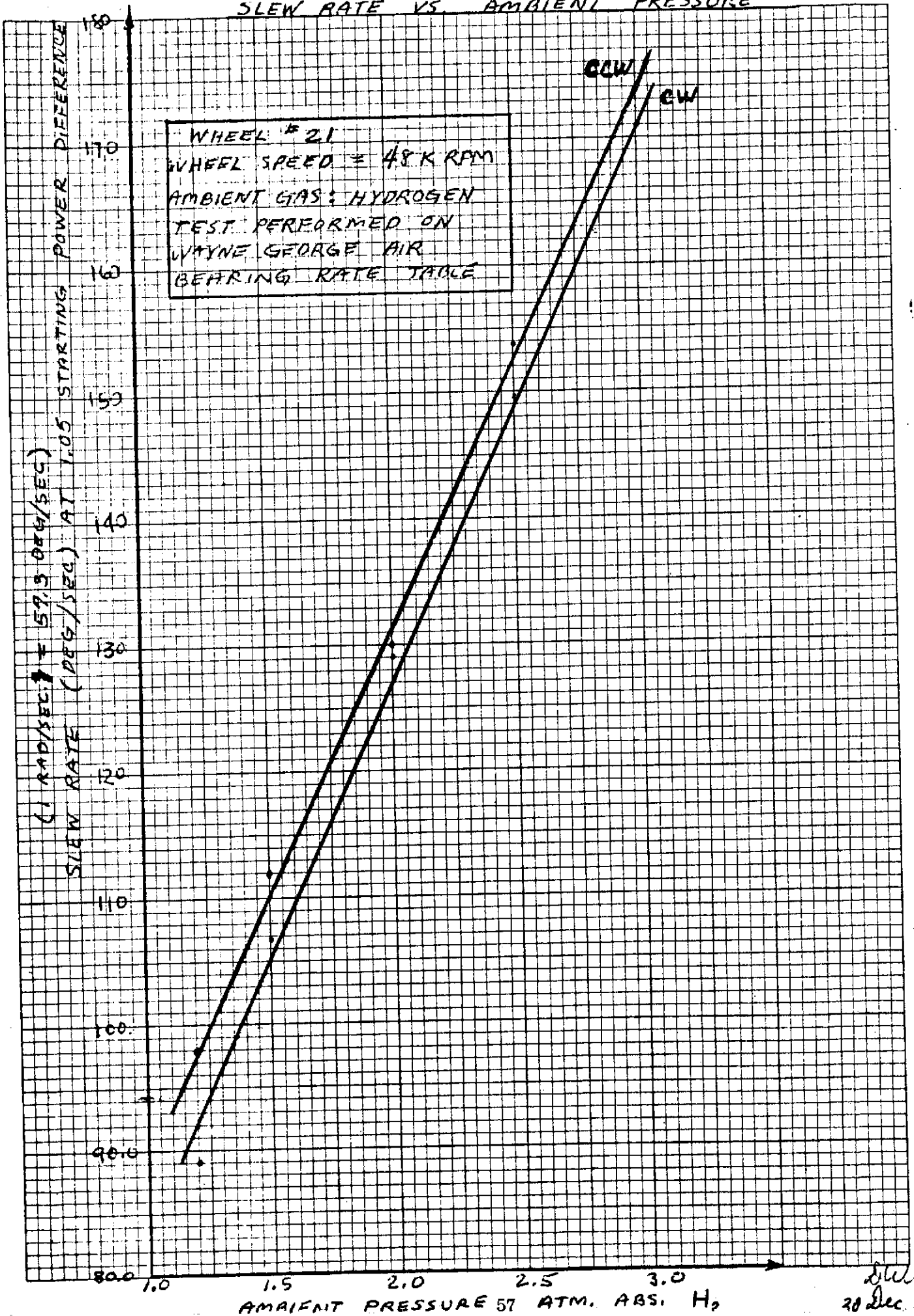
The slew capacity design goal was 5.0 rad/sec. This represents the slew rate at which either the journal or thrust clearance decreased by 75%. Conventional methods of measuring this change in clearance were impractical. Therefore, the power increase method was employed. When the wheel is being slewed, the electrical running power of the wheel was noted. When this power increased to a value 40% above the nominal running power of the wheel, the test was stopped and the last slew rate was taken as the slew capacity. This figure was derived from MIT Instrumentation Lab Report, R-264 Final Report, "Apollo Gas Bearing Material Program", Oct. 1968, Henry H. Rowe, Jr.

NOTE 3

Wheels S/N 021 and S/N 022 were slew tested while these wheels were in an environment of 2 atm abs of  $H_2$ .

It had been confirmed (See Figure 3. 4-2 ) that an increase in ambient pressure raises the wheel slew capacity. Therefore, wheels S/N 021 and S/N 022 were tested in 2 atm abs of  $H_2$ ; however, this still failed to raise the slew capacity of these gas bearings to the design goal level.

Figure 3.4-2  
SLEW RATE VS AMBIENT PRESSURE



20 Dec. 1970

EUGENE DIETZGEN CO.  
MADE IN U. S. A.

NO. 340-10 DIETZGEN GRAPH PAPER  
10 X 10 PER INCH

## 3.4.2.4.1 (Continued)

based on a limiting power increase of 40%; however, the wheel has not seized. Therefore, the slew capacity of this wheel must be greater than 3.5 rad/sec, but there is no way of telling how much greater without actually slewing the wheel until it seizes. Therefore, even though the average slew capacity of S/N 011 appears to be 3.5 rad/sec, it should be understood that the actual slew capacity is at least 3.5 rad/sec and may meet the specification requirement.

The above comments are not applicable to the slew capacity of Wheel S/N 020 because it actually seized at 3.2 rad/sec CW; therefore, 3.2 rad/sec is the true slew capacity of the wheel in the clockwise direction.

Wheels S/N 021 and S/N 022 were slew tested while the wheel was in an environment of 2 atm abs of H<sub>2</sub>.

It has been confirmed (See Graph, Figure 3.4-2) that increase in ambient pressure raises the wheel slew capacity. Therefore, we tested Wheels S/N 021 and S/N 022 in 2 atm abs of H<sub>2</sub>; however, this still failed to raise the slew capacity of these gas bearings to an acceptable level. The slew capacity of these same bearings is even lower in an environment of 1.5 atm abs, the design specification.

3.4.2.4.2 Comparison With Other Gas Bearings

In Appendix D is presented a comparison of typical gas bearings from the three Hamilton Standard gyros which incorporate gas bearing wheels. Examination of this tabulation allows comparison of the specification value of the gyro parameter with the value actually obtained for the three different gyro gas bearings.

3.4.2.5 RI 1170 Start-Stop Failure Report3.4.2.5.1 Introduction

The purpose of performing analysis on RI 1170 Wheel S/N 010 was to determine the cause of the failure of the wheel to start during the start-stop test. By performing the analysis, we also hoped to gain knowledge concerning the behavior of ceramic gas bearing materials when subjected to repeated starting and stopping.

3.4.2.5.2 History of Wheel S/N 010

Since its assembly, Wheel S/N 010 has been run for a total of 934 hours and has sustained 12,000 start-stops before failing to start. Before the start-stop testing, slew tests and static stiffness tests had been performed. Therefore, the run time and start-stops during these tests are also included in the above figures. It should be noted that the shaft had been broken during initial dimensional checks and was repaired with epoxy prior to assembling and testing the gas bearing. Cracks in the bore of the rotor have been found; however, it is not known what caused the cracks. It has been determined that the cracking occurred sometime between wheel assembly and the beginning of the start-stop tests.

3.4.2.5.3 Analysis Methods and Equipment

Analysis of Wheel S/N 010 was performed at United Aircraft Research Labs (UARL) by the Materials Analysis Department. Three pieces of equipment were used for the analysis: scanning electron microscope (SEM), optical microscope, electron probe spectrometer (probe).

The optical microscope (50X - 500X) was used first to determine areas of wear and general surface conditions before examining areas in detail on the SEM under higher magnification.

The research instrument used primarily for investigating the surface conditions of the parts was the SEM. The SEM is capable of magnifications from 20X to 50,000X quite easily and provides a depth of field 500 times that of the optical light microscope. The parts under examination must be conducting or must be made conducting; therefore, a 300-500Å thick coating of gold-palladium was vapor deposited on the ceramic parts.

For determining what substances were present on the critical surfaces, the probe was employed. Using the X-ray spectra obtained during electron bombardment of the specimen, the elements present and their relative concentrations were determined.

3.4.2.5.4 Results of Analysis

The analysis at UARL resulted in SEM photographs of all critical gas bearing surfaces and probe analysis of all pieces which could be analyzed. Following is a general description of the results which can be derived from this information.

3.4.2.5.4.1 Positive Thrust Plate, P/N 31158-1

The optical photographs of the thrust plate's surfaces reveal much severe pitting and many scratches. See Figures 3.4-3 and 3.4-4. On these optical shots (100X), no debris was noted other than that which can be assumed to have originated from the atmosphere while the thrust plate was being prepared for examination. The SEM was then employed to look more closely at the surface in the groove and ridge areas.

The SEM photos show more clearly the nature of the pitting and the severity of the scratches. While the scratches appear very shallow, the pitting appears extensive. See Figures 3.4-5 thru 3.4-6. It can be noted in these photos that there are pieces of ceramic in the pits which could be dislodged at least in part.

3.4.2.5.4.2 Negative Thrust Plate, P/N 31159-1

The optical photos of this thrust plate show the presence of the pitting and scratches as on the other plate. See Figures 3.4-7 and 3.4-8. On Figure 3.4-8, an area of severe wear can be seen.

The SEM photos reveal the fact that the scratches are shallow and the pitting is severe. See Figure 3.4-8. As on the other thrust plate, there are pieces of ceramic in the pits which could be dislodged. In particular, see Figures 3.4-9 and 3.4-10. Examination of Figure 3.4-10 (the close up of the wear mark) leads us to believe that a particle had been dislodged during testing and subsequently caused failure on this thrust plate.

3.4.2.5.4.3 Probe Analysis Results For Thrust Plates

The probe reports on the thrust plate (See electron microprobe reports, EMP No. 1442 and EMP No. 1515) reveal nothing startling. The presence of the gold and palladium is due to the coating deposited for SEM analysis. The detection of iron and chromium is due to there being impurities in the  $Al_2O_3$  mixture, and, of course, the aluminum and oxygen are the main constituents of the thrust plate material. The presence of the silicon can be explained by the fact that the grooving of these thrust plates involved blasting with silicon carbide.

3.4.2.5.4.4 Shaft, P/N 31157-1

The SEM photos of the shaft revealed scratches, much pitting and debris in the pits. See Figures 3.4-11 thru 3.4-12. However, the shape of the pits was different from that of the thrust plates. This is because the

**RESEARCH LABORATORIES**  
 UNITED AIRCRAFT CORPORATION    EAST HARTFORD, CONNECTICUT

HSER 6197

## ELECTRON MICROPROBE REPORT

REPORT TO: Donald Geiling                      EMP NO. 1442  
 SAMPLE NO. \_\_\_\_\_                      DATE SUBMITTED \_\_\_\_\_

### HISTORY OF SAMPLE:

An alumina wafer with two distinct general areas was submitted for elemental analysis (Fig. 1).

### COMMENTS:

Spectral patterns were obtained from eight areas on the surface of the specimen. The results of the analysis showed conclusively the presence of Au, Pd, Fe, Cr, Si and Cl, in addition to Al and O. The Au and Pd were intentionally introduced onto the surface as a thin film ( $<500\text{\AA}$ ) as an aid in SEM analysis. The Cl was detected in only two isolated areas, with a further overall distribution analysis indicating only one other area to contain that element. It is therefore felt that Cl was possibly introduced as a handling impurity. Specific analyses were performed for the remainder of the halogen family but no detectable amounts of these elements were observed. The Fe and Cr were found to be fairly uniformly distributed over the entire surface in both the highly polished areas as well as the rough regions. The Fe concentration is approximately 5 times that of Cr. The Si was found to be positively correlated with rough area and a distribution scan (Fig. 2) documents this finding.

Semi-quantitative analyses were next performed for Fe and Si. The Si was found to be approximately 0.1-0.2 w/o in the rough areas vs.  $<0.01$  w/o in the smooth areas. The maximum Fe detected at any point ( $\sim 20\ \mu\text{m}^3$ ) was  $\sim 2$  w/o. An overall concentration would be  $\sim 0.1$  w/o.

DATE: March 31, 1971

ANALYZED BY: \_\_\_\_\_

APPROVED BY: A. V. Manjiv

# RESEARCH LABORATORIES

UNITED AIRCRAFT CORPORATION EAST HARTFORD, CONNECTICUT

## ELECTRON MICROPROBE REPORT

REPORT TO: Donald Geiling EMP NO. 1515

SAMPLE NO. P/N 31159-1, P/N 31157-1 DATE SUBMITTED July 6, 1971

### HISTORY OF SAMPLE:

A thrust plate (Fig. 1) and shaft assembly were submitted for elemental analysis. Because of size limitations no analysis could be performed upon the shaft assembly.

### COMMENTS:

Spectral patterns were obtained from eight (8) randomly chosen areas on the thrust plate: four (4) in the rough areas and four (4) in the smooth regions. These analyses revealed the presence of the following elements:

	<u>Smooth</u>	<u>Rough</u>
Major:	Al <sub>2</sub> O <sub>3</sub>	Al <sub>2</sub> O <sub>3</sub>
Minor:	Au, Pd	Si, Au, Pd
Trace:	Cr	Cr

(Note: The Au and Pd were intentionally introduced as an aid in SEM analysis)

A distribution scan across the thrust plate documents the high silicon content in the rough areas contrasted to smooth regions (Fig. 2).

DATE: July 28, 1971

ANALYZED BY: J.P. A.V.M.

APPROVED BY: \_\_\_\_\_

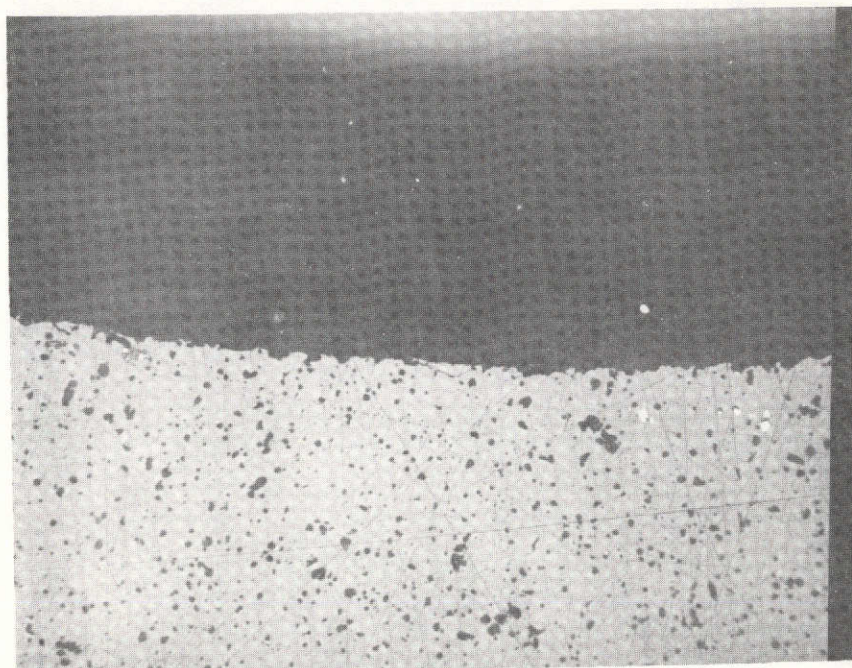


Figure 3.4-3 Positive Thrust Plate Surface Showing Pitting and Scratches, Mag 100X

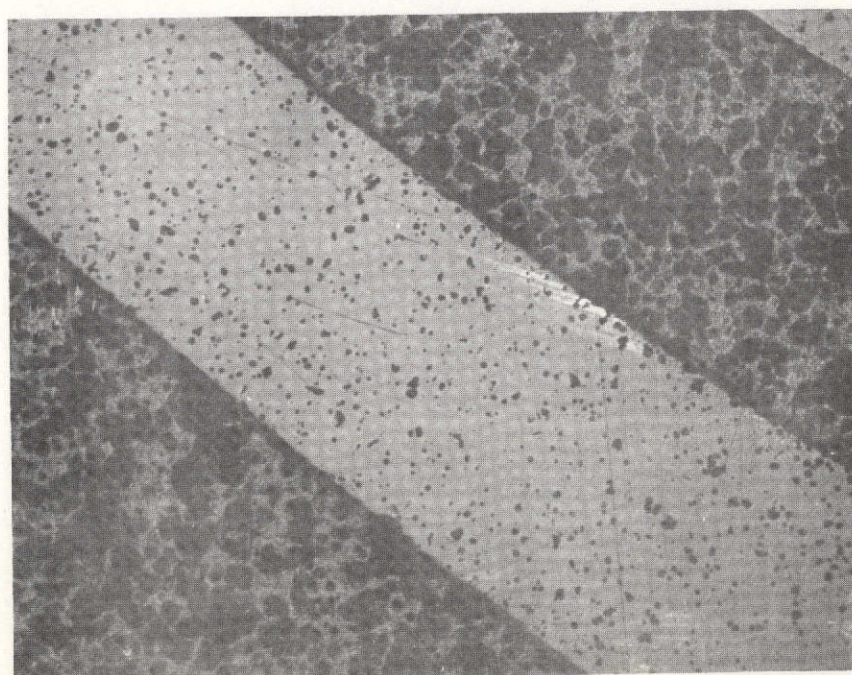


Figure 3.4-4 Positive Thrust Plate Surface Showing Pitting and Scratches, Mag 100X



Figure 3.4-5 SEM Photo of Positive Thrust Plate Surface  
Mag 1000X

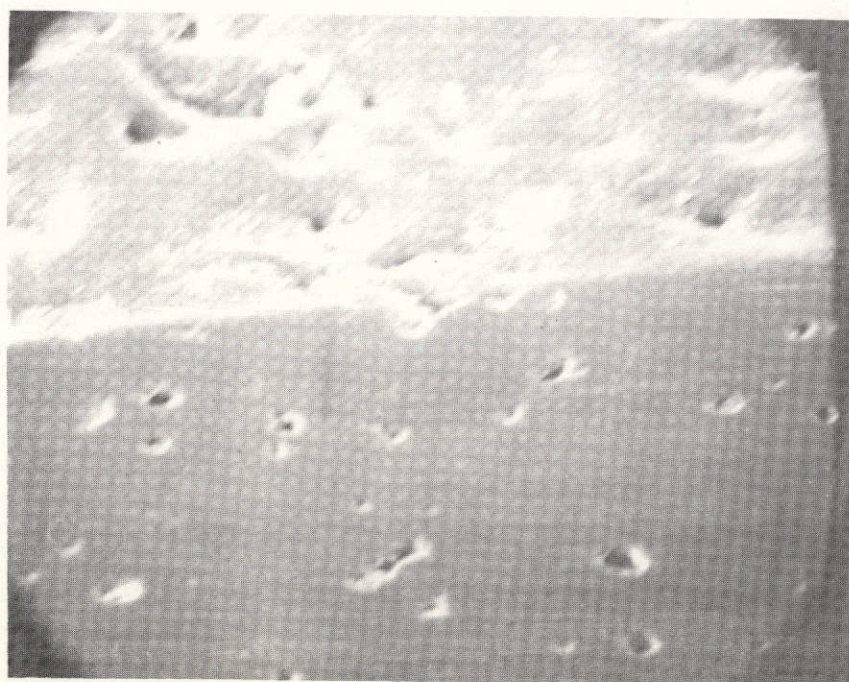


Figure 3.4-6 SEM Photo of Positive Thrust Plate Surface  
Mag 1000X



Figure 3.4-7 Negative Thrust Plate Surface  
Mag 30X



Figure 3.4-8 Negative Thrust Plate Surface  
Showing Wear, Mag 30X

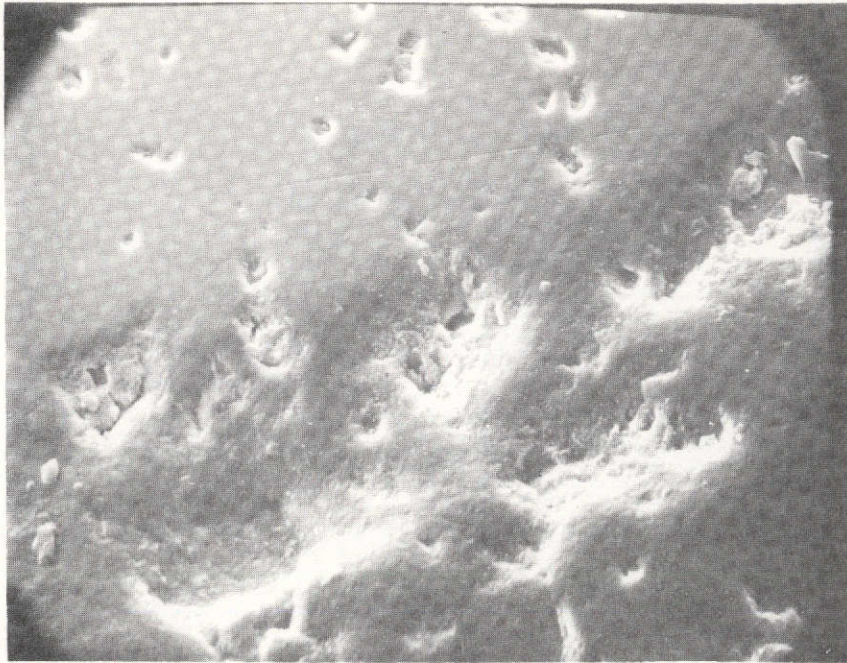


Figure 3.4-9 SEM Photo of Negative Thrust Plate  
Showing Pitting and Scratches, Mag 1000X



Figure 3.4-10 SEM Photo of Wear on Negative Thrust  
Plate, Mag 500X



Figure 3.4-11 SEM Photo of Shaft Showing Debris and Pitting  
Mag 200X

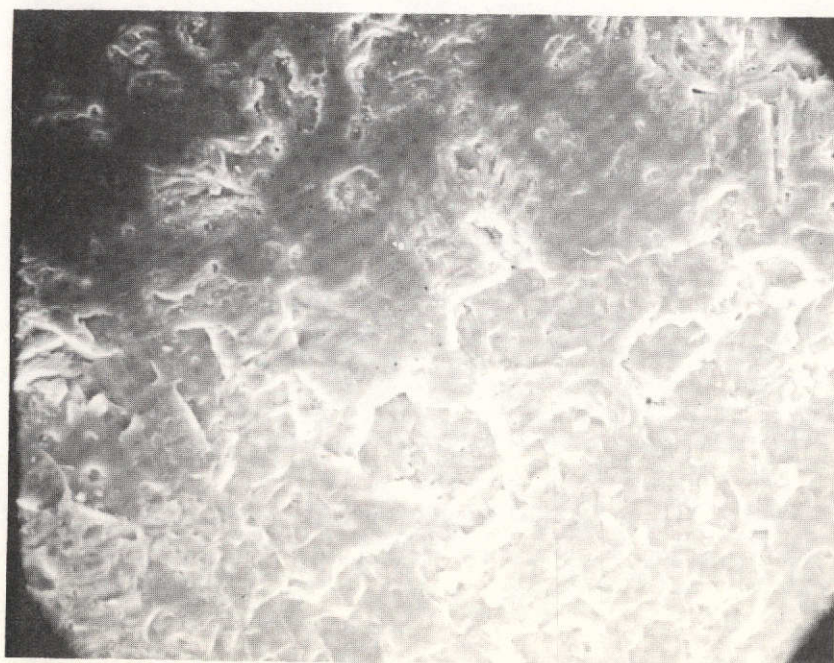


Figure 3.4-12 SEM Photo of Shaft, Mag 1000X

3.4.2.5.4.4 (Continued)

thrust plates are  $Al_2O_3$  and the shaft is BeO. The size of the debris noted in the pits was roughly the same as that found on the thrust plates, thus indicating again the possibility of failure due to debris.

Due to the size of the shaft assembly, it could not be analyzed on the probe.

3.4.2.5.4.5 Rotor Halves, P/N 31153-1

The SEM photos of the rotor halves revealed nothing essentially different than the SEM photos of the thrust plates revealed. Pitting and scratches can be seen and the presence of ceramic debris can be noticed. One point worth noting (Figures 3.4-13, 3.4-14), is that the pits in the bore run circumferentially indicating that they were formed or shaped at least in part by the motion of the rotor halves relative to the shaft.

Due to the size of the rotor halves, they could not be analyzed by the probe.

3.4.2.5.5 Conclusions

The following observations can be made concerning the surface conditions of RI 1170, Wheel S/N 010:

1. Extensive pitting was noted on all bearing running surfaces.
2. Debris was noted in the pits. This debris appeared sufficiently loose that it could have been freed from the pits, at least partially.
3. Probe analysis yielded no information which could reasonably explain the failure.

It has been concluded that particles present in the pitted areas were freed during operation of the gas bearing wheel during the repetitive start-stop testing and thereby caused the wheel to fail to start.

3.4.2.6 RI 1170 Gyro No. 2 Failure (Wheel S/N 021)

Gyro No. 2 failed, exhibiting an open circuit to all motor windings. Failure occurred while the unit was being slewed about the output axis as part of the evaluation of a low loop gain magnetic suspension problem.



Figure 3.4-13 SEM Photo of Rotor Half Showing Pitting, Scratches, and Debris; Mag 800X

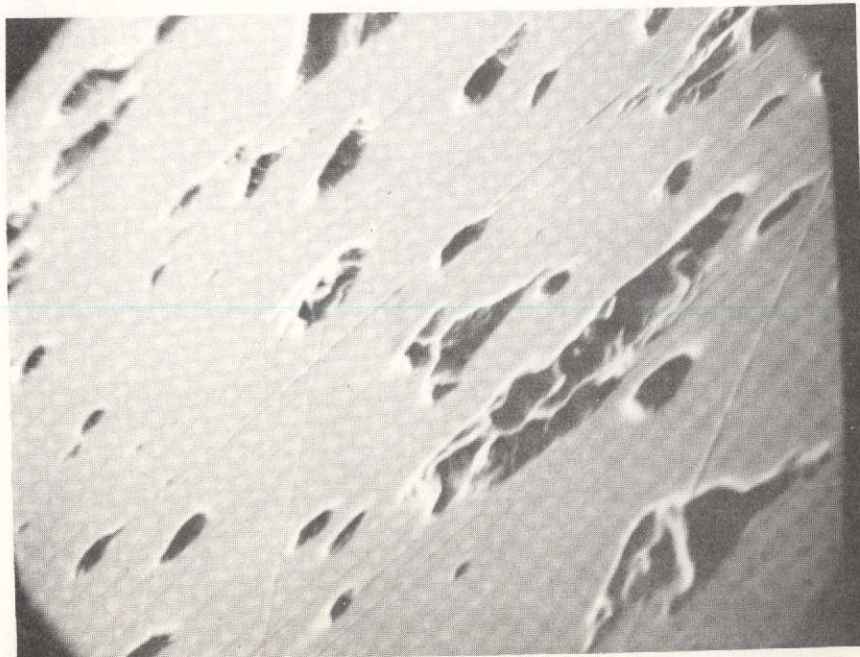


Figure 3.4-14 SEM Photo of Rotor Half, Mag 1600X

3.4.2.6 (Continued)

It was found, after having torn down the gyro, that the slew capacity of the wheel (S/N 021) in this gyro had been exceeded causing touchdown and seizure. This seizure caused the shaft to rotate relative to the float frame breaking the motor leads.

It was found that the rotor halves were cracked by the seizure; however, the shaft remained intact except for two score marks in the grooved areas of the shaft. See Speedring rework section of this report.

3.4.2.7 Speedring Rework of Wheel S/N 021 Shaft and Wheel S/N 011 Rotor

Wheel S/N 021 was seized in Gyro No. 2 causing the wheel halves to sustain cracks; however, its shaft remained intact except for two score marks on the grooved area of the shaft where each end of the wheel made contact with the shaft. It was not believed that these score marks would seriously impair the performance of the shaft.

The shaft of Wheel S/N 011 was broken when it was being built into the first float; however, its wheel halves remained intact.

To combine the shaft of wheel S/N 021 and the rotor halves of Wheel S/N 011, remachining had to be done so that the clearances in the "new" wheel would be within specification limits. The rotor halves and shaft were sent to Speedring Corp. for rework during November, 1971. After remachining by Speedring Corp., the bore radial clearance was found to be  $38 \mu$ " and the thrust plate rotor clearance was found to be  $42 \mu$ ". See Figure 3.4-15.

3.4.3 Integrated RI 1170, Gyro S/N 3

The final configuration of 1170 gyro S/N 3 includes the Fine Temperature Controller and pickoff pre-amplifiers. The chronological history of significant results on this unit is reported in Section 4.3 of this report.

3.4.4 Breadboard System

The delivered RI 1170 Gyro Single Channel Breadboard System consists of a portable set of breadboard electronics which operates from a number of DC supply voltages and delivers the outputs for inertial testing of an RI 1170 gyro using a pulse torque servo amplifier. The RI 1170 gyro S/N 1

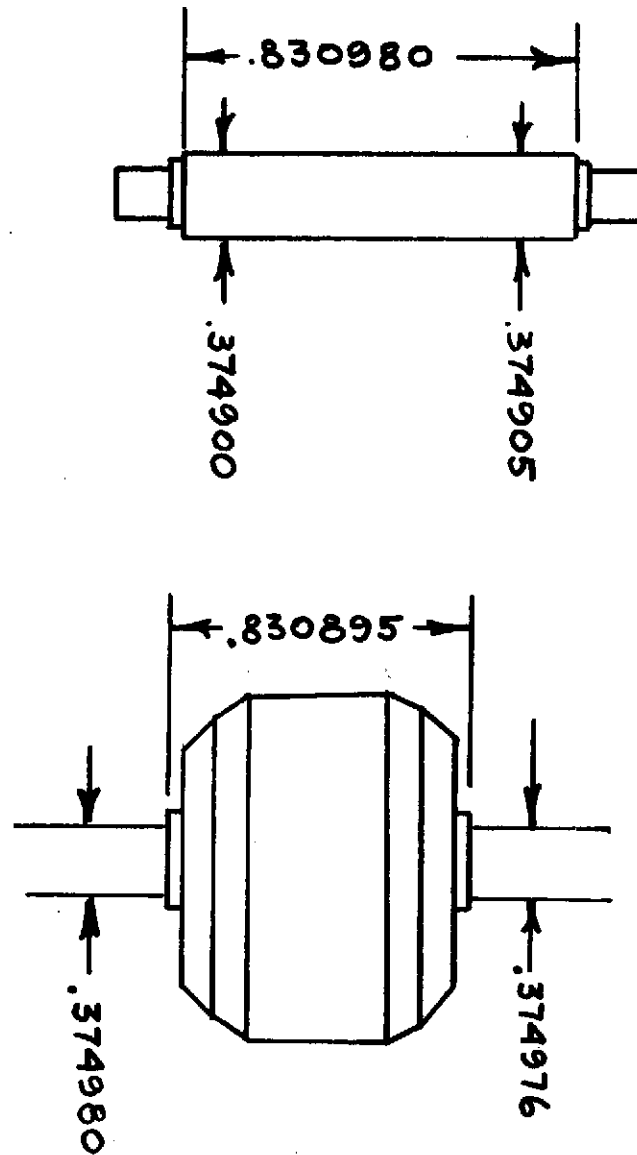


Figure 3.4-15 Bore Radial and Thrust Plate Rotor Clearances

3.4.4 (Continued)

has a magnetic suspension, gas bearing spin motor, and capacitive pickoff. The breadboard electronics feature fourteen (14) individual plug-in type breadboard circuit cards in a standard 19 inch wide rack. Nine circuit boards make up the Magnetic Suspension Electronics (MSE) and one board each make up the Pulse Torque Servo Amplifier (PTSA), Digital Control Electronics (DCE), Fine Temperature Controller (FTC), Synchronizer, and Synchronizer Amplifier.

3.4.5 Excitation and Synchronization Unit

The purpose of the 1170 interface unit is to provide a convenient method for supplying the gyro with the proper DC voltage levels and excitation signals for an internally installed PTSA. This unit was designed to consolidate the non-critical power supplies and the Demodulator Reference and Excitation Generator. The stable power supplies (29.5 V DC and +37.2 V DC) and the 3-phase wheel power supply are not an integral part of the interface unit and must be connected externally.

The Demodulator Reference and Excitation Generator supply the 51 KHz for the gyro excitation, the 51 KHz reference for the PTSA demodulator and the 1.6 KHz for the wheel power supply synchronization. This circuitry also provides a buffered output for the data and sync signal. Appendix A contains the operating instructions for this unit.

The Demodulator Reference and Excitation Generator consist of two vector cards mounted on top of the interface unit. Schematic diagrams of these two cards (C1 and C2) are presented in Appendix A.

The 4.096 MHz crystal oscillator is mounted on board C2. This signal is used for the Demodulator Reference and Excitation Generator and is also carried to the countdown inside the gyro. Also mounted on this board are the countdown chips used to produce the 51 KHz and 1.6 KHz. They include one each of SN54H73, SN7490, and two each of SN54L93. The SN5407 is the buffer chip used to increase the level of the data and sync pulses.

Board C2 contains the discrete component, 51 KHz filter and amplifier for the excitation signal. The amplifier has a split phase transformer to produce 0° and 180° output.

There are also two LM101's located on board C1. The first amplifier is used to shift the phase of the demodulator reference signal with respect to the excitation to trim quadrature as necessary. The second LM101 is a fixed gain amplifier whose output is fed through the PTSA.

## 3.4.5 (Continued)

There are two gain controls located on board C1. A 20 K pot controls the output signal of the excitation amplifier, and the 25 K pot controls the input signal to the demodulator reference signal. Once these signals are trimmed, they should not have to be retrimmed.

The interface unit contains three modular power supplies: +5 V DC,  $\pm 15$  V DC, and +28 V DC. The +5 V DC (MM-5J-0V) and the  $\pm 15$  V DC (MD-15V) are used to power the PTSA and DCE/DSE in the gyro and the Demodulator Reference and Excitation Generator. The +28 V DC (FPS-28-2) is used for the gyro heater only.

3.4.6 Electronic Design Critique

The design approach of the 1170 electronics was based upon the established HSES Pulse Torqued Servo Amplifier design, with minor modifications to optimize performance with the 1170 gyro. The principal differences between this PTSA and the other PTSA models are that the 1170 design has a higher input impedance front end, an active bandpass filter instead of a LC filter, FET's in the demodulator instead of BJT's, FET's as drive elements in the torquer bridge, cascade output stage in the current regulator instead of a single transistor (same 2N2905 as final element in each), and that the 1170 was designed for dual scale factor. Critical areas of this design such as the dual scale factor current regulator and the bridge and driver were breadboard tested. Circuit level testing verified the general design concepts without pointing to any potential problems. The fabricated board, however, shows an increased capacitive loading at the high input impedance gates of the FET's while the FET's themselves appear to have marginal heat sinking. As a result, many of the FET's that were cross-coupled failed during switching transients. This problem was not evident on the breadboard units indicating that the cause was a packaging problem. A simple redesign to eliminate these "pullup" FET's, replacing them with resistors would remove this potential failure mode with only a slight increase in board power and this change was made on one PTSA.

Aside from this shortcoming, the design is nominal. The manufacturing shortcomings are that important test points are difficult to get to or do not exist. Thus, parts may be destroyed by a slip of the test probe while troubleshooting unless extreme care is taken. Another manufacturing flaw appears as the lack of a hermetic seal. While no one failure can be traced to this as a problem, it can only be assumed that resistance values are varying due to moisture absorption and transistor parameters change due to oxidation. This problem would not exist once the boards

3.4.6

(Continued)

were installed in the gyro. A related problem is in interconnections. Several circuit problems were traced to open grounds or poor grounds. Hermetic sealing of the boards and flying lead interconnects should help this. Lastly, the heat sinking capability is questionable. Although complete dissipation data of the electronics was provided, no thermal model of the electronics package is available. This could easily be a factor in the failure of many of the FET's.

With the change from dual scale factor to single and by abandoning the use of magnetic suspension, the circuitry can be condensed. The digital timing section can be fabricated on the same board as the fine temperature controller, the wafers for this board and for the PTSA could both be metal clad to improve heat sinking and act as a RFI shield when these boards are back to back. No specific examples of pickup can be cited, however, the use of short traces for interconnects and the present layout appears adequate and no further improvement has been shown necessary.

4.0 GYRO EVALUATION - SINGLE AXIS TEST

HSES has produced three RI 1170 gyros (S/N's 1, 2, and 3). This section will present a chronological summary of significant events for each of these units.

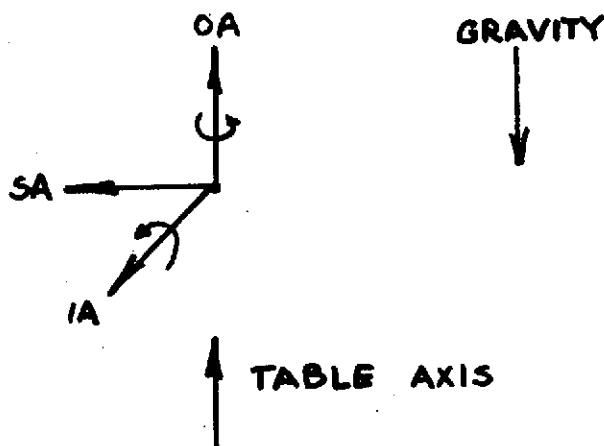
4.1 Gyro S/N 1

Preliminary tests were initiated during May, 1971 to ensure that the gyro and test console interfaces were correct and that the gyro was operational.

A resistance and continuity test was performed with the gyro at room temperature and the test harness connected to the gyro header pins. The resistance was measured between each internal circuit of the gyro with a resistance bridge. The results of the resistance measurements are presented in Figure 4.1-1. Upon verification of normal readings, the gyro was ready for power on testing.

A signal generator and wheel phasing test was then performed to determine the polarity of the signal generator and proper phasing of the gyro spin motor.

With the gyro fully excited, except for the spin motor and suspension, and oriented on the test table as shown below, the output of one preamp was connected to the vertical plates of an X-Y oscilloscope and the reference excitation signal to the horizontal plates. The table was then rotated in a clockwise direction and the direction of rotation of the lissajous oscilloscope pattern was recorded. This direction indicates positive output from the preamp signal since a clockwise rotation of the table top is equivalent to a rotation of the float about the positive output axis. This procedure was



Date 5/12/71

Resistance Measurements of the 1170 Gyro Serial No. 1

<u>Bendix Connector Pin</u>	<u>Function</u>	<u>Approximate Value</u>	<u>Measured Value</u>
A-B	Suspension Coil No. 5	77 ohms	80
C-U	No. 6	77 ohms	80
V-W	No. 7	77 ohms	80
X-T	No. 8	77 ohms	80
<u>n-p</u>	No. 1	77 ohms	80
q-s	No. 2	77 ohms	80
<u>m-AA</u>	No. 3	77 ohms	80
<u>k-z</u>	Suspension Coil No. 4	77 ohms	80
D-E	Spin Motor $\phi 1$	72 ohms	72
E-F	$\phi 2$	72 ohms	72
D-F	Spin Motor $\phi 3$	72 ohms	72
<u>r-s</u>	Torquer Primary	146 ohms	150
Y-Z	Torquer Secondary	Do Not Measure	
CC-DD	Thermistor	117.7 K ohms	85 K
BB-HH	Thermistor	117.7 K ohms	85 K
<u>y-x</u>	Platinum Sensor	1.1 K ohms	1.150 K
GG-FF	Platinum Sensor	1.1 K ohms	1.150 K
P-N	Heater	40 ohms	40

Figure 4. 1-1

## 4.1 (Continued)

repeated for the second preamp signal. With the spin motor supply connected in the same sequence as shown on the gyro wiring diagram, the wheel was momentarily excited. As it coasted down, the table trunion axis was rotated about the gyro positive input axis. This rotation is a positive input and, therefore, the SA should precess about the positive output axis. The lissajous pattern should rotate in the same direction as for the CW snap performed for the signal generator phasing test.

The results of rotating the table CW and CCW on the preamp outputs are summarized as follows:

Flex End Preamp

- Rotating the table in a CW direction caused the preamp output to rotate to the in-phase direction.
- Rotating the table in a CCW direction caused the preamp output to rotate to the out-of-phase direction.

Bellows End Preamp

- Rotating the table in a CW direction caused the preamp output to rotate to the out-of-phase direction.
- Rotating the table in a CCW direction caused the preamp output to rotate to the in-phase direction.

The positive input rotation of the table trunion as the wheel coasted down was observed at the flex end preamp. The lissajous showed an in-phase displacement thereby indicating that the wheel direction was correct.

A suspension coil inductance test was then initiated to obtain a measure for the range of inductance values for each of the suspension coils in order to analytically establish the capacitance value to passively suspend the float.

The range of inductances for each of the suspension coils was determined both with the gyro filled with fluid and with it void of fluid (dry).

The gyro, while dry, was supported by an inclined holding fixture as shown in Figure 4.1-2. The spin axis was directed upward. Using an inductance bridge, the inductance of each of the eight coils was measured and recorded. Following these measurements, the gyro was rotated 45 deg about the OA and again all eight coils were measured. The procedure of rotating 45 deg

## 4.1 (Continued)

about the OA and measuring the inductance was repeated over 360 deg. The same series of measurements were recorded with the OA reversed as shown in Figure 4.1-3.

For the fluid filled condition, the gyro was heated to slightly below its flotation temperature (about 150°F). At this temperature, the positive OA (bellows end of gyro) was positioned vertically down. The low temperature aided in lifting the float, thereby reducing the suspension coil gap at the top or flex end and increasing the coil gaps at the bottom or bellows end. The four coils at the flex end were then series connected, and 50 ma DC was allowed to flow. This procedure assured that the float was fully lifted. At the bellows end, 20 ma DC was applied to a single coil. The coil opposing the energized coil was then measured with an inductance bridge. With minimum delay after interrupting the energized coil's current, the coil's inductance was measured. In a similar manner, all bellows end coils were measured. The flex end coils were measured for maximum and minimum inductance after interrupting the 50 ma current and using the same measuring technique as heretofore described. The entire procedure was repeated with the gyro inverted; that is, with the positive OA (flex end of gyro) positioned up. The data from these tests produced the maximum and minimum coil inductances for all extremes of the float position.

The maximum and minimum coil inductance value with the float at each end of the gyro for the dry and fluid filled condition are summarized in Figure 4.1-4. The inductance values recorded at the 45 deg positions with the gyro dry are presented in Figures 4.1-5 and 4.1-6.

On 3/12/71, inductance measurements were made for the first time. These measurements were performed with a fluid filled gyro. Figure 4.1-4 shows the results. Again on 11/4/71, inductance measurements were made but with the unit dry. These readings are also shown in Figure 4.1-4. The dry condition readings were recorded after a replacement was made at the suspension coil assembly. This replacement was necessary because one of the coils opened (Coil No. 4) during test. On 5/30/72, after having expended considerable effort to actively suspend the float with the breadboard MSE (unsuccessfully), the coil inductances were measured. It was found that the inductances at the flex end had changed. The maximum values increased and the minimum values decreased from the previous measurements with the unit dry. To date, the cause of this change remains uncertain.

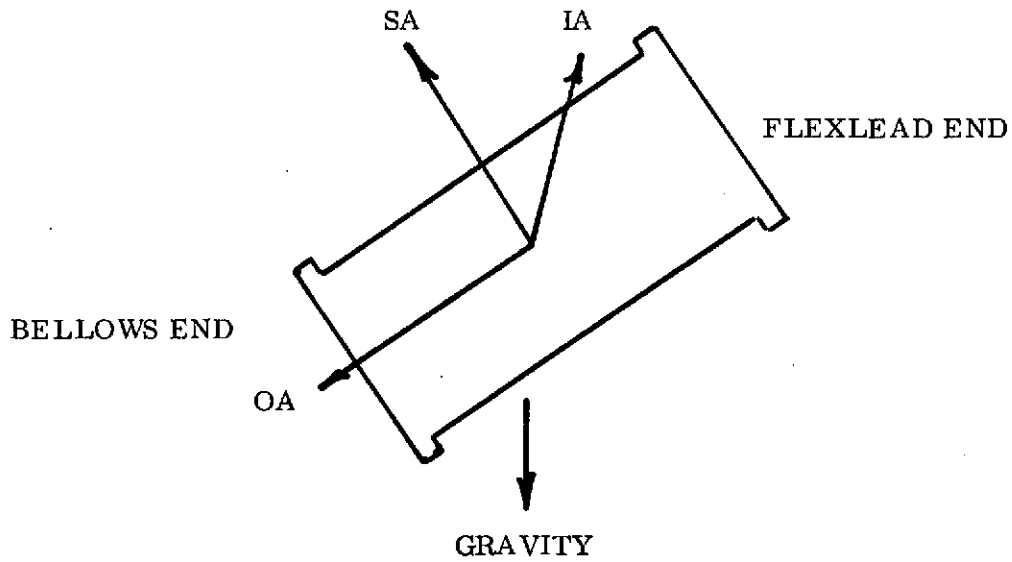


Figure 4.1-2

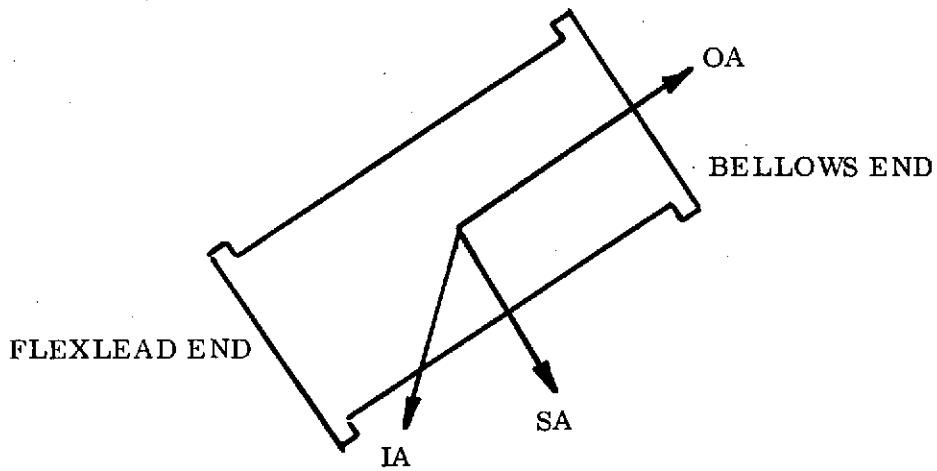


Figure 4.1-3

Gyro Attitudes For Dry Inductance Measurements

Coil No.	Gyro Dry (Tested 11-4-71)				Gyro Filled (Tested 3-12-71)				Gyro Filled (Tested 5-30-72)			
	Float At Bellows End		Float At Flexlead End		Float At Bellows End		Float At Flexlead End		Float At Bellows End		Float At Flexlead End	
	Max	Min	Max	Min	Max	Min	Max	Min	Max	Min	Max	Min
1	278	156	168	122	208	139	150	116	295	160	214	144
2	360	168	182	128	204	136	142	112	390	170	219	161
3	230	140	148	110	180	126	130	108	217	127	162	137
4	238	142	150	112	204	132	148	112	390	137	190	131
5	134	104	194	130	140	106	192	126	400	84	455	92
6	148	110	240	141	152	114	228	140	455	92	464	93
7	164	122	284	152	168	118	270	150	464	93	375	87
8	150	114	232	140	150	114	224	137	335	82	317	191

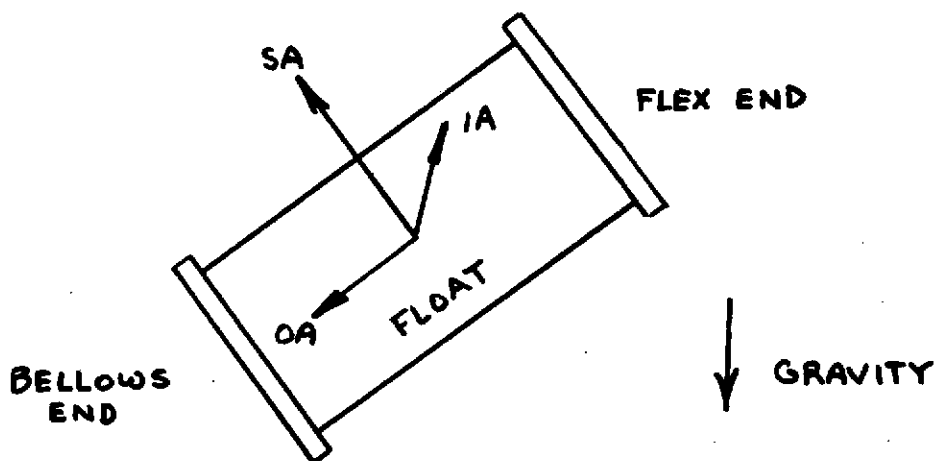
NOTE:

Coils 1, 2, 3, 4 at Bellows End

Coils 5, 6, 7, 8 at Flexlead End

Figure 4.1-4. Coil Inductance Measurements (Millihenries)

Coil No.	S No.		SA↑ 0	45	IA↑ 90	135	SA↓ 180	225	IA↓ 270	315
Flexlead	5	9, 10	118	108	104	108	117	131	135	131
	6	11, 12	149	142	126	114	111	117	127	143
	7	13, 14	136	155	164	154	136	121	118	122
	8	15, 16	111	115	130	145	150	139	127	115
Bellows	1	1, 2	251	278	239	202	165	157	162	200
	2	3, 4	337	218	179	169	182	207	276	360
	3	5, 6	150	140	152	171	215	230	216	173
	4	7, 8	147	185	221	238	215	188	155	141

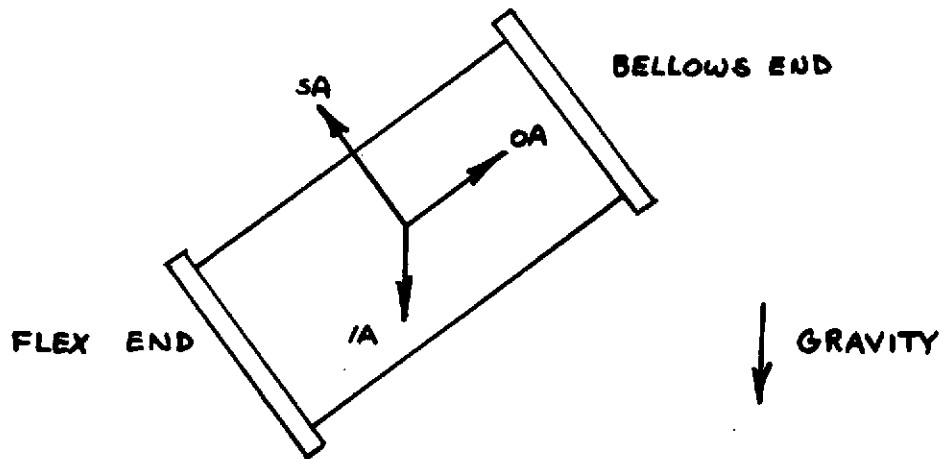


GYRO ATTITUDE OA DOWN

All measurements in millihenries @ room temperature ≈ 75°F.

Figure 4.1-5. Dry Inductance Measurements of Magnetic Suspension Coils in 1170 Gyro, Serial No. 1

Coil No.	S No.		SA↑		IA↑		SA↓		IA↓	
			0	45	90	135	180	225	270	315
Flexlead	5	9, 10	160	137	130	128	163	180	195	181
	6	11, 12	240	217	200	162	141	148	184	215
	7	13, 14	187	235	270	284	183	162	152	162
	8	15, 16	139	147	160	194	232	210	164	146
Bellows	1	1, 2	158	167	161	141	123	121	126	141
	2	3, 4	174	152	136	127	134	151	170	182
	3	5, 6	116	111	113	126	145	148	141	126
	4	7, 8	116	129	140	151	141	127	117	113



GYRO ATTITUDE OA UP

All measurements in millihenries @ 72°F.

Figure 4. 1-6. Dry Inductance Measurements of Magnetic Suspension Coils in 1170 Gyro Serial No. 1

## 4.1 (Continued)

Relative to trimming the magnetic suspension, it was first necessary to determine the series capacitance for each coil which would passively suspend the float. The equation which supposedly provided the capacitance value for suspension at the upper half power point was given as:

$$C = \frac{1}{\omega R} \left( \frac{1}{Q-1} \right)$$

where

$$Q = \frac{\omega L}{R}$$

This equation, however, left two uncertainties; namely, the value of L and the value of R. The approach to determine the value for L was to average all of the inductance values measured on the coils. When this was done, it yielded an average value of 163 millihenries. The value of R was then computed from a measure of the voltage, current and phase angle relationship of one coil while excited at 1 KHz. Using the measured values, R computed as 334 ohms. Applying these now known values into the previous equation, a value for capacitance (C) of 0.23  $\mu$ f was obtained.

Next, each inductor was series connected with a capacitor having a value as close to 0.23  $\mu$ f as was practical. The power was then turned on. Observing the current flow through the coils across a 1 ohm resistor inserted in series, seemingly showed no changes in current which indicated that the float was not moving. The float was moved off by applying a DC current through a coil but upon returning to the normal configuration, little or no motion could be detected. It was concluded that the float was not centering.

Literature was researched on magnetic supports. It was found that if the Q factor of a coil were less than 2, the support would be unstable and the float would not center. The range of inductance values was reviewed and measured and their Q factors determined. It was found that several of the coils were operating with a Q around the 2 value. At this point, it was decided to increase the operating frequency of the passive excitation frequency from 1 KHz to 2 KHz. This, in effect, doubled the Q of the coils and more nearly satisfied what had been determined from the literature.

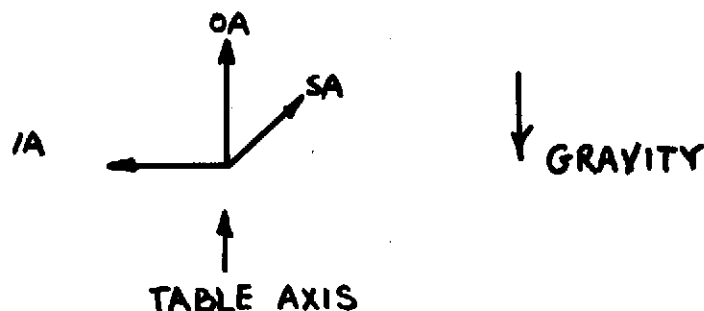
With the new operating frequency of 2 KHz for this passive excitation, the Q factors of the coils increased and accordingly reduced the capacitance value for suspension at the second half power point to a value of 0.046  $\mu$ f.

## 4.1 (Continued)

Once again, 0.046  $\mu\text{f}$  caps were incorporated in series with the suspension coils and power was applied. This time, the suspension appeared to work except for one occasion after the unit had been cooled. Again, research showed that some inductors could be 130 millihenries or less when unsuspended which would cause the LC circuit to resonate and pass to the unstable slope on the resonance curve. In order to remain on the stable portion of the slope, it was postulated that  $\omega L$  must be greater than  $1/\omega C$ . If  $\omega L$  were equal to  $1/\omega C$ , resonance would occur, and if  $\omega L$  were less than  $1/\omega C$ , an unstable condition would result. With this in mind, those capacitors that were operating with low value inductors were increased. The values were selected from the curve of Figure 4.1-7. For example, if a coil had its lowest inductance as 150 millihenries, a capacitor value of at least 0.043  $\mu\text{f}$  was selected. This technique of selecting the capacitors for each coil was demonstrated to suspend the float.

To verify that the float was suspended, manual CW and CCW rates were applied about the OA of the gyro. Since a rate about the OA causes precession about the IA in a systematic direction, a predictable means of displacing the float was achieved. As an OA rate was applied, a polaroid picture of the oscilloscope trace showing the coil current through a 1 ohm resistor was taken. Each coil in turn was recorded. The results showed that the coil current increased or decreased in a manner predictable by the direction of the OA rate and recovered to its original level after removing the rate. A copy of one of the coil current traces showing a current decrease during the applied rate and recovery is shown in Figure 4.1-8.

A gyro nominal torquer scale factor test was performed to determine the value of the gyro scale factor to be used during future tests. With the float passively suspended and the wheel operating at 48 K rpm, the gyro was oriented as shown below. With the loop closed, the table top was rotated until the input axis pointed North. The torquer current was then sampled for 100 seconds using an integrating digital voltmeter across a 1 K ohm resistor in series with the torquer. Several samples were recorded with the input axis North. The table was then rotated 180 degrees to place the input axis South. Again, several samples were recorded. The average torquer current value for each position was used for the scale factor determination.



# Passive Magnetic Suspension

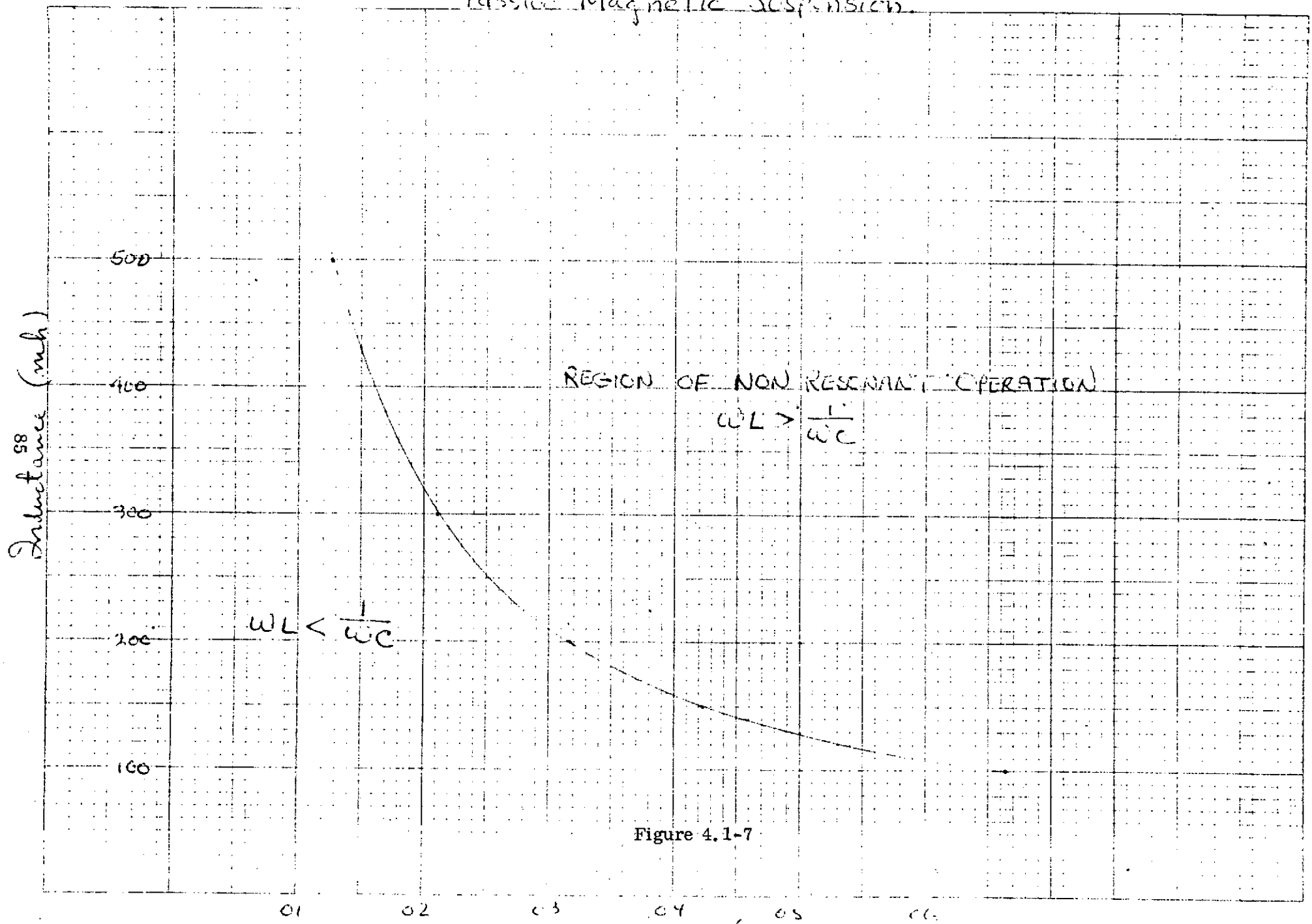
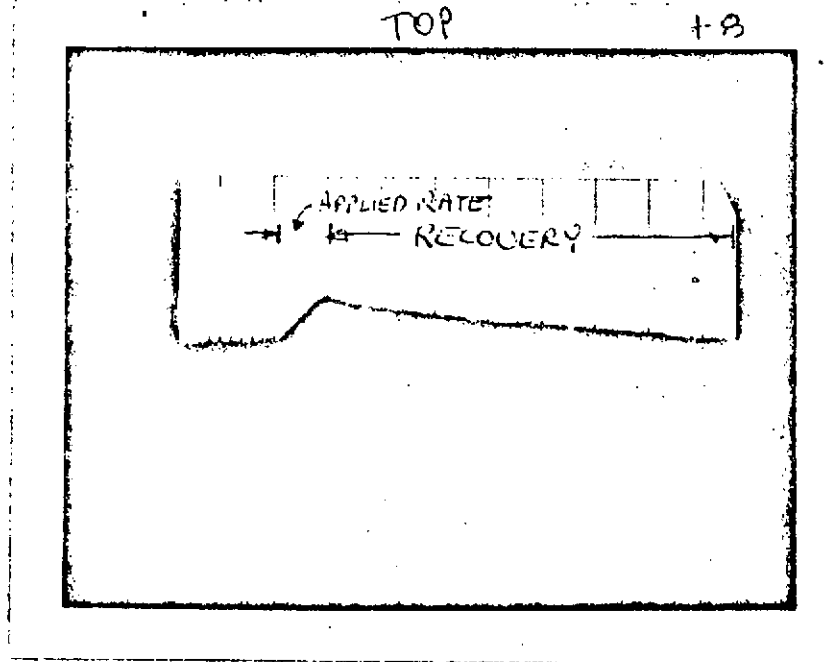


Figure 4.1-7

Figure 4.1-8

SEARCH COIL 8 OUTPUT



VERTICAL 1 mA/cm.  
HORIZONTAL 5 SEC./cm.

## 4.1 (Continued)

The average current for the IA-North position was  $+4.7502 \mu\text{a}$ , and the average current for the IA-South position was  $-7.3882 \mu\text{a}$ .

The combined North plus South earth rate component for the latitude at HSES is  $22.458 \text{ deg/hr}$ . Therefore, the scale factor for the gyro was calculated to be:

$$\begin{aligned} 22.458 \text{ deg hr} &\div (4.7502 + 7.3882) \\ &= 22.458 \div 12.1384 = 1.850 \text{ deg/hr}/\mu\text{a} \end{aligned}$$

Gyro performance tests were then conducted to determine the gyro performance coefficients for fixed bias (BF), Spin Axis Unbalance ( $U_{SA}$ ) and Input Axis Unbalance ( $U_{IA}$ ).

The gyro was tested in six different positions with the electrical rate loop closed between the gyro signal generator and gyro torque generator. For this test, the gyro was fully excited. In each position, the loop current in  $\text{deg/hr}$  was determined using the digital integrating voltmeter readout system. The gyro was set to different positions by manipulating the drive screws of the dividing head. The drift rates obtained in the 6-positions yielded the values for the gyro performance coefficients.

The six positions of the test were as follows:

Position 1	Output Axis Up, Input Axis South
Position 2	Output Axis Up, Input Axis North
Position 3	Output Axis North, Input Axis Down
Position 4	Output Axis North, Input Axis East
Position 5	Output Axis North, Input Axis Up
Position 6	Output Axis North, Input Axis West

The following table lists the coefficients measured in 6-position tests with consistent passive suspension excitation and the analog rate loop for all tests.

## 4.1 (Continued)

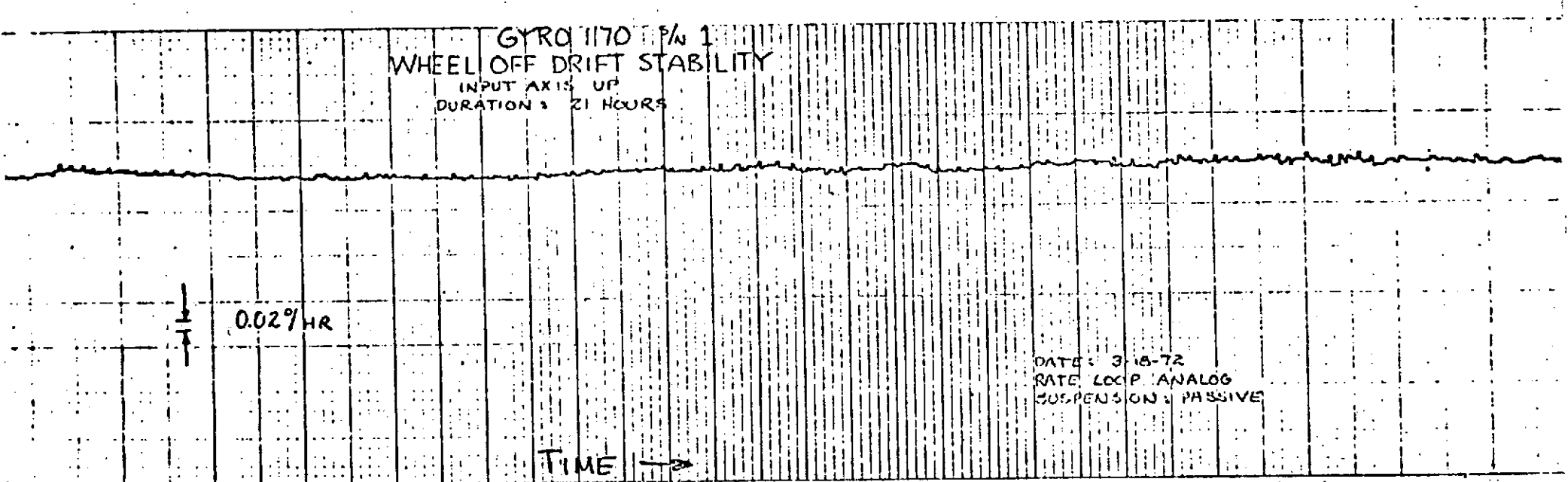
<u>Date</u>	<u>Performance Coefficients</u>		
	$B_F$ <u>deg/hr</u>	$U_{IA}$ <u>deg/hr/g</u>	$U_{SA}$ <u>deg/hr/g</u>
3-28-72	-5.913	+1.657	-3.477
3-29-72	-5.642	+1.734	-3.535
4-18-72	-4.915	+1.788	-3.960
4-20-72	-4.989	+1.660	-4.306
4-21-72	-----	+1.381	-4.417
5-11-72	-3.281	+1.874	-4.567

Stability tests were performed to determine the gyro drift stability during continuous operation. With the gyro in a fixed attitude, the rebalance current was continuously monitored. The monitoring equipment consisted of a direct writing analog recorder and a digital integrating voltmeter which produced a series of printouts. Typically, these tests were conducted overnight. Some were conducted with the gyro wheel operating, and others were performed with the wheel off.

Figures 4.1-9, 4.1-10, and 4.1-11 present wheel off test results in each of the three major gravity orientations; OA, IA, and SA vertical. Figures 4.1-12 and 4.1-13 present wheel on test results in the IA and SA vertical attitudes. The wheel off OA and IA vertical test results show good short-term and long-term stability with short-term peak-to-peak spreads of less than 0.02 deg/hr and long-term spreads of 0.04 to 0.06 deg/hr. The SA vertical test results, however, demonstrate a ramping characteristic of about 0.13 deg/hr<sup>2</sup>. This ramping appears to be a gravity induced bias coefficient. A 6-position test, across the SA vertical test on 3/28/72 which demonstrated a ramp of 0.32 deg/hr, showed a bias shift of +0.27 deg/hr, but less than 0.1 deg/hr non-repeatability in both the mass unbalance terms. The coincidence of the SA vertical ramp and the resultant shift of the bias coefficient suggest the gravity induced bias mechanism.

The wheel on IA vertical attitude showed short-term stability of less than 0.02 deg/hr and long-term stability of about 0.05 deg/hr peak-to-peak. The SA vertical test showed a ramping characteristic of about 0.2 deg/hr<sup>2</sup>.

Figure 4.1-9



68

HEWLETT-PACKARD/MODELLY DIVISION 92701018

HSER 6197

Figure 4.1-10

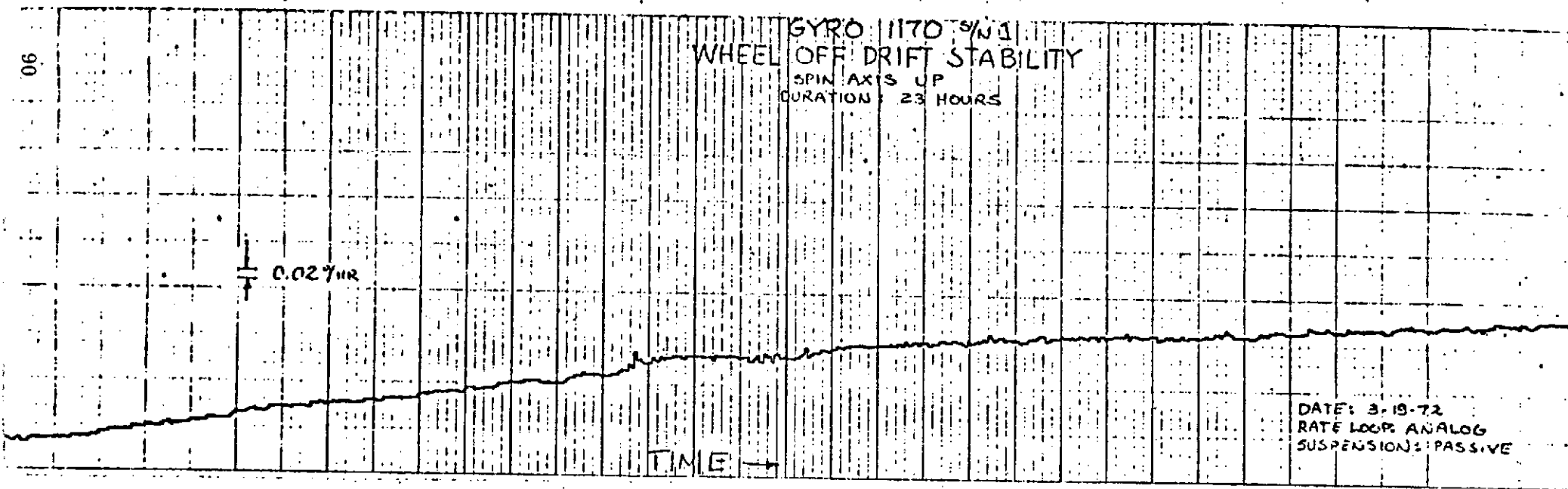


Figure 4.1-11

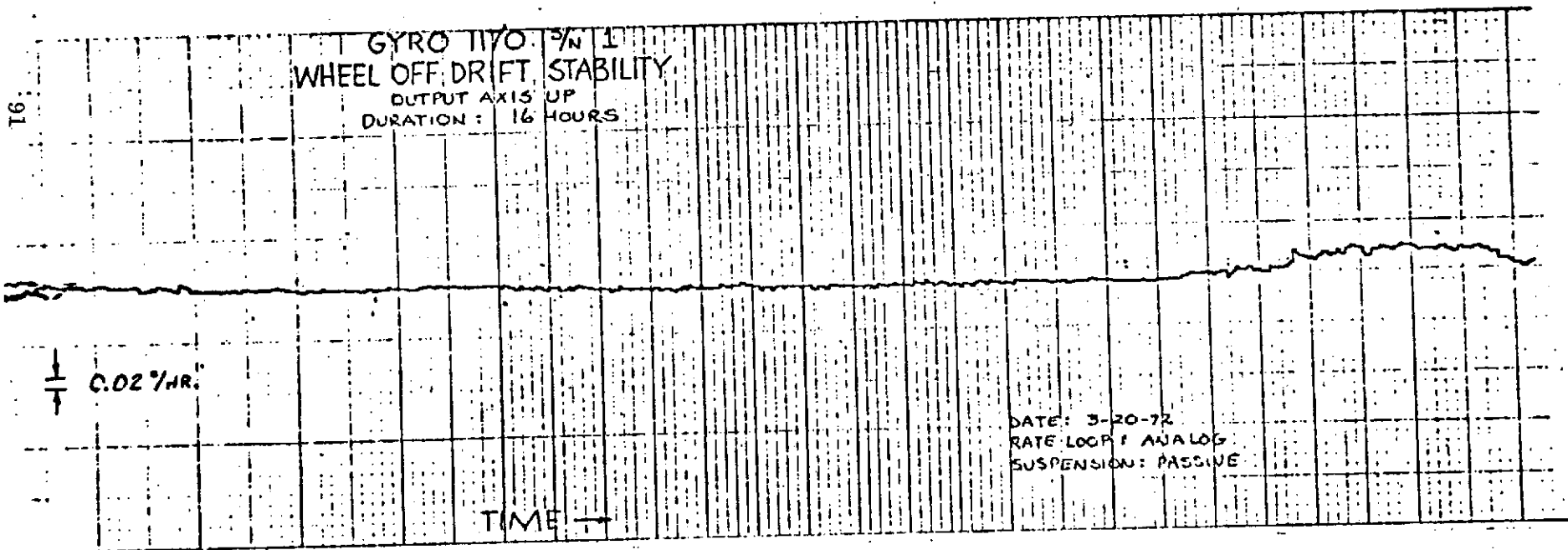


Figure 4.1-12

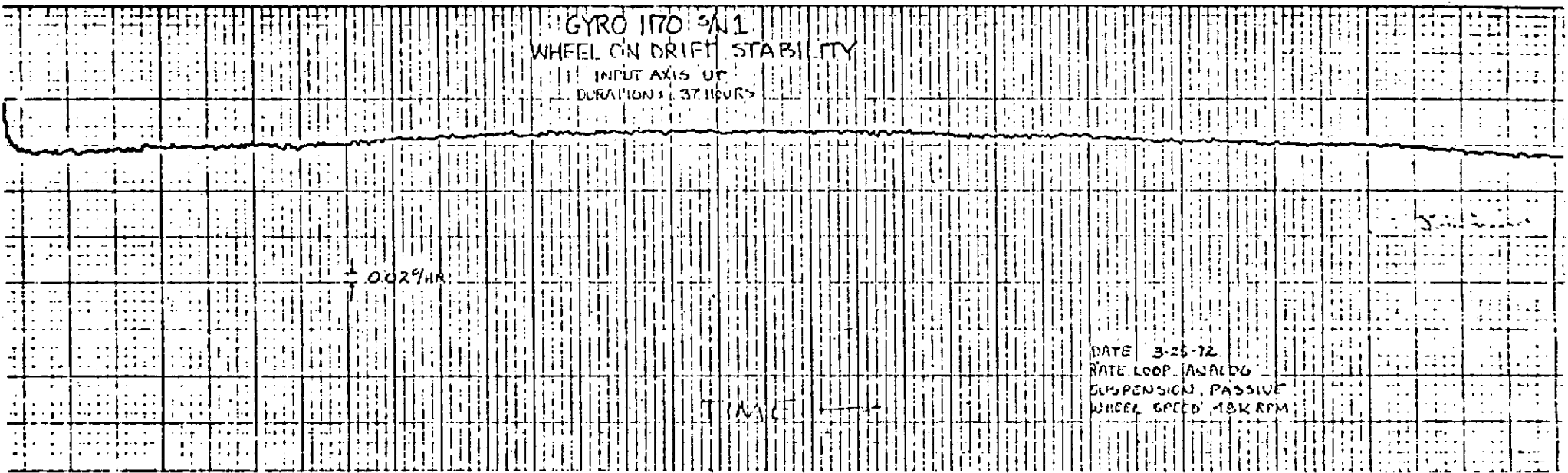
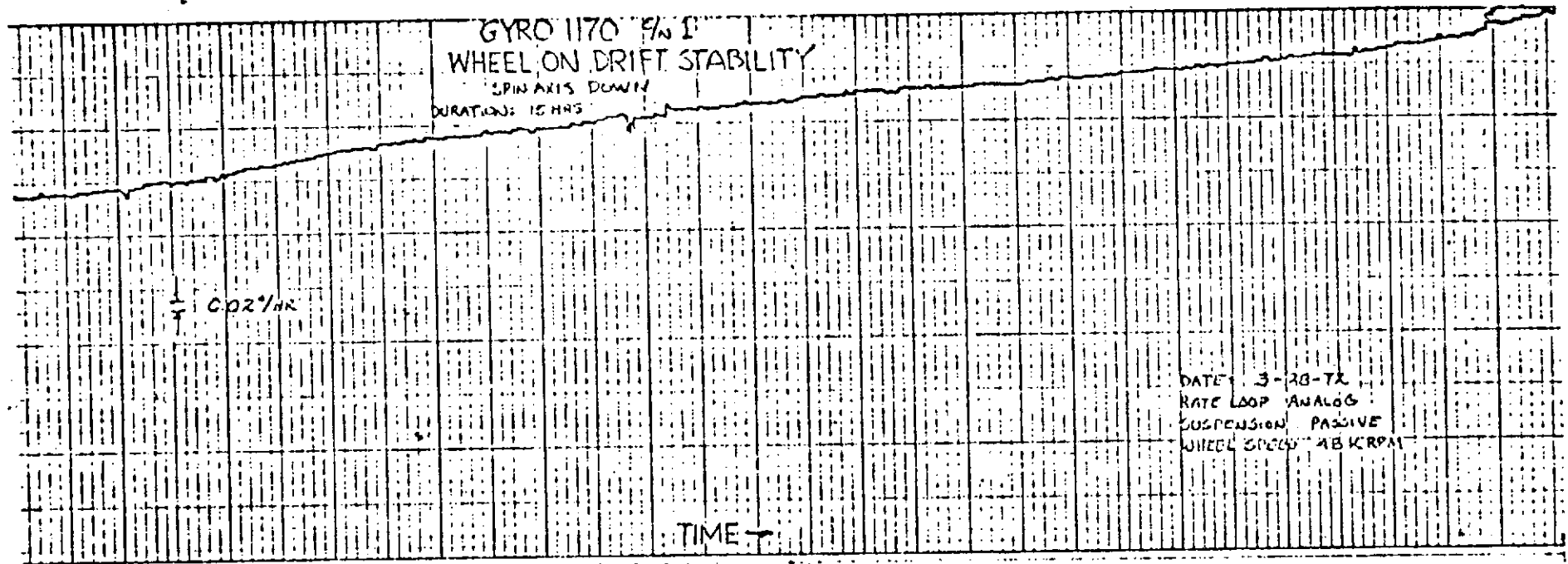


Figure 4.1-13



98

HEWLETT-PACKARD

0870-1018

CODE 66

HSEF 6197

## 4.1 (Continued)

A polar tumble test (analog loop and passive suspension) was then performed to determine the gyro performance coefficients during low level tumbling (20 X earth rate) about the output axis.

With the gyro fully excited and oriented on a rate table with the OA parallel to the earth polar axis, the test was performed with the positive output axis directed first South and then North. A rotation about the OA at 300 deg/hr was performed, and at least one CW and CCW run was made in each of the tumble test attitudes. Because of the magnitude of the gyro's mass unbalance terms (about 3 deg/hr), the standard strip chart resolution of the torque-to-balance current would have been poor. Therefore, a special instrumentation step was devised for this test to enable precise data sampling as a function of rate table angle. Using digital output angular information from the rate table readout, an integrating voltmeter was programmed to measure the gyro's torque-to-balance current during each 9.9 degrees of table rotation concurrent with a measure of the time for the table to traverse this angle. This enabled a precise measurement of the average gyro torque demand for every 9.9 degree increment of table angle. After each data sample, a reset delay time equal to exactly 0.1 degrees of table rotation was initiated, resulting in exactly 36 data samples for each 360 degree rotation of the table.

With the gyro positive output axis polar and South, two CW and two CCW rotations were performed. Only one CW and one CCW rotation was permissible with the OA polar and North because of limitations imposed by cable lengths. A Fourier analysis of the data resulted in the coefficient breakdown shown in Figure 4.1-14.

A settling test was performed to obtain a measure of the time required for the output axis (OA) torques to settle following OA up/down (gyro end for end) and input axis (IA) up/down rotations.

The gyro was oriented as shown below and the table rotated first to the OA up then to the OA down position. The gyro was then oriented alternately IA up and IA down. The output axis up/down rotations about the SA produce only a gravity input change. At each position, the torquer rebalance current was integrated using a Digital Voltmeter with the integration period set for 100 seconds. The integration periods were repeatedly printed until the data showed the torque-to-balance current had settled.

Figure 4.1-14. Gyro Coefficient Summary From Polar Tumble Test

<u>Gyro Attitude</u>	<u>Table Direction</u>	$U_{SA}$ <u>deg/hr/g</u>	$U_{IA}$ <u>deg/hr/g</u>	$B_F$ <u>deg/hr</u>	<u>Anisoelectricity</u> <u>deg/hr/g<sup>2</sup></u>
OA-N	CW	-4.42	1.48	-4.16	0.05
OA-N	CCW	-4.49	1.62	-4.15	0.04
OA-S	CW	-4.57	1.64	-4.58	0.04
OA-S	CCW	-4.60	1.71	-4.51	0.09

A computerized summary of the Fourier coefficients for each 360 deg cycle is provided on the subsequent pages as follows:

<u>Gyro Attitude</u>	<u>Table Direction</u>	<u>Rotation No.</u>	<u>Page No.</u>
OA-N	CW	1	<u>96</u> & <u>97</u>
OA-N	CCW	1	<u>98</u> & <u>99</u>
OA-S	CW	1	<u>100</u> & <u>101</u>
OA-S	CW	2	<u>102</u> & <u>103</u>
OA-S	CCW	1	<u>104</u> & <u>105</u>
OA-S	CCW	2	<u>106</u> & <u>107</u>

FOURIER ANALYSIS  
HSSC GYRO S/N 1170 OAN AND POLAR DATE 5-2-72  
CW ROTATION 1

COEFFICIENTS

A	0	-4.16349996	B, 1	-1.10876111
A	1	-3.30049324	B, 2	0.02915309
A	2	-0.05159696	B, 3	-0.00307360
A	3	-0.00105277	B, 4	0.01589013
A	4	0.00106383	B, 5	0.01759614
A	5	0.00312629		

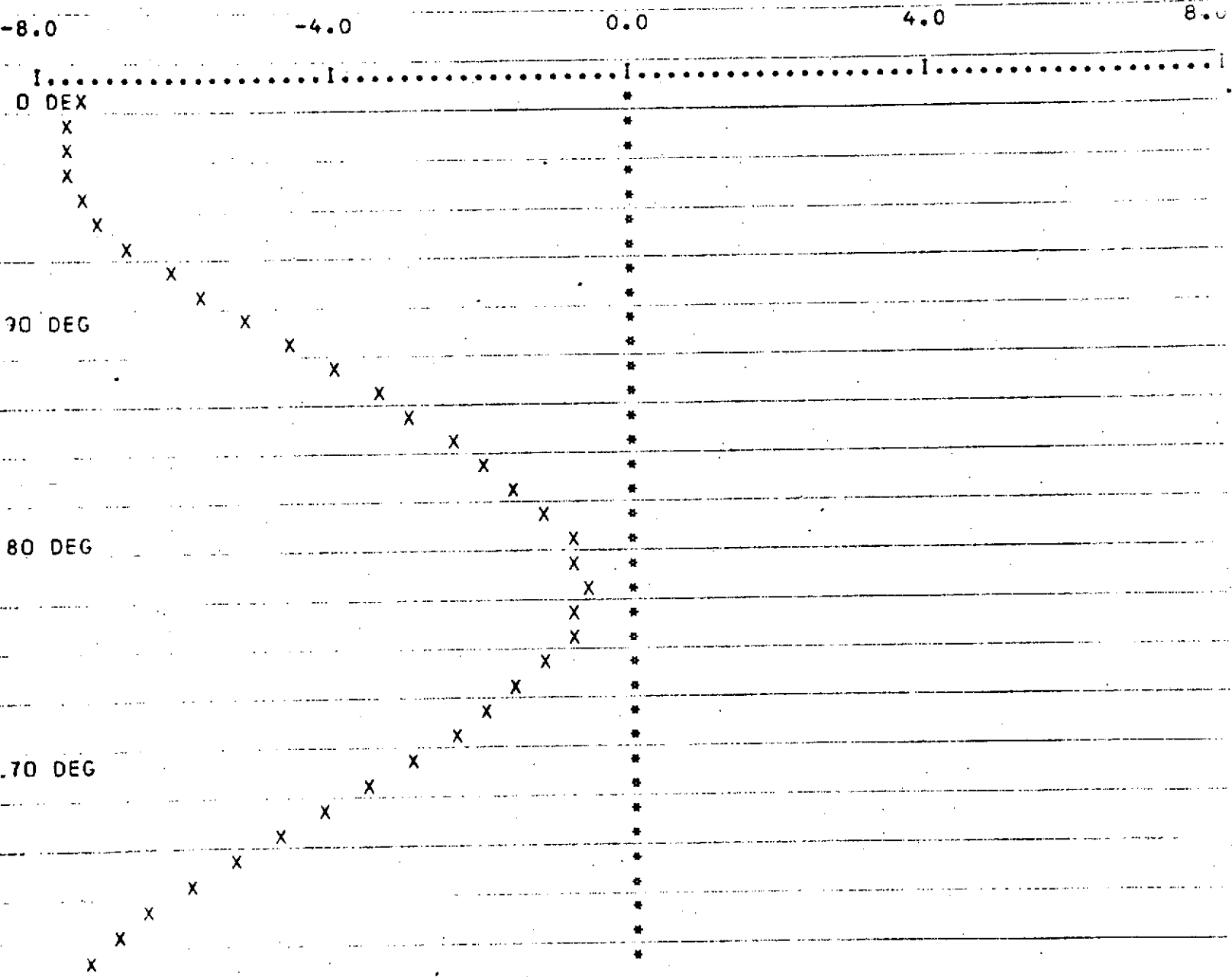
ANGLE	ACTUAL	PERFORMANCE	RESIDUAL
DEG	MODEL	MODEL	DEG/HR
	DEG/HR	DEG/HR	
0.0	-7.40	-7.46	0.05
10.0	-7.61	-7.59	-0.01
20.0	-7.65	-7.62	-0.03
30.0	-7.58	-7.55	-0.03
40.0	-7.39	-7.37	-0.02
50.0	-7.11	-7.10	-0.00
60.0	-6.70	-6.74	0.03
70.0	-6.26	-6.31	0.04
80.0	-5.78	-5.81	0.03
90.0	-5.19	-5.27	0.07
100.0	-4.63	-4.69	0.05
110.0	-4.06	-4.09	0.03
120.0	-3.49	-3.49	0.00
130.0	-2.93	-2.92	-0.01
140.0	-2.40	-2.37	-0.02
150.0	-1.92	-1.88	-0.03
160.0	-1.50	-1.46	-0.04
170.0	-1.16	-1.11	-0.05
180.0	-0.89	-0.86	-0.02
190.0	-0.74	-0.71	-0.03
200.0	-0.68	-0.66	-0.02
210.0	-0.74	-0.72	-0.02
220.0	-0.86	-0.89	0.02
230.0	-1.14	-1.16	0.02
240.0	-1.51	-1.52	0.01
250.0	-1.96	-1.97	0.01
260.0	-2.46	-2.48	0.02
270.0	-3.01	-3.05	0.03
280.0	-3.60	-3.65	0.05
290.0	-4.21	-4.26	0.05
300.0	-4.82	-4.87	0.05
310.0	-5.45	-5.46	0.00
320.0	-6.02	-6.00	-0.01
330.0	-6.56	-6.49	-0.07
340.0	-6.99	-6.90	-0.08
350.0	-7.31	-7.23	-0.08

DRIFT RATE = -4.163 DEG/HR  
UIA = 1.485 DEG/HR//G  
RMS = 0.041 DEG/HR

ANISO TERM = 0.052 DEG/HR//GXG  
USA = -4.420 DEG/HR//G  
NO. OF HARMONICS = 5.

PRINT IDENT NO 1

TORQUER CURRENT VARIATION DEG/HR



ACTUAL MODEL =X RESIDUE =\*

UIA = 1.485 DEG/HR//G  
DR IT RATE = -4.163 DEG/HR

USA = -4.420 DEG/HR//G  
ANISO TERM = 0.052 DEG/HR//GXG

PRINT IDENT NO 1

FOURIER ANALYSIS

HSSC GYRO S/N 1170 OAN AND POLAR DATE 5-2-72

CCW ROTATION 1

COEFFICIENTS

A	0	-4.15355553			
A	1	-3.35215529	B, 1	-1.20691692	
A	2	-0.03143764	B, 2	0.02086464	
A	3	-0.02257267	B, 3	-0.00215759	
A	4	-0.00108036	B, 4	0.00246126	
A	5	0.00808589	B, 5	-0.00020314	

ANGLE	ACTUAL MODEL	PERFORMANCE MODEL	RESIDUAL
DEG	DEG/HR	DEG/HR	DEG/HR
0.0	-7.56	-7.50	-0.05
10.0	-7.70	-7.65	-0.04
20.0	-7.72	-7.70	-0.02
30.0	-7.64	-7.64	-0.00
40.0	-7.47	-7.47	0.00
50.0	-7.17	-7.21	0.04
60.0	-6.81	-6.85	0.03
70.0	-6.37	-6.42	0.04
80.0	-5.88	-5.91	0.03
90.0	-5.34	-5.36	0.01
100.0	-4.75	-4.76	0.00
110.0	-4.16	-4.15	-0.00
120.0	-3.55	-3.54	-0.00
130.0	-2.95	-2.94	-0.01
140.0	-2.39	-2.38	-0.01
150.0	-1.88	-1.87	-0.01
160.0	-1.43	-1.42	-0.00
170.0	-1.08	-1.06	-0.01
180.0	-0.82	-0.80	-0.01
190.0	-0.64	-0.63	-0.01
200.0	-0.57	-0.57	0.00
210.0	-0.63	-0.62	-0.00
220.0	-0.79	-0.78	-0.00
230.0	-1.07	-1.05	-0.01
240.0	-1.43	-1.41	-0.01
250.0	-1.86	-1.85	-0.00
260.0	-2.35	-2.37	0.01
270.0	-2.90	-2.94	0.03
280.0	-3.50	-3.55	0.05
290.0	-4.12	-4.17	0.05
300.0	-4.77	-4.80	0.03
310.0	-5.41	-5.40	-0.00
320.0	-5.97	-5.96	-0.00
330.0	-6.49	-6.47	-0.02
340.0	-6.94	-6.90	-0.03
350.0	-7.28	-7.25	-0.03

DRIFT RATE = -4.153 DEG/HR  
 UIA = 1.616 DEG/HR//G  
 RMS = 0.026 DEG/HR

ANISO TERM = 0.037 DEG/HR//GXG  
 USA = -4.490 DEG/HR//G  
 NO. OF HARMONICS = 5.

PRINT IDENT NO 2



FOURIER ANALYSIS

HSSC GYRO S/N 1170 OAS AND POLAR DATE 5-2-72

CW ROTATION 1

COEFFICIENTS

A	0	-4.57694441	B, 1	-1.22866512
A	1	-3.41625303	B, 2	0.02459721
A	2	-0.02415232	B, 3	-0.02470604
A	3	-0.01740138	B, 4	0.00114157
A	4	-0.00262614	B, 5	0.00331976
A	5	-0.00049325		

ANGLE	ACTUAL	PERFORMANCE	RESIDUAL
DEG	MODEL	MODEL	DEG/HR
	DEG/HR	DEG/HR	
0.0	-8.04	-7.99	-0.05
10.0	-8.19	-8.14	-0.05
20.0	-8.22	-8.19	-0.03
30.0	-8.13	-8.12	-0.01
40.0	-7.95	-7.95	0.00
50.0	-7.68	-7.68	0.00
60.0	-7.29	-7.32	0.02
70.0	-6.83	-6.88	0.04
80.0	-6.31	-6.37	0.05
90.0	-5.76	-5.80	0.03
100.0	-5.18	-5.20	0.02
110.0	-4.57	-4.57	-0.00
120.0	-3.97	-3.95	-0.02
130.0	-3.37	-3.34	-0.02
140.0	-2.80	-2.77	-0.03
150.0	-2.28	-2.25	-0.02
160.0	-1.82	-1.80	-0.02
170.0	-1.42	-1.43	0.00
180.0	-1.17	-1.16	-0.01
190.0	-0.98	-0.99	0.00
200.0	-0.91	-0.93	0.01
210.0	-0.94	-0.98	0.03
220.0	-1.15	-1.14	-0.01
230.0	-1.41	-1.41	0.00
240.0	-1.78	-1.78	-0.00
250.0	-2.25	-2.23	-0.01
260.0	-2.78	-2.76	-0.01
270.0	-3.34	-3.34	0.00
280.0	-3.95	-3.96	0.01
290.0	-4.57	-4.60	0.03
300.0	-5.20	-5.24	0.03
310.0	-5.82	-5.85	0.03
320.0	-6.41	-6.42	0.01
330.0	-6.94	-6.94	-0.00
340.0	-7.39	-7.38	-0.01
350.0	-7.76	-7.73	-0.02

DRIFT RATE = -4.576 DEG/HR

UIA = 1.645 DEG/HR//G

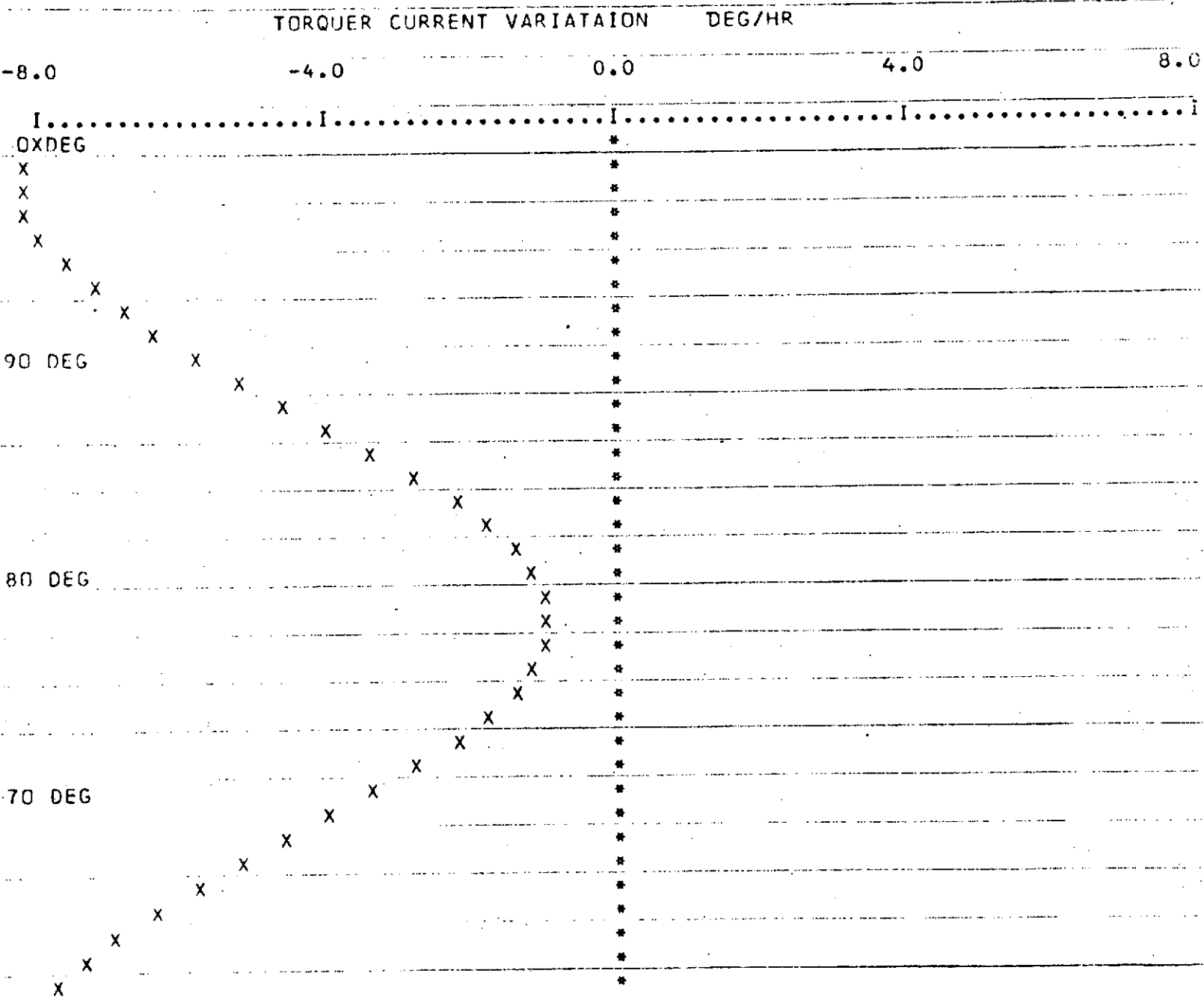
RMS = 0.026 DEG/HR

ANISO TERM = 0.044 DEG/HR//GXG

USA = -4.575 DEG/HR//G

NO. OF HARMONICS = 5.

PRINT IDENT NO 1



ACTUAL MODEL = X

RESIDUE = \*

UIA = 1.645 DEG/HR//G  
 DR RATE = -4.576 DEG/HR

USA = -4.575 DEG/HR//G  
 ANISO TERM = 0.044 DEG/HR//GXG

PRINT IDENT NO 1

FOURIER ANALYSIS  
 HSSC GYRO S/N 1170 OAS AND POLAR DATE 5-2-72  
 CW ROTATION 2

COEFFICIENTS

A	0	-4.57905552	B, 1	-1.23314015
A	1	-3.41152826	B, 2	0.02815703
A	2	-0.02233352	B, 3	-0.02188708
A	3	-0.01364765	B, 4	0.00187154
A	4	0.00056758	B, 5	0.00108244
A	5	0.00019771		

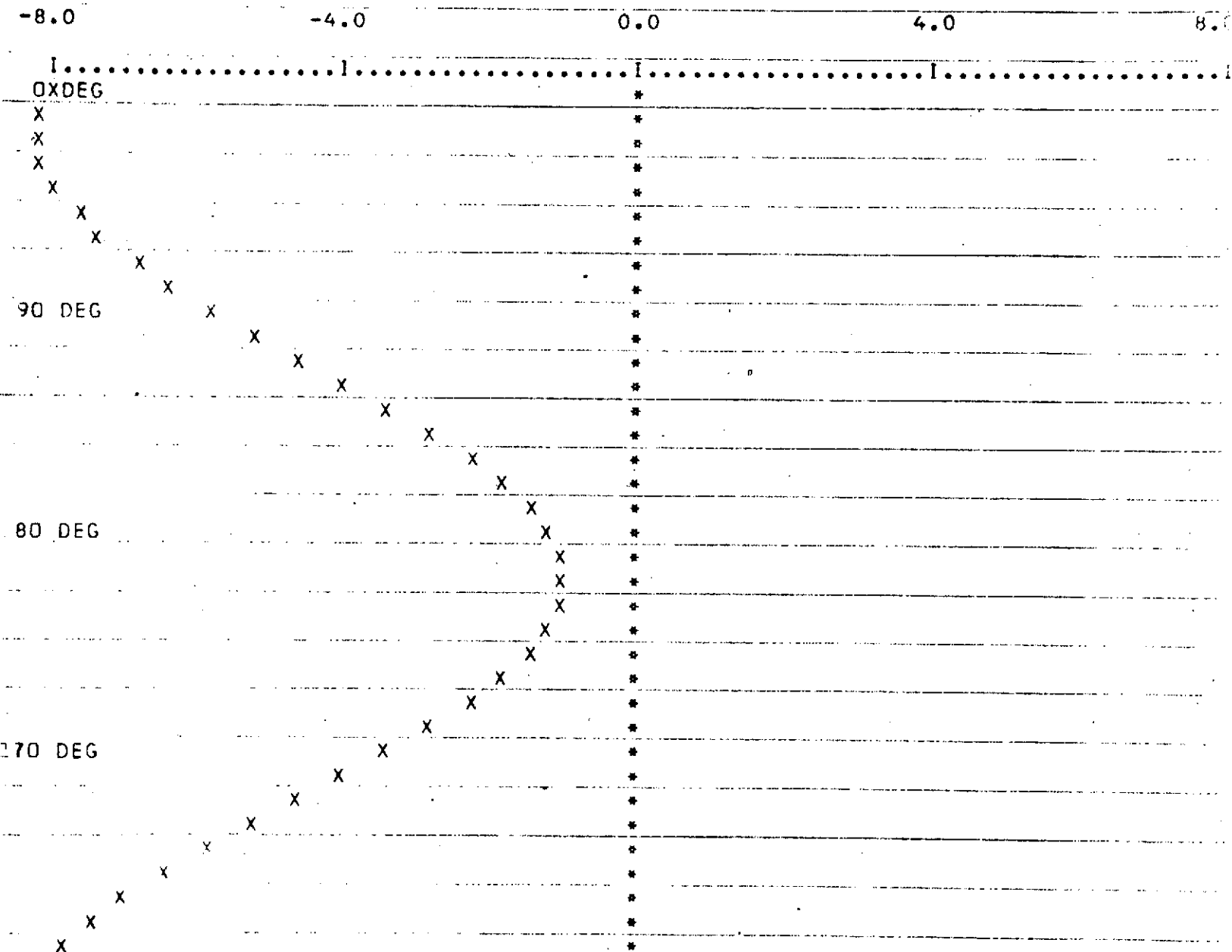
ANGLE	ACTUAL MODEL	PERFORMANCE MODEL	RESIDUAL
DEG	DEG/HR	DEG/HR	DEG/HR
0.0	-8.02	-7.99	-0.03
10.0	-8.17	-8.14	-0.03
20.0	-8.22	-8.18	-0.03
30.0	-8.14	-8.12	-0.02
40.0	-7.95	-7.95	0.00
50.0	-7.67	-7.68	0.00
60.0	-7.30	-7.32	0.02
70.0	-6.84	-6.88	0.04
80.0	-6.33	-6.37	0.04
90.0	-5.78	-5.81	0.03
100.0	-5.19	-5.21	0.02
110.0	-4.58	-4.58	0.00
120.0	-3.97	-3.96	-0.01
130.0	-3.38	-3.35	-0.02
140.0	-2.82	-2.78	-0.03
150.0	-2.29	-2.26	-0.02
160.0	-1.82	-1.81	-0.01
170.0	-1.44	-1.44	-0.00
180.0	-1.16	-1.16	-0.00
190.0	-0.98	-0.99	0.01
200.0	-0.92	-0.93	0.01
210.0	-0.97	-0.98	0.01
220.0	-1.13	-1.14	0.01
230.0	-1.42	-1.41	-0.01
240.0	-1.79	-1.78	-0.01
250.0	-2.24	-2.23	-0.01
260.0	-2.76	-2.76	-0.00
270.0	-3.34	-3.34	0.00
280.0	-3.95	-3.96	0.01
290.0	-4.58	-4.60	0.02
300.0	-5.21	-5.24	0.02
310.0	-5.82	-5.85	0.03
320.0	-6.41	-6.42	0.01
330.0	-6.94	-6.94	-0.00
340.0	-7.38	-7.38	-0.00
350.0	-7.76	-7.73	-0.03

DRIFT RATE = -4.579 DEG/HR  
 UIA = 1.651 DEG/HR//G  
 RMS = 0.022 DEG/HR

ANISO TERM = 0.050 DEG/HR//GXG  
 USA = -4.569 DEG/HR//G  
 NO. OF HARMONICS = 5.

PRINT IDENT NO 2

TORQUER CURRENT VARIATION DEG/HR



ACTUAL MODEL =X

RESIDUE =\*

UIA = 1.651 DEG/HR//G  
 DR T RATE = -4.579 DEG/HR

USA = -4.569 DEG/HR//G  
 ANISO TERM = 0.050 DEG/HR//GXG

PRINT IDENT NO 2

FOURIER ANALYSIS  
HSSC GYRO S/N 1170 DAS AND POLAR DATE 5-2-72  
CCW ROTATION 1

COEFFICIENTS

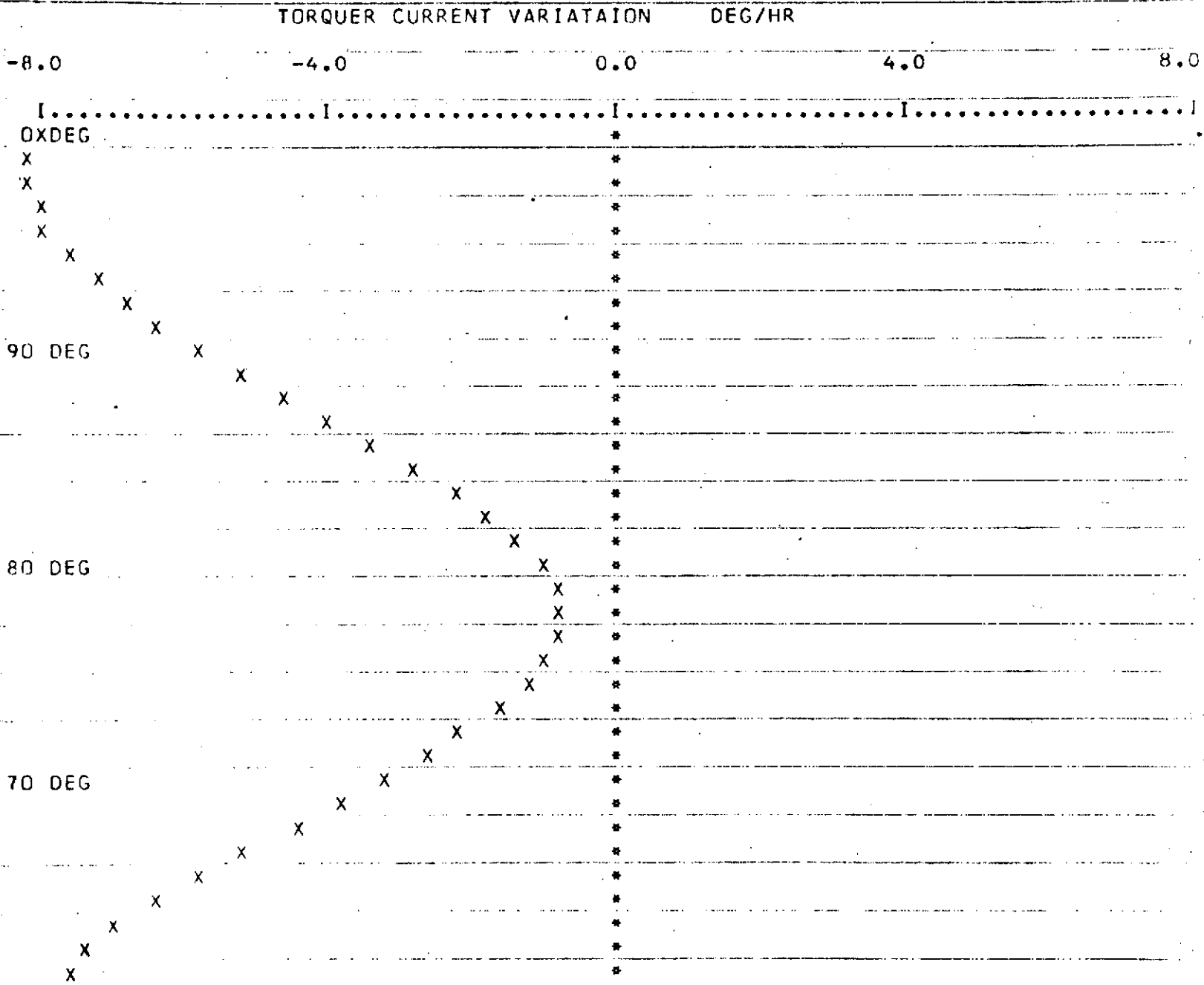
A	0	-4.51344442	B, 1	-1.28068234
A	1	-3.43679405	B, 2	0.05251160
A	2	-0.01278584	B, 3	-0.01346206
A	3	-0.02790521	B, 4	0.00362792
A	4	-0.00012377	B, 5	0.00211197
A	5	0.00333910		

ANGLE	ACTUAL	PERFORMANCE	RESIDUAL
DEG	MODEL	MODEL	DEG/HR
	DEG/HR	DEG/HR	
0.0	-8.01	-7.95	-0.06
10.0	-8.12	-8.10	-0.02
20.0	-8.15	-8.14	-0.00
30.0	-8.07	-8.08	0.00
40.0	-7.91	-7.91	-0.00
50.0	-7.62	-7.65	0.02
60.0	-7.26	-7.29	0.03
70.0	-6.82	-6.85	0.02
80.0	-6.32	-6.35	0.02
90.0	-5.78	-5.79	0.01
100.0	-5.20	-5.19	-0.00
110.0	-4.60	-4.57	-0.03
120.0	-3.98	-3.94	-0.03
130.0	-3.35	-3.33	-0.01
140.0	-2.78	-2.75	-0.02
150.0	-2.23	-2.22	-0.00
160.0	-1.74	-1.75	0.00
170.0	-1.34	-1.36	0.02
180.0	-1.05	-1.07	0.02
190.0	-0.86	-0.88	0.02
200.0	-0.79	-0.81	0.01
210.0	-0.83	-0.85	0.01
220.0	-1.01	-1.00	-0.00
230.0	-1.29	-1.27	-0.02
240.0	-1.67	-1.64	-0.03
250.0	-2.13	-2.10	-0.03
260.0	-2.65	-2.63	-0.01
270.0	-3.23	-3.23	-0.00
280.0	-3.84	-3.86	0.02
290.0	-4.48	-4.51	0.03
300.0	-5.13	-5.16	0.03
310.0	-5.76	-5.79	0.02
320.0	-6.37	-6.37	-0.00
330.0	-6.90	-6.89	-0.00
340.0	-7.34	-7.33	-0.01
350.0	-7.69	-7.69	-0.00

DRIFT RATE = -4.513 DEG/HR  
UIA = 1.715 DEG/HR//G  
RMS = 0.024 DEG/HR

ANISO TERM = 0.094 DEG/HR//GXG  
USA = -4.603 DEG/HR//G  
NO. OF HARMONICS = 5.

PRINT IDENT NO 3



ACTUAL MODEL = X

RESIDUE = \*

UIA = 1.715 DEG/HR//G  
 DR, RATE = -4.513 DEG/HR

USA = -4.603 DEG/HR//G  
 ANISO TERM = 0.094 DEG/HR//GXG

PRINT IDENT NO 3

FOURIER ANALYSIS  
HSSC GYRO S/N 1170 DAS AND POLAR DATE 5-2-72  
CCW ROTATION 2

COEFFICIENTS

A 0	-4.51591664	B, 1	-1.27776743
A 1	-3.44314148	B, 2	0.06885317
A 2	-0.01184131	B, 3	-0.00727683
A 3	-0.03074539	B, 4	0.00682559
A 4	-0.00134091	B, 5	0.00555900
A 5	-0.00072009		

ANGLE	ACTUAL	PERFORMANCE	RESIDUAL
DEG	MODEL	MODEL	DEG/HR
	DEG/HR	DEG/HR	
0.0	-7.98	-7.95	-0.02
10.0	-8.12	-8.10	-0.01
20.0	-8.14	-8.14	0.00
30.0	-8.06	-8.07	0.01
40.0	-7.89	-7.90	0.00
50.0	-7.60	-7.64	0.03
60.0	-7.26	-7.28	0.01
70.0	-6.83	-6.84	0.01
80.0	-6.33	-6.34	0.01
90.0	-5.79	-5.79	0.00
100.0	-5.20	-5.19	-0.00
110.0	-4.60	-4.58	-0.02
120.0	-3.99	-3.96	-0.03
130.0	-3.38	-3.34	-0.03
140.0	-2.79	-2.76	-0.02
150.0	-2.21	-2.23	0.02
160.0	-1.74	-1.76	0.01
170.0	-1.34	-1.37	0.02
180.0	-1.04	-1.07	0.02
190.0	-0.85	-0.87	0.02
200.0	-0.78	-0.79	0.01
210.0	-0.83	-0.83	0.00
220.0	-1.00	-0.98	-0.01
230.0	-1.28	-1.25	-0.02
240.0	-1.66	-1.62	-0.04
250.0	-2.12	-2.09	-0.03
260.0	-2.65	-2.63	-0.01
270.0	-3.23	-3.23	0.00
280.0	-3.85	-3.87	0.02
290.0	-4.49	-4.53	0.03
300.0	-5.15	-5.19	0.03
310.0	-5.78	-5.81	0.03
320.0	-6.39	-6.39	0.00
330.0	-6.93	-6.91	-0.01
340.0	-7.37	-7.35	-0.01
350.0	-7.74	-7.70	-0.04

DRIFT RATE = -4.515 DEG/HR

UIA = 1.711 DEG/HR//G

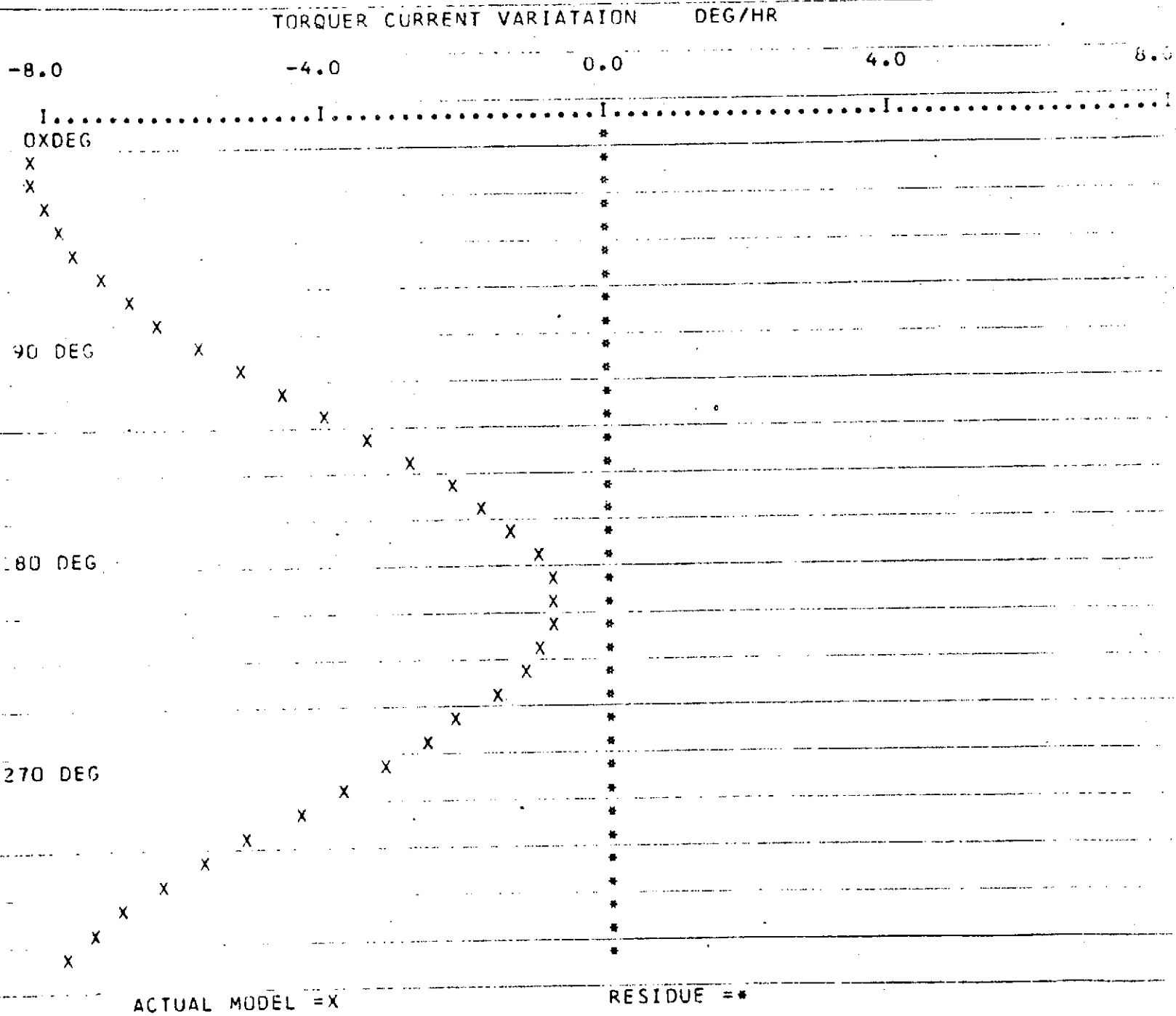
RMS = 0.023 DEG/HR

ANISO TERM = 0.123 DEG/HR//GXG

USA = -4.611 DEG/HR//G

NO. OF HARMONICS = 5.

PRINT IDENT NO 4



UTΔ = 1.711 DEG/HR//G  
 Δ FT RATE = -4.515 DEG/HR

USA = -4.611 DEG/HR//G  
 ANISO TERM = 0.123 DEG/HR//GXG

PRINT IDENT NO 4

4.1 (Continued)



Listed below are the results of the OA up/down and IA up/down (both about SA) settling tests.

<u>Position</u>	<u>Settling Test</u> <u><math>\Delta</math> Drift Deg/Hr</u> <u>Across Settling</u>	<u>Time to Settle</u> <u>(minutes)</u>
<u>10 V Passive Suspension</u>		
OA Up	-0.26	24
OA Down	+0.29	24
IA Up	-0.06	8
IA Down	-0.04	6
<u>15 V Passive Suspension</u>		
OA Up	-0.16	18
OA Down	+0.12	12
IA Up	-0.07	10
IA Down	-0.04	8

## 4.1 (Continued)

During the OA up/down tests, the currents to several suspension coils were monitored after the gyro was positioned. The measuring instrument was a differential AC meter. These observations showed no measurable difference in coil current between the gyro OA up and OA down position. This implied that either the float was not moving or the float motion was too small to be detected by the measuring instrument. In view of this uncertainty, two additional tests were tried. One was to increase the suspension voltage to determine if this would increase the stiffness, thereby reducing settling. The second was to raise and lower the gyro operating temperature to see if the float was off flotation. Increasing the suspension voltage from 10 volts to 15 volts reduced the time to settle and delta drift for the OA up/down tests. The IA up/down results remained essentially the same as with the 10 volt suspension. Raising and lowering the gyro temperature several degrees from nominal made no appreciable difference in the time required to settle or produce a change in drift rate across settling.

The difference in settling time for the OA up/down and IA up/down attitudes indicates that the damping for motions along the OA (piston effect) is higher than the damping for radial motion of the float. The geometry of the gyro would tend to verify this ratio of damping. These tests were performed with an average suspension coil power of 0.01 watts. An increase in the operating power would, as verified by the voltage test, shorten the settling time proportionately.

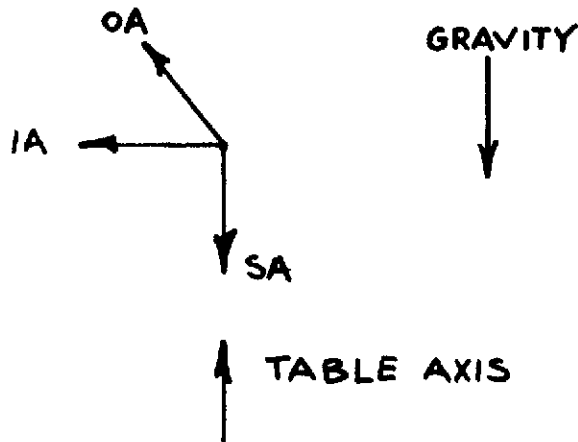
The drift rate changes noted during the settling tests were less than 0.3 deg/hr for both attitude changes. These drift rate changes are believed to be primarily due to flexlead induced torques, in terms of both their gravity sensitivity and their geometrical torque producing capability under differently "stretched" conditions. Again, under higher powered suspension conditions, these drift rate changes are shown to decrease.

An IA about OA misalignment test was then performed. In addition to providing an indication of this misalignment, this test also provided a basis for determining:

1. Gyro Pickoff Gradient
2. Gyro Mechanical Gain
3. Gyro Output Axis Damping

## 4.1 (Continued)

For this test, the gyro was oriented as shown below:



The gyro was initially positioned IA-West and a series of 100 second integration periods were sampled with the integrating digital voltmeter. During a 100 second sampling period, the gyro was rotated CCW 360 deg to IA-West. Following the data printout, the gyro was again rotated, this time 360 deg CW to IA-West during a 100 second sampling period, and the data sample allowed to printout. From these data, the IA about OA misalignment was established as presented below.

1. IA-West static number for a 100-second sampling period = -5.260 deg/hr.
2. CCW rate applied for 360 deg during a 100-second sampling period = +58.703 deg/hr.
3. CW rate applied for 360 deg during a 100-second sampling period = -69.534 deg/hr.
4. Rate applied to IA as a result of misalignment
  - a) CCW Rate(2.) - IA-West(1.) = +58.703 - (-5.260) = +63.963 deg/hr
  - b) CW Rate(3.) - IA-West(1.) = -69.534 - (-5.260) = -64.274 deg/hr
5. Average rate applied to IA as a result of misalignment
  - a)  $- b) \div 2 = (63.963 + 64.274) \div 2 = 64.118 \text{ deg/hr}$

4.1 (Continued)

6. Average table rate, 360 deg/100 sec = 3.6 deg/sec

7. Misalignment

$$\sin \theta = \frac{5}{6} = \frac{64.118}{3600 \times 3.6} = 4.947 \times 10^{-3}$$

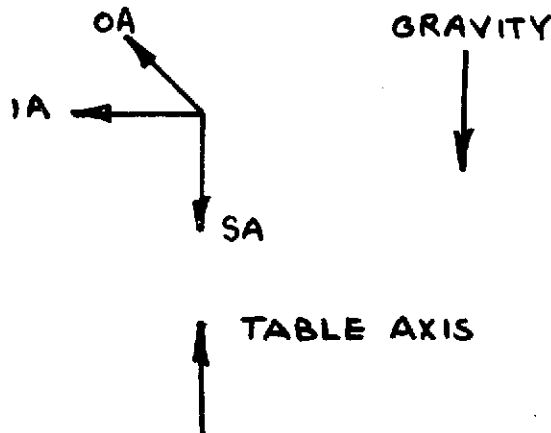
$$= 17' 2''$$

The technique used to determine the IA about OA misalignment was a simplified manual rotation method subject to errors from non-constant rotational rates. However, these errors are small for the misalignment angle determination. The 17 arc minute misalignment is not considered significant in itself insofar as no attempt had been made to align the gyro either before or after positioning the end caps to the case. The misalignment could be corrected by lapping one or more of the gyro mounting pads.

A gyro pickoff gradient test was conducted to obtain a measure of the gyro pickoff gradient. A prerequisite for this test was the IA about OA misalignment test. The gradient test also provided a basis for determining:

1. Gyro Mechanical Gain
2. Output Axis Damping
3. Gyro Torsional Gradient

The gyro was oriented as shown below:



4.1 (Continued)

With the gyro rate loop closed, one preamp output was measured with an oscilloscope. The rate loop was then opened, and the gyro rotated about the SA until the preamp output had fully settled. The settled output from the preamp was again measured. The results were as follows:

1. The preamp output under closed loop conditions measured 1.20 V peak-to-peak (50 KHz excitation component) or 0.43 V rms.
2. The preamp output following rotation about the SA with the loop open measured 0.65 V peak-to-peak (50 KHz excitation component) or 0.23 V rms.

Having measured the misalignment angle previously, it was now possible to measure the pickoff gradient. With the loop closed, the IA was then rotated 17 arc minutes about the OA and, therefore, the SA was 17 minutes off the table rotational axis in the IA-SA plane. By rotating the table with the loop open, the SA aligned itself with the table axis of rotation, which required an OA rotation equal to the 17 minute misalignment angle.

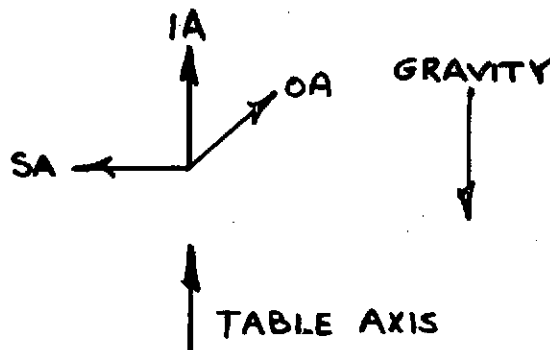
The gyro pickoff gradient was computed as follows:

$$\frac{1 - 2}{17' 2''} \times 3600 \text{ sec/deg} = \frac{1.20 - 0.64}{1022} \times 3600 = \frac{1.937 \text{ V P-P}}{1 \text{ deg OA}}$$

$$G_{po} = \frac{1.937 \text{ V P-P}}{1 \text{ deg OA}} = \frac{0.685 \text{ V rms}}{1 \text{ deg OA}}$$

A gyro mechanical gain test was performed to obtain a measure of the gyro mechanical gain. A prerequisite for this test was the gyro pickoff gradient measurement. The gain test also provided a basis for establishing the gyro output axis damping and the gyro time constant.

To measure the gyro mechanical gain, the gyro orientation was as shown below:



## 4.1 (Continued)

With the rate loop open, the output of the same preamp used during the pickoff gradient test was measured. The gyro was then rotated 1 degree about the input axis and again the pickoff output was measured. The measurements were recorded from an oscilloscope display.

1. Preamp output change for a 1 degree rotation about the input axis = 0.4 V Peak-to-Peak.
2. Pickoff gradient = 1.937 V Peak-to-Peak/1 deg OA.

The gyro mechanical gain could then be computed from the measured values as follows:

$$\text{Gyro Mechanical Gain} = \frac{\text{Output}}{\text{Input}} = \frac{0.4}{1.937} = 0.206$$

The gyro mechanical gain measurement enabled a computation of the output axis damping. The spin motor momentum, necessary for this computation, was based on the design value of  $5 \times 10^5$ .

$$D = \frac{H}{K} = \frac{5 \times 10^5}{0.206} = 2.42 \times 10^6 \text{ dyne cm/rad/sec}$$

The time constant could then be calculated as follows:

$$= \frac{J}{D} = \frac{610}{2.42 \times 10^6} = 0.25 \text{ milliseconds}$$

The output axis torsional gradient was determined as follows: With the gyro rate loop closed, the same preamp used to determine the gyro pickoff gradient was measured, and its output was recorded. Under the same conditions, the gyro drift in deg/hr was recorded. An offset signal was then inserted into the loop which changed the float to case angle to other than the normal pickoff null position. With the pickoff at this new position, the gyro drift in deg/hr was again recorded.

Having previously measured the gyro pickoff gradient in volts/deg about OA, the torsional gradient could then be obtained.

1. Preamp output under closed loop condition and with pickoff at its normal null position - 1.18 V Peak-to-Peak.

## 4.1 (Continued)

2. Gyro drift rate under conditions measured at (1.) - +5.95 deg/hr.
3. Preamp output under closed loop condition and with pickoff offset - 1.25 V Peak-to-Peak.
4. Gyro drift rate under conditions measured at (3.) - +5.27 deg/hr.
5. Delta drift rate (2.) - (4.) = 5.95 - 5.27 = 0.68 deg/hr.
6. Delta pickoff output (3.) - (1.) = 1.25 - 1.18 = 0.07 V p-p.
7. Equivalent OA offset = 
$$\frac{0.07 \text{ V p-p}}{1.937^* \text{ V p-p/1 deg OA}}$$
$$= 0.0361 \text{ deg}$$
8. Torsional gradient = 
$$\frac{0.68}{0.0361 \text{ deg}} = 18.8 \text{ deg/hr/1 deg OA.}$$

A phenomena will be experienced in digital operation of gyros in the existence of a bias torque proportional to the square of the amplitude of the AC component of applied torquer current. This bias torque is due to the interaction of the torquer magnet flux with the torquer coil current generated flux, and results in a difference in effective torquer scale factor for positive and negative current flow. Adjustment of the position of the torquer magnets to the torquer coils enables this bias torque to be adjusted to "zero"; however, the adjustment is best done with a full-up gyro where sensitive measurements of the bias can be made.

Another phenomena less understood is an apparent mass unbalance sensitivity to AC torquer current. This sensitivity presently appears to be a thermally induced phenomena possibly due to flexlead heating that causes damping fluid flow in gravity environments that result in g-sensitive coefficients due to viscous shear.

Each of these sensitivities were measured on the S/N 1 gyro with the following results:

---

\*This value is the pickoff gradient in V peak-to-peak/1 deg OA.

## 4.1 (Continued)

Applied Square Wave AC Current: 100 ma, peak

Bias Change From 0 Current to 100 ma: -13 deg/hr

Input Axis Unbalance Change From 0 Current to 100 ma:  
+0.4 deg/hr/g

Spin Axis Unbalance Change From 0 Current to 100 ma:  
-0.5 deg/hr/g

A measure of output axis hysteresis and frictional effects has been made in a return from stops test. The test was performed by measuring the drift rate after the gyro float had been driven away from the null position first in one direction then the other. The float displacement angle used was  $\pm 1$  deg and the drift rate difference measured was 0.2 deg/hr.

Upon completion of the above tests, gyro S/N 1 was delivered to MSC as part of the breadboard system.

4.2 Gyro S/N 2

Testing was initiated on gyro S/N 2 in April, 1971. The resistance and continuity were checked. The spin motor failed to sync at 1600 Hz excitation.

The sync was investigated at various voltages. It was found that one pick-off output was not functioning (output shorted to ground). The gyro was returned to manufacturing. The wheel was refilled with helium and the pickoff output was repaired. The gyro was returned to test and the resistance and continuity were checked. The heater, sensor, and thermistor circuitry was checked out using an external commercial controller (Harrel).

The wheel was turned on and the loop closed (analog mode). The gyro suspension mode was passive. A nominal torquer scale factor test was performed (2069 deg/hr/ma). The results of a 6-position cal were as follows:

Bias:	-12.46 deg/hr
$U_{IA}$ :	+13.77 deg/hr/g
$U_{SA}$ :	-25.92 deg/hr/g

The bias changed during OA-H attitude to approximately 8.7 deg/hr.

## 4.2 (Continued)

A second 6-position cal was performed

Bias: + 8.3 deg/hr  
 $U_{IA}$ : + 9.0 deg/hr/g  
 $U_{SA}$ : -18.5 deg/hr/g

The gyro harness was then rewired because of difficulty with leads breaking. The axial suspension did not seem to hold. The range of inductance was measured for each suspension coil with various float positions. An active magnetic suspension was energized, and the suspension circuits were trimmed. The loop gains appeared to be too low.

A 6-position cal was performed

Bias: +10.59 deg/hr  
 $U_{IA}$ : + 9.15 deg/hr/g  
 $U_{SA}$ : -19.43 deg/hr/g

The 6-position cal was repeated

Bias: + 9.52 deg/hr  
 $U_{IA}$ : + 8.66 deg/hr/g  
 $U_{SA}$ : -18.83 deg/hr/g

A five hour drift stability test was conducted with the active suspension energized and the wheel at 48 K rpm. The bias changed (-0.6 deg/hr) during the initial 1.5 hours of running, then remained with 0.1 deg/hr for the duration of the test. However, difficulties continued with the axial suspension. The gyro was returned to manufacturing to increase the axial end play of the float by the addition of shims.

A 6-position cal was performed with the active magnetic suspension energized and an analog rate loop:

## 4.2 (Continued)

Bias: + 9.14 deg/hr  
 $U_{IA}$ : +10.28 deg/hr/g  
 $U_{SA}$ : -23.29 deg/hr/g

Difficulty with axial suspension continued. The float did not remain axially suspended. Efforts were continued to try to actively suspend the float. During this period, the spin motor winding opened because of an excessive angular rate input about the gyro's output axis. The gyro was subsequently disassembled. It was noted that the bearing had been fractured as a result of the high slew rates experienced by the gyro. Also, disassembly difficulties resulted in a damaged float assembly. Efforts to repair the gyro were, therefore, discontinued.

4.3 Gyro S/N 3

Testing on this unit commenced in September, 1971. Dry measurements were made on the inductance coils. During the resistance and continuity test, it was noted that the preamplifier at the bellows end was not working. The gyro was subsequently rebuilt. The cause of the trouble had been an open solder joint at the preamp.

Upon completion of the repair, another resistance and continuity test was performed, and wet measurements of the inductance coils were made.

A bias stability trace was then obtained, and the resulting data were erratic. This anomalous condition appeared to be related to poor suspension.

Overtemperature circuits were incorporated to prevent the gyro from overheating in the event of a controller failure.

The first overnight stability run was partially satisfactory. However, the suspension was again observed to be unstable. The swings of the inductance coils were measured, and the capacitance values for passive suspension were reevaluated.

The suspension continued to be unstable. The capacitance values were increased to avoid resonance. Resonance curves were established for the coils. An overnight stability run was performed with the OA-up, magnetic suspension on, and wheel off. The bias ramped at a rate of 0.1 deg/hr<sup>2</sup>. An OA-down overnight run was then performed with the suspension on and the wheel off. The bias continued to ramp at a rate of 0.08 deg/hr<sup>2</sup>.

(Continued)

A weekend OA-up stability run with the demodulator reference and torquer phasing reversed demonstrated a bias ramp with the ramp changing direction. This phenomenon indicated that the gyro was causing the ramp.

The plexiglass cover was removed from the fixture to inspect terminals with gyro OA-H. Upon returning the gyro to OA-V, the bias shifted to 90 deg/hr. It was noted that, by changing the suspension capacitor values, the gyro bias could be changed to 0 deg/hr. The bias stability continued to be erratic. The two preamps were powered up (rate loop disabled), and the preamp at bellows end exhibited noise with the amplitude jumping. The gyro was removed from the stand, the end cap was opened, and the wiring was inspected. All leads were resoldered. The bellows end preamp continued to be noisy.

A short stability run with suspension off showed that the bias ramp was still present. Operating with only flex end preamp, suspension on gave an OA-up p-p spread in data of 0.30 deg/hr but no large bias jumps as before. Gyro realigned on 22 V stability with the common mode rejection circuit disabled. The gyro was operated with the bellows end preamp only - large bias jumps were noted, confirming the defective preamp.

Tests were continued with both preamps on a weekend run, OA-up, and the ramp continued. An overnight run OA-up, suspension on, was performed. A ramp of 0.026 deg/hr<sup>2</sup> p-p excursion (0.15 deg/hr) was noted. A hybrid PTSA was then incorporated. Inability to achieve stability to any better than 0.5 deg/hr resulted. Current regulation in PTSA was not functioning properly.

The gyro was then submitted to manufacturing for rework of the preamps. Upon return to test, it was interfaced with a DIGS PTSA and a passive suspension. The wheel would not start at the normal operating temperature, but did start at 100°F.

The float was centered with the passive suspension, and an overnight run was conducted with the DIGS PTSA. This test was continued for five days. The suspension appeared to be drifting, and the data stability was poor. An analog loop was incorporated. The bellows end preamp failed to drive, and the flex end preamp fluttered. The gyro was removed from test and submitted to manufacturing where both preamps were mounted external to the fluid through one megohm resistors. During subsequent testing, low oscillation appeared in the analog capture loop. Again, the wheel would not start at the normal temperature, but did start at approximately 100°F.

4.3 (Continued)

It was determined that the gain of the loop was too low. The loop would not function. The gyro was returned to manufacturing to shorten the leads in the preamp. The loop oscillation continued, however, with the shortened leads.

The gyro was again interfaced with a DIGS PTSA. Similar low frequency loop oscillation occurred, indicative of low gain.

The gyro was integrated with the breadboard MSE and hybrid PTSA. However, due to the low pickoff gradient, the loop was sluggish and stability was poor. Further testing on this unit was temporarily halted.

The preamplifiers were subsequently removed from the fluid to be placed in the end caps; however, during removal, the preamplifiers were damaged. The gyro was rebuilt following the selection of new hybrid preamplifiers, and a design modification was incorporated in the end caps to allow trimming after final assembly.

Upon completion of the rework, testing indicated that higher-than-normal inductances of some coils is a problem inherent with the active suspension. Comparative tests of output stability versus the three modes of suspension (active, passive, and no magnetic suspension) indicate that the most stable condition is achieved with no magnetic suspension.

The decision was made to replace the magnetic suspension with a ball bearing suspension system.

The gyro was disassembled to allow the replacement of the magnetic suspension with a ball bearing suspension. The magnetic suspension was disabled by increasing the clearance between the suspension coils and the stator to 0.065 inch; this reduced any suspension residue torques by 250. Complete removal of the suspension coils would have increased the gyro fluid capacity enough to exceed the bellows compliance range.

The gyro end caps were machined to accept the ball bearing assemblies. The gyro was assembled, flushed and filled.

Preliminary tests were made with the gyro integrated with external electronics. These tests indicated that the hysteresis problem that existed with the magnetic suspension had been eliminated.

## 4.3 (Continued)

Figure 4.3-1 is a graph indicating bias versus time. From this graph, it can be seen that the bias was ramping at 0.24 deg/hr/hr. The cause of the bias ramp was investigated. With the bias ramp removed from the bias, the short term stability becomes 0.015 deg/hr.

Figure 4.3-2 is a graph of gyro output versus input axis direction. This graph indicated that the output no longer showed the dependence on the direction of rotation the unmodified gyro showed (Figure 4.3-3). The difference between the 0 degree points on the graph in Figure 4.3-2 is due to the bias change with time. The points on the graph for 300, 330, and 360 degrees have minimum time separation and show negligible separation in gyro output for direction of rotation. The results of a 6-position calibration and a gyro phase reversal are tabulated below.

Scale Factor	=	0.95713 arc sec/pulse
Loop Bias	=	50.44 deg/hr
Unbalance SA	=	9.41
Unbalance IA	=	-17.9
PTSA Bias	=	1.49
Gyro Bias	=	48.94

During test, it was found that the compliance range of the PTSA current regulator was too small, causing increased noise sensitivity. The compliance range was increased by adjustment of the PTSA's DC supplies. The ramp that has been observed in the data appeared to decrease after the increase in compliance.

The last effort was directed toward installation of the PTSA, temperature controller and DCE/DSF discs. The temperature controller was successfully installed in the end cap and functioned normally with the gyro. The PTSA had been assembled to the end cap but checkout revealed malfunctions. Several installations were attempted but each resulted in a malfunction. During this phase, the following repairs had to be made to the PTSA:

- Removed and replaced IC4 on B-161 (LM101A) Amp & Demod Section (1 time)
- Removed and replaced IC1 on B-163 (2 times) (SN5400)

121

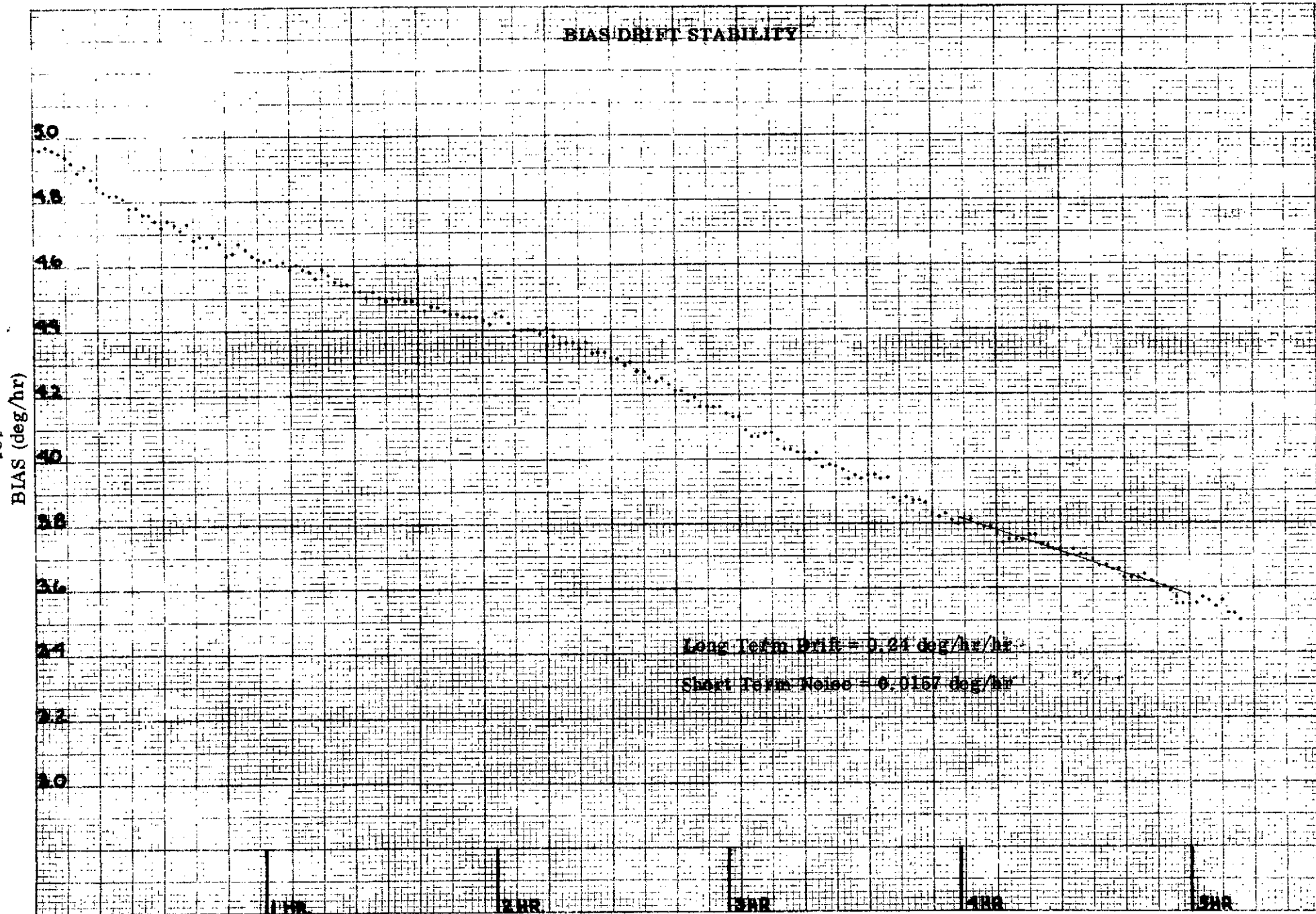
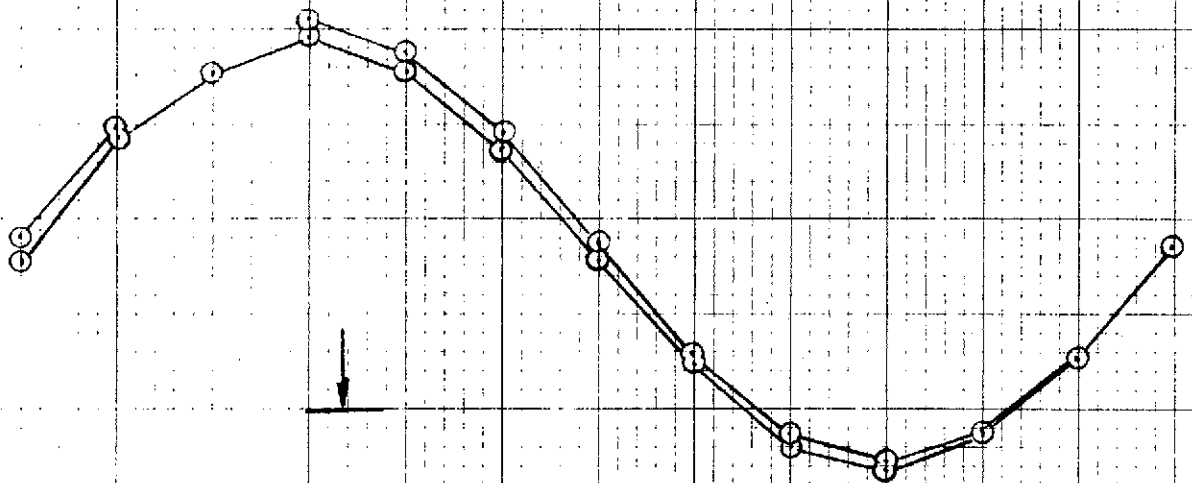


Figure 4.3-1

HSER 6197

1170 S/N 3  
OUTPUT VS EARTH RATE  
GYRO OA-V  
BALL BEARING SUSPENSION  
3-14-73



IAE  
0

IAN  
90

IAW  
180

IAS  
270

IAE  
0

Figure 4.3-2  
122

1170 SN<sup>3</sup>  
 OUTPUT VS EARTH RATE  
 GYRO OAY  
 PASSIVE SUSPENSION  
 1-25-73

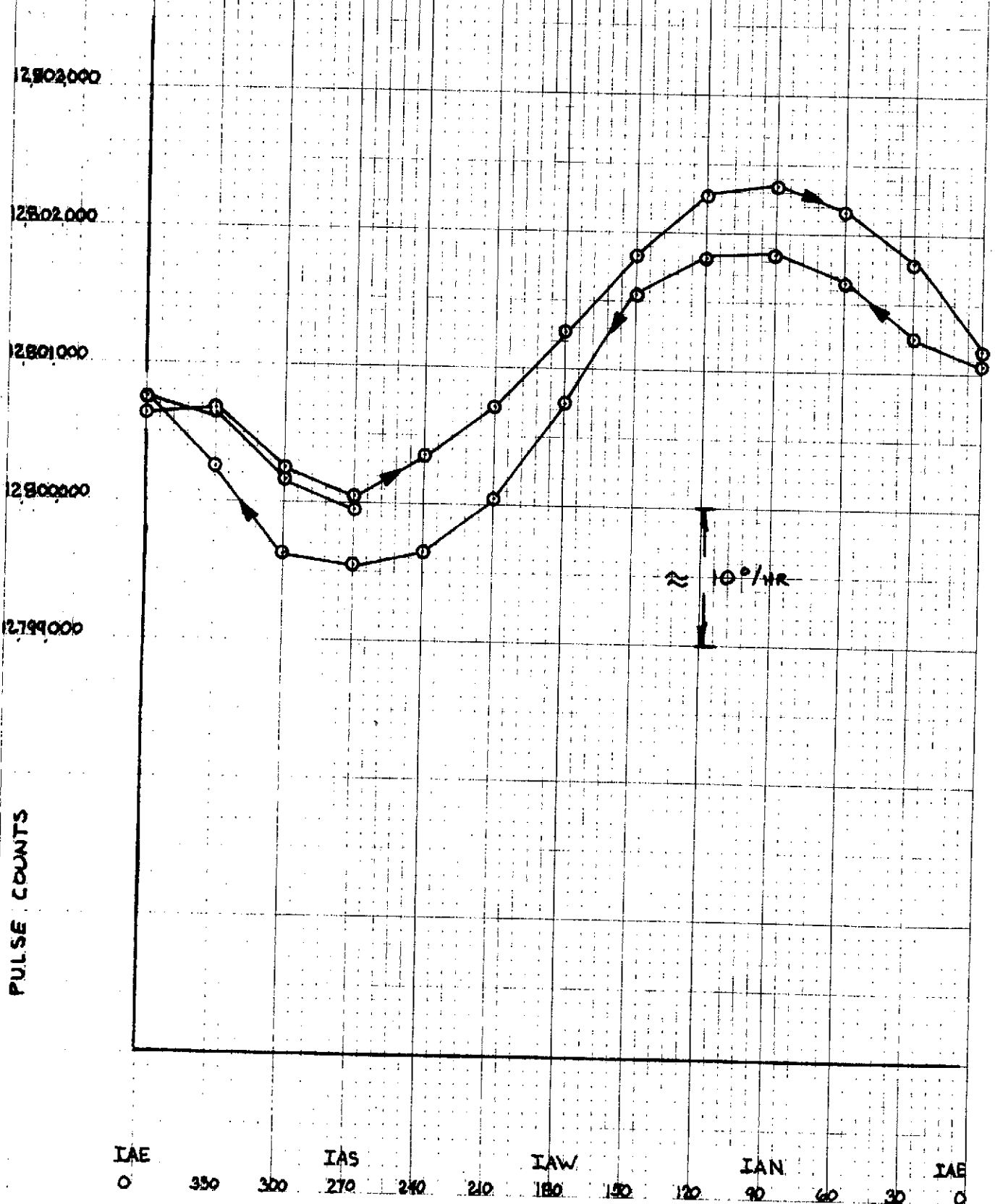


Figure 4.3-3  
 123

4.3 (Continued)

- Removed and replaced IC2 on B-163 (2 times) (SN54H103)
- Removed and replaced Q3 and Q4 on B-163 (2 times) (2N2222)
- Removed and replaced Q12 on B-163 (M116 MOS FET) (1 time)
- Repaired ground trace (2 times)
- Removed and replaced Q1 - Q2 on B-163 (IT 1701 MOS FET) (3 times)
- Removed and replaced Q1 - Q2 with 10K resistors (1 time)

Because of the numerous failures encountered, it has been concluded that successful installation of the present hardware beyond the FTC is not feasible. Therefore, the S/N 3 gyro has been wired to operate with the breadboard electronics rack. Thus, either the S/N 1 or S/N 3 gyro may be operated with the breadboard rack and any of the hybrid discs may be used in the rack for operation with the appropriate gyro.

**APPENDIX A**

**OPERATING INSTRUCTIONS**

**FOR THE**

**EXCITATION AND SYNCHRONIZATION UNIT**

## APPENDIX A

OPERATING INSTRUCTIONS FOR THE  
EXCITATION AND SYNCHRONIZATION UNITA. 1 TURN-ON PROCEDURE

A. 1. 1 Connect the interface cable between the excitation and synchronization unit the RI 1170 gyro.

A. 1. 2 Connect regulated +29.5 V DC and +37.2 V DC power supplies and a three-phase, 90 V AC wheel supply to the excitation and synchronization unit as follows:

1. Positive side of +29.5 V DC supply to red jack (No. 2) on fuse side of excitation and synchronization unit (hereafter referred to as the Interface Unit - IU).
2. Negative side of +29.5 V DC supply to black jack (No. 5) on IU.
3. Positive side of +37.2 V DC supply to red jack (No. 1) on IU.
4. Negative side of +37.2 V DC supply to black jack (No. 4) on IU.
5. "A" phase of 90 V AC, 1600 Hz, three-phase supply to black jack (A) on IU.
6. "B" phase of same supply to red jack (B) on IU.
7. "C" phase of same supply to green jack (C) on IU.

NOTE: A 1.6 KHz sync signal is located on the end of the IU chassis. This signal may be utilized to synchronize the three-phase wheel supply with the IU. Refer to Wiring Diagram - Interface Unit, Drawing No. 31611.

A. 1. 3 Connect the IU to a 110 V AC outlet.

A. 1. 4 Connect the RI 1170 gyro to the IU as follows:

1. Connect a counter to the low mode data output terminal on the IU. The low mode sync may also be connected to the counter if a sync pulse is required (1  $\mu$ sec, pulse at 1 KHz rate).

A. 1. 4 (Continued)

2. Connect an oscilloscope to the high mode data output terminal on the IU.
  3. Connect the high mode sync terminal on the IU to the external sync terminal of the scope.
- A. 1. 5 Close switch S1 located on the top of the IU chassis. This will supply power to the three modular supplies and close relay No. 1. At this time, either 16 or 240 pulses at a 1 KHz rate will be displayed on the scope.
- A. 1. 6 Turn on the +27.5 V DC and +37.2 V DC supplies. The pulse information displayed on the scope may change state, i. e. , 16 pulses will change to 240 pulses, or vice versa.
- A. 1. 7 Close switch S2. Power will be supplied to the internal gyro heater. The gyro is equipped with a thermistor for external monitoring of the gyro temperature. Attach a PVB 300 portametric bridge, or equivalent, to jacks 3 and 6 on the fuse side of the IU. Refer to the thermistor calibration curve included in this appendix.
- A. 1. 8 Immediately set the wheel supply to 90 V AC RMS at 1600 Hz (or 24 V AC RMS at 400 Hz). Allow the gyro to stabilize. The thermistor reading should be  $3000 \pm 50 \Omega$  ( $150^\circ\text{F}$ ).
- A. 1. 9 Close switch S3 (37.2 V DC), then switch S4 (29.5 V DC) in that order. This sequence closes the loop. The counter will start to accumulate data pulses, and the trace on the oscilloscope will disappear.
- A. 1. 10 Monitor the gyro thermistor until a reading of  $1700 \pm 40 \Omega$  is obtained. This indicates that the gyro has reached its operational temperature of  $175 \pm 1^\circ\text{F}$ .

A. 2 TURN-OFF PROCEDURE

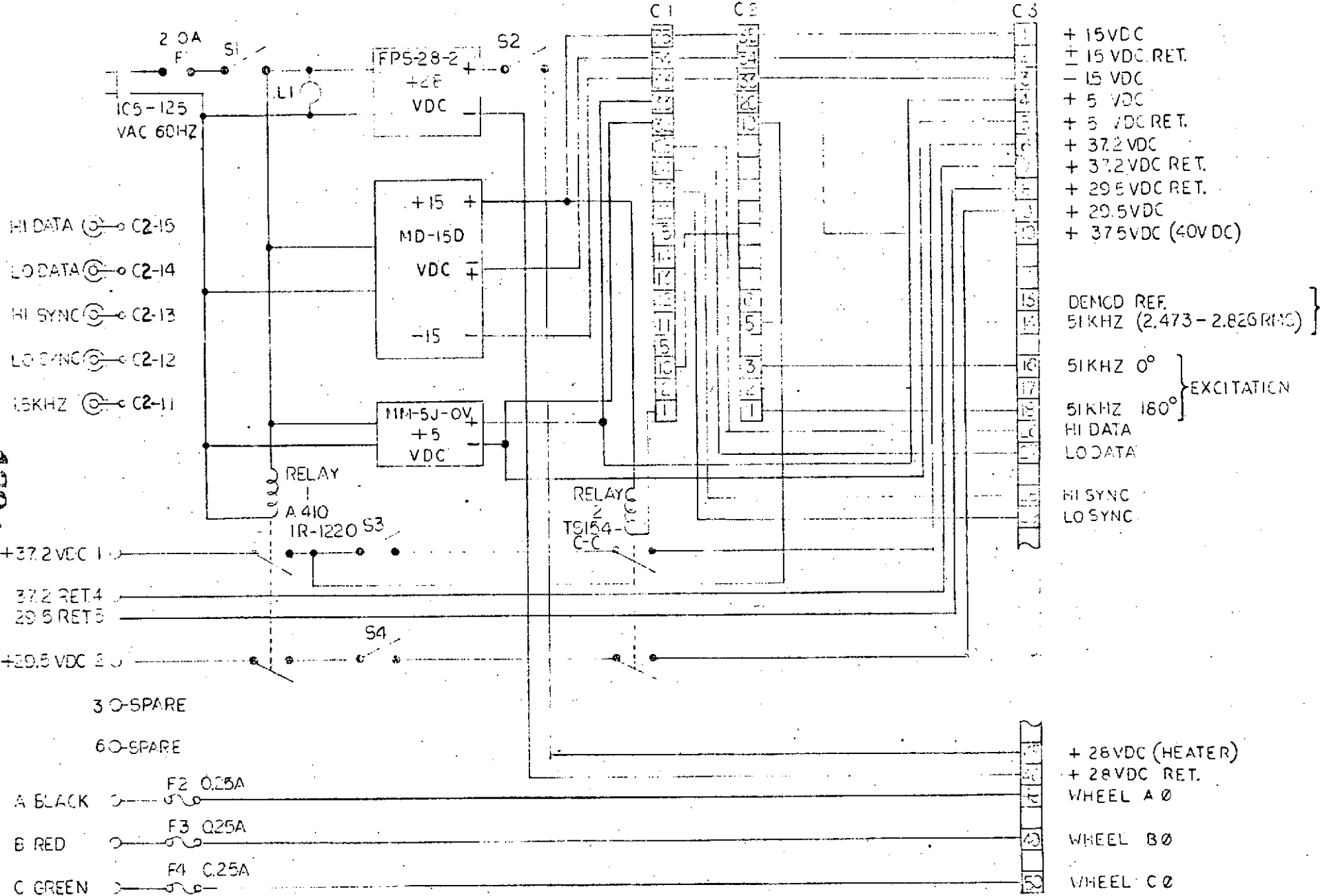
- A. 2. 1 Turn off the wheel supply. Allow 3 minutes for wheel run-down.
- A. 2. 2 Turn off switches S4, S3, and S2 on the IU in that order. The gyro is completely shut down at this point.

APPENDIX A

ATTACHMENTS

1. Wiring Diagram Interface Unit (Drawing No. 31611)
2. Demodulator Reference and Excitation Generator (Drawing No. 31612, Sheets 1 and 2)
3. 1170 Gyro Thermistor Calibration Chart

RI 1170 WIRING DIAGRAM INTERFACE UNIT



- + 15VDC
- + 15 VDC RET.
- 15 VDC
- + 5 VDC
- + 5 VDC RET.
- + 37.2 VDC
- + 37.2 VDC RET.
- + 29.5 VDC RET.
- + 29.5 VDC
- + 37.5 VDC (40VDC)

DEMCD REF.  
51KHZ (2.473-2.826 RMS) }

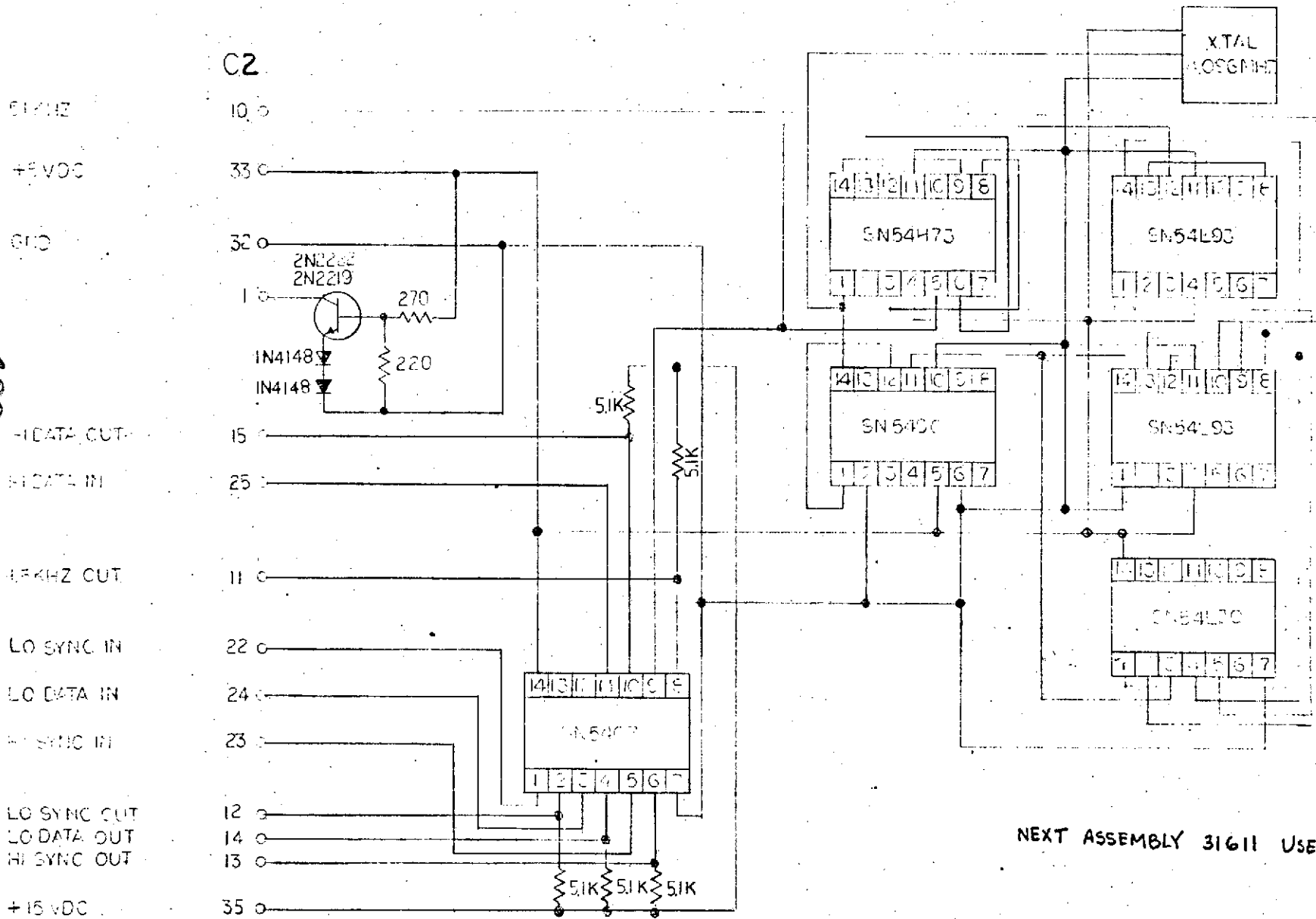
51KHZ 0° } EXCITATION  
51KHZ 180° }

HI DATA  
LO DATA  
  
HI SYNC  
LO SYNC

+ 28VDC (HEATER)  
+ 28VDC RET.  
WHEEL A 0  
WHEEL B 0  
WHEEL C 0

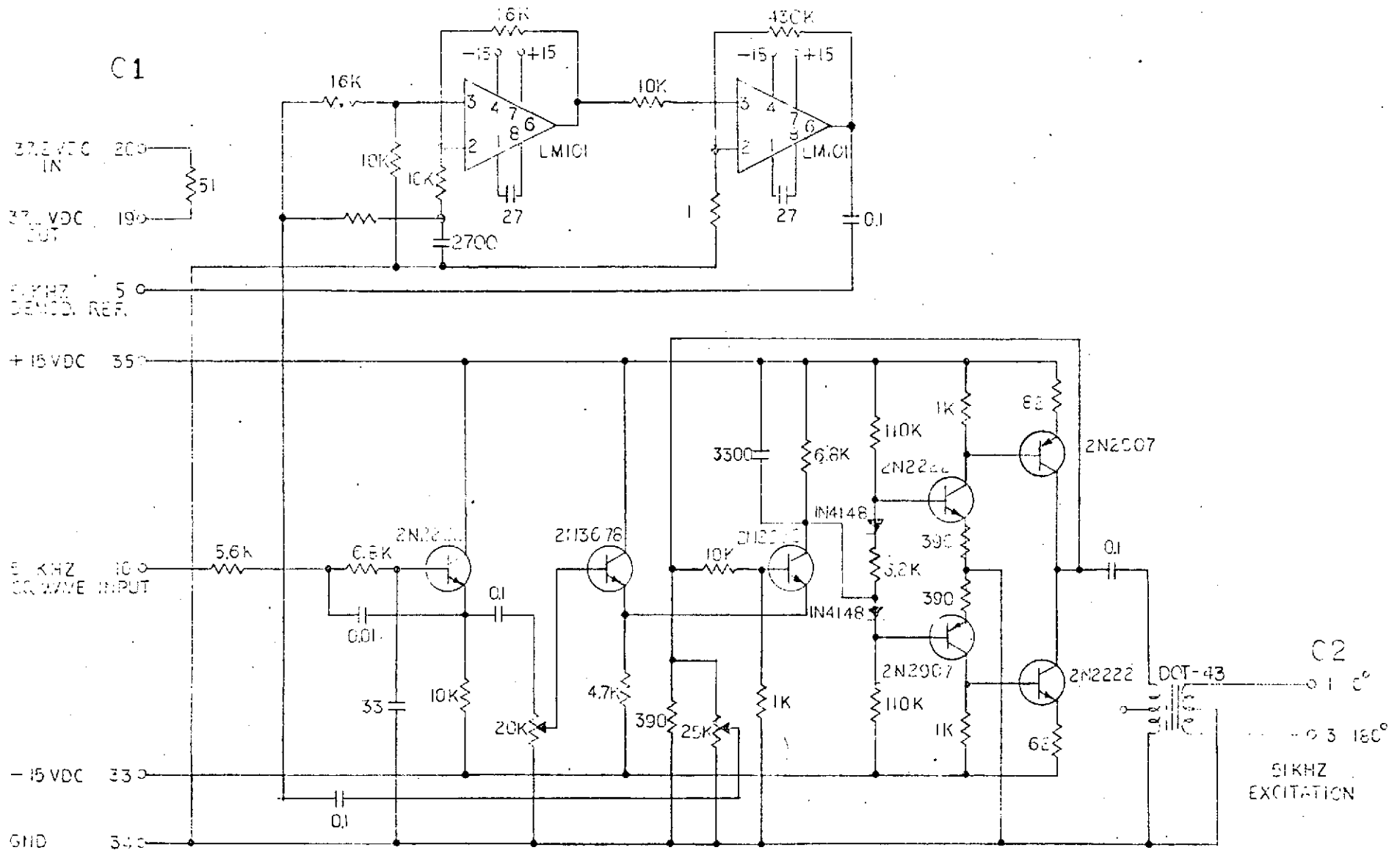
129 <

RI 1170 SCHEMATIC DEMODULATOR REFERENCE AND EXCITATION GENERATOR



NEXT ASSEMBLY 31611 USED ON C2

RI 1170 SCHEMATIC DEMODULATOR REFERENCE AND EXCITATION GENERATOR



NEXT ASSEMBLY 31611 USED ON C1

131 >

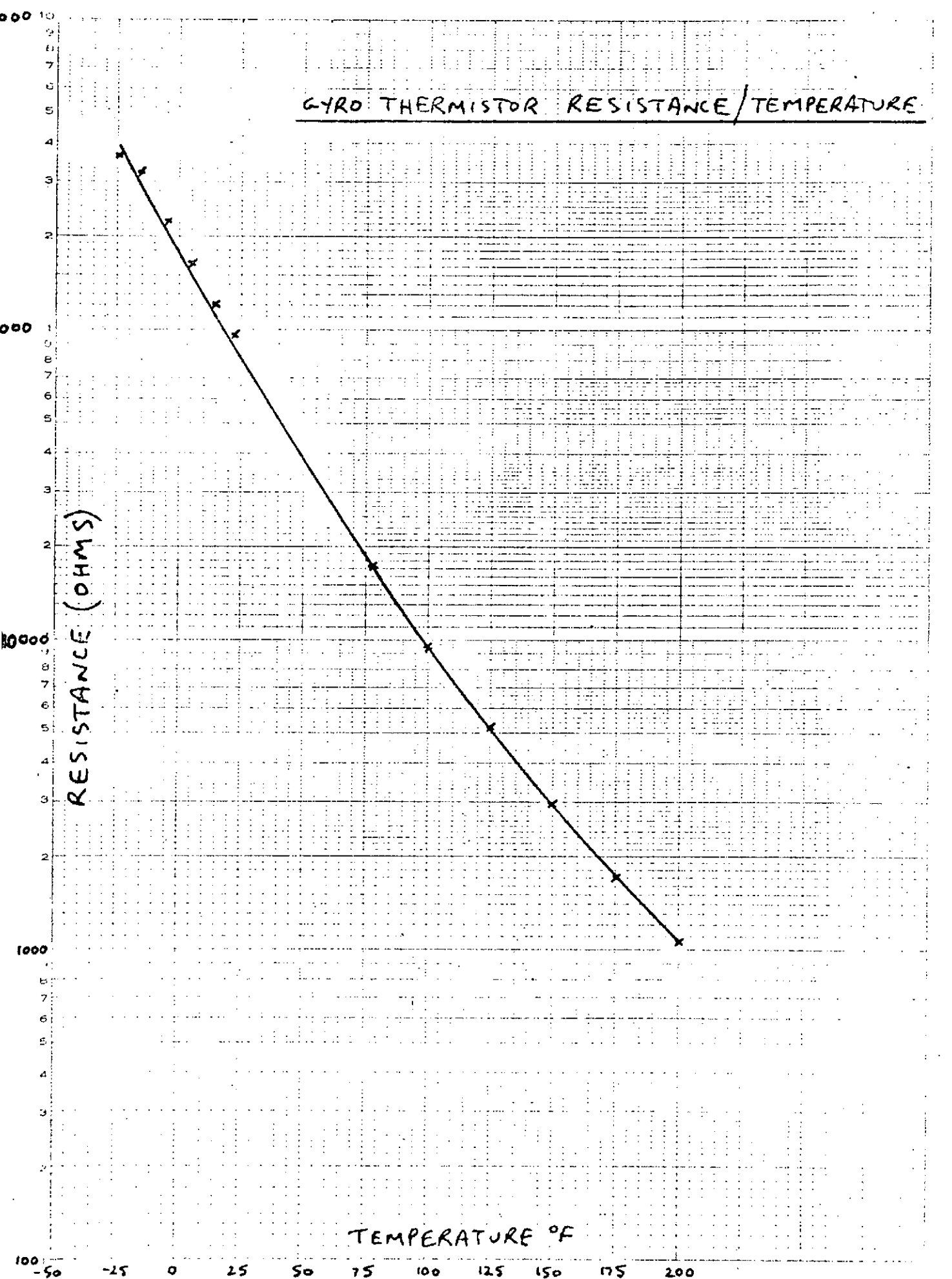
GYRO THERMISTOR RESISTANCE / TEMPERATURE

EUGENE DIEZSEN CO  
MILWAUKEE, WIS.

NO. 250-1410 DIEZSEN GRAPH PAPER  
SEMILOGARITHMIC  
4 CYCLES X 10 DIVISIONS PER INCH

RESISTANCE (OHMS)

TEMPERATURE °F



APPENDIX B

AN ANALYSIS OF  
THE FAILURE OF RI 1170  
GAS BEARING, S/N 12

PROJECT NO G260AAGASA

REFERENCE UCA-176

DATE December 12, 1969

TITLE An Analysis of the Failure of RI-1170 Gas Bearing,  
Serial Number 12.

BY M. H. Pope

**NOTICE TO ALL PERSONS RECEIVING THIS DOCUMENT**

THIS DOCUMENT CONTAINS PRELIMINARY DATA AND IS FOR INFORMATION OR REVIEW PURPOSES ONLY. THE CONTENTS MAY LATER BE MODIFIED OR SUPERSEDED. HSSC ASSUMES NO RESPONSIBILITY FOR THE ACCURACY OR SUITABILITY FOR USE OF THE INFORMATION CONTAINED HEREIN.

**Hamilton  
Standard**  
System Center

**U  
A®**  
DIVISION OF UNITED AIRCRAFT CORPORATION  
FARMINGTON, CONNECTICUT 06032

ABSTRACT

The events leading up to the failure of gas bearing assembly 012 are enumerated, and the subsequent failure described. The various tests run to investigate possible reasons for failure are described. Several alternative explanations for the failure are given. The most likely explanation, which was due to excessive unbalance forces, is given in some detail. Salvage schemes for wheels 010 and 011 are given, and design changes for future wheels are described.

ANALYSIS OF THE FAILURE OF THE  
RI-1170 GAS BEARING WHEEL NUMBER 012

Contents

- 1.0 INTRODUCTION
  
- 2.0 DESCRIPTION OF FAILURE
  - 2.1 Run Number 1
  - 2.2 Run Number 2
  - 2.3 Run Number 3
  - 2.4 Run Number 4
  
- 3.0 POSSIBLE MECHANISMS OF FAILURE
  - 3.1 Hydrodynamic Instability
  - 3.2 Initial Failure at O. D.
  - 3.3 Initial Failure at I. D.
  - 3.4 Excessive Temperatures in Hysteresis Ring
  - 3.5 Excessive Centrifugal Forces
  
- 4.0 ANALYSIS OF FAILURE
  - 4.1 Stress Levels
  - 4.2 Stress Concentrations
  - 4.3 Prior History
  - 4.4 Contribution From Screws
  - 4.5 Material
  - 4.6 Classification of Failure
  
- 5.0 PROBABLE FAILURE MODE

Contents (cont'd)

6.0 REMEDIAL ACTION

6.1 Salvage of Wheels Numbers 010, and 011

6.2 Design Changes

7.0 CONCLUSIONS

8.0 REFERENCES

## 1.0 INTRODUCTION

The gas bearing number 012 was one of several being evaluated for the RI-1170 gyro. The gyro R&D program is being funded by NASA/ERC and is monitored by Dr. Weinstock.

The gas bearing (see figure 1) is composed of a shaft (a), split rotor halves (b), thrust bearings (c), shaft nuts (d), rotor nuts (3), and bolts (f), hysteresis rings (g), and the motor stator (h). The shaft is made of beryllia, either cold pressed (#010 and 012) or hot pressed (#011). The rotor halves and thrust plates are made of cold pressed alumina. The rotor nuts and bolts are Mallory 1000, the hysteresis ring P6, and the shaft nuts TI 6AL 4V.

## 2.0 DESCRIPTION OF FAILURE

The gas bearing wheel failed (i.e., ceased to rotate) on its first run. However, following this initial failure the wheel was run three more times before its final and catastrophic failure. The following section describes the various runs.

### 2.1 Run Number 1.

The wheel was cleaned, assembled, and aligned. The wheel was run in air at speeds up to 23.5 K rpm and was found to consume 10W.

The running pot was then evacuated and refilled with hydrogen at 22 psia. Power was applied to the wheel with the intention of running it up to 48 K rpm. However at approximately 32 K rpm there was a loud screech from the wheel, and rotation ceased. Attempts were made to restart the wheel, but these proved to be unsuccessful.

Subsequently the wheel was removed from the running rig and taken to the clean room for disassembly. At this point, it appeared that the wheel had wholly or partly seized because it was extremely difficult to rotate the wheel relative



to the shaft. On teardown there was no difficulty in either taking the thrust plates off the shaft or in removing the rotor halves.

Examination of the parts showed no damage to the shaft or thrust plates, but did reveal cracking of both rotor halves (see figures 2-4) and score marks on both thrust faces. The outside of rotor half B showed cracks propogating from two of the screw holes (figure 2) while the outside of rotor half A showed no cracks. The inside of rotor half B showed a Y-shaped crack. This was located approximately  $180^{\circ}$  from the crack on rotor half B, but in this case it did extend approximately 60% of the way down the bore (figure 5). Careful examination revealed that the pole points of the Y-shaped cracks appeared to have one or more crystals missing. A photographic record of the cracks was made and is shown in figures 6 through 10.

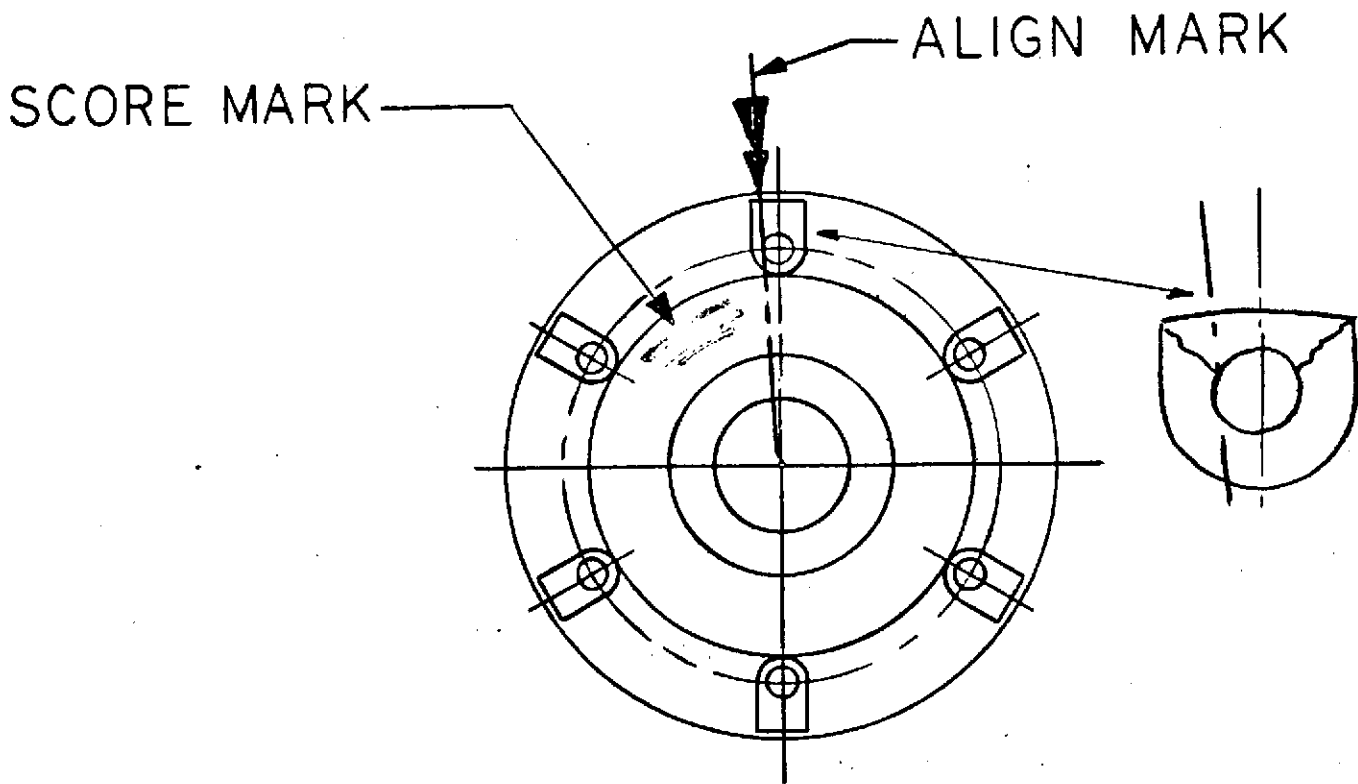
Normal microscopic examination of the scored surface did not reveal anything of significance. However on the Unitron metallurgical microscope at high magnifications (X 100 or X 200) and at high normal illumination, it was possible to see that the scored area was covered with microcracks (see figures 11 and 12).

Following this comprehensive examination, the roundness of the parts was assessed on the Talyrond roundness measuring machine. In general there was no significant change in the roundness of the inside diameter (see figures 13 and 14). However, one outside diameter showed a  $40 \mu$ " change in roundness (see figures 15 and 16).

## 2.2 Run Number 2

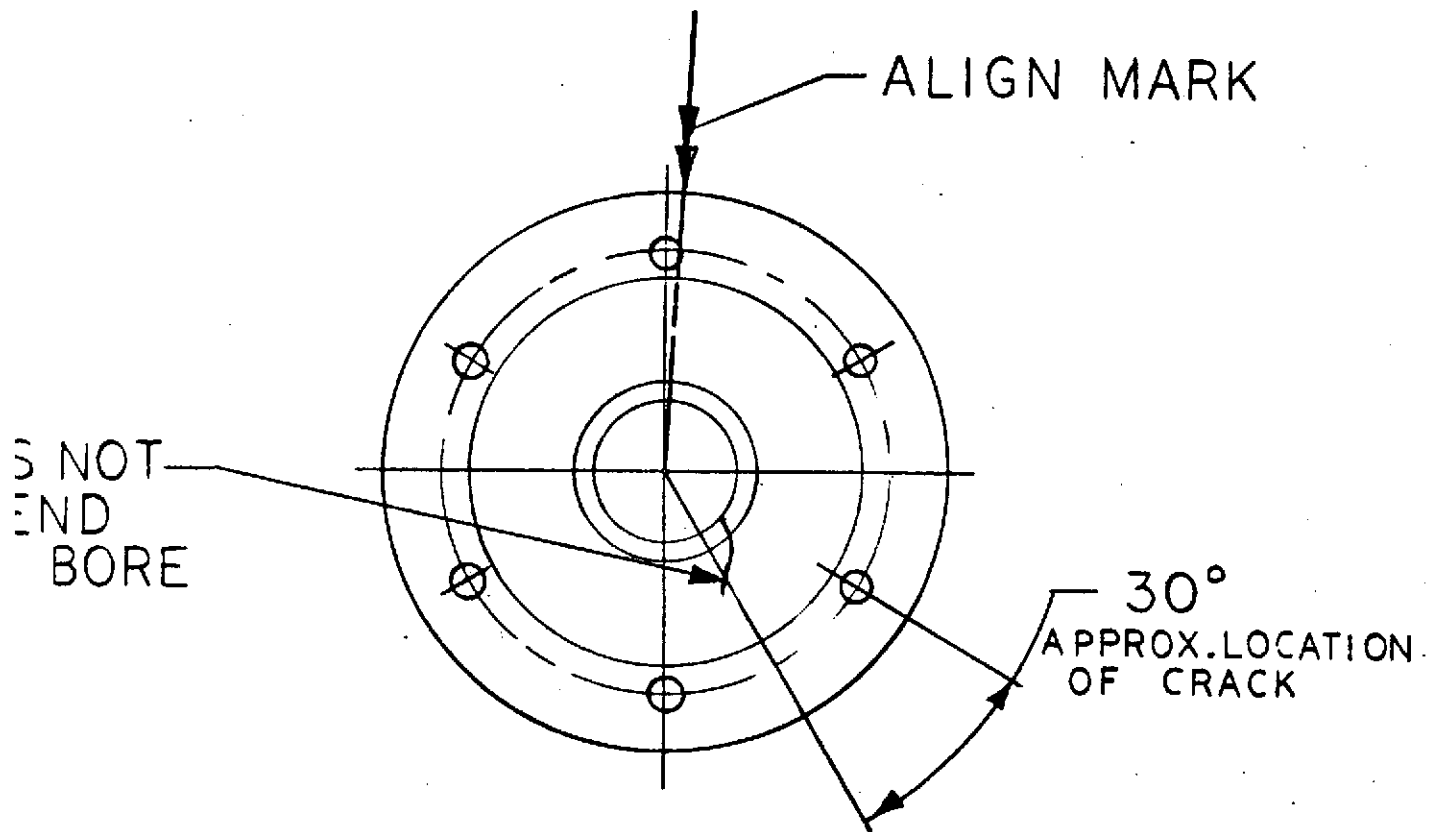
The wheel was then cleaned, reassembled, and realigned. The wheel was placed in a running rig which was instrumented with capacitance probes. The wheel was then run in 22 psia of hydrogen at 1000 rpm increments from a starting

ROTOR HALF NO. 012-B  
(NON-METALIZED)



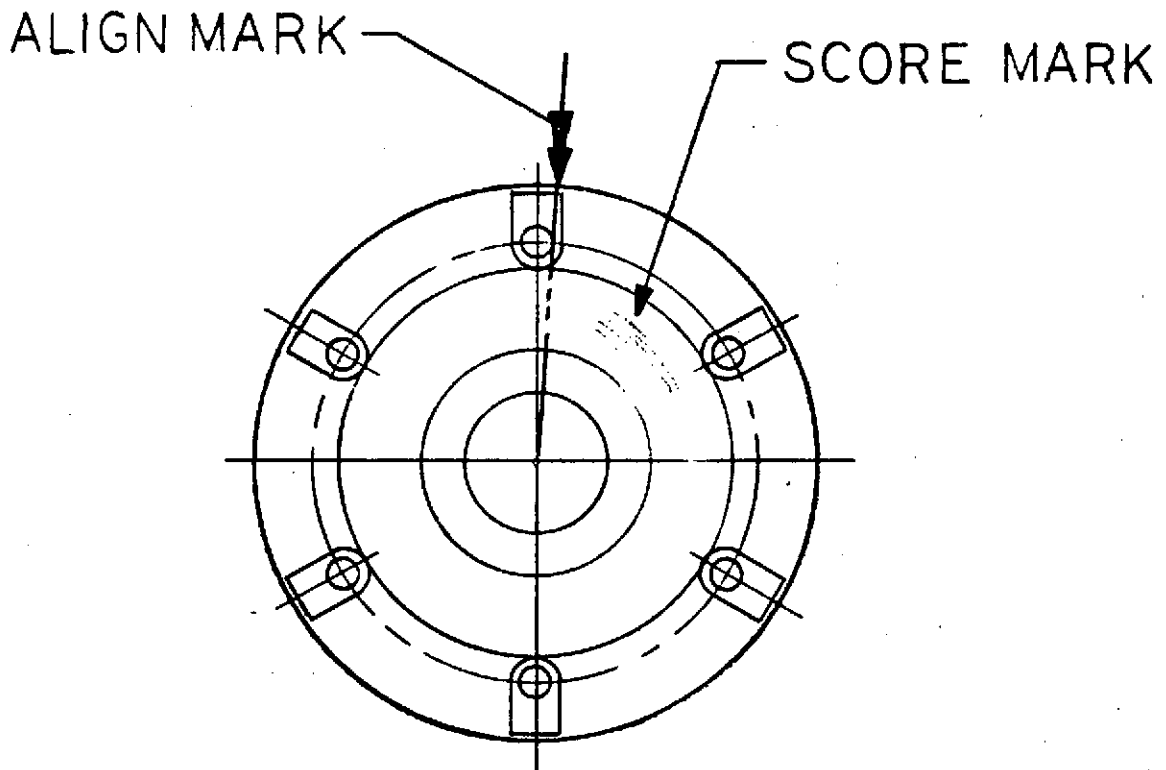
FRONT OUTSIDE VIEW ("B" HALF)

ROTOR HALF NO. 012-B  
(NON-METALIZED)



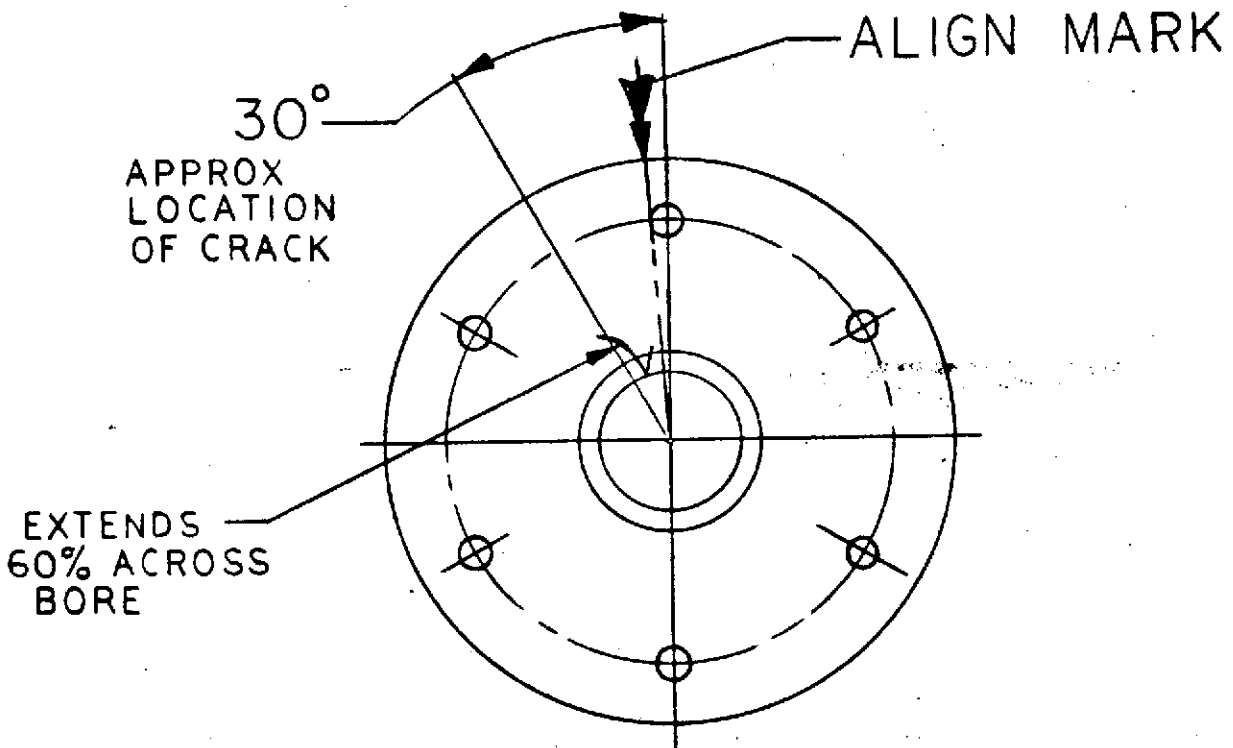
FRONT OUTSIDE VIEW ("B" HALF)

ROTOR HALF NO. 012-A  
(METALIZED)



FRONT OUTSIDE VIEW ("A" HALF)

# ROTOR HALF NO. 012-A (METALIZED)



FRONT INSIDE VIEW ("A" HALF)

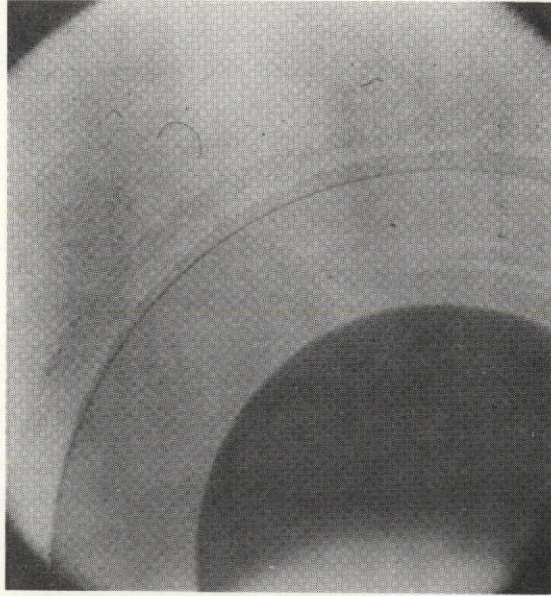


FIGURE 6. METALIZED HALF - SCORES ON THRUST SURFACE. (x15)



FIGURE 7. METALIZED HALF-Y' SHAPED CRACK AT BORE (x15)

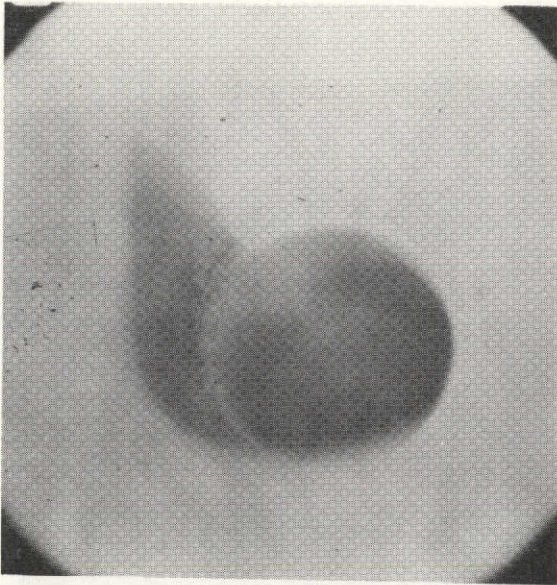


FIGURE 8. NON-METALIZED (B') HALF  
CRACK AT SCREW HOLE  
(X15)

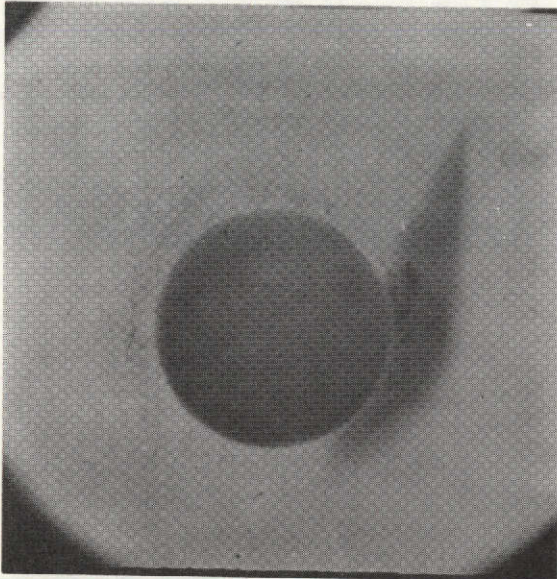


FIGURE 9. B HALF . CRACK AT  
SCREW HOLE (X15)



FIGURE 10. B HALF . Y SHAPED  
CRACK AT BORE (X15)

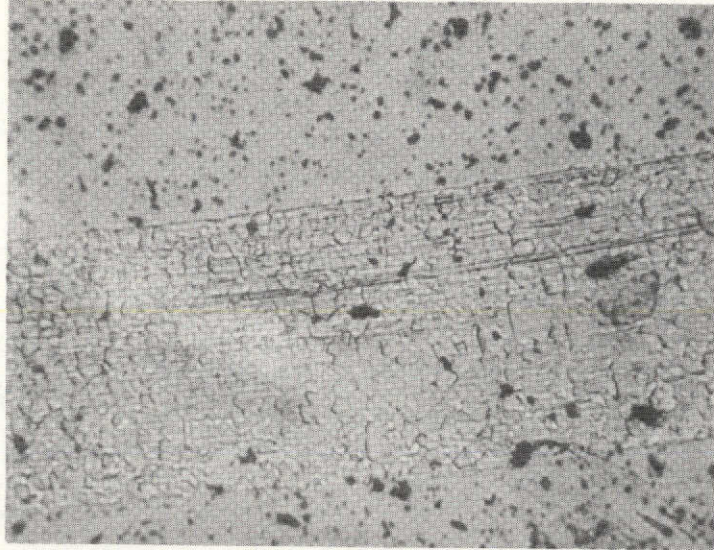


FIGURE 11 CLOSEUP OF SCORE (X100)

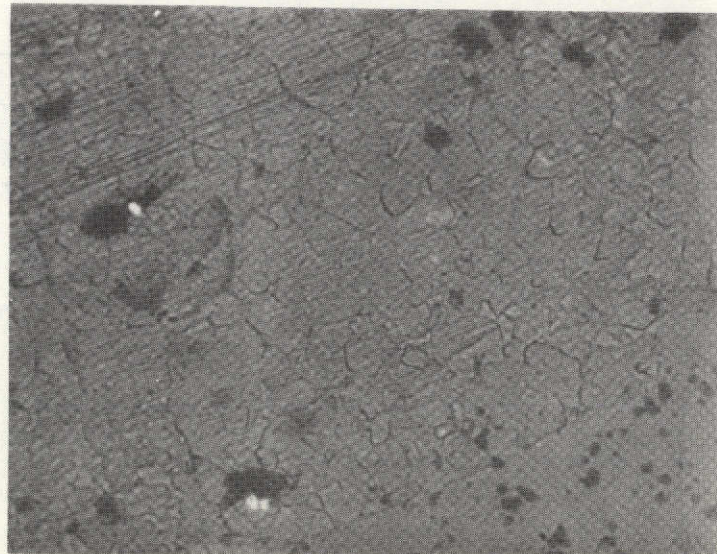
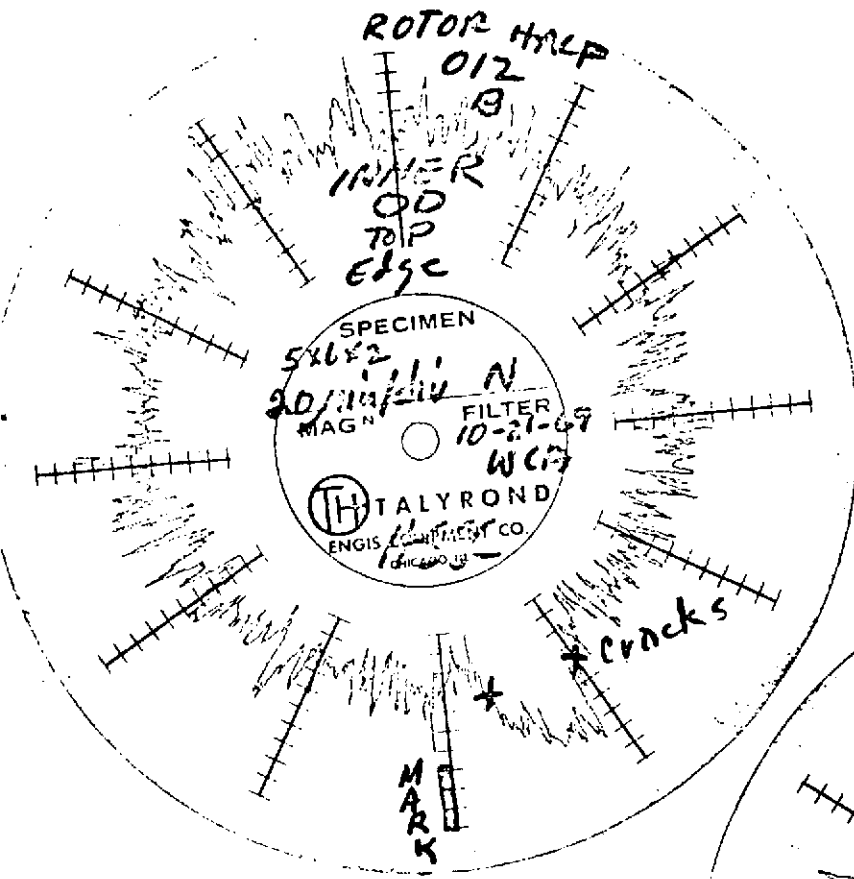


FIGURE 12 CLOSEUP OF SCORE (X200)

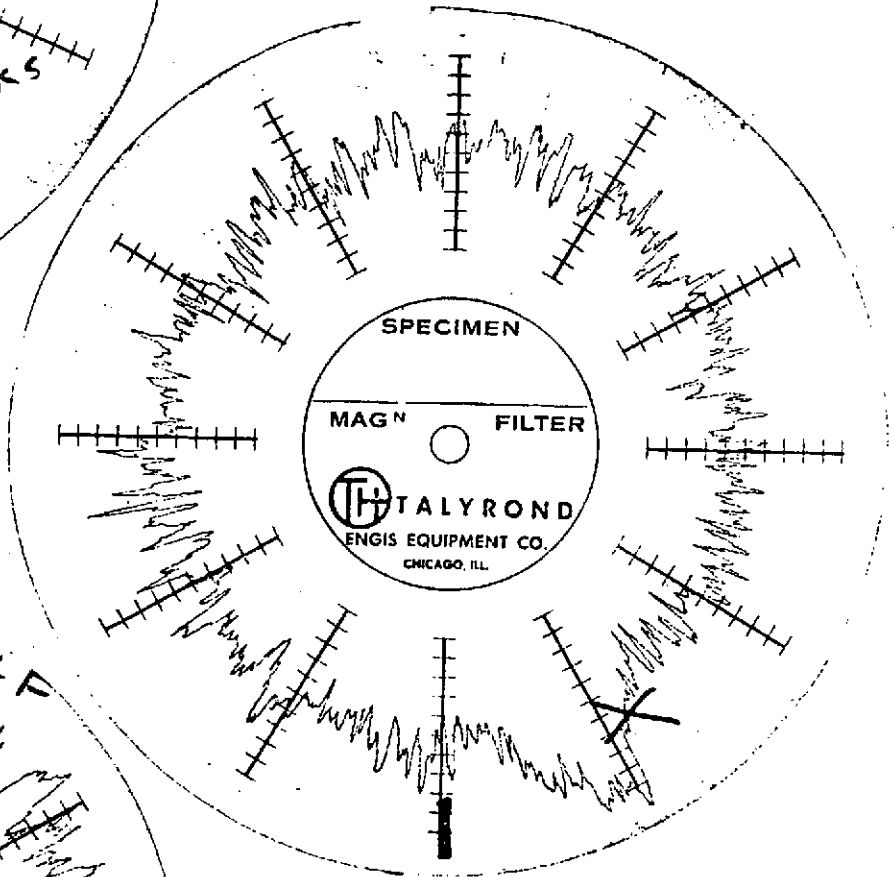
TALYROND TRACES

FIG. 13

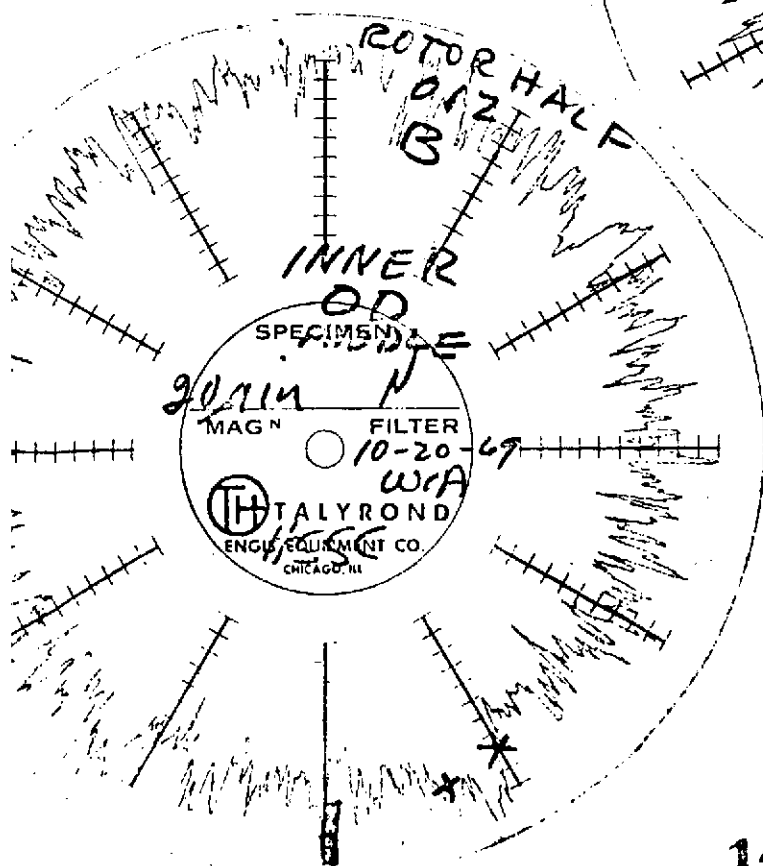
ROTOR HALF #012B



a)



b)



c)

FIGURE 14.  
 TALYROND TRACES  
 ROTOR HALF # 012 B

- 12 -

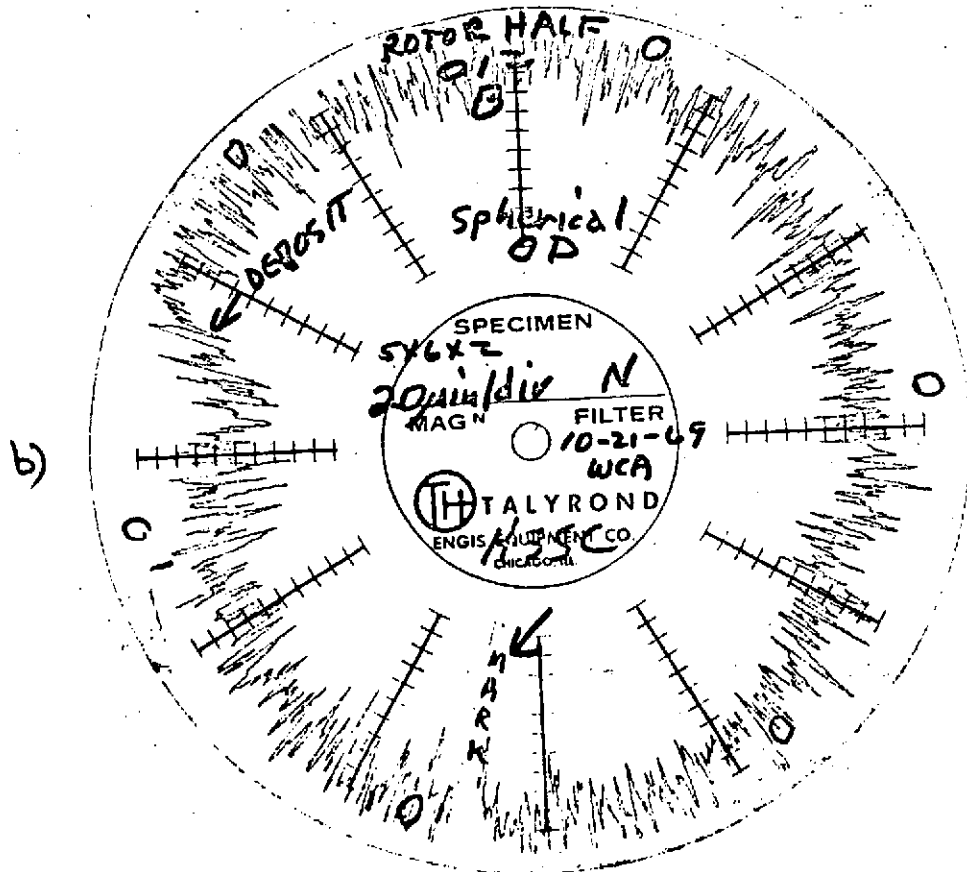
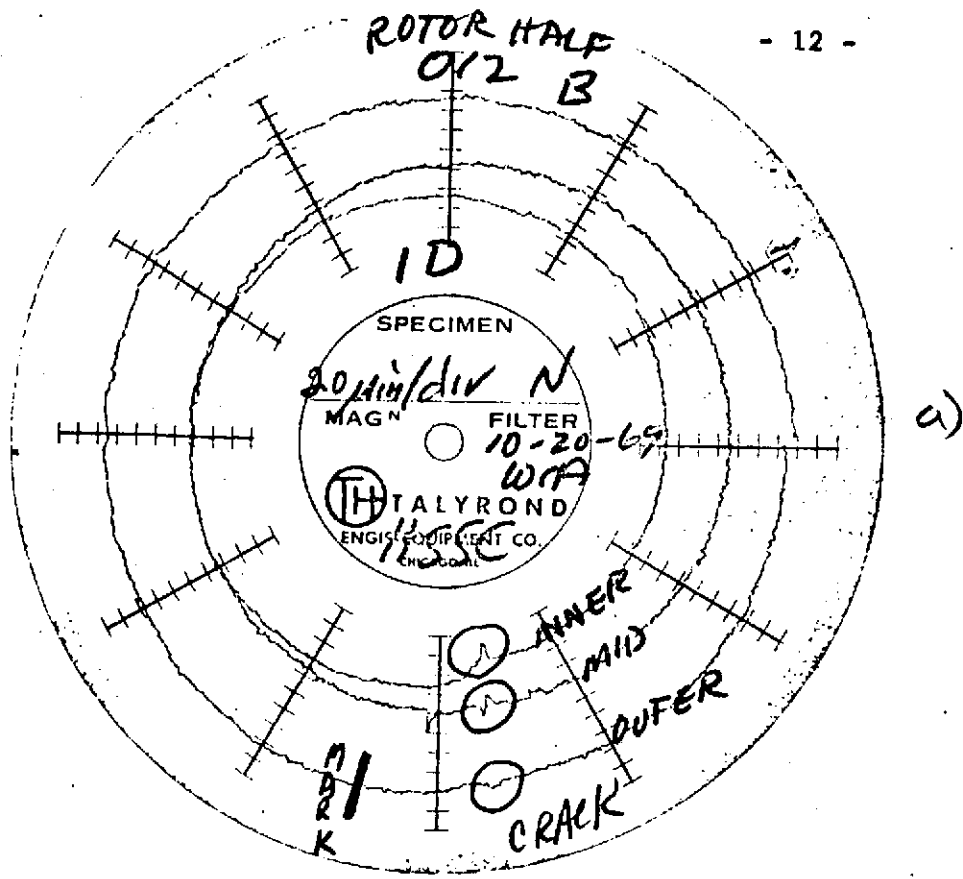
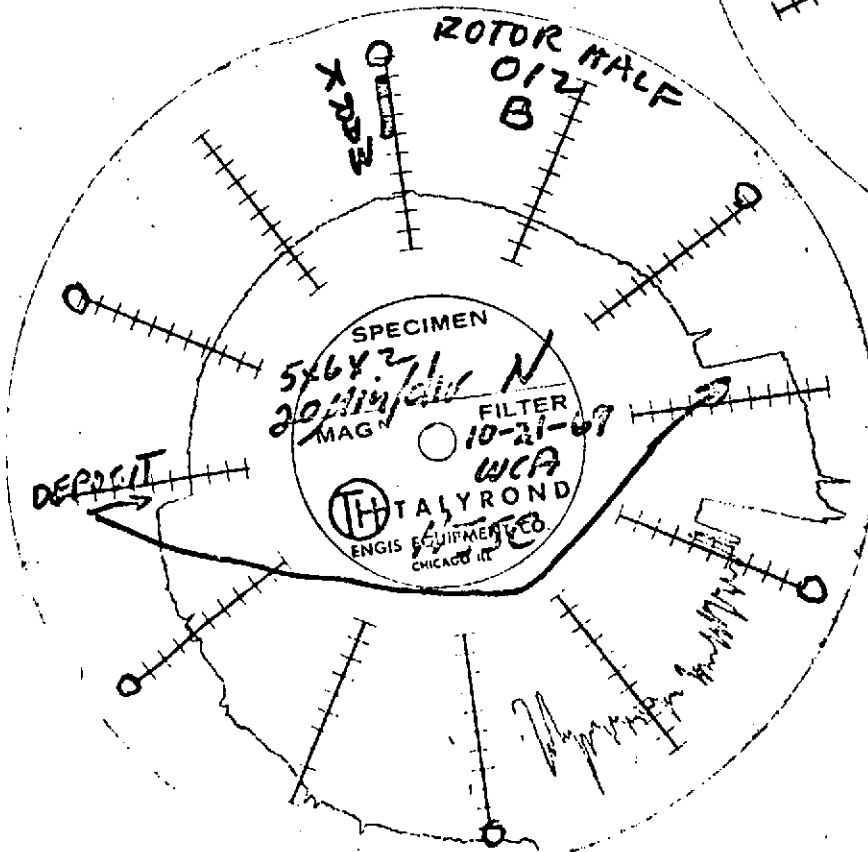
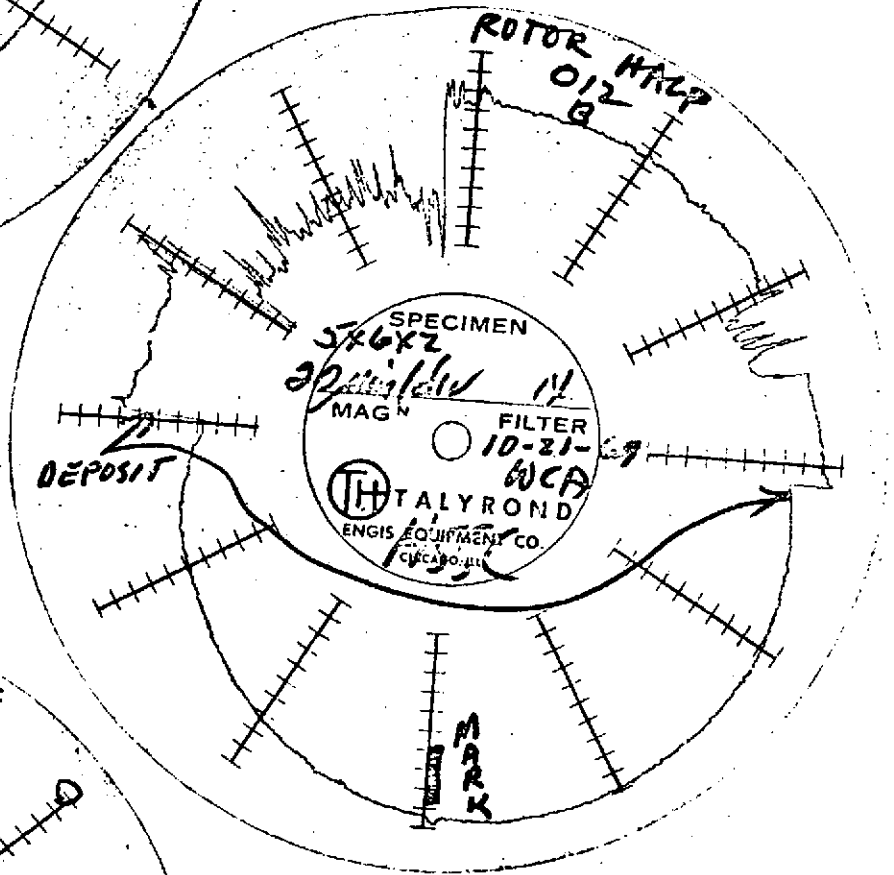
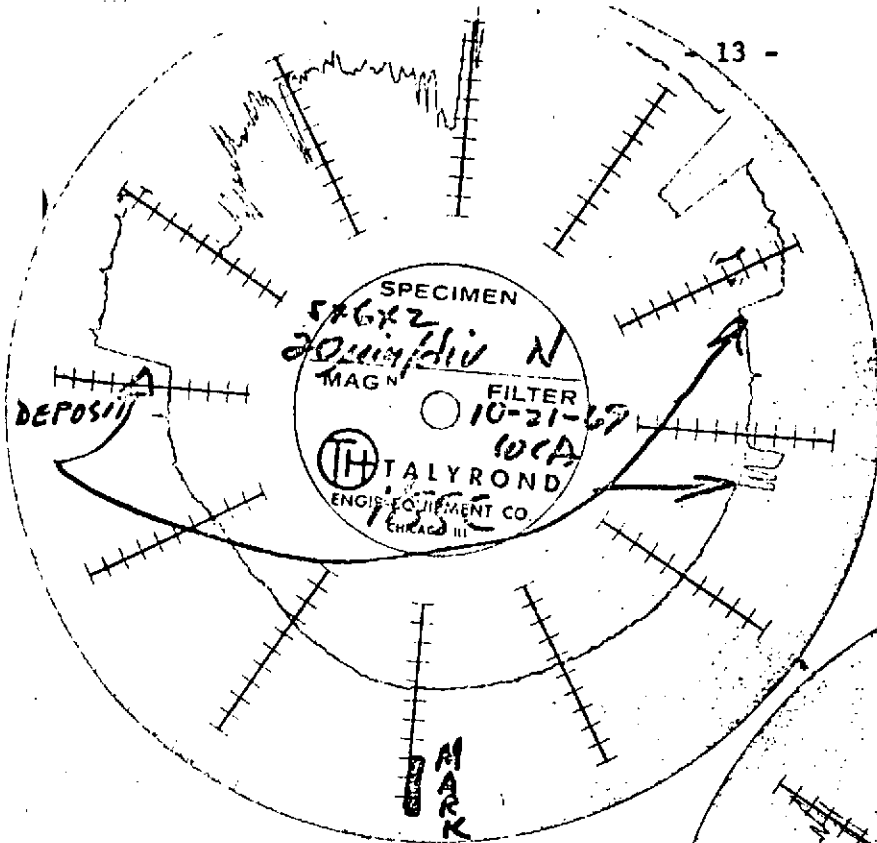


FIGURE 15  
TALYROND TRACE  
ROTOR HALF 012B

13 -





speed of 6000 rpm. At 30 K rpm the wheel began to exhibit an axial disturbance as seen on the axial probes. The radial probes, set at the largest diameter, did not indicate any thing which would lead one to believe that the motion was conical in nature. As the speed was increased, the amplitude of the disturbance increased until at 32.5 K rpm sudden failure occurred. After failure the Talyrond showed that one wheel half had slipped relative to the other. Teardown revealed that none of the cracks had grown as a result of the failure.

### 2.3 Run Number 3

The wheel was then cleaned, reassembled, and run on the Schenck balancer. An unbalance of 91 mg was detected on one rotor half and 50 mg on the other rotor half. The wheel was then assembled to an instrumented test fixture and run in 11.25 psia of hydrogen. The wheel was run up to 30 K rpm, and no disturbance was detected.

### 2.4 Run Number 4

Without disassembling the wheel the wheel was balanced by removing material from the rotor screws and nuts. At this time, it was found that at speeds up to 24 K rpm, there was a shift in balance indicating movement of the screws. For this reason, the torque on the screws was changed from 22 oz. ins. to 44 oz. ins. and mass shifts were no longer found to be a problem.

The wheel was then placed in the running rig in 22 psia of hydrogen. The wheel was then run at 3 K rpm increments from 30 K rpm to 48 K rpm without difficulty. The wheel ran for several minutes at 48 K rpm until suddenly the axial capacitance probe detected a disturbance at the same frequency as the wheel speed. This disturbance began to increase in amplitude, and before the wheel

supply could be turned off, there was a sound from the rig like a minor explosion at which point the instrumentation indicated that the wheel was no longer rotating.

Upon removal of the lid of the running pot (figure 17), it was discovered that the wheel had disintegrated into many small pieces (figure 18). When the running rig was removed from the pressure pot, it was observed that the rotor had completely fractured and had delaminated the hysteresis rings (figure 19). The delaminated rings are shown in figure 20.

One thrust plate had broken, but one was still intact (figure 21). One screw was intact, one had broken into three pieces, and the remainder had broken into two pieces (figure 22). The shaft had broken into three pieces, figure 23, with the threaded area at either end being broken off.

Apparently the impact of the failure was sufficient to gouge pieces out of the running rig as shown in figure 24. This is hardly surprising in view of the fact that the peripheral velocity at the moment of failure would have been approximately 200 miles/hour.

### 3.0 POSSIBLE MECHANISMS OF FAILURE

#### 3.1 Hydrodynamic Instability

It is possible, but not very probable, that wheel failure was initiated by a hydrodynamic instability (such as conical whirl). This could have led to a high speed touchdown in the bores. It is possible that the wheel could have a fair stability margin at 24 K rpm in air and yet be unstable at 32 K rpm in hydrogen. To check this possibility, the stability parameter ( $\bar{M}$ ) was checked for a range of compressibility numbers for the running conditions and actual geometry of wheel 012 (see figure 25). Comparing these results with the critical mass parameters for whirl instability, given in reference 8, it can be seen that

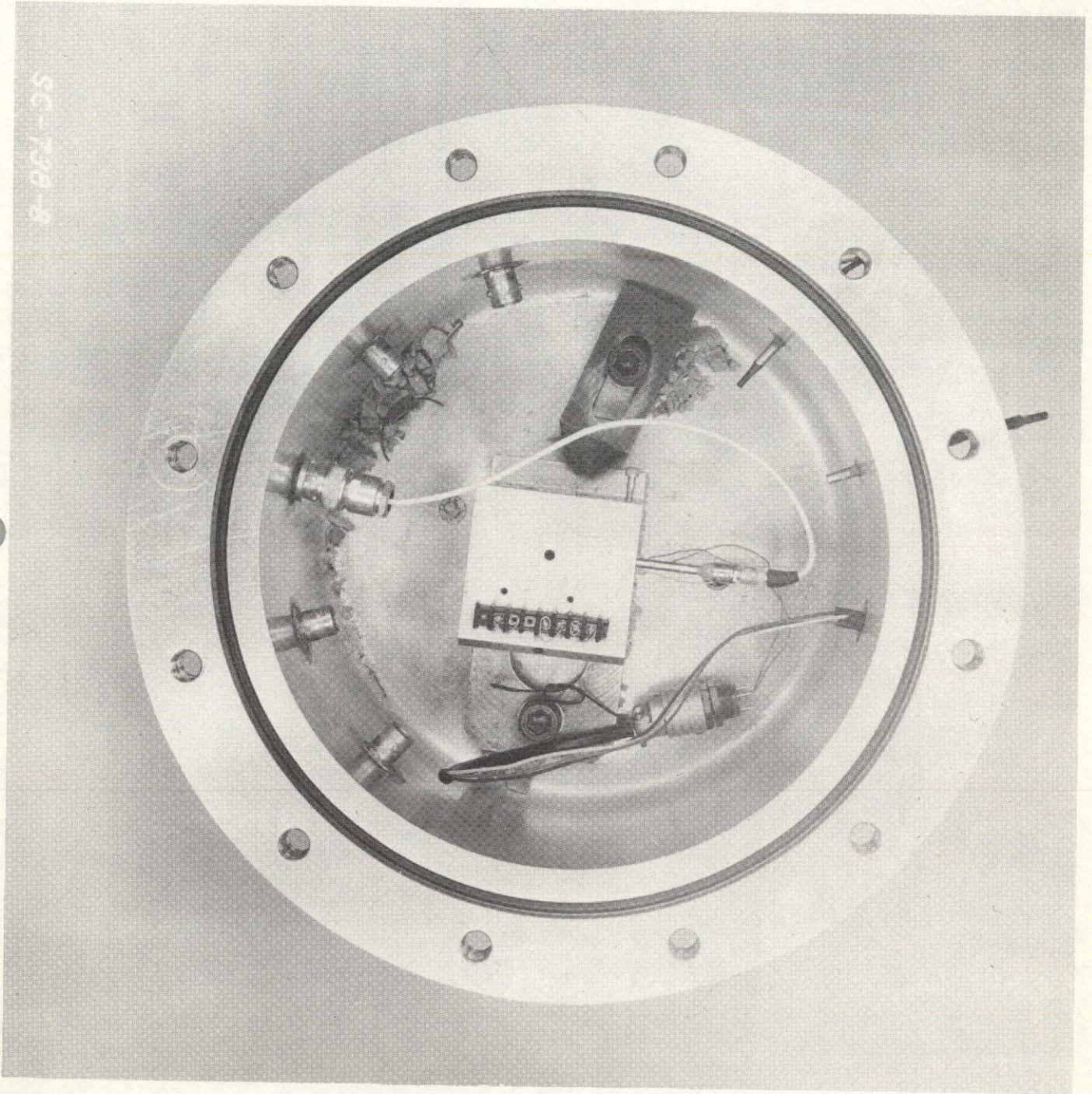


FIGURE 17.

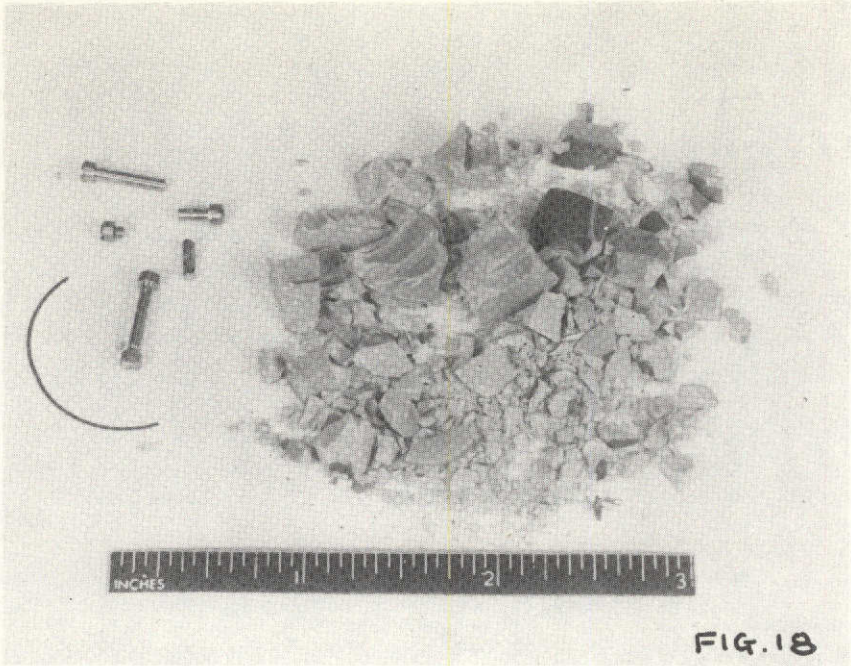


FIG. 18

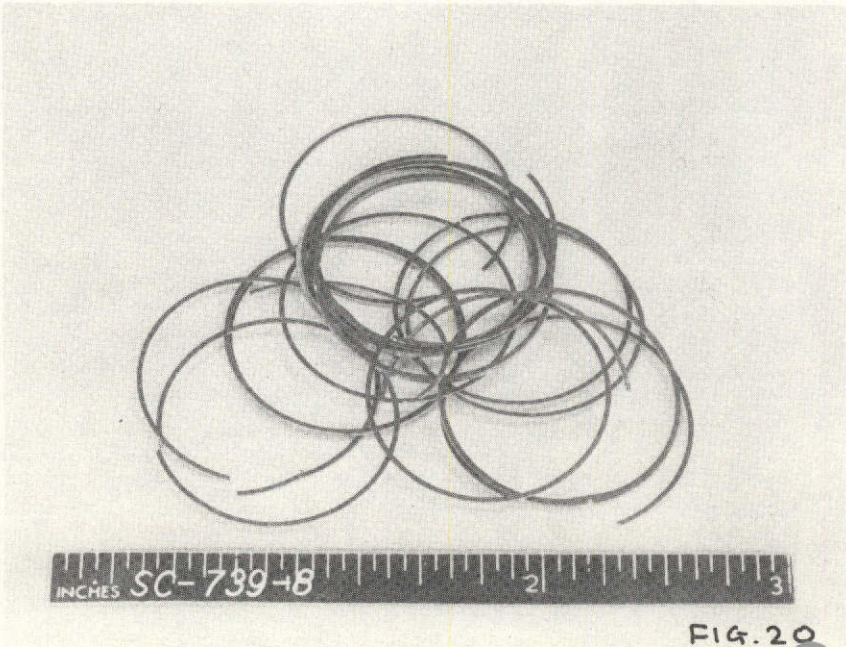


FIG. 20

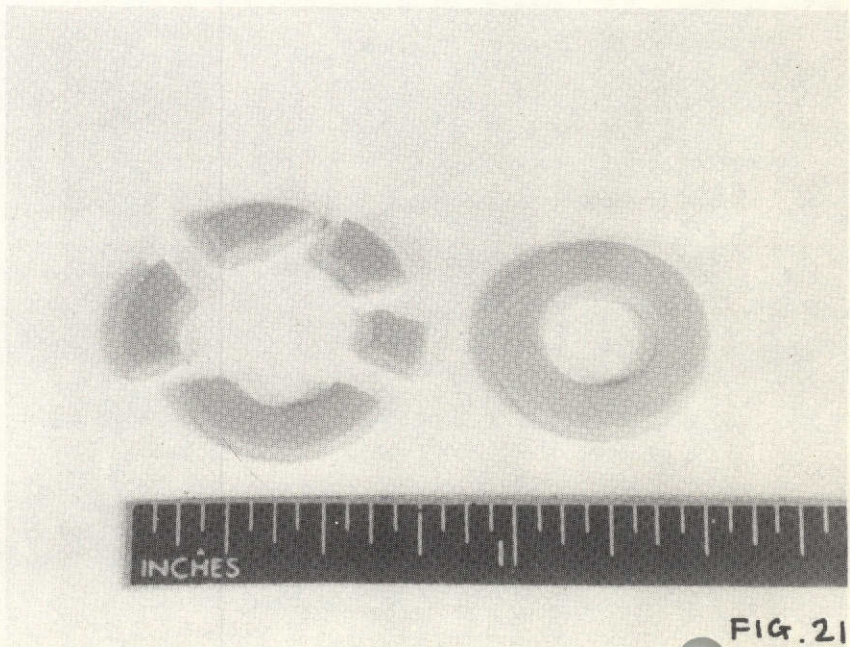


FIG. 21

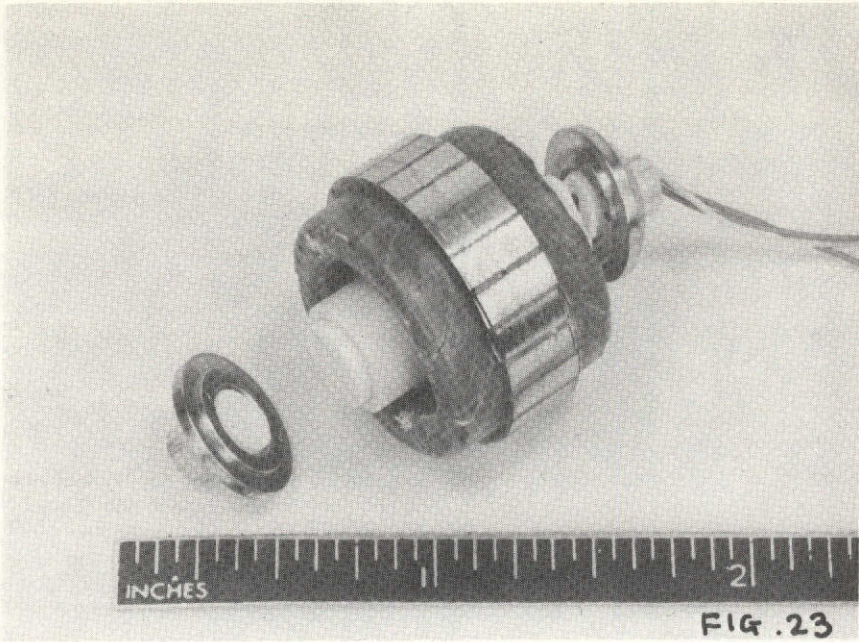


FIG. 23

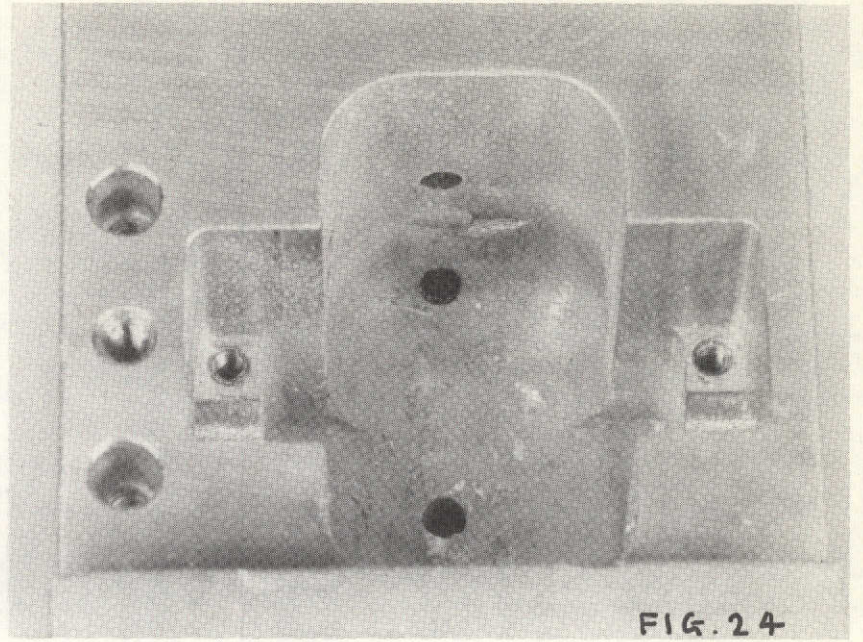


FIG. 24



FIG. 22

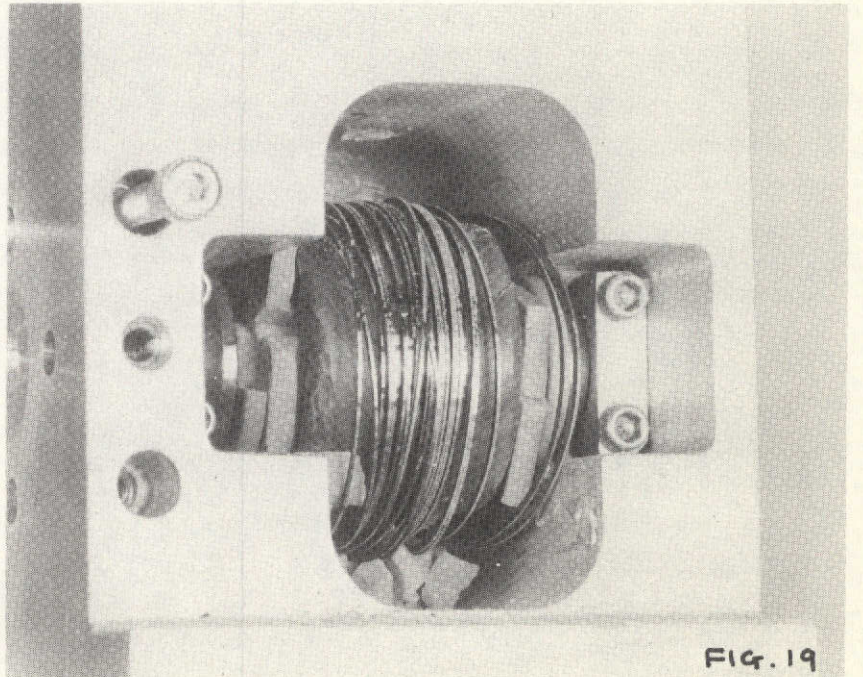


FIG. 19

M

EUBENE DIETZGEN CO.  
MADE IN U. S. A.

NO. 340-L312 DIETZGEN GRAPH PAPER  
SEMI-LOGARITHMIC  
3 CYCLES X 12 DIVISIONS PER INCH

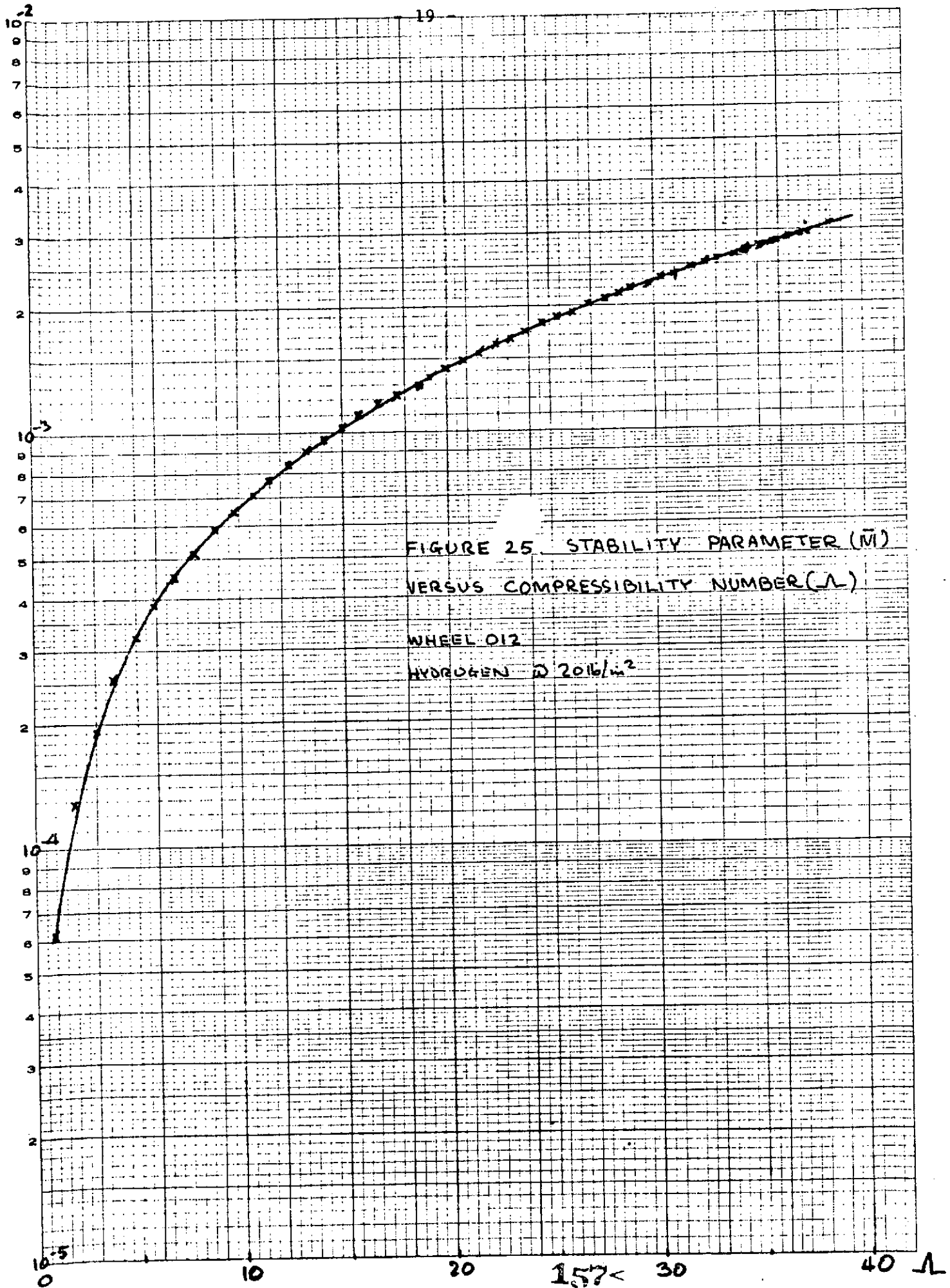


FIGURE 25. STABILITY PARAMETER ( $M$ )  
VERSUS COMPRESSIBILITY NUMBER ( $\Lambda$ )

WHEEL 012  
HYDROGEN @ 20 lb/in<sup>2</sup>

0 10 20 30 40  $\Lambda$

wheel 012 should be running an order of magnitude within the stability envelope.

It is concluded that a hydrodynamic instability was not responsible for the failure of wheel 012 for the following reasons:

- a) The wheel was running well within the published<sup>8</sup> stability boundary.
- b) A hydrodynamic instability would have been expected to manifest itself at half wheel speed rather than at wheel speed.
- c) If the wheel had failed at 32.5 K rpm in 22 psia of hydrogen due to a hydrodynamic instability one would have expected it to fail at a speed  $< 30$  K rpm in 11.25 psia of hydrogen.
- d) A failure due to whirl, either cylindrical or conical, would result in a high speed touchdown. This could account for the cracks in the bore, but it is difficult to see how cracks at the screw holes at the outside diameter could be formed. In addition, one would expect to see circumferential score marks in the bore as the result of this type of failure.

### 3.2 Initial Failure at O. D.

It is most unlikely that simultaneous failure occurred at both the inside and outside diameters. If failure occurred initially at the outside then a mechanism must be proposed that could lead to subsequent failure at the inside. This could occur, it is hypothesized, if failure on the outside had resulted in slip between the two interfaces of the rotor halves, as shown in figure 24. The consequence of this would be that the two rotor halves would touch in the shaft with sufficient velocity to initiate cracking on the inside. The fact that the cracks occurred at the points A (figure 26) but not at B can be explained by the thicker section which exists at B. It can be shown (Appendix A) that the

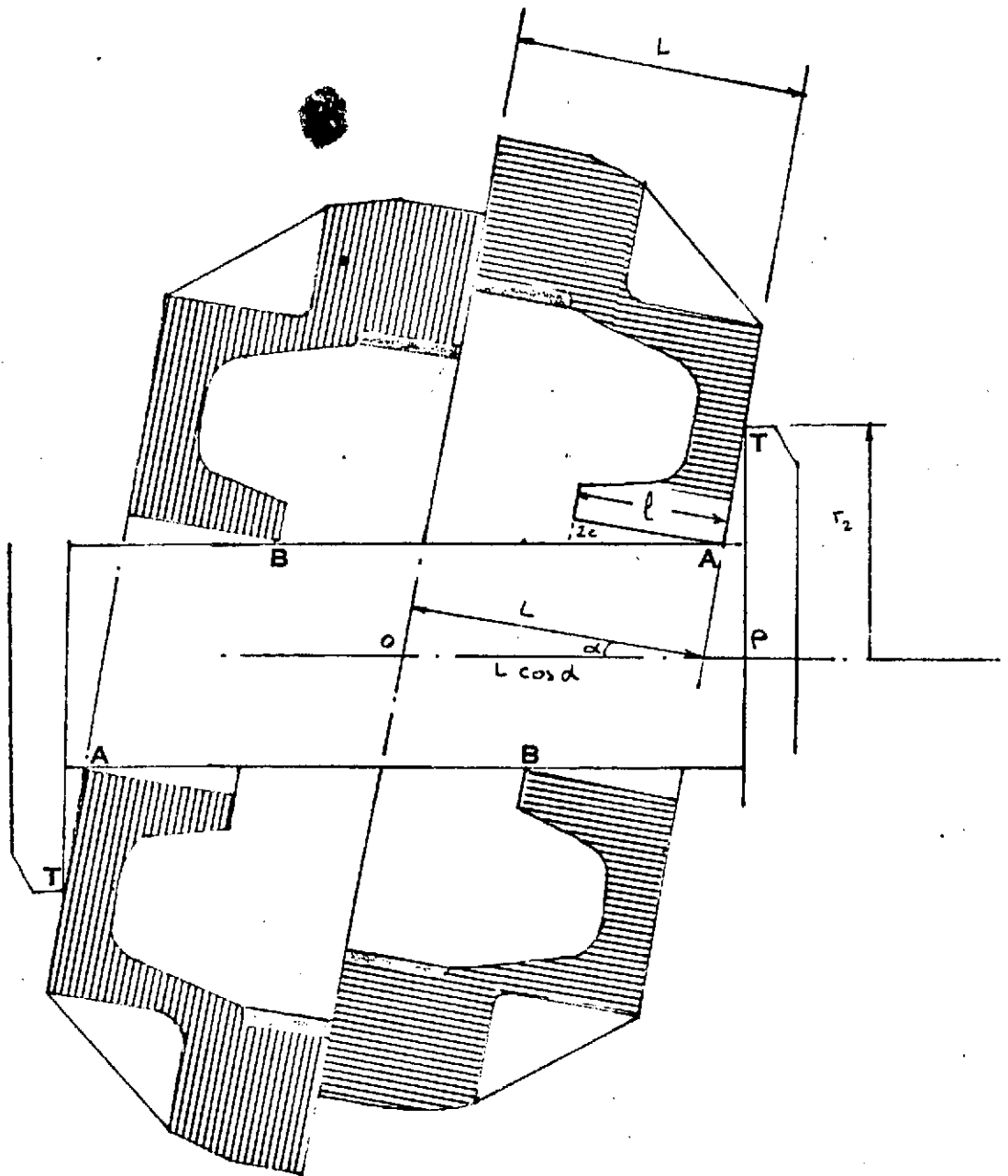


FIGURE 26. MISALIGNMENT OF GAS BEARING

wheel will touchdown on the shaft first, assuming that it is running centrally located between the two thrust plates. This does not, of course, preclude touchdown on the thrust surface at one end as a result of impact on the journal.

(This could explain some of the scoring on the thrust face.)

Of course, this whole theory relies on crack initiation occurring at the O.D. This in itself could have occurred, it is proposed, due to one or more of the following reasons:

- a) excessive stress levels at O.D.
- b) excessive stress concentration at screw holes
- c) residual stresses
- d) material properties out of specification
- e) cracks remaining in surface
- f) overtightening of screws
- g) poor load distribution from screws (causing high Hertzian stresses)

These factors are discussed in some detail in section 4.

### 3.3 Initial Failure on the Inside Diameter

Although it is more usual for a rotating body to fail initially on the I.D. (higher stresses) it is difficult to postulate a theory whereby such a failure would result in cracking on the outside. For this reason, initial failure on the I.D. due to excessive stress levels would seem to be unlikely.

Figure 27 shows how the computed tangential stresses vary from 3700 lbs/in<sup>2</sup> at the fracture zone at the inside diameter to 2000 lbs/in<sup>2</sup> at the fracture zone at the outside diameter. Figure 28 shows how the radial stresses vary from 1800 lbs/in<sup>2</sup> at the fracture zone at the inside to 350 lbs/in<sup>2</sup> at the fracture zone at the outside.

VARIATION OF TANGENTIAL STRESSES WITH RADIUS.

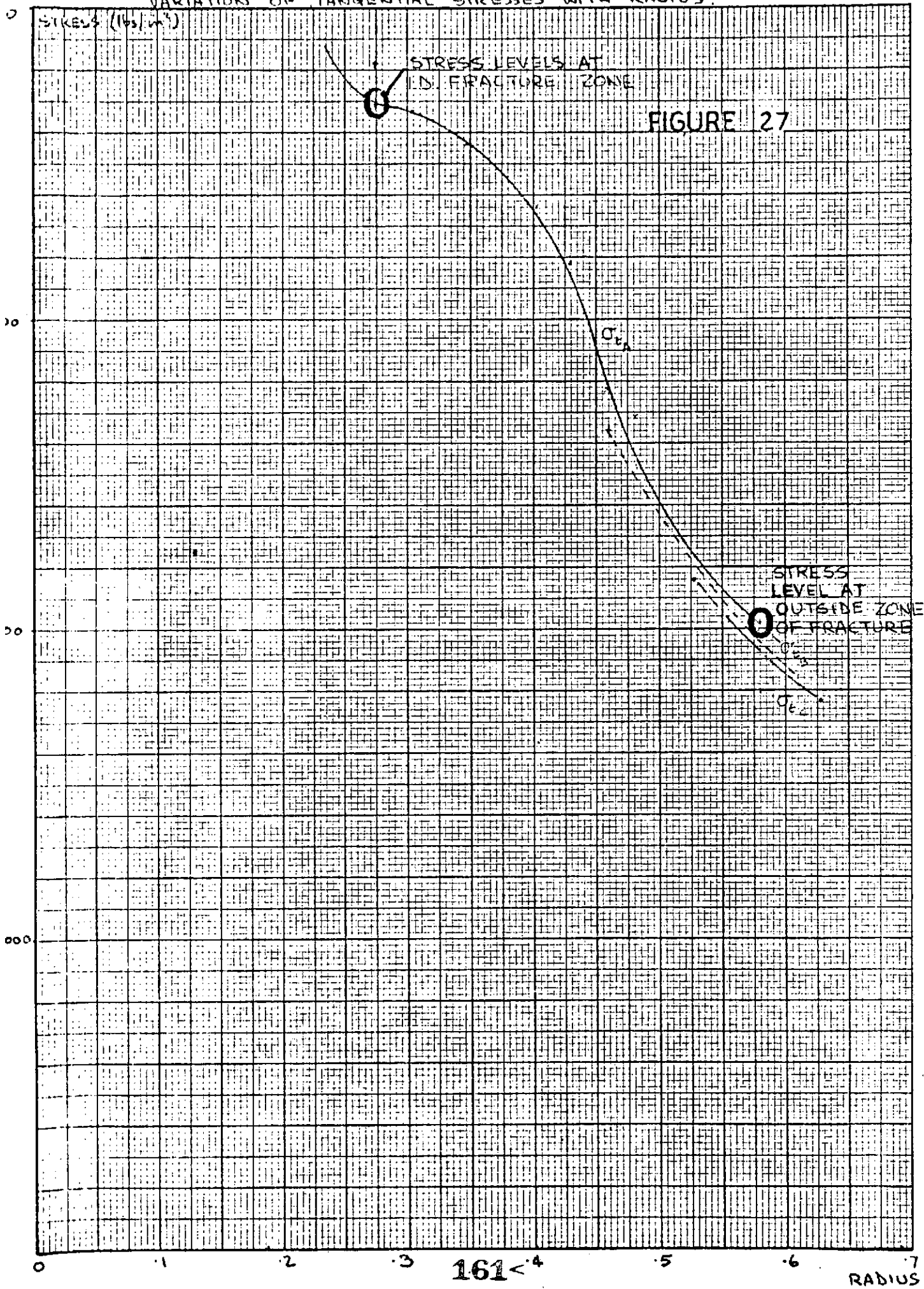


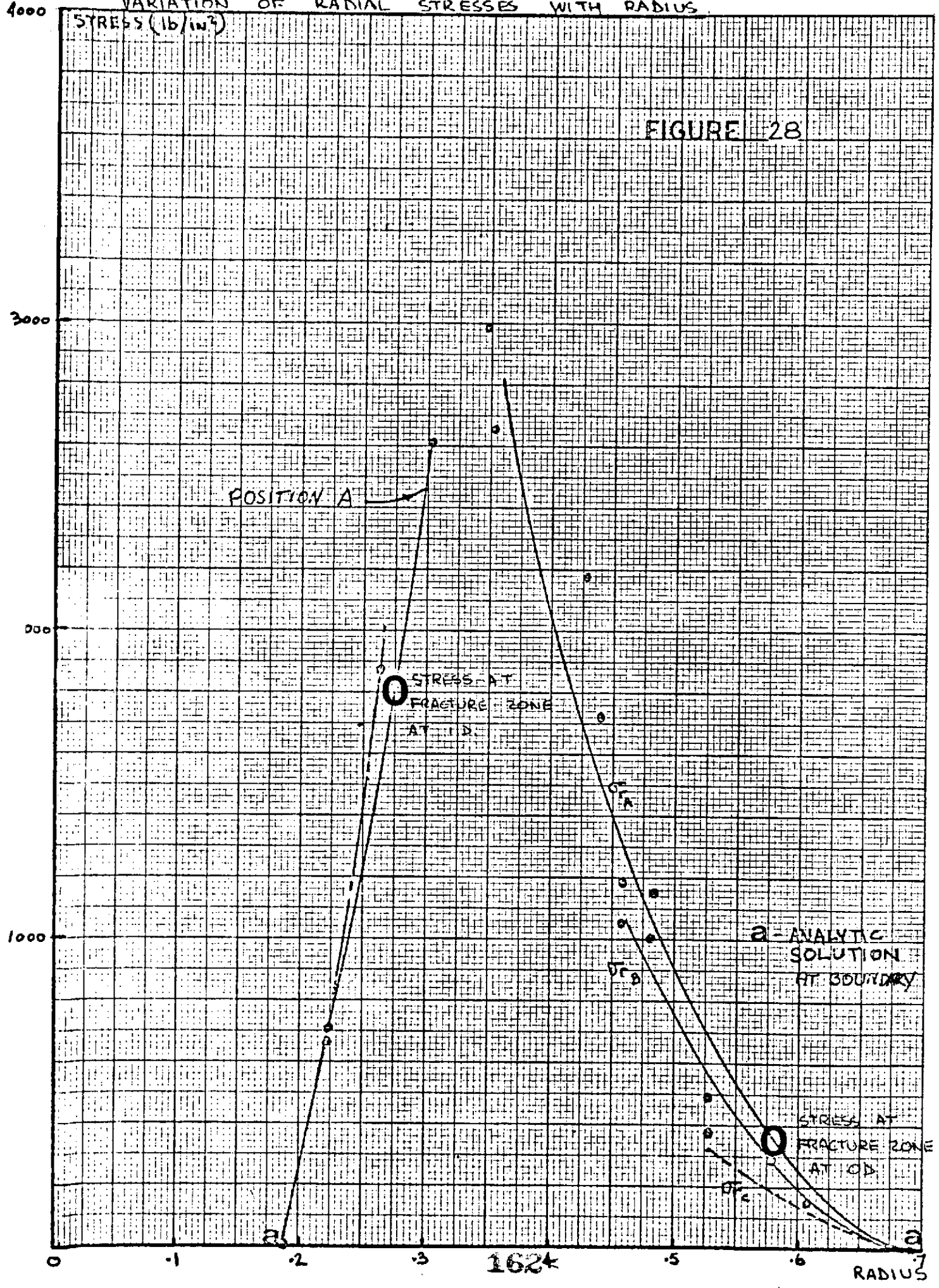
FIGURE 27

161<sup>4</sup>

RADIUS

VARIATION OF RADIAL STRESSES WITH RADIUS

FIGURE 28



7 X 10 INCHES  
KEUFFEL & ESSER CO.

### 3.4 Excessive Temperatures in the Hysteresis Ring

At one point during the initial test sequence the connections to the hysteresis motor were accidentally reversed, and the bearing tried to run in reverse. As a result of the motor running out of the synchronous condition, it began to heat up. It was estimated that the temperature in the hysteresis ring at one point reached 50°F above ambient. As a worst case calculation, it was assumed that the nodes in the hysteresis ring (see figure 29) were at 50°F above ambient while the adjacent elements were at ambient temperature. Table 1 shows that the stresses due to this gradient were insignificant in the rotor, and all occurred in the hysteresis ring.

### 3.5 Excessive Centrifugal Forces

If the rotor halves have an unbalance, then the net centrifugal force at a given speed is proportional to the speed squared. Thus, if

$$w = \text{unbalance}$$

$$U_1 = \text{centrifugal force} = \frac{w}{g} \omega^2 r$$

The resultant force (see figure 29) causing slip between the interfaces is U.

Where

$$U = U_1 + U_2$$

This resultant force is opposed by  $F = \mu_i P_i A_i$

Where

$$\mu_i = \text{interfacial friction coefficient}$$

$$P_i = \text{interfacial pressure}$$

$$A_i = \text{contact area between interfaces}$$

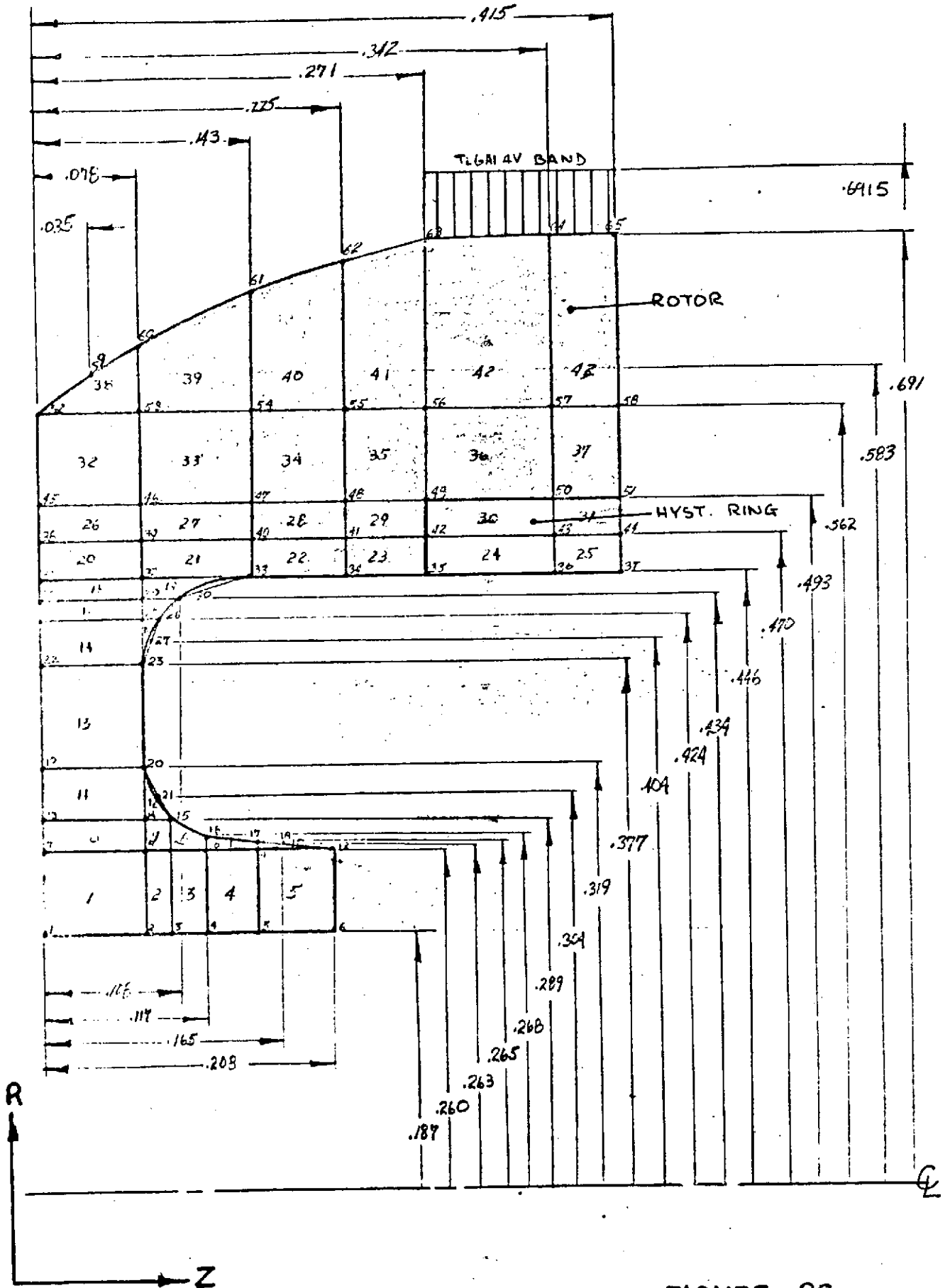
TABLE 1

Nodal Stresses Due to Severe Thermal Gradient

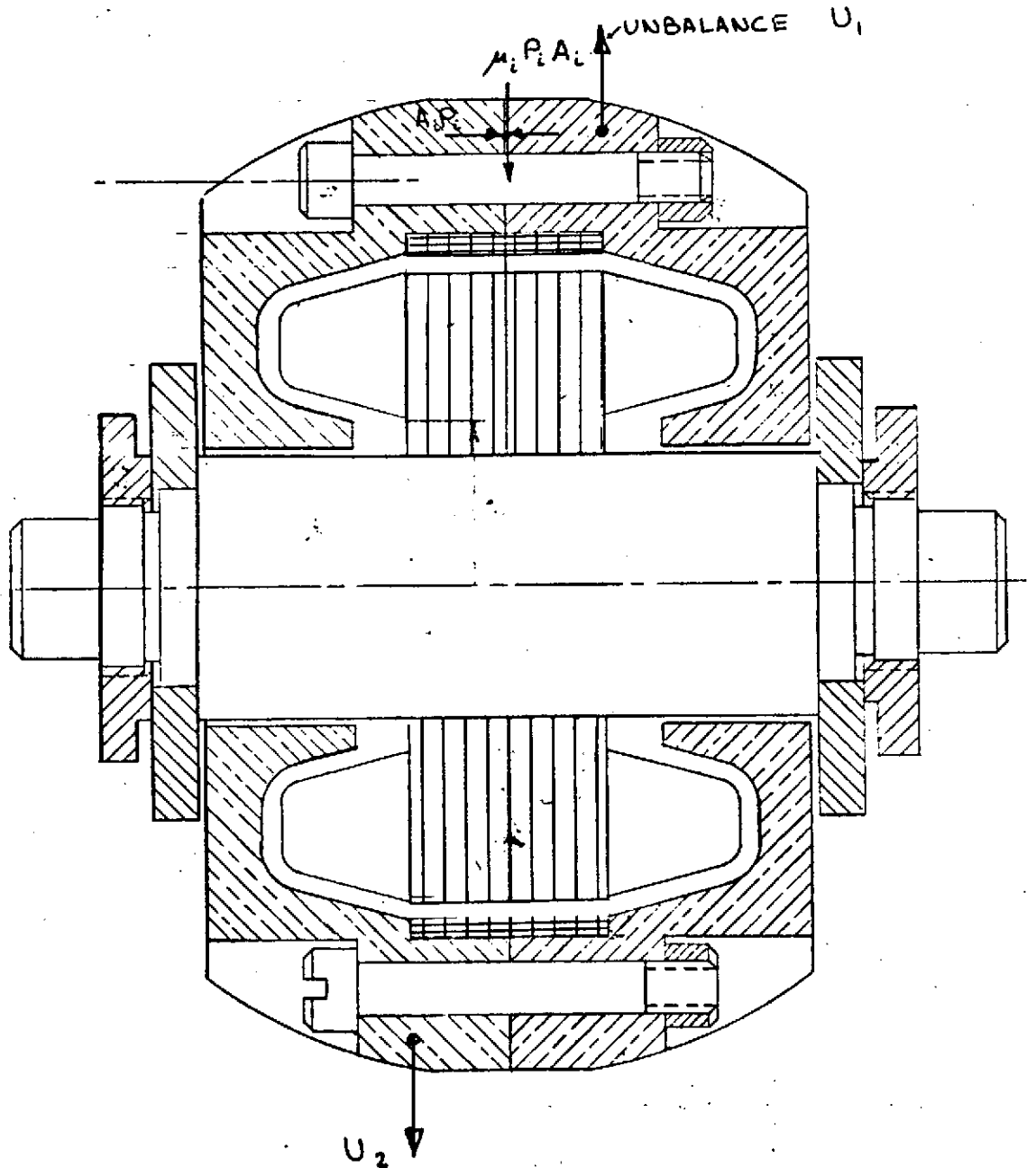
<u>ment Number*</u>	<u>Wheel Component</u>	<u>Radius</u>	<u>Temperature (°F)</u>	<u>Stresses (lb/in<sup>2</sup> x 10<sup>3</sup>)</u>	
				<u>Radial</u>	<u>Tangential</u>
23	Rotor	.458	70	5.8721	3.0648
29	Rotor	.4815	70	6.4649	3.9341
35	Rotor	.5275	70	-0.2495	2.6685
36	Rotor	.5275	70	0.6449	3.5968
37	Rotor	.5275	70	0.8008	3.7834
42	Rotor	.6238	70	0.1923	2.6211
43	Rotor	.6265	70	0.2593	2.6733
30	Hysteresis Ring	.4815	120	-12.217	-14.821
31	Hysteresis Ring	.4815	120	-12.779	-15.448
24	Hysteresis Ring	.458	120	-11.417	-14.349
25	Hysteresis Ring	.458	120	-11.751	-14.793

\*Refer to nodal map (figure 29)

# RI1170 ROTOR HALF STRESS MODEL



# RI 1170 GAS BEARING



166<

FORCES ACTING ON GAS BEARING ASSEMBLY. FIGURE 30

It is feasible that if the unbalance is substantial, the centrifugal force could increase with speed to a point where it exceeds the resisting force due to the interfacial pressure.

To check this theory, the interfacial force was computed using the model shown in figure 30. Again, the finite element program was utilized, but in this case the constraint against movements at the interface was removed. From this program an interfacial force of 33.8 pounds was obtained, yielding an average interfacial pressure of 50 lbs/in<sup>2</sup>.

Using the friction coefficients given in appendix B, then the opposing force F becomes:

$$F = \mu_i (P_i A_i) = 0.185 \times 33.8 = 6.25 \text{ lbs}$$

For slip to occur,

$$F \leq U_1$$

Whence

$$w_1 = \frac{6.25g}{\omega^2 r_1} = 162.9 \text{ mg}$$

however, the measured unbalance is (91 + 50) mg = 141 mg which is very close to that which would cause interfacial slip.

#### 4.0 ANALYSIS OF FAILURE

##### 4.1 Stress Levels

A comprehensive stress analysis of the gas bearing assembly was done using both conventional and finite element techniques (reference 1). However, in view of the wheel failure, it was felt to be necessary to repeat the wheel calculations using more conservative calculations where necessary.

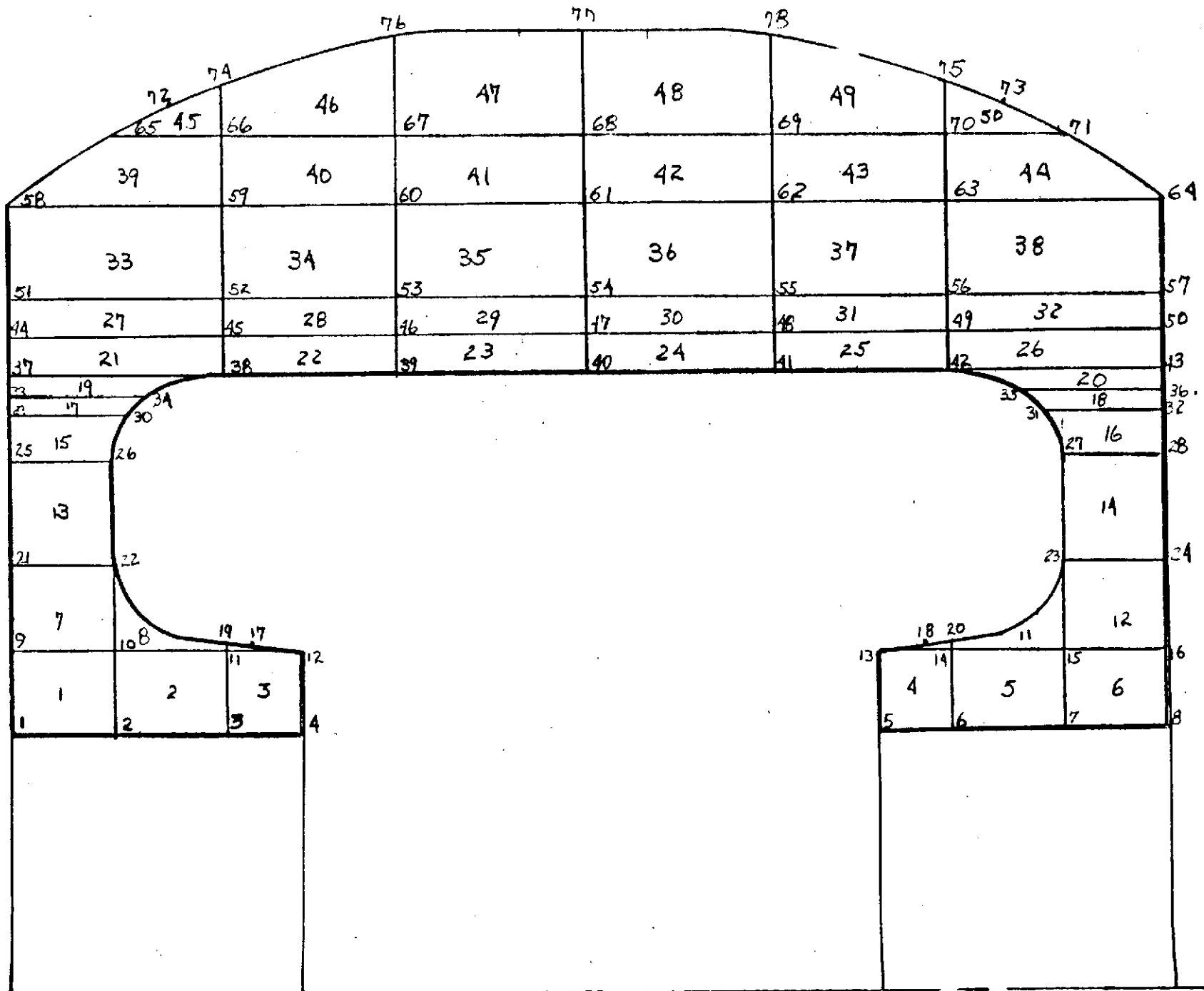


FIGURE 31. FINITE ELEMENT MODEL TO EVALUATE INTERFACIAL PRESSURES 168

Considering the rotor half stress model, as shown in figure 29, initially without the Ti 6Al 4V band, the stresses in elements 38, 39, and 40 (outside) and elements 3, 4, and 5 (inside) are of interest. As shown in Table 2 and figures 19 and 20 the radial stresses are  $616 \text{ lbs/in}^2$  and  $290 \text{ lbs/in}^2$  at the I.D. and O.D. respectively. The tangential stresses are  $2050 \text{ lb/in}^2$  at the O.D. rising to  $4117 \text{ lbs/in}^2$  at the I.D.

To the stresses on the O.D., one must add the effect of stress concentrations and the effect of radial forces from the screws. These effects are discussed in appendix C where it is shown that the maximum stress due to stress concentration in the hole is  $8200 \text{ lbs/in}^2$ . The maximum compressive stress (figure 31) due to the radial force from the screws is  $600 \text{ lbs/in}^2$ .

Thus, the maximum stresses are  $5710 \text{ lbs/in}^2$  radial, and  $8200 \text{ lbs/in}^2$  tangential which are way below the strength of the material.

#### 4.2 Stress Concentrations

The above calculation (see also appendix C) has taken into account the effect of stress concentrations at the holes, namely the effect of the hole itself and of the bolt in the hole. The forces from the bolts should be regarded as a worst case since in practice not all screws will act on the holes due to the effect of friction under the head of the screw.

#### 4.3 Prior History

It is well known that in metals there can be considerable residual stresses due to the effect of the prior deformation history. In most cases this would result in a thin layer in compression. These stresses can be extremely high; for example, stresses of up to  $70,000 \text{ lbs/in}^2$  have been reported in gage blocks<sup>4</sup>. These stresses are due to dislocations which are trapped in a mesh of dislocation

TABLE 2

ROTOR HALF THERMOELASTIC STRESS ANALYSIS RE 1170 J. GENELLA

ELEMENT	R-ORDINATE	ELEMENT STRESSES (PSI)				
		Z-ORDINATE	TAU(1)	TAU(2)	TAU(R,Z)	
1	0.22347E 00	0.39000E-01	0.70290E 03	0.42037E 04	-0.47249E 02	-0.15389E 02
2	0.22349E 00	0.84000E-01	0.67166E 03	0.41747E 04	-0.37836E 02	-0.63049E 01
3	0.22349E 00	0.10849E 00	0.64232E 03	0.41434E 04	-0.36796E 02	-0.48171E 01
4	0.22349E 00	0.13000E 00	0.64569E 03	0.41467E 04	-0.23067E 02	-0.11262E 01
5	0.22349E 00	0.17500E 00	0.61581E 03	0.41169E 04	-0.18728E 02	0.22317E 02
6	0.22349E 00	0.39000E-01	0.18245E 04	0.37858E 04	0.23340E 01	0.25076E 02
7	0.22349E 00	0.84000E-01	0.17957E 04	0.36570E 04	0.12187E 02	-0.45640E 02
8	0.22349E 00	0.10849E 00	0.18367E 04	0.37346E 04	0.12749E 03	-0.56297E 02
9	0.22349E 00	0.13000E 00	0.18616E 04	0.37993E 04	0.18286E 03	-0.26364E 02
10	0.22349E 00	0.16474E 00	0.18773E 04	0.38222E 04	0.24079E 03	-0.21507E 02
11	0.22349E 00	0.39000E-01	0.26170E 04	0.36646E 04	0.30937E 02	0.86919E 01
12	0.22349E 00	0.84000E-01	0.26281E 04	0.36938E 04	0.94750E 02	-0.54916E 02
13	0.22349E 00	0.10849E 00	0.29848E 04	0.39720E 04	0.31755E 02	-0.22647E-02
14	0.22349E 00	0.13000E 00	0.26541E 04	0.33697E 04	0.72729E 02	-0.81182E 01
15	0.22349E 00	0.17500E 00	0.26281E 04	0.33320E 04	0.10441E 03	0.49737E 02
16	0.22349E 00	0.39000E-01	0.21810E 04	0.31808E 04	0.84369E 02	-0.58496E 02
17	0.22349E 00	0.84000E-01	0.27404E 04	0.32401E 04	0.29440E 03	0.20770E 03
18	0.22349E 00	0.10849E 00	0.17204E 04	0.30056E 04	0.23931E 02	-0.77553E 02
19	0.22349E 00	0.13000E 00	0.17569E 04	0.30403E 04	0.25808E 03	0.12632E 03
20	0.22349E 00	0.17500E 00	0.11941E 04	0.27787E 04	-0.37684E 02	-0.78108E 02
21	0.22349E 00	0.39000E-01	0.12002E 04	0.27876E 04	0.10883E 03	0.43561E 02
22	0.22349E 00	0.84000E-01	0.10518E 04	0.26420E 04	-0.43021E 02	0.86359E 02
23	0.22349E 00	0.10849E 00	0.85438E 03	0.24438E 04	-0.32405E 03	0.86981E 02
24	0.22349E 00	0.13000E 00	-0.81955E 03	0.19643E 03	-0.67582E 03	0.45182E 02
25	0.22349E 00	0.17500E 00	-0.84390E 03	0.86295E 02	-0.76739E 03	-0.12881E 03
26	0.22349E 00	0.39000E-01	0.11835E 04	0.26980E 04	0.70014E 02	-0.92850E 02
27	0.22349E 00	0.11050E 00	0.11000E 04	0.26404E 04	0.85383E 02	0.31838E 02
28	0.22349E 00	0.18399E 00	0.10031E 04	0.25149E 04	0.37706E 02	0.11510E 03
29	0.22349E 00	0.24800E 00	0.91523E 03	0.24394E 04	-0.89533E 02	0.29733E 03
30	0.22349E 00	0.30650E 00	-0.72762E 03	0.22052E 02	-0.87661E 03	0.13871E 03
31	0.22349E 00	0.37849E 00	-0.86108E 03	-0.12274E 03	-0.10678E 04	0.30663E 02
32	0.22349E 00	0.39000E-01	0.44506E 03	0.22868E 04	-0.63881E 02	-0.52364E 02
33	0.22349E 00	0.11050E 00	0.38027E 03	0.22231E 04	-0.65230E 02	-0.17772E 02
34	0.22349E 00	0.18399E 00	0.36001E 03	0.22055E 04	-0.13997E 02	0.10549E 03
35	0.22349E 00	0.24800E 00	0.29934E 03	0.21476E 04	0.84126E 01	9.18549E 03
36	0.22349E 00	0.30650E 00	0.16424E 03	0.20157E 04	0.21324E 03	0.14135E 03
37	0.22349E 00	0.37849E 00	0.31174E 03	0.21666E 04	0.30274E 03	0.34932E 02
38	0.22349E 00	0.47750E-01	0.28567E 03	0.20597E 04	-0.59422E 02	-0.31017E 02
39	0.22349E 00	0.11050E 00	0.21957E 03	0.19364E 04	-0.42416E 02	-0.42583E 01
40	0.22349E 00	0.18399E 00	0.15529E 03	0.18328E 04	-0.99136E 01	0.27440E 02
41	0.22349E 00	0.24800E 00	0.20016E 03	0.18508E 04	0.62024E 02	0.42689E 02
42	0.22349E 00	0.30650E 00	0.18027E 03	0.18134E 04	0.11887E 03	0.28130E 02
43	0.22349E 00	0.37849E 00	0.14644E 03	0.17721E 04	0.11881E 03	0.78843E 01

STRESSES IN FRACTURE ZONES SHOWN THUS 

intersections all containing numerous jogs (the process is similar in principle to strain hardening).

It is feasible, but not proven in the literature that similar mechanisms could exist in ceramic materials. Smith<sup>6</sup> of Coors makes the point that residual stress or microcracks can occur due to any of the following factors:

1. Mismatch of expansion coefficient between the matrix and crystal
2. Differences in compaction within the workpiece
3. Differences in firing temperatures over the workpiece
4. Differences in shrinkage over the workpiece
5. Subsurface damage due to grinding, honing, or lapping.

In general these problems can be obviated by extraordinary care during processing. Smith said that had Speedring advised Coors of the eventual use of the component then these precautions would have been taken. Clearly much more care in coordinating the activities of the various vendors is required.

So far as the finishing operations are concerned, grinding and particularly lapping can be regarded as severe from the point of view of surface deformation. In particular, the vast amount of energy expended during the ultrasonic machining of the screw holes on the O.D. could have resulted in some surface damage.

#### 4.4 Contribution from Screws

Investigation of the bearing area under the screw heads on the rotor halves showed that there had been transfer of metal from the screw heads to the rotor halves. However, it appeared that there had not been contact under all of the heads. The effect of this would be to increase the contact stress due to the torque on the bolts. This, in combination with incorrect torque levels being applied, may account for excessive stresses in this area of the assembly.

#### 4.5 Material

The material call-out on the rotor halves was Coors AD 999 alumina (cold pressed) or Avco high density alumina (hot pressed). However, due to delivery problems the call-out was changed to Coors AD 995. The relevant properties of these materials are contrasted in Table 3 (taken from manufacturers handbooks).

Table 3

#### PROPERTIES OF ALUMINAS

Name	Youngs Modulus (lb/in <sup>2</sup> )	Flexural Strength (lb/in <sup>3</sup> )
Avco	59 x 10 <sup>6</sup>	60 x 10 <sup>3</sup>
AD 995	52 x 10 <sup>6</sup>	46 x 10 <sup>3</sup>
AD 999	56 x 10 <sup>6</sup>	105 x 10 <sup>3</sup>

However as shown in figure 33, the material does not always meet its quoted strength. Clearly the stress levels calculated are insufficient to cause failure if the strength of the ceramic is anywhere close to that quoted.

If the material has cracks or flaws, then the fracture strength will be well below that which would be otherwise expected. In appendix D the fracture stress for a cracked material is discussed according to the Griffith criteria (see figure 34).

#### 4.6 Classification of Failure

Examination of the fractures indicates that they are intercrystalline brittle failures. The cracks at the outside were initiated at the stress concentration from the bolt holes. These cracks would continue to propagate until the energy had been dissipated.

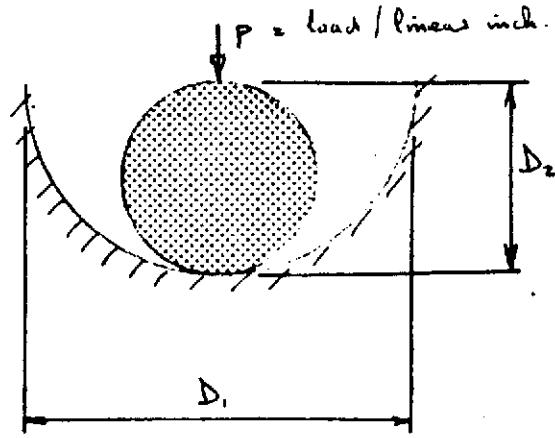
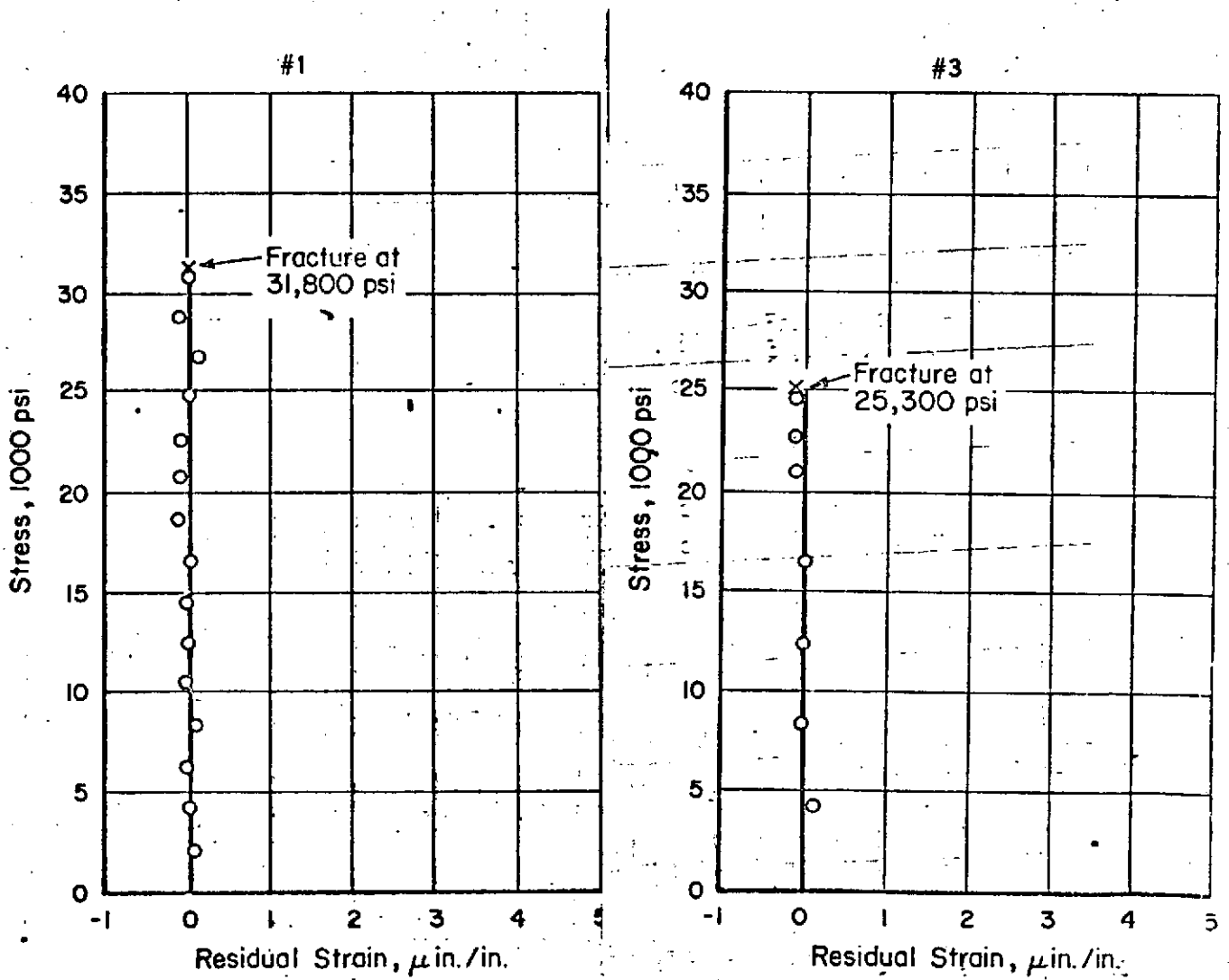


FIGURE 32 CYLINDER IN CIRCULAR GROOVE



MICROYIELD STRESS OF AD 995 ALUMINUM OXIDE SPECIMEN 1 & 3 AFTER IMGRAM<sup>5</sup>

FIGURE 33

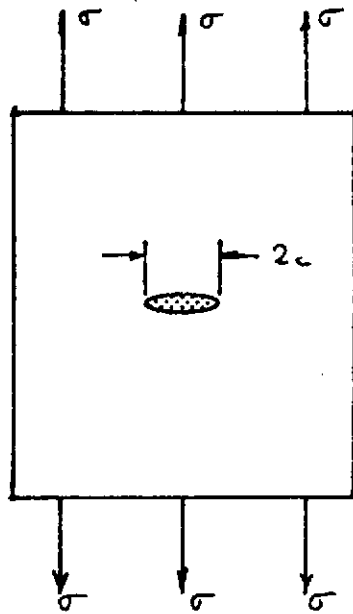


FIGURE 34 ELLIPTICAL CRACK IN A PLATE.

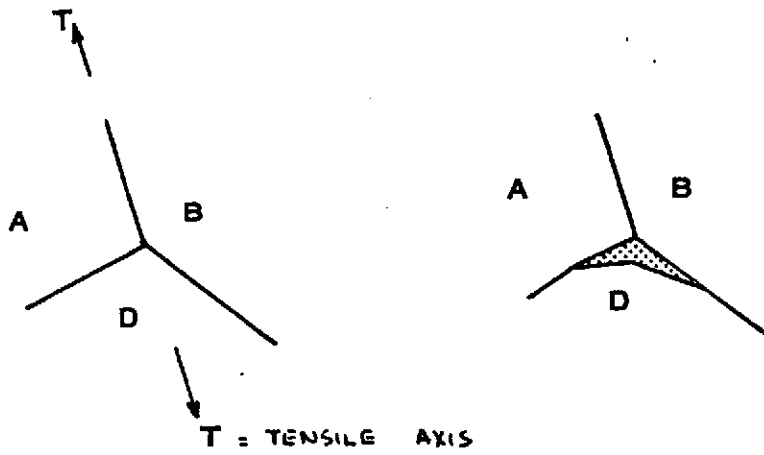


FIGURE 35 FORMATION OF CRACK IN BCC MATERIAL

Of special interest are the Y shaped cracks close to the bores. In BCC materials, cracks of this type can result from successive intersections of deformation twins (see figure 35). A similar mechanism occurs in high temperature creep tests, where some of the deformation is caused by sliding along grain boundaries. In this case a crack forms at a grain boundary which is normal to the applied tensile stress and intersects two other grain boundaries along which some sliding has already occurred. HCP ceramics such as  $Al_2O_3$  have an extremely complex structure which results in an insufficient number of independent slip systems for general deformation. However, it is suggested that a high energy impulse could propagate a crack along the TT axis (figure 35) in an intergranular fashion up to the triple point. Here two other grain boundaries would make it energetically favorable to split into the "Y" configuration.

#### 5.0 PROBABLE FAILURE MODE

The wheel did not fail at speeds up to 30 K rpm in 11.25 psia of hydrogen. In addition a review of the stability parameters reveals that #012 was well within the stability parameter. Also the disturbance detected by the axial capacitance probe was at wheel speed rather than half wheel speed. In addition the wheel ran up to 48 K rpm after balancing without any sign of a disturbance at a frequency of half wheel speed. These pieces of evidence lead one to the conclusion that a hydrodynamic instability was not responsible for the failure of the wheel.

A careful review of the stress levels in the wheel under normal running conditions, but using high stress concentration factors, leads one to the conclusion that this was not a stress failure per se. There is no doubt that design modifications can be made to reduce stress concentrations. Material processing could be more carefully monitored and a superior grade of alumina could be used.

However, it is evident that these factors, albeit reducing the safety factor, were not in themselves responsible for the failure.

Further, the review of the effect of excessive temperatures in the hysteresis ring show that this could not have been the reason for failure.

Conversely the analysis of the effect of centrifugal forces in an unbalanced wheel shows that an unbalance of the order of that detected is very close to the value which would initiate slip between the two halves. Also the unbalance forces are not located at the interface and would result in a couple which would tend to initiate a coning motion to the wheel. This motion would be at wheel speed, rather than half wheel speed, which would fit in with the observations made from the axial capacitance gage, on runs #2 and #4.

Once slip between the two halves had occurred there would be an impact between the rotor halves and the shaft resulting in the two cracks in the area of point B (figure 26). The cracks at the outside diameter would be caused by the relative motion of the two halves acting through the stress concentration of the bolts in the bolt holes. One can envision a situation where some screws would be preferentially located so that slip could occur without the screws contacting the sides of the holes.

On the last run, where catastrophic failure occurred, the fact that stable running at 48 K rpm was followed by an apparent instability at wheel speed leads one to the conclusion that a shift of one or more of the screws had occurred. The result of this was probably that a severe unbalance was induced in the wheel and touchdown occurred. In view of the fact that the wheel was already cracked, the impact at this speed would have caused sufficiently high stresses to destroy the wheel.

## 6.0 REMEDIAL ACTION

### 6.1 Salvage of Wheels 010 and 011

A salvage scheme has been proposed which would reduce stresses in the outside diameter by shrink fitting a Ti 6 Al 4V sleeve in this area. The theory is that before rotational stresses can occur the induced compressive stresses from the shrink fit must be overcome. This case has been stress analyzed using the finite element program (see figure 29), and the stresses at the outside are indeed substantially reduced. However, in view of the conclusion that the failure was due to centrifugal effects it has been decided not to incorporate this scheme at this stage.

The following action will be taken to obviate failure on 010 and 011 before they are run:

- a) The wheels will be balanced on the Schenck balancing machine.
- b) The Mallory 1000 nuts and screws will be removed and Ti 6 Al 4V ones substituted. This will substitute a light, high strength alloy for a dense, low strength alloy (see table 4). Thus the Hertzian stresses from the screws will be lower but the torque on the screws can be increased without danger of exceeding the MYS. Ti 6 Al 4V does not match the expansion coefficient of  $Al_2O_3$ , but is not very different. This change will result in a change in the overall angular momentum to  $4.74 \times 10^5$  gm cm<sup>2</sup>/sec from  $5.0 \times 10^5$  gm cm<sup>2</sup>/sec but in a test wheel this is not considered to be a serious objection.
- c) A thin film of epoxy will be applied around the outside diameter of each rotor screw to prevent movement. The clearance of the screw in the other rotor half will still be sufficient to allow for alignment of one rotor half with respect to the other.
- d) The screw torque will be increased from 22 oz. ins. to 45 oz. ins.

TABLE 4

Comparison of Mallory 1000 and Ti 6 Al 4V

<u>Alloy</u>	<u>Density (lb/in<sup>3</sup>)</u>	<u>Expansion Coefficient (in/in/<sup>o</sup>F)</u>	<u>MYS (lb/in<sup>2</sup> x 10<sup>3</sup>)</u>
Mallory 1000	.6	3.23	<u>8</u>
Ti 6 Al 4V	.16	4.9	70

6.2 Design Changes

- a) The material utilized will change from AD 995 to Avco high density alumina or Coors AD 999.
- b) The Mallory 1000 screws and nuts shall be changed to Ti 6 Al 4V.
- c) Dimensional tolerances on the rotor halves, screws and nuts shall be tightened so as to reduce the possibility of unbalance.
- d) The flatness and surface finish of the screw and nut seating faces shall be improved so as to ensure uniform distribution of the loads.
- e) Similarly the flatness and perpendicularity of the nut and screw seating faces shall be improved.
- f) Radii around the screw holes will be increased wherever possible so as to reduce the stress concentration factors.
- g) The torque call-out on the rotor screws shall be increased.
- h) A thin film of epoxy shall be applied around the outside of the rotor screws so as to prevent movement.
- i) The ceramic blanks shall be routed via HSSC for inspection before being sent to the vendor for machining.
- j) Care will be taken to ensure that the ceramic manufacturer is aware of the eventual use of the blanks so that extraordinary care can be taken during processing.

## 7.0 CONCLUSIONS

It is concluded that the initial failure of wheel number 012 was due to an unbalance in the wheel resulting in interfacial slip and eventual touchdown. Procedures have been outlined to ensure that this does not occur again. Subsequent failure was due to an unbalance resulting from the shift of a rotor screw. Remedial action has been taken to avoid this in the future.

As an offshoot of this investigating design and material changes have been recommended which will result in a superior assembly.

## 8.0 REFERENCES

1. DeMella, J., Pope, M. H., "Stress and Deflection Analysis of Gimbal and Gas Bearing Assemblies of the RI 1170", G260AAGESA, UGA-2, October 13, 1969.
2. Peterson, R. E., "Stress Concentration Design Factors", Wiley.
3. Roark, R. J., "Formulas for Stress and Strain", McGraw Hill.
4. Meyerson, M. R., Sola, M. C., "Gage Blocks of Superior Stability III - The Attainment of Ultrastability", Trans ASM, Vol. 57, 1964.
5. Ingram, A. G., et al, "Study of Microplastic Properties and Dimensional Stability of Materials", AFML-TR-67-232, Part II.
6. Smith, R. Private communication, 23 October 1969.
7. Griffith, A. A. Phil. Trans. Roy. Soc. A, 221, 163 (1920).
8. Pan, C., Vohr, J., "Design Data: Gas Lubricated Spin Axis Bearings for Gyroscopes", MFI 68, TR29, 17 June 1968.
9. Gitzen, W. H., "Alumina Ceramics", AFML-TR-66-13, January 1966.
10. Davidge, R. W., "Mechanical Properties of Ceramic Materials, Contemp. Phys., V 10, No. 2, 105-124, (1969).
11. Hayden H. W., et al, "The Structure and Properties of Materials, Vol III, Wiley (1965).

APPENDIX A OF UCA-176

Geometry in Failure Mode

Referring to figure 26 with the wheel half fully misaligned

$$\tan \alpha = 2c/l$$

and  $x = r_2 \tan \alpha$

but  $OP = L \cos \alpha - x = L \cos \alpha - r_2 \tan \alpha$

and  $OP = L + h_{20}$  in the aligned condition.

The rotor touches on the journal first if:

$$L \cos \alpha + r_2 \tan \alpha > L + h_{20}$$

Now, assuming  $\alpha$  very small

then  $\tan \alpha = 2c/l$

$$\cos \alpha = 1$$

if  $r_2 \frac{2c}{l} > h_{20}$  then touchdown will occur on the journal first.

Using the actual figures obtained on the wheel

$$r_2 = 0.29$$

$$l = 21$$

$$c = 37 \mu''$$

$$h_{20} = 57 \mu''$$

$$r_2 \frac{2c}{l} = 102$$

So,  $r_2 \frac{2c}{l} > h_{20}$ , and the journal touches first.

APPENDIX B of UCA-176

Friction Coefficient Between the Rotor Halves

Sliding friction tests were conducted on the rotor halves comprising assembly 011. Both rotor halves were cleaned and one half was securely fixed to the top of a rotary and inclining table. The perpendicularity of the table to the local gravity vector was checked with a Talyvel and the zero error (10') recorded.

The other rotor half was then placed on the first and the table inclined until slip was just starting. The table angle, less the zero error was then recorded. This test was repeated five times, and the average friction coefficient computed ( $\mu = .158$ ).

The above tests were then repeated but with a normal force of about 10 pounds and sliding being induced to the two rotor halves as one was placed on the other, to simulate assembly. In this case  $\mu = .185$  due to the slight amount of wringing that occurred.

APPENDIX C of UCA-176

Stress Levels in Rotor Halves

a) Stress Concentration

Using published stress concentration factors<sup>2</sup>

$K_t$  = stress concentration factor

$$= \frac{\sigma_{\max}}{\sigma_t}$$

where,  $\sigma_{\max}$  = maximum stress due to concentration

$\sigma_t$  = tangential stress

Conservatively, take  $K_t = 4$

then  $\sigma_{\max} = 4 \times 2050 = 8200 \text{ lbs/in}^2$

b) Radial Force From Screws

$F$  = force due to each screw

$$= \frac{W}{g} \omega^2 r$$

where  $W = 1.843 \times 10^{-3} \text{ lbs}$

$\omega^2 = 25.4 \times 10^6 \text{ rad/sec}^2$

$r = .576 \text{ ins}$

$F = 70.2 \text{ lbs}$

Considering the model shown in figure 3 $\ddagger$ <sup>3</sup>

$\sigma_{c \max}$  = maximum compressive stress

$$= 0.798 \sqrt{\left\{ \frac{P \frac{D1 - D2}{D1D2}}{1 - \nu_1^2 + 1 - \nu_2^2} \right\} \frac{1}{\frac{E1}{E2}}} = 600 \text{ lb/in}^2$$

is stress is in opposite sense to the radial stress.

APPENDIX D of UCA-176

Fracture of a Brittle Material

A brittle material with cracks or flaws will have a fracture strength well below that of an undamaged material. The original thermodynamic treatment is due to Griffith<sup>7</sup> who based his prediction on the energy balance at the instant of fracture initiation. The crack cannot start to grow unless the elastic energy released by the specimen, plus any external work done, is equal to or greater than the surface energy of the material, i.e., when

$$- (\partial U / \partial A) \geq \gamma$$

where A is the area of the fracture face.

Considering a crack of elliptical section, as in figure 34, with a major axis of length 2c, in a thin plate of material of unit thickness under a tensile stress normal to the major axis

$$\text{Then } A = 4C$$

and Griffith showed that, for a narrow slit crack with sharp ends

$$- (\partial U / \partial A) = \frac{\pi c \sigma_F^2}{2E}$$

where  $\sigma_F$  = fracture stress

$$= \sqrt{\left\{ \frac{2E \gamma_a}{\pi C} \right\}}$$

Thus the fracture stress is proportional to  $(1/\sqrt{C})$  and any increase of crack

APPENDIX D (Cont'd)

length will adversely affect the strength of the material. This can be seen when one considers that the theoretical strength<sup>9</sup> of  $\text{Al}_2\text{O}_3$  is  $5.5 \times 10^6$  lbs/in<sup>2</sup> but in practice this is never reached due to microcracks.

$$\sigma_{th} = \text{theoretical strength} = 5.5 \times 10^6 \text{ lbs/in}^2$$

$$E_{th} = \text{elastic modulus} = 10 \times \sigma_{th} = 55 \times 10^6$$

$$\gamma = \text{surface energy at surface} = 18 \times 10^3 \text{ erg/cm}^2$$

$$\begin{aligned} \gamma_a &= \text{surface energy in intercrystalline area} \\ &= 9 \times 10^3 \text{ erg/cm}^2 \end{aligned}$$

$$c = 1 \mu = 40 \times 10^{-6} \text{ ins (assumed)}$$

$$\text{then } \sigma_F = 1143 \text{ lbs/in}^2$$

**APPENDIX C**

**MATHEMATICAL ANALYSIS  
GAS BEARING WHEEL  
COMPUTER PROGRAM  
AWL-5**

```
SUBROUTINE STRT1%DATA,TITLE<
DIMENSION DATA%1<,TITLE%20<,BUF%5<
IR#2
IW#5
K#0
```

```
C TEST FOR BLANK CARD TO END RUN.
```

```
DO 10 I#1,10
J#10&I
IF %TITLE%I<-TITLE%J<< 12,10,12
```

```
10 CONTINUE
WRITE %IW,2<
CALL EXIT
```

```
C READ INPUT DATA IN HS STANDARD FORM.
```

```
12 READ %IR,3< K,XLOC,BUF
IF %K< 14,22,14
```

```
14 IF %XLOC< 16,18,16
```

```
16 J#ABS%XLOC<
```

```
18 DO 20 I#1,<
DATA%J<#BUF%I<
```

```
20 J#J&1
```

```
22 IF %XLOC< 24,12,12
```

```
24 RETURN
```

```
1 FORMAT%20A4<
```

```
2 FORMAT%//@ END OF JOB@<
```

```
3 FORMAT%I1,E11.4,SE12.5<
```

```
END
```

```
FUNCTION HDELT%TCLEA,DELT,AJLEN,RADJ,CLEAR,RADT,THMIS,DELH<
```

```
C
C CALCULATE THRUST PLATE- ROTOR CLEARANCE
```

```
TART1#2.*SIN%DELT/2.<
```

```
TART2#%AJLEN/2.-TCLEA<#%AJLEN/2.-TCLEA<
```

```
TART3#RADT*RADT
```

```
TART4#SQRT%TART2&TART3<
```

```
TART5#1.570795-DELT/2.-ATAN%%AJLEN/2.-TCLEA</RADT<
```

```
TART6#SIN%TART5<
```

```
TART7#TART1*TART4*TART6
```

```
TART0#COS%TART5<
```

```
TART8#TART1*TART4*TART0
```

```
TART9# RADT-TART8
```

```
HDELT#TCLEA-TART7 &TART9*SIN%THMIS</COS%THMIS<
```

```
HDELT#HDELT-DELH
```

```
RETURN
```

```
END
```

```
FUNCTION CDELT%CLEAR,DELT,AJLEN,TCLEA,RADJ,DELC<
```

```
C
C CALCULATE SHAFT-ROTOR CLEARANCE
```

```
PART1#2.*SIN%DELT/2.<
```

```
PART2#%AJLEN/2.-TCLEA<#%AJLEN/2.-TCLEA<
```

```
PART3#%RADJ&CLEAR<#%RADJ&CLEAR<
```

```
PART4#SQRT%PART2&PART3<
```

```
PART5#COS%1.570795-DELT/2.-ATAN%%AJLEN/2.-TCLEA</%RADJ&CLEAR<<<
```

```
PART6#PART1*PART4*PART5
```

```
CDELT#CLEAR-PART6
```

```
CDELT#CDELT-DELC
```

```
RETURN
```

```
END
```

```
FUNCTION GB1(GAMMA,ALPHA,DELTA)
```

```
H=DELTA/(1.+DELTA)
```

```
8120010
88170010
```

```

C=H**3
DEN=(1.+GAMMA*C)*(GAMMA+C)+C*(COS(ALPHA)/SIN(ALPHA))**2*(1.+GAMMA)
1**2
GB1=H**2*(1.+GAMMA)*(1.+(COS(ALPHA)/SIN(ALPHA))**2)*(GAMMA+C)/DEN
RETURN
END
FUNCTION CORAD%GROOV,ALPHA,GAMMA,DELTA<
H#DELTA/%1.&DELTA<
C#H*H*H
A#3.1416*SIN%ALPHA</%1.&GAMMA*C<
A#A/%GROOV*COS%ALPHA</%1.&GAMMA</%1.&C<<
CORAD#EXP%A*%1.-ALPHA/1.5708<<
RETURN
END
FUNCTION GS2(GAMMA,ALPHA,DELTA)
H=DELTA/(1.+DELTA)
C=H**3
DEN=(1.+GAMMA*C)*(GAMMA+C)+C*(COS(ALPHA)/SIN(ALPHA))**2*(1.+GAMMA)
1**2
FRAC=3.*GAMMA*H*(1.-H)**2*(1.+GAMMA*H**3)/DEN
SUM=GAMMA+H+FRAC
GS2=SUM/(1.+GAMMA)
RETURN
END
FUNCTION GS1%GAMMA,ALPHA,DELTA<
H#DELTA/%1.&DELTA<
C#H*H*H
DEN#%1.&GAMMA*C</%GAMMA<&C<&C*%COS%ALPHA</SIN%ALPHA<</%1.&GAMMA<
1**2
GS1#GAMMA*H**2*COS%ALPHA</SIN%ALPHA</%1.-H</%1.-C</DEN
RETURN
END
SUBROUTINE SLEW%CLEAR,WMIS,AJLEN,TCLEA,RADJ,RADT,THMIS,ECCT,ECCJ,
1IER,ECCMA,CD,HD,DELT,DELC,DELH,K<

```

```

C
C   CALCULATE WHETHER ROTOR HITS SHAFT OR THRUST PLATE FIRST DURING SLEW
C
IF%K-1<3000,3001,3001
3001 IF%WMIS<3002,3004,3004
3002 DELH#-DELH
DELC#-DELC
GO TO 5000
3004 DELH#DELH
DELC#DELC
GO TO 5000
3000 IF%WMIS<3004,3004,3002
5000 J#0
DDELT#.8725 E-04
THMIS#THMIS*4.8467 E-06
TOL#.01
DELT#0
DO 900 I#1,500,1
801 DELT#DELT+DDELT
CD#CDEL%CLEAR,DELT,AJLEN,TCLEA,RADJ,DELC<
HD#HDEL%TCLEA,DELT,AJLEN,RADJ,CLEAR,RADT,THMIS,DELH<
ECCJ#%CLEAR-CD</CLEAR
ECCT#%TCLEA-HD</TCLEA
IF%ECCMA-ECCJ<101,102,103
101 IF%ECCMA-ECCT<109,109,107
102 IF%ECCMA-ECCT<109,105,104
103 IF%ECCMA-ECCT<108,106,900

```

```

104 IER#1
    GO TO 200
105 IER#2
    GO TO 200
106 IER#3
    GO TO 200
107 IF%ABS%ECCMA-ECCJ<-TOL<104,104,109
108 IF%ABS%ECCMA-ECCT<-TOL<106,106,109
109 DELT#DELT-DDELT
    DDELT#0.1*DDELT
    J#JA1
    IF%J-1000<801,801,110
900 CONTINUE
    IER#4
    GO TO 200
110 IER#5
200 CONTINUE
    RETURN
END
FUNCTION AUSM%COMP,S<
    CC#COMP*COMP
    ALPHA#SQRT%.5*%SQRT%1&CC<&1<<
    BETA#SQRT%.5*%SQRT%1&CC<-1<<
    AA#2*ALPH*S
    AB#2*BETA*S
    EA#EXP%AA<
    CHOS#.5*%EA&1/EA<
    SHIN#.5*%EA-1/EA<
    BRAK#C4OS-COS%AB<
    AC#1/CC
    DEN#S*SQRT%AC<*BRAK<
    AH#COMP*ALPH%BETA
    AK#COMP*BETA-ALPH
    ANUM#3*%AH*SHIN-AK*SIN%AB<<
    BNUM#3*%AK*SHIN%AH*SIN%AB<<
    TERMA#ANUM/DEN
    TERMB#BNUM/DEN
    AM1#COMP*%COMP%6*COMP/%S*S*AC< - TERMA</AC
    AM2#COMP*%1&3*%1-CC</%S*S*AC< & TERMB</AC
    AUSM#SQRT%AM1*AM1&AM2*AM2<
    RETURN
END
FUNCTION TORQ%ALPHD,ALAM,DELTZ,GAMMA,ECC,NLAM,NTHET<
    DIMENSION XLAM%100<,THETA%60<,PRES%100,60<
    ALPHA#ALPHD*.01745
    TORQ#0.
    THETA#6.28318/NTHET
    N#NTHET/4
    M#2*N
    NBLOK#50/%M/4<
    IX#0
C GENERATE AND STORE 1ST AND 4TH QUADRANT ANGLES
    DO 30 I=1,N
        THETA#I<#2*I-1<#THETA/2.
        IPV#I&N
        THETA#IPV<#6.28318-THETA*I<
C GENERATE AND STORE ELEMENT RADII
        DLAM#1.-ALAM</NLAM
        DO 70 IO=1,NLAM
            XLAM#IO<#1.-%2*IO-1<#DLAM/2.
C CALCULATE PRESSURES IN MIDDLE OF ELEMENTS

```

```

DO 20 IB#1,M
PRES%1,IB<#0.
S#SIN%THETA%IB<<
THETA%IB<#THETA%IB</>.01745
A#ECC*5
D#S*DTHET
DO 10 IA#1,NLAM
ZLAM#XLAM%IA<
B#1.SA*ZLAM
DELTA#DELTZ*B
H=DELTA/(1.+DELTA)

```

65170010

```

C#H*H*H:
T#COS%ALPHA</SIN%ALPHA<
DEN=(1.+GAMMA*C)*(GAMMA+C)+C*T*T*(1.+GAMMA)**2
GONE#GAMMA*H*H*T*(1.-H)*(1.-C)/DEN
PINK#6.*GONE*ZLAM*DLAM/B/B
PRESM#PRES%IA,IB<&PINK/2.
PRES%IA&1,IB<#PRES%IA,IB<&PINK

```

```

C CALCULATE ELEMENTS RESTORING TORQUE
10 TORK#PRESM*ZLAM*ZLAM*DLAM*D&TORK
IF%IB-N<20,12,20
12 ATORK#TORK
TORK#0.
20 CONTINUE
TORQ #-2.*%TORK&ATORK<
RETURN
END

```

\*\*GAS BEARING GYRO WHEEL DESIGN.

C THIS PROGRAM IS DESCRIBED IN MEMO G02BA0000A URA-19, NOV 70.  
C EXTENDED TO LONG JOURNAL, AND MORE ACCURATE THRUST SLEW ADDED,  
DEC 70.

```

REAL JLEN,JLOAD,JLENE,KLEW
DIMENSION TITLE%20<,&DATA%35<
EQUIVALENCE (DATA( 1),RADTE),(DATA( 2),RADBE),(DATA( 3),ECLRT) AWLS 30
EQUIVALENCE (DATA( 4),EGRDT),(DATA( 5),GROOV),(DATA( 6),ALPHT) AWLS 40
EQUIVALENCE (DATA( 7),GAMT),(DATA( 8),EFFA),(DATA( 9),RADJE) AWLS 50
EQUIVALENCE (DATA(10),JLENE),(DATA(11),GRLE),(DATA(12),ECLRJ) AWLS 60
EQUIVALENCE (DATA(13),EGRDJ),(DATA(14),ALPHJ),(DATA(15),GAMJ) AWLS 70
EQUIVALENCE (DATA(16),EFFR),(DATA(17),WLENE),(DATA(18),SPEED) AWLS 80
EQUIVALENCE (DATA(19),EPRSF),(DATA(20),DELTA),(DATA(21),ECCMI) AWLS 90
EQUIVALENCE (DATA(22),ECCMA),(DATA(23),ANGM0),(DATA(24),AMAS) AWLS 100
EQUIVALENCE (DATA(25),EDCJ),(DATA(26),EDCT),(DATA(27),EDGJ) AWLS 110
EQUIVALENCE (DATA(28),EDGT),(DATA(29),DSPED),(DATA(30),EDFPR) AWLS 120
EQUIVALENCE (DATA(31),ANSTP),(DATA(32),ANGAS),&DATA%33<,&WMIS<
EQUIVALENCE&DATA%34<,&THMIS<,&DATA%35<,&TCMIS<

```

```

1 CALL STRT1(DATA,TITLE) AWLS 140
C RADTE THRUST OUTSIDE RADIUS (INCH) AWLS 150
C RADBE THRUST SEAL RADIUS (INCH) AWLS 160
C ECLRT THRUST CLEARANCE (INCH) AWLS 170
C EGRDT THRUST GROOVE DEPTH (INCH) AWLS 180
C GROOV NO. OF THRUST BRG. GROOVES AWLS 190
C ALPHT THRUST GROOVE ANGLE (DEG) AWLS 200
C GAMT LAND/GROOVE RATIO-THRUST AWLS 210
C EFFA AXIAL (THRUST) EFFICIENCY AWLS 220
C RADJE JOURNAL RADIUS (INCH) AWLS 230
C JLENE ACTIVE LENGTH OF JOURNAL (INCH) AWLS 240
C GRLE JOURNAL AXIAL GROOVE LENGTH (INCH) AWLS 250
C ECLRJ JOURNAL CLEARANCE (INCH) AWLS 260
C EGRDJ JOURNAL GROOVE DEPTH (INCH) AWLS 270
C ALPHJ JOURNAL GROOVE ANGLE (DEG) AWLS 280
C GAMJ LAND/GROOVE RATIO-JOURNAL AWLS 290

```

C	EFFR	RADIAL (JOURNAL) EFFICIENCY		AWL5 300
C	WLENE	AXIAL LENGTH BETWEEN THRUST BRGS.	(INCH)	AWL5 310
C	SPEED	ROTOR SPEED	(RAD/SEC)	AWL5 320
C	EPRSF	FLOAT PRESSURE	(LB/SQ.IN)	AWL5 330
C	DELTA	DRAG FACTOR	(MKS)	AWL5 340
C	ECCMI	MINOR ECCENTRICITY RATIO		AWL5 350
C	ECCMA	MAJOR ECCENTRICITY RATIO		AWL5 360
C	ANGMO	ANGULAR MOMENTUM (MKS. = CGS X E-7)		AWL5 370
C	AMAS	ROTOR MASS	(KG)	AWL5 380
C	THMIS	THRUST PLATE 1 MISALIGNMENT	%ARCSEC<	
C		THRUST PLATE 1 IS ON NEG.END OF SPIN VECTOR		
C		POSITIVE IF CW WITH & SPIN VECTOR AT LEFT		
C	TCMIS	THRUST PLATE 2 MISALIGNMENT	%ARCSEC<	
C		THRUST PLATE 2 IS ON POS.END OF SPIN VECTOR		
C		& IF CCW WITH & SPIN VECTOR AT LEFT		
C	WMIS	WHEEL MISALIGNMENT	%INCH<	
C		& IF & SA SIDE IS HIGHER		
C	EDCJ	JOURNAL CLEARANCE INCREMENT	(INCH)	AWL5 390
C	EDCT	THRUST CLEARANCE INCREMENT	(INCH)	AWL5 400
C	EDGJ	JOURNAL GROOVE DEPTH INCREMENT	(INCH)	AWL5 410
C	EDGT	THRUST GROOVE DEPTH INCREMENT	(INCH)	AWL5 420
C	DSPED	SPEED INCREMENT	(RAD/SEC)	AWL5 430
C	EDFPR	FLOAT PRESSURE INCREMENT	(LB/SQ.IN)	AWL5 440
C	NSTEP	NO. OF STEPS EACH SIDE OF NOMINAL REQUIRED		AWL5 450
C	NGAS=CODE.	1=HYDROGEN	2=HELIUM	3=NEON
C		4=AIR	5,6 NOT ALLOCATED.	
C				AWL5 460
C	NPAGE=1			AWL5 490
C	NSTEP=ANSTP			AWL5 490
C	NGAS=ANGAS			AWL5 500
C	WRITE(5, 51)TITLE,NPAGE			AWL5 510
C	IF (NGAS)9,9,2			AWL5 520
C	2 GO TO (3,4,5,6,7,8),NGAS			AWL5 530
C	3 VISC=8.8E-6			AWL5 540
C	RHO=0.09			AWL5 550
C		AMFP#MEAN FREE PATH AT ONE ATM*ATM. PRESSURE	%MKS<	
C	AMFP#1.176E-2			AWL5 560
C	WRITE (5, 59)			AWL5 570
C	GO TO 10			AWL5 580
C	4 VISC=1.97E-5			AWL5 580
C	RHO=0.18			AWL5 590
C	AMFP#1.855E-2			
C	WRITE (5, 60)			AWL5 600
C	GO TO 10			AWL5 610
C	5 VISC=3.1E-5			AWL5 620
C	RHO=0.9			AWL5 630
C	AMFP#1.318E-2			
C	WRITE (5, 61)			AWL5 640
C	GO TO 10			AWL5 650
C	6 VISC=1.83E-5			AWL5 660
C	RHO=1.293			AWL5 670
C	AMFP#6.39E-3			
C	WRITE (5, 62)			AWL5 680
C	GO TO 10			AWL5 690
C	7 CONTINUE			AWL5 700
C	8 CONTINUE			AWL5 710
C	9 WRITE (5, 63)			AWL5 720
C	GO TO 1			AWL5 730
C	10 SLEN=JLENE/(2.*RADJE<			AWL5 740
C	EVISC=VISC*1.49E-4			AWL5 750
C	WRITE(5, 52)ANGMO,AMAS,ECCMI,ECCMA,EVISC,RHO,DELTA			AWL5 760
C	WRITE(5, 53)RADJE,GRLE ,SLEN,WLENE,ALPHJ,GAMJ,EFFR			AWL5 770

WRITE(5, 54)RADTE,RADBE,GROOV,ALPHT,GAMT,EFFA,WMIS,THMIS,TCMIS

CONVERT TO MKS UNITS FOR COMPUTATION.

RADJ=RADJE*0.0254	AWL5 790
RADT=RADTE*0.0254	AWL5 800
RADB=RADBE*0.0254	AWL5 81
JLEN=JLENE*0.0254	AWL5 82
WLEN=WLENE*0.0254	AWL5 83
GRLEN=GRLE *0.0254	AWL5 84
CLRT =ECLRT*0.0254	AWL5 85
CLRJ =ECLRJ*0.0254	AWL5 860
GRDT=EGRDT*0.0254	AWL5 870
GRDJ=EGRDJ*0.0254	AWL5 880
DCJ=EDCJ *0.0254	AWL5 890
DCT=EDCT *0.0254	AWL5 900
DGJ=EDGJ *0.0254	AWL5 910
DGT=EDGT *0.0254	AWL5 920
PRESF=EPRSF*6895.24	AWL5 930
DFLPR=EDFPR*6895.24	AWL5 940
IA#1	AWL5 950
IB=0	AWL5 960
M=NSTEP+1	AWL5 970
N=2*NSTEP+1	AWL5 980
KOUNT=1	AWL5 990
TAUN=(GRDJ+CLRJ)/CLRJ	AWL51000
ANGMX=ANGMO	AWL51010
STOR1=CLRT	AWL51020
STOR2=CLRJ	AWL51030
STOR3=GRDT	AWL51040
STOR4=GRDJ	AWL51050
STOR5=SPEED	AWL51060
A1=3.*VISC*EFFA	AWL51070
EA=1.-ECCMI	AWL51080
EAX=1.-ECCMA	AWL51090
EB=1.+ECCMI	AWL51100
EBX=1.+ECCMA	AWL51110
E=EA**(-3)+EB**(-3)	AWL51120
EX=EAX**(-3)+EBX**(-3)	AWL51130
ALO=RADJ/RADT	AWL51140
ALB=RADB/RADT	AWL51150
A20=ALOG(ALB)	AWL51160
A4=(1.-ALB**4)*1.5708	AWL51170
A5=(ALB**4-ALO**4)/(1.-ECCMI**2)*3.1416	AWL51180
A2=1.11*SLEN	AWL51190
A3=VISC*RADT**4	AWL51200
A6=A3*EFFA	AWL51210
A33=6.*VISC*RADT*RADT	AWL51220
A7=6.*VISC*RADJ	AWL51230
A8=1.5*SLEN*EFFR*RADJ*RADJ	AWL51240
A9=A7*RADJ	AWL51250
A10=A7*GRLEN*EFFR	AWL51260
A11=9.9E6*AMAS*AMAS	AWL51270
A13=AMAS/(4.*SLEN*RADJ*RADJ)	AWL51280
A14=ECCMA/(AMAS*9.81)	AWL51290
X=ECCMA/ECCMA	AWL51300
A15=2.*(1.-SQRT(1.-X))/(X*SQRT(1.-X))	AWL51310
BL=SLEN*RADJ	AWL51320
TEST=WLEN/3.	AWL51330
A16=4.905*AMAS*(WLEN-RADJ*SLEN)**2/WLEN/ECCMA	AWL51340
A18=11.8*VISC*RADJ**4*SLEN	AWL51350
A19=DELTA*SQRT(RHO*VISC)	AWL51360

	A29=1.-ALB*ALB	AWL51390
	AAJ#EFFR*.52359	
	ALPRT=ALPHT*.01745	AWL51400
	ALPRJ=ALPHJ*.01745	AWL51410
		AWL51420
	START THRUST BEARING CALCS.	AWL51430
11	DELTT=CLRT/GRDT	AWL51440
	TKNUD#AMFP/%PRESF*CLRT<	
	GS1T=GS1(GAMT,ALPRT,DELTT)	AWL51450
	COR=CORAD(GROOV,ALPRT,GAMT,DELTT)	AWL51460
	CRADT=RADT/COR	AWL51470
	CLO=RADJ/CRADT	AWL51480
	CLB#RADB/CRADT	AWL51485
	A21=A20-ALOG(CLO)	AWL51490
	A30=A29+2.*CLO*CLO*A20	AWL51500
	A31=ALB*ALB-CLO*CLO-2.*CLO*CLO*A21	AWL51510
	A32=1.+ALB*ALB-2.*CLO*CLO	AWL51520
	D1=DELTT*EA	AWL51530
	D1X=DELTT*EAX	AWL51540
	D2=DELTT*EB	AWL51550
	D2X=DELTT*EBX	AWL51560
	GB11=GB1(GAMT,ALPRT,D1)	AWL51570
	GB11X=GB1(GAMT,ALPRT,D1X)	AWL51580
	GB12=GB1(GAMT,ALPRT,D2)	AWL51590
	GB12X=GB1(GAMT,ALPRT,D2X)	AWL51600
	GBE=GB11/(EA*EA*(1./DELTT+EA))+GB12/(EB*EB*(1./DELTT+EB))	AWL51610
	GBEX=GB11X/(EAX*EAX*(1./DELTT+EAX))+GB12X/(EBX*EBX*(1./DELTT+EBX))	AWL51620
	GS11=GS1(GAMT,ALPRT,D1)	AWL51630
	GS11X=GS1(GAMT,ALPRT,D1X)	AWL51640
	GS12=GS1(GAMT,ALPRT,D2)	AWL51650
	GS12X=GS1(GAMT,ALPRT,D2X)	AWL51660
	GS1E=GS11/EA**2-GS12/EB**2	AWL51670
	GS1X=GS11X/EAX**2-GS12X/EBX**2	AWL51680
	A17#2.00*EFFA*VISC*CRADT**5	AWL51690
	GS21=GS2(GAMT,ALPRT,D1)	AWL51700
	GS22=GS2(GAMT,ALPRT,D2)	AWL51710
	GS2E=GS21/EA+GS22/EB	AWL51720
	ANUM=GBE*A30+E*A31	AWL51730
	ANUMX=GBEX*A30+EX*A31	AWL51740
12	FJ=A2*(CLRT/CLRJ)**3	AWL51750
	DENX=FJ+EX*A21-GBEX*A20	AWL51760
	DEN=FJ+E*A21-GBE*A20	AWL51770
	FRAC=ANUM/DEN	AWL51780
	FRACX=ANUMX/DENX	AWL51790
	BRAK=A32-FRAC	AWL51800
	BRAKX=A32-FRACX	AWL51810
	SIGMA=4.71/ECCMI*GS1E*A29*BRAK	AWL51820
13	ASTIF=A6*SIGMA*SPEED/CLRT**3	AWL51830
	TLOAD=.480*GS1X*A29*BRAKX*A6*SPEED/(CLRT*CLRT*AMAS)	AWL51840
	TPRES=A1*SPEED*GS1T/CLRT/CLRT*(CRADT*CRADT-RADB*RADB)	AWL51850
	PT=(A5+A4*GS2E)*A3*SPEED*SPEED/CLRT	AWL51860
		AWL51870
	START JOURNAL BEARING CALCS.	AWL51880
	DELTJ=CLRJ/GRDJ	AWL51890
	GS1J=GS1(GAMJ,ALPRJ,DELTJ)	AWL51900
	APRES=TPRES+PRESF	AWL51910
	AJKNU#AMFP/%APRES*CLRJ<	
	GLAM=A9*SPEED/(APRES*CLRJ*CLRJ)	AWL51920
	IF(KOUNT-4)14,50,14	AWL51930
14	RSTIF=A8*GLAM**.534*APRES/CLRJ	AWL51940
15	PRESJ=A10*SPEED*GS1J/CLRJ/CLRJ	AWL51950

```

PMA=APRES+PRESJ
FI=ATAN(3.78/GLAM-.12)
S=SIN(FI)
DCA=A11*S/RSTIF/ANGMX
CA=1./ASTIF
CW=(SQRT(1.-S*S))/RSTIF
ANISO=A11*(CA-CW)/ANGMX
STAB=A13*CLRJ*SPEED*SPEED/(APRES*GLAM)
JLOAD=A14*CLRJ*RSTIF*A15

```

```

AWL51960
AWL51970
AWL51980
AWL51990
AWL52000
AWL52010
AWL52020
AWL52030
AWL52040

```

C  
C  
C

CALCULATE WHEEL SLEW CAPACITY

THIS CALCULATION NOW INCLUDES TH. PLATE MISALIGN AND WHEEL MISALIGN  
K#0

```

IF%THMIS<2001,2003,2002
2001 IF%TCMIS<2004,2006,2008
2008 IF%ABS%THMIS<-ABS%TCMIS<<2009,2009,2005
2002 IF%TCMIS<2010,2012,2013
2003 IF%TCMIS<2014,2015,2016
2010 IF%ABS%THMIS<-ABS%TCMIS<<2007,2007,2011
2013 AMIS#-TCMIS
BMIS#-THMIS
GO TO 903
2012 AMIS#TCMIS
BMIS#-THMIS
GO TO 903
2014 AMIS#THMIS
BMIS#TCMIS
GO TO 903
2015 AMIS#THMIS
BMIS#THMIS
GO TO 903
2016 AMIS#-TCMIS
BMIS#THMIS
GO TO 903
2006 AMIS#THMIS
BMIS#TCMIS
GO TO 903
2004 AMIS#THMIS
BMIS#TCMIS
GO TO 903
2011 AMIS#-TCMIS
BMIS#-THMIS
GO TO 903
2009 AMIS#-TCMIS
BMIS#-THMIS
GO TO 903
2005 AMIS#THMIS
BMIS#TCMIS
GO TO 903
2007 AMIS#THMIS
BMIS#TCMIS
GO TO 903
903 JL#JLENE/2.
SDELK#ABS%WMIS</%2.*%WLENE-JL<<
DELC#2.*SDELK**RADJE*SDELK&WLENE/2.*SQRT%1.-SDELK*SDELK<<
DELH#2.*SDELK**RADTE*SQRT%1.-SDELK*SDELK<-WLENE/2.*SDELK<
CALL SLEW%ECLRJ,WMIS,WLENE,ECLRT,RADJE,RADTE, AMIS,ECCT,ECCJ,IER,
1ECCMA,CO,HD,DELT,DELC,DELH,K<
250 IF%K-1<251,252,252
251 WRITE%5,121<
GO TO 902

```

Reproduced from best available copy.

```

252 WRITE%5,122<
902 GO TO%18,8000,19,904,905<,IER
904 WRITE%5,1001<DELT,CD,HD,ECCJ,ECCT
WRITE%5,70<
GO TO 906
705 WRITE%5,1000<DELT,CD,HD,ECCJ,ECCT
WRITE%5,90<
GO TO 906
8000 ECCJ#ECCMA
WRITE%5,120<
GO TO 20
18 ECCJ=ECCMA
WRITE%5,90<ECCT,ECCJ
GO TO 20
19 ECCT=ECCMA
WRITE%5,100<ECCT,ECCJ
20 TMOM#TORQ%ALPHT,CLB,DELTT,GAMT,ECCT,15,30<
TTHR#A17*TMOM*SPEED/%CLRT*CLRT<
906 IF(TEST=BL)16,17,17
16 WRITE(5, 57)
C
C USE AUSMAN LONG JOURNAL THEORY.
AMOM#AUSM%GLAM,SLFN<
TJNL#AMOM*APRES*RAJ*WLEN*WLEN*ECCJ*AAJ
GO TO 7000
C
C USE SEPARATED JOURNAL THEORY.
17 TJNL#ECCJ*JLOAD*A16
7000 IF%K-1<101,102,102
101 BLEW#*TJNL*TTTHR</ANGMX
K#1
GO TO 103
102 KLEW#*TJNL*TTTHR</ANGMX
GO TO 21
103 CALL SLEW%ECLRJ,WMTS,WLENE,ECLRT,RAJ,RAJTE, RMIS,ECCT,ECCJ,IER,
1ECCM,CD,HD,DELT,DELC,DELH,K<
GO TO 250
C
C CALCULATE POWER DEMAND.
21 CONTINUE
PJNL=A17*SPEED*SPEED/CLRJ
PWIND=A19*SQRT(PRESF*SPEED**5)
POWER=PT+PJNL+PWIND
TLAM=A33*SPEED/(PRESF*CLRT*CLRT)
C
C CONVERT BACK FROM MKS TO ENGLISH UNITS
BCLRT=CLRT/0.0254
BGRDT=GRDT/0.0254
BCLRJ=CLRJ/0.0254
BGRDJ=GRDJ/0.0254
BPRSF=PRSF/6895.24
BTPRS=TPRS/6895.24
BPRSJ=PRSJ/6895.24
BPMAX=PMAX/6895.24
WRITE(5, 55)BCLRT,BGRDT,BCLRJ,BGRDJ,SPEED,BPRSF,BTPRS,BPRSJ,BPMAX
WRITE(5, 56)DCA,ANISO,STAB, PT,PJNL,PWIND,POWER,BLEW
WRITE%5, 58<GLAM,AJKNU,JLOAD,TLAM,TKNUD,TLOAD,KLEW
IF(NSTEP)1,1,22
C
C PROCEED TO TOLERANCE STUDY.
22 IA=IA+1

```

4 L52140  
 4 L52160  
 4 L52170  
 4 L52080  
 4 L52220  
 4 L52230  
 4 L52250  
 4 L52260  
 4 L52270  
 4 L52280  
 4 L52290  
 4 L52300  
 4 L52310  
 4 L52320  
 4 L52330  
 4 L52340  
 4 L52350  
 4 L52360  
 4 L52370  
 4 L52380  
 4 L52410  
 4 L52420  
 4 L52430  
 4 L52440

	IF (IA-3)24,23,23	AWL52450
23	NPAGE=NPAGE+1	AWL52460
	WRITE(5, 51)TITLE,NPAGE	AWL52470
	IA=0	AWL52480
24	IB=IR+1	AWL52490
	IF (IB-1)26,25,43	AWL52500
25	STIFN=RSTIF	AWL52510
26	GO TO(27,28,29,30,31,34),KOUNT	AWL52520
27	TEMP=DCT	AWL52530
	WORK=CLRT-NSTEP*DCT	AWL52540
	GO TO 32	AWL52550
28	TEMP=DGT	AWL52560
	WORK=GRDT-NSTEP*DGT	AWL52570
	GO TO 32	AWL52580
29	TEMP=DCJ	AWL52590
	WORK=CLRJ-NSTEP*DCJ	AWL52600
	GO TO 32	AWL52610
30	TEMP=DGJ	AWL52620
	WORK=GRDJ-NSTEP*DGJ	AWL52630
	GO TO 32	AWL52640
31	TEMP=DSPED	AWL52650
	WORK=SPEED-NSTEP*DSPED	AWL52660
32	IF (TEMP)35,33,35	AWL52670
33	KOUNT=KOUNT+1	AWL52680
	GO TO 26	AWL52690
34	TEMP=DFLPR	AWL52700
	WORK=PRESF-NSTEP*DFLPR	AWL52710
	IF (TEMP)35,1,35	AWL52720
35	DO 43 I=1,N	AWL52730
	IF (M-I)36,43,36	AWL52740
36	GO TO(37,38,39,40,41,42),KOUNT	AWL52750
37	CLRT=WORK	AWL52760
	GO TO 11	AWL52770
38	GRDT=WORK	AWL52780
	GO TO 11	AWL52790
39	CLRJ=WORK	AWL52800
	GO TO 11	AWL52810
40	GRDJ=WORK	AWL52820
	GO TO 12	AWL52830
41	SPEED=WORK	AWL52840
	ANGMX=ANGMO*SPEED/STORS	AWL52850
	GO TO 13	AWL52860
42	PRESF=WORK	AWL52870
	GO TO 13	AWL52880
43	WORK=WORK+TEMP	AWL52890
	GO TO(44,45,46,47,48,1),KOUNT	AWL52900
44	CLRT=STOR1	AWL52910
	GO TO 49	AWL52920
45	GRDT=STOR3	AWL52930
	GO TO 49	AWL52940
46	CLRJ=STOR2	AWL52950
	GO TO 49	AWL52960
47	GRDJ=STOR4	AWL52970
	GO TO 49	AWL52980
48	SPEED=STOR5	AWL52990
	ANGMX=ANGMO	AWL53000
49	KOUNT=KOUNT+1	AWL53010
	GO TO 26	AWL53020
50	TAU=(GRDJ+CLRJ)/CLRJ	AWL53030
	DTAU=TAUN-TAU	AWL53040
	FACTR=(1.53*SLEN+2.6)*1.E-3*GLAM+(.13*SLEN+.96)	AWL53050

```

DSTIF=STIFN*FACTR*(DTAU/TAU)**2
RSTIF=STIFN-DSTIF
GO TO 15
51 FORMAT('1'///1X,120('-')// 'GAS BEARING WHEEL DESIGN '20A4,
1 ' PAGE'13/1X,120('-')// 'CLOSED SPOOL. MIXED UNITS.1)
52 FORMAT('0',21('* '),4X'F I X E ' V A L U E S'4X,21('* ')//
3 T2,'ANGLR.MOM. ROTOR MASS MINOR ECC. MA
4JOP ECC. VISCOSITY DENSITY DRAG FACT./T5,'(MKS)',T18,'(KA
5G)',T58,'(REYN)',T70,'(MKS)'T83,'(MKS)'/T2,7(E11.4,2X))
53 FORMAT('0JNL.RADIUS GROOVE LEN. L/D RATIO LENGTH O.A.
1 GRV.ANGLE GRV.RATIO JNL.EFFIC./T5,'(IN)'T19,'(IN)'T44,'(IN)
2)'T58,'(DEG)'/T2,7(E11.4,2X))
1000 FORMAT'///@ ECCENTRICITY CANNOT BE MADE WITHIN TOL OF MAJ.ECC.///
1@ SLEW ANGLE#@E12.4,3X@%RAD.<@/@ ROTOR SHAFT CLEARANCE#@E12.4,3X
2@%INCH<@/@ ROTOR THRUST PLATE CLEARANCE#@E12.4,3X@%INCH<@/
3@ JOURNAL ECCENTRICITY#@E12.4/@ THRUST PLATE ECCENTRICITY#@E12.4/<
1001 FORMAT'///^ ROTOR HAS NOT REACHED THRUST PLATE OR SHAFT^/
1@ SLEW ANGLE#@E12.4,3X@%RAD.<@/@ ROTOR SHAFT CLEARANCE#@E12.4,3X
2@%INCH<@/@ ROTOR THRUST PLATE CLEARANCE#@E12.4,3X@%INCH<@/
3@ JOURNAL ECCENTRICITY#@E12.4/@ THRUST PLATE ECCENTRICITY#@E12.4/<
54 FORMAT' @THR.RADIUS SEAL RAD. NO.GROOVES GRV.ANGLE
1 GRV.RATIO THR.EFFIC@4X@WHEEL MIS.@/T5,@%IN<@T18,@%IN<@T45
2,@%DEG<@T83,@%IN<@/T2,7%E11.4,2X<@/0THR.MIS.-@5X@THR.MIS &@/
3T5,@%SEC<@T18,@%SEC<@/T2,2%E11.4,2X<///1X,21% @<,4X@V A R I A B
4L - S@X,21% @<///<
121 FORMAT'@ CCW SLEW RESULT...@/ <
122 FORMAT'@ CW SLEW RESULT...@/ <
70 FORMAT'T10@ROTOR HAS REACHED NEITHER THRUST PLATE NOR SHAFT'/// <
80 FORMAT'T10@ECCENTRICITY WILL NOT CONVERGE TO ECCM@'/// <
100 FORMAT'T10@ROTOR HIT THRUST PLATE FIRST@2X@THR. PL. ECC.#@E14.7,
12X@JOURNAL ECC.#@E11.4'/// <
90 FORMAT'T10@ROTOR HIT SHAFT FIRST@2X@THR. PL. ECC.#@E14.7,2X
1@JOURNAL ECC.#@E11.4'/// <
120 FORMAT'T10@ROTOR HIT SHAFT AND THRUST PLATE SIMULTANEOUSLY'/// <
55 FORMAT('0',T2,'THR.CLEAR THR.GR.DEP JNL.CLEAR JNL.GR.DEP
1 SPEED) FLOAT PRES THR.PRESS JNL.PRESS TOT.PRESS'//
2T4,'(IN)'T19,'(IN)'T31,'(IN)'T42,'(IN)'T54,'(RAD/SEC)',T68,'(LB/SQ
3.IN)'T41,'(LB/SQ.IN)'T94,'(LB/SQ.IN)'T107,'(LB/SQ.IN)'/T2,9(E11.4,
42X))
56 FORMAT('0',T2,'CROSSANISO NORM ANISO STABILITY
1 THR.POWER JNL.POWER WIND.POWER TOT.POWER SLEW CAPAC%CC
2W<@/T2,@%DEG/HR/SQG< %DEG/HR/SQG<@, T54,@%ATT<@,T70,@%WATT<
3',T82,'(WATT)',T95,'(WATT)',T107,'(RAD/SEC)'/T2,3(E11.4,2X),
4T54,5(E11.4,2X))
57 FORMAT'@ LONG JOURNAL SLEW CALCULATED FROM AUGMAN THEORY. @ <
58 FORMAT'@JOURNAL@T16@COMPR.NO@T29@KNUDSEN NO@T42@LOAD CAPAC@
1T59@THRUST@T68@COMPR.NO@T81@KNUDSEN NO@T94@LOAD CAPAC@2X@SLEW CAPA
2C%<@ /@ -----@T17,F7.2,T31,F6.4,T44,F7.2,@G@T59@-----@T69,F7
3.2,T82,F6.4,T96,F7.2@G@T107,@%RAD/SEC<@/T107,E11.4'/// <
59 FORMAT ('+',T50,'GAS IS HYDROGEN')
60 FORMAT ('+',T50,'GAS IS HELIUM')
61 FORMAT ('+',T50,'GAS IS NEON')
62 FORMAT ('+',T50,'GAS IS AIR')
63 FORMAT ('+',T50,'GAS IS NOT SPECIFIED. PUN TERMINATED.1)
EN)

```

```

@L53060
@L53070
@L53080
@L53090
@L53100
@L53110
@L53120
@L53130
@L53140
@L53150
@L53160
@L53170
@L53210
@L53220
@L53230
@L53240
@L53250
@L53260
@L53280
@L53300
@L53350
@L53360
@L53370
@L53380
@L53390
@L53400

```

**Hamilton  
Standard**

**U**  
DIVISION OF UNITED AIRCRAFT CORPORATION  
**A®**

**HSER 6197**

**APPENDIX D**  
**COMPARISON OF**  
**TYPICAL**  
**GAS BEARINGS**

COMPARISON OF TYPICAL GAS BEARINGS

Parameter	Units	RI 1170 WHEEL NO. 21					RI 1010 F N 04					RI 1139DG WHEEL NO. 1						
		Spec Value	Measured Value	Code	Computer Output		Spec Value	Measured Value	Code	Computer Hydrogen Output		Computer Helium Output		Spec Value	Measured Value	Code	Computer Output	
					Using Spec Values	Using Actual Values				Using Spec Values	Using Actual Values	Using Spec Values	Using Actual Values				Using Spec Values	Using Actual Values
Angular Momentum	cgs	5 x 10 <sup>5</sup>	NM		Input		2 x 10 <sup>5</sup>	NM		Input		Input		5 x 10 <sup>5</sup>	NM		Input	
Rotor Mass	gm	50.	41.713	1	Input		37.45	NM		Input		Input		32.39	71.38	1	Input	
Operating Wheel Speed	rpm	48K	48K	1	Input		24K	24K	1	Input		Input		24K	24K	1	Input	
Gas Viscosity	Reyn	Hydrogen 1.311 x 10 <sup>-9</sup>	NA NM		Input Input		Helium 2.935 x 10 <sup>-9</sup>	NA NM		Input Input		Input Input		Helium 2.935 x 10 <sup>-9</sup>	NA NM		Input Input	
Density	gm./liter	.709	NM		Input		.18	NM		Input		Input		.18	NM		Input	
Flat Pressure	Atm Abs	1.5	1.5	1	Input		1.7	1.7	1	Input		Input		2.5	2.5	1	Input	
Journal Material		Solid Pressed High Purity Beryllia	NA		NA		Alumina Coated Al	NA		NA		NA		No. 5 Be Coated With Cr <sub>2</sub> O <sub>3</sub>	NA		NA	
Clearance	μ"	40 ± 5	45	1	Input		40 ± 5	56 39/40	1 2	Input		Input		60 ± 5	56	3	Input	
Groove Length	in.	.105	OK	3	Input		.105	.104/.1042	2	Input		Input		.14	OK	3	Input	
Length	in.	.830/.831	.831030	1	Input		.900/.901	.9031	2	Input		Input		.933/.932	.932135	3	Input	
Diameter	in.	.374/.375	.374895	1	Input		.374/.375	375015/.375020	2	Input		Input		.500/.501	.500723	3	Input	
Groove Angle	deg	25	OK	3	Input		25	25	2	Input		Input		25	OK	3	Input	
Groove Depth	μ"	53 ± 10	(-)+57	1	Input		65 ± 15	(-)+115/174 (+)+109/131	2	Input		Input		80 ± 10	138	3	Input	
Land: Groove Ratio		1.85	NM		Input		1.85	NM		Input		Input		1.85	NM		Input	
No. of Grooves		15	15	1	Assumed ∞		15	15	1	Assumed ∞		Assumed ∞		15	15	3	Assumed ∞	
Load Capacity	g's	66	NM		72   76		50	NM		43   41		72   64		40	NM		107   488	
Power Demand	watts	Low as Poss.	NM		1.5   1.3		Low as Poss.	NM		.3   .3		.6   .6		Low as Poss.	NM		1.92   2.66	
Flat Plate Mat		Coors AD 999 Alumina	NA		NA		Alumina	NA		NA		NA		No. 5 Be Coated With Cr <sub>2</sub> O <sub>3</sub>	NA		NA	
Clearance	μ"	40 ± 5	45	1	Input		50 ± 5	88	1	Input		Input		60 ± 5	57	3	Input	
Outer Radius	in.	.275 Min [.290]	OK	3	Input		.292	(-).2915 (+).2914	2	Input		Input		.365	OK	3	Input	
Seal Radius	in.	.216	OK	3	Input		.232	(-).2325 (+).2325	2	Input		Input		.255	OK	3	Input	
Groove Angle	deg	12	NM		Input		12	NM		Input		Input		12	NM		Input	
Groove Depth	μ"	100 ± 20	(-)+136 (+)+88	1	Input		115 ± 15	(-)+124/145 (+)+94/103	2	Input		Input		150 ± 10	143	3	Input	
No. of Grooves		15	15	1	Assumed ∞		15	15	1	Assumed ∞		Assumed ∞		15	15	3	Assumed ∞	
Land: Groove Ratio		1.0	NM		Input		1.0	NM		Input		Input		1.0	NM		Input	
Load Capacity	g's	66	NM		49   72		50	NM		33   21		73   46		40	NM		47   218	
Power Demand	watts	Low as Poss.	NM		1.0   1.1		Low as Poss.	NM		.3   .2		.6   .4		Low as Poss.	NM		1.14   1.19	
Airage Power	watts	Low as Poss.	NA		1.9   1.9		Low as Poss.	NA		.4   .4		.7   .7		Low as Poss.	NA		.90   .90	
Total Mech Power	watts	Low as Poss.	4.12	1	4.4   4.3		Low as Poss.	He 1.54	1	.9   .8		2.0   1.7		Low as Poss.	3.84 Wheel No. 4	1	3.96   4.16	
Slew Capacity	rad/sec	5.0	3.0	1	4.4   4.1		5.0	cw 1.75 ccw 2.25	1	5.7   5.1		9.7   8.0		2.0	cw 2.7 ccw 1.6	1	9.65   10.5	
Cross Aniso Error	°/hr/g <sup>2</sup>	Abs Value <.01	NM		+.0008   +.0014		Abs Value <.01	NM		+.03   +.03		+.007   +.005		Abs Value <.01	NM		.004   .0002	
Normal Aniso Error	°/hr/g <sup>2</sup>	Abs Value <.01	NM		+.004   -.0017		Abs Value <.01	NM		+.014   +.47		-.008   +.19		Abs Value <.01	NM		.016   .0008	

NA - Not Applicable  
NM - Not Measured

CODE: 1 = Based on HSD Data  
2 = Based on Locomoth Data  
3 = Based on Speedring Data